IMPROVING THE SENSITIVITY AND UTILITY OF PULSED DIPOLAR EXPERIMENTS IN EPR AT 94 GHZ

Claire Louise Motion

A Thesis Submitted for the Degree of PhD
at the
University of St Andrews

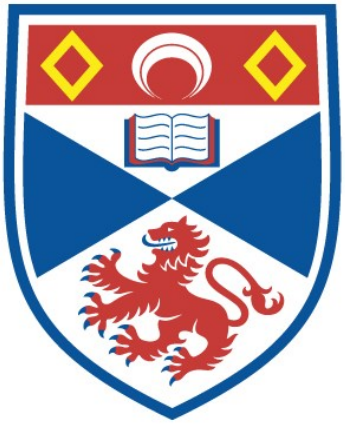

2018

Improving the sensitivity and utility of Pulsed Dipolar Experiments in EPR at 94 GHz

Claire Louise Motion

University of
St Andrews

This thesis is submitted in partial fulfilment for the degree of
PhD
at the University of St Andrews

21st September 2017

Declarations

Candidate's declaration

I, Claire Louise Motion, hereby certify that this thesis, which is approximately 52,000 words in length, has been written by me, and that it is the record of work carried out by me, or principally by myself in collaboration with others as acknowledged, and that it has not been submitted in any previous application for a higher degree.

Date Signature of candidate

I was admitted as a research student in September 2013 and as a candidate for the degree of PhD in September 2014; the higher study for which this is a record was carried out in the University of St Andrews between 2013 and 2017.

Date Signature of candidate

Supervisor's declaration

I hereby certify that the candidate has fulfilled the conditions of the Resolution and Regulations appropriate for the degree of PhD in the University of St Andrews and that the candidate is qualified to submit this thesis in application for that degree.

Date Signature of supervisor

Copyright Agreement

In submitting this thesis to the University of St Andrews I understand that I am giving permission for it to be made available for use in accordance with the regulations of the University Library for the time being in force, subject to any copyright vested in the work not being affected thereby. I also understand that the title and the abstract will be published, and that a copy of the work may be made and supplied to any bona fide library or research worker, that my thesis will be electronically accessible for personal or research use unless exempt by award of an embargo as requested below, and that the library has the right to migrate my thesis into new electronic forms as required to ensure continued access to the thesis. I have obtained any third-party copyright permissions that may be required in order to allow such access and migration, or have requested the appropriate embargo below.

The following is an agreed request by candidate and supervisor regarding the publication of this thesis:

PRINTED COPY

Embargo on all of print copy for a period of 1 year on the following ground(s):
– Publication would preclude future publication

ELECTRONIC COPY

Embargo on all of electronic copy for a period of 1 year on the following ground(s):
– Publication would preclude future publication

Date Signature of candidate

Date Signature of supervisor

Abstract

Pulsed dipolar spectroscopy (PDS) is an electron paramagnetic resonance (EPR) technique, used to conduct long range distance measurements in proteins in the nanometre range. This thesis presents a number of methodological and instrumental techniques to improve the sensitivity and utility of PDS experiments using a home-built high power pulsed spectrometer, HiPER, operating at 94 GHz. These include the implementation of phase-modulated composite pulses, which correct for imperfections arising due to inhomogeneity, and offer increased excitation bandwidth as well as experimental protocols such as annealing and glassing of samples. A theoretical study into the use of matched filtering to reduce echo noise during measurements, has predicted gains of up to a factor of 3 enhancement in signal-to-noise.

Using such techniques we demonstrate sensitivity enhancements of more than 30 on PDS experiments, between nitroxides and Fe centres, in haem-proteins, corresponding to a reduction in averaging time of almost 1,000, in comparison to standard commercial spectrometers operating at X-band. The use of composite pulses in PDS experiments on nitroxide biradicals were also investigated, including their limitations due to intramolecular effects. The thesis then describes a single frequency dipolar modulation experiment, RIDME, and uses high field measurements to determine both the distance and relative orientation of a cobalt-nitroxide system, for the first time. Finally, a design study is conducted to implement frequency and amplitude modulated pulses on a spectrometer at 9/34 GHz to improve sensitivity.

Collaborative Statement

This thesis is the result of my own work carried out at the University of St Andrews between September 2013 and September 2017. Parts of the work presented in this thesis have been peer reviewed and published. All of the text written in the identified chapters was written entirely by me. All figures have been produced by me or reproduced with permission.

- Chapters 2,4 and 5 feature work presented in: **C. L. Motion**, S. L. Cassidy, P. A. S. Cruickshank, D. R. Bolton, R. I. Hunter, H. El Mkami, S. Van Doorslaer, J. E. Lovett and G. M. Smith, *The use of composite pulses for improving DEER signal at 94 GHz.* J. Magn. Reson., vol. 278 , pp. 122-133, Apr. 2017. All experimental work presented was carried out by me, and written by me with scientific advice from co-authors. The echo simulation code used was adapted from work by Dr Scott Cassidy.

- Chapter 6 is based on **C. L. Motion**, S. L. Cassidy, P. A. S. Cruickshank, D. R. Bolton, R. I. Hunter, H. El Mkami, S. Van Doorslaer, J. E. Lovett and G. M. Smith, *The use of composite pulses for improving DEER signal at 94 GHz.* J. Magn. Reson., vol. 278 , pp. 122-133, Apr. 2017. All W-band experimental work was carried out by me, with Q-band results performed by Dr Janet Lovett, and X-band results by Prof Sabine van Doorslaer's group at University of Antwerp. All analysis of the data, including molecular simulations was carried out by me.

- The work presented in Chapter 7 is being prepared for submission to Journal of Physical Chemistry Letters. This work has benefited greatly from collaboration with the Bode Lab and Prof Michael Bühl in the School of Chemistry at St Andrews, who synthesized the sample, performed DFT calculations and provided advice during measurements. All measurements, data analysis presented here was completed and written by me. Drs Bela Bode and Angeliki Giannoulis provided scientific advice.

Claire Louise Motion

September 2017

Acknowledgements

I am extremely grateful to Dr Graham Smith as primary supervisor, providing me with not only an excellent project, but also with unwavering enthusiasm throughout. Your ability to see the positives in practically any situation has definitely helped keep this project on target.

I'm also indebted to Dr Janet Lovett as (unofficial) second supervisor, who swooped in a year into my project, and provided fruitful collaboration as well as encouragement throughout. I'd also like to thank all of the JEL Lab, in particular Dr Stacey Bell for all the myoglobin mutant synthesis and to Ms Anokhi Shah for putting together the TEMPO samples.

As the first woman to complete a PhD in the Millimetre Wave & EPR group, it is only fair that I thank all of the men of the group for their support throughout this PhD. Without whom, this PhD would definitely not have been possible.

Firstly, I'm grateful to Dr Paul Cruickshank for taking me on as an undergraduate summer student and showing me the ropes of HiPER and getting me hooked on EPR. Quite frankly, this is all your fault, Paul! I'm also indebted also to Dr Rob Hunter and Dr Hassane El Mkami who have both assisted greatly in all my experimental work throughout the PhD, and for always coming to assist when something went wrong.

I'm also extremely thankful to Dr Duncan Robertson for all of his assistance, loans of equipment and useful discussions as I attempted to put together AWG stuff. And to Dr David Macfarlane for all help in learning the ropes of both MatLAB and CVI LabWindows. I'd also like to thank Dr Johannes Mckay for, not only all is his help while he was here, but for answering my incessant emails after he ~~escaped~~ left, about all things AWG, and providing me with helpful code to do the waveform corrections.

I also have a heap of gratitude to all my wonderful friends and family who have put up with me and passion for complaining and ranting about nothing in particular, especially during the ups and downs of completing a PhD. I owe you all many pints. In particular, I have to thank Kirstin who has had to put up with me more than anyone, and always been there to drag me out of the lab or to bring me coffee (and occasionally lunch). This thesis most definitely would not have happened without you.

Publications and Presentations

Publications

The following publications have resulted from the work presented within this thesis:

C. L. Motion, J. E. Lovett, S. Bell, S. L. Cassidy, P. A. S. Cruickshank, D. R. Bolton, R. I. Hunter, H. El Mkami, S. Van Doorslaer, and G. M. Smith, **'DEER Sensitivity between Iron Centers and Nitroxides in Heme-Containing Proteins Improves Dramatically Using Broadband, High-Field EPR,'** J. Phys. Chem. Lett., vol. 7, no. 8, pp. 1411-1415, Apr. 2016. URL: dx.doi.org/10.1021/acs.jpclett.6b00456

C. L. Motion, S. L. Cassidy, P. A. S. Cruickshank, D. R. Bolton, R. I. Hunter, H. El Mkami, S. Van Doorslaer, J. E. Lovett and G. M. Smith, **The use of composite pulses for improving DEER signal at 94 GHz.** J. Magn. Reson., vol. 278 , pp. 122-133, Apr. 2017.
URL: http://doi.org/10.1016/j.jmr.2017.03.018

A. Giannoulis, C. L. Motion, M. Oranges, G. M. Smith, M. Bühl and B. E. Bode, **Orientation selection in high-field RIDME and PELDOR experiments involving low-spin Co^{II} ions** Phys. Chem. Chem. Phys., vol. 20, pp. 2151-2154, Dec. 2017.

Presentations

- "*Enhancing the modulation depth and sensitivity in high field PELDOR experiments*", Royal Society of Chemistry EPR Group Conference, Southampton, UK. April 2015

- "*DEER Sensitivity Between Iron Centres and Nitroxides in Heme-containing Proteins Improves Dramatically Using Broadband, High-field EPR*", Integrated Magnetic Resonance Research Conference, Marwell Hotel, Southampton, UK. March 2016

- "*Improving sensitivity using composite pulses at 94 GHz*", Centre for Magnetic Resonance 7th Annual Meeting, St Andrews, UK. June 2017

Posters

- "*Enhancing the modulation depth and sensitivity in PELDOR experiments at 94 GHz*", 56th Rocky Mountain Conference on Magnetic Resonance, Copper Mountain, Colorado, USA. July 2014.
- "*DEER Sensitivity Between Iron Centres and Nitroxides in Heme-containing Proteins Improves Dramatically Using Broadband, High-field EPR*", Royal Society of Chemistry EPR Group Conference, Colchester, UK. April 2016
- "*Sensitivity considerations when using shaped pulses at 94 GHz*", 50th Anniversary Royal Society of Chemistry EPR Group Conference, Oxford, UK. April 2017

Awards

- *Best Poster Prize*, 56th Rocky Mountain Conference on Magnetic Resonance, Copper Mountain, Colorado, USA. July 2014.
- *International EPR (ESR) Society Best Poster Prize*, Royal Society of Chemistry EPR Group Conference, Colchester, UK. April 2016
- *Oxford University Press Best Poster Prize*, 50th Anniversary Royal Society of Chemistry EPR Group Conference, Oxford, UK. April 2017

Table of acronyms

AWG	Arbitrary Waveform Generator
DEER	Double Electron-Electron Resonance
DRO	Dielectric Resonator Oscillator
EIKA	Extended Interaction Klystron Amplifier
EPR	Electron Paramagnetic Resonance
ESEEM	Electron Spin Envelope Modulation
FEP	Fluorinated Ethylene Propylene
HiPER	High Power Electron Resonance (the home built W-band instrument)
IF	Intermediate Frequency
LO	Local oscillator
MMM	Multiscale Modelling of Molecular Distances (software package)
MTS	methanethiosulfonate a commonly used nitroxyl spin label
NMR	Nuclear Magnetic Resonance
osPELDOR	Application of PELDOR to conduct orientation measurements
osRIDME	Application of RIDME to conduct orientation measurements
PDS	Pulsed Dipolar Spectroscopy
PELDOR	Pulsed Electron Double Resonance
PMYTO	Permanent Magnet YIG (yttirum iron garget) Tuned Oscillator
Q-band	Referring to measurements around 34 GHz
RF	Radio Frequency
RIDME	Relaxation Inducted Dipolar Modulation Enhancement
SDSL	Site Directed Spin Labelling
SNR	Signal-to-Noise Ratio
SRF	Sequence Repetition Frequency
W-band	Measurements conducted at 94 GHz
X-band	Measurements conducted at 9-10 GHz

Contents

List of Figures

List of Tables

We arrived not yet knowing what was not possible.
Consequently, we expected a lot.

– Hillary D. Rodham (Clinton)
Wellesley College Commencement Speech, 1969.

1 Introduction

1.1 Background

This thesis concerns methodology and instrumentation to improve the sensitivity of pulsed electron paramagnetic resonance (EPR) experiments, used to measure distances in proteins in the nanometre range. Proteins are the most abundant and functionally diverse molecules in living systems. Virtually every life process depends on this class of macromolecules [1]. Understanding the 3D structure of biomolecules is important as it provides crucial insight into the mechanisms that drive their function.

There are many tools available to study the microscopic structure of macromolecules such as nuclear magnetic resonance (NMR), florescence resonance energy transfer (FRET) and X-Ray crystallography. The aim of each technique is to identify and characterise the local and surrounding structure of small, complex biological systems. Electron Paramagnetic Resonance (EPR) spectroscopy has been shown to be a powerful technique to measure and identify the local surroundings of unpaired electrons that can be found within some biological systems. EPR is a magnetic resonance technique where the sample of interest is immersed in a strong

magnetic field (typically 0.3 to 4 Tesla) and is irradiated by microwave radiation. The magnetic field causes the paramagnetic centres (unpaired electrons) present to orientate parallel or anti-parallel to the field, which results in Zeeman splitting that is observable in the emitted or absorbed radiation. The energy difference between the split levels is proportional to the external field, and transitions between states occur when a photon whose energy matches the difference between the levels is absorbed or emitted. In the case of EPR, this energy is typically in the microwave to millimetre wave regime. The resonance of a paramagnetic centre, or unpaired electron, in an atom or molecule is typically spread over a range of frequencies, caused by the underlying coupling of the paramagnetic centre to its local environment. From a spectroscopist's point of view, this means that one can tune one's magnetic field strength and frequency to probe different parts of the paramagnetic centre. By employing pulses of radiation, one can measure distances between two paramagnetic centres present, using dipolar spin-spin coupling. This can be carried out by applying pulses at one frequency, and exciting another part of the spectrum using pulses of another frequency. The dipole-dipole coupling between the unpaired electrons' spin is proportional to the inverse cube of their separation, and is measured using the Pulsed Electron Double Resonance (PELDOR) experiment. This experiment can be routinely used to measure distances between 1.5 and 6 nm, and in more favourable cases, up to 10 nm [2–4]. This is carried out between either embedded intrinsic paramagnetic centres, or extrinsic centres known as spin labels. These can be engineered into the protein of interest using site-directed spin labelling (SDSL) enabling measurements between specific sites in the structure [5–9]. This allows for structural and in some cases, functional information to be obtained about the system, by monitoring its conformational changes, as seen through changes in the separation of the labels under the action of different processes [10, 11].

PELDOR was first reported by Milov et al. in 1984 describing a pulsed technique which measures the dipole-dipole coupling between nearby unpaired electrons [12]. By observing an echo on one set of spins, and inverting its nearby partner spin using pulses of a different frequency, their dipole-dipole interaction leads to a modulation of the observed echo, which is dependent on their relative separation, and in some cases, orientation. This technique was extended to the more ubiquitous 'dead-time free' 4-pulse version [13] which traces this modulation through the echo maximum, allowing for much more accurate fitting, and thus extraction of distance between the spin centres.

Most experiments using PELDOR that are typically carried out on biomacromolecules use spin labels containing a nitroxyl radical. The paramagnetic centre in the spin label is generally at the end of of linker, which, for the commonly used MTS label, is approximately 1 nm long. Due to its flexibility, it can occupy many conformations, dependent on its surroundings. This can be successfully modelled and simulated, and software packages now exist for comparison with experimental findings [14, 15]. Recently there has been significant interest in conducting measurements using intrinsic paramagnetic centres present in the structure, to remove the ambiguity of the spin label and its potential for inducing structural changes to the protein [16–20]. This however can be extremely challenging as embedded centres tend to be metallic, which are spectrally broad and exhibit fast relaxation, strongly inhibiting the sensitivity required for PELDOR. Generally, such measurements are carried out between the embedded centre and a spin label that is attached to the surrounding protein. This has added advantage the centres have different spectroscopic properties, thus it is trivial to excite the spins separately. PELDOR measurements have been reported between low-spin ferric haem and a nitroxide label, with separations of 2.1 and 2.7 nm [17, 18] at X- and Q-band respectively. These experiments required long averaging times to produce sufficient signal-to-noise, which degrades with increasing spectral width of the metal centre.

At lower fields and frequencies, such as X-band at ∼9 GHz (0.33 T) the nitroxide label has a spectral width of ∼ 100 MHz, allowing for sufficient separation of observer and pump pulses in a PELDOR experiment, and adequate excitation of the spin centre using moderate length pulses. However, it is not possible at X-band to distinguish orientation of the nitroxyl centre, as the field strength does not resolve its g-tensor components. To observe and measure the orientation of the label, higher fields (>3 T) must be utilised [21]. However, the extra definition of the nitroxyl centre's spectra is gained by spreading out its spectral components allowing for selective excitation of its orthogonal components. At W-band (94 GHz, 3.35 T) this stretches over 400 MHz, requiring broad, short pulses to ensure suitable excitation [22, 23]. This is further complicated when measurements are carried out using metal centres, whose spectra can stretch over several GHz. This presents a significant challenge in terms of instrumentation to develop spectrometers that can carry out measurements on broad line systems, with sufficient signal-to-noise and short averaging times.

Most EPR spectrometers utilise cavity based resonators to measure spins within samples of interest, where the cavity is engineered to produce enhanced B_1 fields over a narrow range.

Alternatively, broad cavities have also been created which operate over larger frequency bandwidths, but with reduced B_1 field amplitudes which reduce excitation bandwidths of pulses. The sensitivity of PELDOR experiments relies on the number of spins excited by both the observer and pump pulses, thus to improve sensitivity one requires to increase the number of spins excited, and the fidelity with which they are manipulated. A W-band spectrometer, HiPER, has been developed at St Andrews which uses a non-resonant sample holder, allowing for broadband excitation using high power pulses [24]. The spectrometer operates in induction mode[1], with samples placed inside a cylindrical waveguide, supporting a TE_{11} mode. While this supports operation over several GHz, it comes at the cost of the B_1homogeneity of the field, which degrades performance of the pulses, reducing echo amplitudes and fidelity of spin manipulation.

The problem of applied field inhomogeneity has also affected NMR, where surface coils and other RF coil set ups result in inhomogeneous distributions of fields within samples. In 1979 Levitt et al. [25] proposed a new contiguous, phase modulated pulse sequence to compensate for applied field inhomogeneity. By changing the phase, the axis and thus, direction of rotation of the spins is altered, allowing for sequences that correct for imperfections that reduce the fidelity across the sample. In most cases, they also broaden the excitation bandwidth in comparison with standard pulses. Various composite pulses have been developed for use, mainly in NMR, including spatial localisation [26]; double-quantum excitation [27]; sensitivity enhancements in pulse train experiments [28], and many more [29–32]. Their use in EPR however is quite limited, with their first demonstration by the Freed group in 1989, where excitation bandwidths of over 200 MHz was demonstrated using composite pulses [33]. The narrowband BB1 composite pulse was utilised by Morton et al. for use in quantum computing applications. Turro et al. used composite pulses to enhance inversion recovery experiments on nitroxides at X-band [34].

The somewhat limited use of composite pulses in EPR can be attributed to the requirements for high-speed instrumentation for implementation. Development of such instrumentation has also coincided with the availability of high speed arbitrary waveform generators (AWGs). In the last few years, improvements in excitation bandwidths and thus sensitivity in lower frequency (9-35 GHz) pulsed EPR experiments has been provided using much more sophisticated

[1]Induction mode refers to the operation where the sample will absorb or emit a circularly polarised beam on-resonance, with power transferred to the orthogonal polarisation state. This allows for the detection signal (from the sample) to be isolated from the transmitted signals using Faraday rotators and polarising grid.

pulse techniques such as frequency and amplitude modulated pulses, which offer far larger improvements in comparison with composite pulses [35–38]. Their implementation requires the use of an arbitrary waveform generator to produce modulated pulse sequences. However their use at higher frequency becomes much more challenging as the performance of components becomes much more critical. It is only recently (August 2017) that their use at W-band has been successfully reported [39] showing large improvements in modulation depth in PELDOR experiments. The implementation of an AWG at 200 GHz has also been reported, however its use is extremely limited [40]. The implementation of composite pulses, which require discrete phase modulation is somewhat more straightforward at higher frequencies, and can still offer up to a factor of 3 improvement over traditional rectangular pulses when used in PELDOR experiments [41].

Another technique to measure distances between electrons in EPR that has gained interest over the last few years is the Relaxation Induced Dipolar Modulation Enhancement (RIDME) experiment [42, 43]. Unlike PELDOR, this technique uses single frequency pulses to measure distance between electrons, using the dipole-dipole coupling between the observed and nearby spins. This relies on spontaneous relaxation of the partner spin to induce modulation of the observed echo. It has been shown to work well where the partner spin has a much faster electronic relaxation than the observed spin, allowing the user to exploit the much more favourable slow relaxing spin for observation purposes, such as in the case of nitroxide spin labels [44, 45]. In comparison with PELDOR, it has been shown that RIDME can provide up to 7 times enhancement in SNR when measuring distances between a low-spin ferric haem centre and a nitroxide label in a haem-protein [18]. One of the main advantages of this technique comes from the fact it does not require two frequencies to be accommodated within the resonator, like in PELDOR, meaning that the observer pulse can be easily optimised. However, RIDME has the disadvantage that it requires relaxation of the centre to be set as a function of temperature to ensure relaxation occurs to induce modulation. It has also been found to commonly suffer from electron-nuclear modulation effects, although pulse sequences have been proposed to remove this [46]. Due to the fact that RIDME only probes one of the two spins selectively, the effects of orientation selection are not expected to be as strong as observed using PELDOR. However, it has been shown recently that orientation effects have been observed at Q-band, albeit only weakly [44]. It does however suggest that experiments at higher field may render more convincing orientation selective results.

1.2 Overview of thesis

1.2.1 Chapter 2: EPR theory and instrumentation

Chapter 2 contains background theory relevant to EPR, PELDOR and other pulsed techniques such as RIDME. It also provides background theory of composite pulses, and provides an introduction to shaped pulses and necessary electronics. The chapter also includes background on the instrumentation used in thesis, in particular that of the home-built W-band spectrometer, HiPER [24].

1.2.2 Chapter 3: Assessing and improving sensitivity

Chapter 3 describes methods to measure and compare the sensitivity of HiPER in comparison with other spectrometers, and how experimental protocols can be used to improve this. It includes comparison of different types of sample tubes and temperature cycling protocols that have been developed to maximise sensitivity. The chapter concludes by examining how simple digital filtering techniques can be used to reduce noise on echo signals measured on the spectrometer.

1.2.3 Chapter 4: Simulating composite echoes and modelling B_1 inhomogeneity

Chapter 4 describes modelling of the B_1 profile of the non-resonant sample holder used in HiPER, and how this is used in echo simulations to calculate the expected gains in echo amplitude when using composite pulses. It describes the effect of different cavity set ups on the expected gains and how B_1 amplitude can be optimised on HiPER to produce the largest gains in sensitivity.

1.2.4 Chapter 5: Composite PELDOR: Nitroxide biradicals

Chapter 5 examines the use of composite pulses in PELDOR experiments on systems containing two nitroxyl spin labels. Initially, it examines the expected gains in echo amplitude when using composite pulses in comparison with standard pulses, on a nitroxyl mono-radical as a function of orientation. It then examines the performance of composite pulses in refocused echo experiments and in PELDOR experiments on a model bi-radical sample. The chapter finishes by comparing the performance of composite pulses on the mono- and bi-radical nitroxide samples using phase memory time (T_m) measurements to underpin the degraded performance

in the case of the bi-radical.

1.2.5 Chapter 6: Composite PELDOR: Iron-nitroxides

Chapter 6 describes PELDOR experiments carried out between broad metallic paramagnetic centres and nitroxyl spin labels, in this case between the intrinsic low-spin haem iron centre in a protein, and a spin label attached to the protein. This chapter compares the sensitivity enhancement provided using composite observer pulses and composite pump pulses in PELDOR sequences, on a spin-labelled neuroglobin system. It also examines the enhancement provided by composite pulses in echo experiments when observing using the broad iron centre. It also describes experiments on myoglobin samples which have been spin labelled on multiple sites. It also compares the relative sensitivity of PELDOR experiments conducted at lower field on both samples and examines how moving to higher field can, despite broadening of the spectra, provide significant improvement in sensitivity.

1.2.6 Chapter 7: Cobalt-Nitroxide orientational PELDOR and RIDME study

This chapter describes orientational PELDOR (osPELDOR) and orientational RIDME (osRIDME) measurements carried out on a cobalt-nitroxide model system on HiPER. RIDME is a single-frequency PDS technique that exploits the last relaxation of a partner spin to induce echo modulation on an observed spin centre. The experiments conducted involved orientational measurements between an broad metal centre and two nitroxide labels, which are positioned the ends of a rigid structure with the metal centre in the middle. At W-band, it is possible to resolve the relative orientations of the nitroxyl label. Thus, experiments were conducted firstly between metal centre and the relative orientations of the nitroxyl labels to assign their relative orientation. Orientation selective measurements were then carried out between the two nitroxide labels to assign their relative orientations. Orientational measurements were also carried out using RIDME, demonstrating differences in dipolar frequency dependent on the relative orientation of the nitroxide label to the vector joining it and the metal centre, $\vec{r}_{AB}$.

1.2.7 Chapter 8: Frequency and Amplitude Modulated Pulses for use in EPR experiments

Finally, chapter 8 discusses preliminary work carried out to implement frequency and amplitude modulated pulses on a X/Q-band pulsed spectrometer using an arbitrary waveform generator (AWG). It includes design specifications to implement both coherent (detection)

modulation as well as incoherent ELDOR (pump) channel modulation. The chapter describes in detail how imperfections such as amplitude deviations as a function of frequency and phase roll-off from the AWG can be corrected. It then discusses protocols to remove distortions when using double-balanced mixers to produce the modulated pulses around 9 GHz and takes a look at future work.

2

EPR theory and instrumentation

This chapter will discuss the background theory behind the experiments conducted in this thesis, including the PELDOR and RIDME experiments, and theory behind broadband compensation pulses such as composite pulses. The theory discussed here is based on a number of texts which the author has found extremely useful [25, 47–49]. The chapter also includes operational details of the home built spectrometer, HiPER, which has been used for the majority of experiments in this thesis.

2.1 Theory of Pulsed EPR

2.1.1 The Spin Hamiltonian

A paramagnetic substance can be defined as one which possesses no resultant magnetic moment in the absence of an external magnetic field, but acquires a magnetic moment in the direction of the applied field, whose magnitude is a function of the field [50]. The fundamental paramagnetic considered here, is that of the electron. It is known from experiments that the electron possesses intrinsic angular momentum, $\hbar\mathbf{S}$, known as spin, where $\mathbf{S}$ is the spin

operator given by $\mathbf{S} = (S_x, S_y, S_z)$. By considering the particle's mass m, and charge q, we can assign its magnetic moment, μ as

$$\mu = \frac{q}{2m}\hbar\mathbf{S} \tag{2.1}$$

which in the case of the electron, simplifies to

$$\beta_\mathbf{e} = -g\mu_B\mathbf{S} \tag{2.2}$$

where $\beta_\mathbf{e} = \frac{e\hbar}{2m_e}$. From a full quantum mechanical treatment, the fundamental property that the electron has a spin $= 1/2$ emerges. The factor g is included to account for deviations of the behaviour of the electron as a quantum mechanical object, from that of a classically charged particle. For a free electron, this quantity is $g_e \sim 2.002319$.

The behaviour of an electron and its nearby environment, while immersed in an external magnetic field, $\mathbf{B}_0$, is described using the static spin Hamiltonian, $\mathscr{H}_0$ given by

$$\mathscr{H}_0 = \frac{\beta_e\tilde{\mathbf{B}}_0\mathbf{g_e}\mathbf{S}}{\hbar} + \tilde{\mathbf{S}}\mathbf{D}\mathbf{S} + \sum_{k=1}^{m}\tilde{\mathbf{S}}\mathbf{A}_k\mathbf{I}_k - \beta_n\sum_{k=1}^{m}\frac{g_{n,k}\tilde{\mathbf{B}}_0\mathbf{I}_k}{\hbar} + \sum_{I_k>1/2}^{m}\tilde{\mathbf{I}}_k\mathbf{P}_k\mathbf{I}_k + \sum_{i\neq k}^{m}\tilde{\mathbf{I}}_i\mathbf{d}^{(i,k)}\mathbf{I}_k \tag{2.3}$$

The first term of the Hamiltonian, $\beta_e\tilde{\mathbf{B}}_0\mathbf{g}_e\mathbf{S}/\hbar$ is the electron Zeeman interaction, which describes the interaction of the electron spin, $\mathbf{S}$ and the external magnetic field $\mathbf{B}_0$. When the external magnetic field is applied along the z-direction, the Hamiltonian becomes

$$\mathscr{H}_{EZ} = \frac{\beta_e\mathbf{g}_e}{\hbar}B_0S_z \tag{2.4}$$

For an electron with spin, $S = 1/2$, and considering that the electron can be in one of two states, either parallel or anti-parallel (1/2 or -1/2) to the external field, its corresponding energy will be one of two values,

$$E_\pm = \pm(1/2)\,g|\beta_B|B_0 \tag{2.5}$$

This relation infers that if one were to supply an electron in the lower state with electro-

magnetic energy equal to the difference between the two states, the energy would be absorbed, placing the electron in the higher energy state.

The second term in the full Hamiltonian, $\tilde{\mathbf{S}}\mathbf{D}\mathbf{S}$ describes the zero field splitting that occurs when the spin $\mathbf{S}$ of the electron is greater than $1/2$. The presence of more than one spin results in dipole-dipole coupling between the electron spins, which removes the degeneracy of the ground state, leading to a field-independent splitting.

The third term, $\sum_{k=1}^{m} \tilde{\mathbf{S}}\mathbf{A}_k\mathbf{I}_k$ describes the hyperfine interaction between an electron $\mathbf{S}$ and a nuclear spin $\mathbf{I}$. The hyperfine interaction is governed by the hyperfine tensor $\mathbf{A}$ and comprises of two parts, the isotropic or Fermi contact interaction $\mathscr{H}_F$ and the electron-nuclear dipole-dipole coupling $\mathscr{H}_{dd}$. The Fermi contact interaction is given by

$$\mathscr{H}_F = a_{iso}\tilde{\mathbf{S}}\mathbf{I} \tag{2.6}$$

$$= \frac{2}{3}\frac{\mu_0}{\hbar} g_e\beta_e g_n\beta_n |\psi_0(0)|^2 \tilde{\mathbf{S}}\mathbf{I} \tag{2.7}$$

where $|\psi_0(0)|^2$ is the electron spin density at the nucleus, and μ_0 is the magnetic permeability of the vacuum. The electron-nuclear dipolar interaction is anisotropic and can be described similar to a classical dipolar interaction as

$$\mathscr{H}_{dd} = \frac{\mu_0}{4\pi\hbar} g_e\beta_e g_n\beta_n \left(\frac{(3\tilde{\mathbf{S}}\mathbf{r})(\check{\mathbf{r}}\mathbf{I})}{r^5} - \frac{\tilde{\mathbf{S}}\mathbf{I}}{r^3} \right) \tag{2.8}$$

$$= \tilde{\mathbf{S}}\ \mathbf{T}\ \mathbf{I} \tag{2.9}$$

where r is the vector connecting the electron and the nuclear spin. When integrated over spatial electron distribution, it reduces to the anisotropic dipole-dipole coupling tensor, $\mathbf{T}$. The total hyperfine interaction tensor is thus given by

$$\mathbf{A} = a_{iso}\mathbf{1} + \mathbf{T} \tag{2.10}$$

The fourth term, $\beta_n \sum_{k=1}^{m} g_{n,k}\tilde{\mathbf{B}}_0\mathbf{I}_k/\hbar$ describes the interaction of the nucleus with the external magnetic field, known as the nuclear Zeeman interaction.

The fifth term, $\sum_{I_k>1/2}^{m} \tilde{\mathbf{I}}_k\mathbf{P}_k\mathbf{I}_k$ describes the nuclear quadrupole interaction, which arises

in cases where spin I $\geq$ 1. This results in a non-spherical charge distribution on the nucleus, which interacts with the electrostatic gradient of the electrons, given by the nuclear quadrupole tensor, **P**.

The final term in the Hamiltonian, $\sum_{i\neq k}^{m} \tilde{\mathbf{I}}_i \mathbf{d}^{(i,k)} \mathbf{I}_k$ describes the dipole-dipole interaction between two nuclear spins, I_i and I_k.

2.1.2 Weak coupling between electron spins

In the scope of this thesis, we are generally concerned with the interaction of two weakly coupled unpaired electrons, S_A and S_B. Their interaction is characterised by an exchange coupling tensor, **J** and a dipole coupling tensor, **D** and can be described using the following Hamiltonian

$$\mathscr{H}_0(S_A, S_B) = \mathscr{H}_0(S_A) + \mathscr{H}_0(S_B) + \mathscr{H}_{exch}(S_A, S_B) + \mathscr{H}_{dd}(S_A, S_B) \tag{2.11}$$

$$= \mathscr{H}_0(S_A) + \mathscr{H}_0(S_B) + \tilde{\mathbf{S}}_A \cdot \mathbf{J} \cdot \mathbf{S}_B + \tilde{\mathbf{S}}_B \cdot \mathbf{D} \cdot \mathbf{S}_B \tag{2.12}$$

The exchange coupling term accounts for cases where the orbitals of the two electrons overlap, resulting in exchange of the two unpaired electrons. This can occur when the separation between the electrons is less than 1.5 nm. The dipolar term is analogous to the electron-nuclear dipolar interaction, and can also be described by considering the classical interaction of two magnetic moments, μ_A and μ_B. Their energy of interaction is given by

$$E = \frac{\mu_\mathbf{A} \cdot \mu_\mathbf{B}}{r_{AB}^3} - \frac{3(\mu_\mathbf{A} \cdot \mathbf{r}_{AB})(\mu_\mathbf{B} \cdot \mathbf{r}_{AB})}{r_{AB}^5} \tag{2.13}$$

by defining r_{AB}, the vector joining the two spin centres in spherical coordinates as, $\mathbf{r}_{AB}$ = (r cos θ sin ϕ, r sin θ cos ϕ, r cos θ), and the spin S as **S**=(S_x,S_y,S_z), the dipolar Hamiltonian becomes

$$\mathscr{H}_{dd} = \frac{g_A g_B \beta_e^2}{r_{AB}^3}(A + B + C + D + E + F) \tag{2.14}$$

where the terms, A-F are given by

$$
\begin{aligned}
A &= S_z^1 S_z^2 \left(1 - 3\cos^2\theta\right) \\
B &= -\frac{1}{4}(S_+^1 S_-^2 + S_-^1 S_+^2)\left(1 - 3\cos^2\theta\right) \\
C &= -\frac{3}{2}(S_+^1 S_z^2 + S_z^1 S_+^2)\sin\theta\cos\theta e^{-i\varphi} \\
D &= -\frac{3}{2}(S_-^1 S_z^2 + S_z^1 S_-^2)\sin\theta\cos\theta e^{i\varphi} \\
E &= -\frac{3}{4} S_+^1 S_+^2 \sin^2\theta \cdot e^{-2i\varphi} \\
F &= -\frac{3}{4} S_-^1 S_-^2 \sin^2\theta \cdot e^{2i\varphi}
\end{aligned}
\tag{2.15}
$$

where S_z is the $\hat{\mathbf{z}}$ component of the full spin angular momentum operator $\mathbf{S}$, and $\mathbf{S}_+$ and $\mathbf{S}_-$ are the raising and lowering operators, given by $S_x^i + iS_y^i$ and $S_x^i - iS_y^i$ respectively. In order to simplify the terms involved in dipolar interaction, it is useful to explore what their functions are. Term A is the secular term of the dipolar interaction and it describes the splitting of each EPR line due to the dipolar interaction, into a doublet with energy of separation equal to A, as illustrated in Figure 2.1(b).

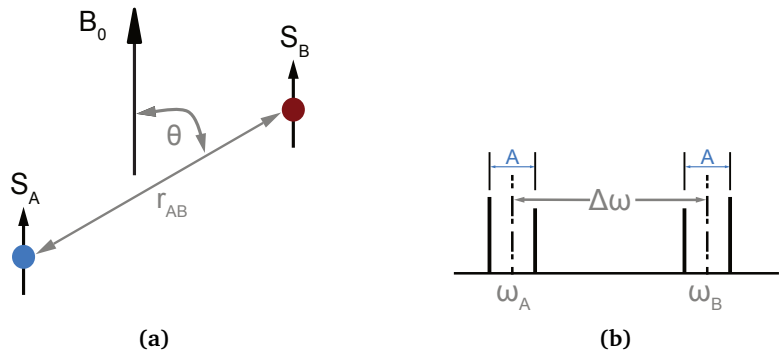

Figure 2.1: (a) Diagram showing the two spins involved in the weakly coupled system, the orientation of the field, and their separation, $\vec{r}_{AB}$. (b) shows the splitting of the two spin's resonant frequencies, ω_A and ω_B due to term A, the secular term of the dipolar interaction. Adapted from [51].

Term B is the pseudo-secular term which can lead to the mutual flip-flop of both spins, which occurs when both spins are simultaneously inverted. This term only becomes significant if the difference in Zeeman energies for both spins is small and comparable to the dipolar coupling frequency. This case occurs most generally at lower fields, where the spectra is much narrower or where the separations between spins is much smaller. It can become significant in the case of rigid labels with strong orientation dependence, where the dipolar coupling strength increases. In most cases considered here, it can be neglected.

Terms C and D, and E and F consider the secular and pseudo-secular single and double quantum transitions between the states, which require spin flips of either or both spins. The probability of such transitions occurring requires the difference of the Zeeman energies of both spins to be comparable to the dipolar splitting energy. For most experiments considered here at fields around 3.4 T and spin separations of greater than 2 nm, the separation in Zeeman energy between the two states is much larger than the dipolar coupling, and in this limit terms C-F can also be neglected.

The static spin Hamiltonian for two weakly coupled electrons (in the limit of no exchange interaction), reduces to

$$\mathscr{H}_0(S_A, S_B) = \mathscr{H}_0(S_A) + \mathscr{H}_0(S_B) + \mathscr{H}_{dd}(S_A, S_B) \tag{2.16}$$

With

$$\mathscr{H}_{dd} = \omega_{dd}\left(S_A^z S_B^z - \frac{1}{4}\left[S_A^+ S_B^- + S_A^- S_B^+\right]\right) \tag{2.17}$$

$$\omega_{dd} = \frac{\mu_B^2 g_A g_B}{4\pi\hbar r_{AB}^3}\left(1 - 3\cos^2\theta\right) \tag{2.18}$$

where ω_{dd} is referred to as the dipolar frequency. In the case of two nitroxide labels, both with g≈2.006 for example, the dipolar coupling between the spins when $\vec{r}_{AB} = 2$ nm is 41 MHz (θ=90°), and for a typical $\Delta\omega = |\omega_A - \omega_B| = 100$ MHz, the pseudo-secular term has no effect, and thus can be neglected [52]. In the systems considered within the scope of this thesis, all inter-spin distances are greater than 2 nm, and at high field (3.35 T) it is trivial to ensure frequency separation, $\Delta\omega$ is much greater than ω_{dd}. Thus, the Hamiltonian shown in Equation 2.17 reduces to terms dependent on the z components of the spin operators for each spin, and a term that describes the dipolar coupling frequency which is dependent on the separations of the spins $\vec{r}_{AB}$, and the orientation of the dipolar axis $\vec{r}_{AB}$ to the static field, B_0. The dipolar frequency ω_{dd} varies from -2 $D_{dd}/\vec{r}_{AB}{}^3$ to +$D_{dd}/\vec{r}_{AB}{}^3$ as θ from 0° (parallel) to 90° (perpendicular).

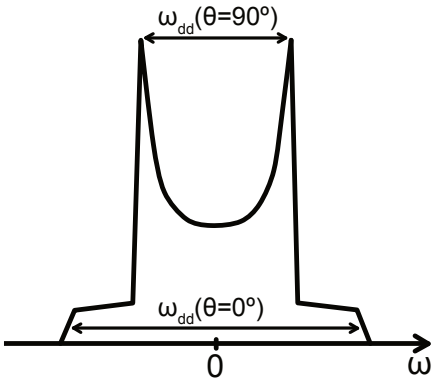

Figure 2.2: Diagram showing the Pake doublet, showing the position of the peaks corresponding to the parallel (θ=0°) and perpendicular (θ=90°) components of dipolar coupling frequencies.

The paramagnetic containing samples which are considered here consist of randomly orientated molecules, such that an average over all orientations of θ is sampled. This results in spectra which resembles a Pake doublet [53], with peaks at $\omega_{dd} = 90°$and further peaks at $\omega_{dd} = 0°$, as illustrated in Figure 2.2.

2.1.3 The vector picture

In the systems considered here, it is not singular electrons that are observed, but ensembles of electrons, which possess a net magnetic moment, expressed per unit volume as the macroscopic magnetisation, **M** given by

$$\mathbf{M} = \frac{1}{V}\sum_{i=1}^{N}\mu_i \tag{2.19}$$

where μ_i is the magnetic moment of an electron, as defined in Eq. 2.1. In the absence of relaxation, the magnetisation, **M** may be treated in the same way as a single classical magnetic moment, which, at thermal equilibrium is aligned parallel to the magnetic field, $\mathbf{B}_0$. The equation of motion for a magnetic moment in the presence of the external magnetic field is given by

$$\hbar\frac{d\mathbf{S}}{dt} = \mu \times \mathbf{B} \tag{2.20}$$

where **S** is the spin operator. Thus for an ensemble, with net magnetisation, **M**, its equation of motion is given by

$$\frac{d\mathbf{M}}{dt} = \mathbf{M} \times -\frac{g_e\mu_B}{\hbar}\mathbf{B}_0 \tag{2.21}$$

If the magnitude of **M** and its angle to $\mathbf{B}_0$ is constant, the magnetisation will precess on a

cone about $\mathbf{B}_0$, with precessional frequency,

$$\omega_s = \frac{g_e \mu_B B_0}{\hbar} \tag{2.22}$$

This is considered in the laboratory frame, which is stationary, with z^L collinear with $\mathbf{B}_0$. In order to explore the action of a time-varying applied magnetic field, $\mathbf{B}_1$, it is more convenient to move to the rotating frame, which rotates around z^L at the frequency of a circulary polarised field, of frequency ω_{mw}, such that, with respect to the stationary lab frame, $B_{1x^L} = B_1 \cos(\omega_{mw} t)$, $B_{1y^L} = B_1 \sin(\omega_{mw} t)$ and $B_{1z^L} = 0$. Thus, the equation of motion for the magnetisation in this frame becomes

$$\begin{aligned} \frac{dM_x}{dt} &= -(\omega_s - \omega_{mw}) M_y = -\Omega_s M_y \\ \frac{dM_y}{dt} &= (\omega_s - \omega_{mw}) M_x - \frac{g_e \mu_B B_1}{\hbar} M_z = \Omega_s M_x - \omega_1 M_z \\ \frac{dM_z}{dt} &= \frac{g_e \mu_B B_1}{\hbar} M_y = \omega_1 M_y \end{aligned} \tag{2.23}$$

In this frame, when there is no radiation present, the magnetisation precesses around $\mathbf{B}_0$ at the resonance offset frequency, $\Omega_s = (\omega_s - \omega_{mw})$, as shown in Figure 2.3(a). When the radiation field is applied, it produces an additional precessional frequency ω_1, about its direction, with magnitude,

$$\omega_1 = \frac{g_e \mu_B B_1}{\hbar} \tag{2.24}$$

The combination of the external field $\mathbf{B}_0$ and the applied radiation field $\mathbf{B}_1$ results in an effective field, $\mathbf{B_{eff}}$, which is the vector product of both $\mathbf{B}_1$ and $\mathbf{B}_0$. The effective field is angled at θ with respect to the $\mathbf{B}_0$, where

$$\theta = \arctan\left(\frac{\omega_1}{\Omega_s}\right) \tag{2.25}$$

The spin then follows a nutation around $\mathbf{B_{eff}}$ with precessional frequency, $\omega_{\text{eff}} = \sqrt{\omega_1^2 + \Omega_s^2}$. This set up is shown in Figure 2.3(b) In most of the experiments considered in the context of this thesis, the applied magnetic field $\mathbf{B}_1$ linearly polarised. Its phase ϕ, which describes the angle between the direction of the B_1 field and the x-axis in the rotating frame. Thus, ϕ

determine the direction that the resulting linearly polarised field will be applied along.

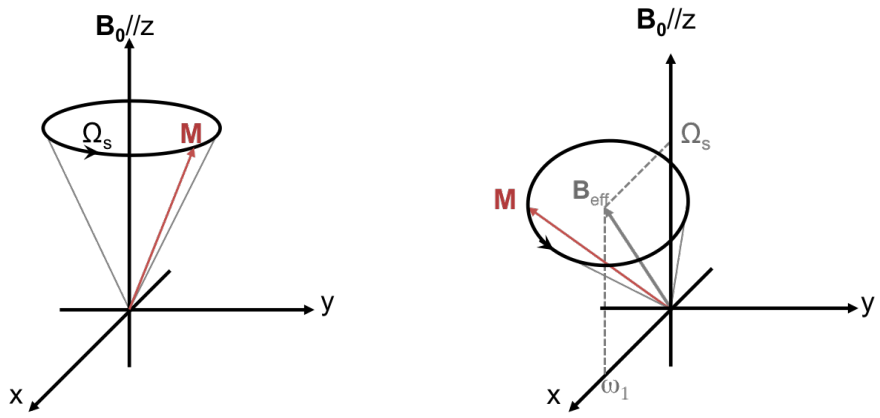

(a) Free precession **(b)** Nutation

Figure 2.3: Diagrams illustrating (a) free evolution of the spins at the precession frequency Ω_0, (b) prcession of the magnetisation at frequency ω_{eff} about the effective B-field, resulting in a nutation precession. (Adapted from [47].)

In the pulsed EPR experiments described here, the applied magnetic field is provided by short pulses of millimetre wave radiation, where $\mathbf{B}_1$ is turned on at t = 0 and switched off at t=t_p. At thermal equilibrium, all spins are aligned with the field, such that $\mathbf{M}//\mathbf{B}_0$. The action of the applied field rotates the spins from equilibrium, about the axis of the applied field, by the flip angle, $\beta = \omega_1 t_p$, such that the duration t_p and the amplitude ω_1 of the applied field determine how far the spin is rotated from equilibrium. The most common examples are $\beta = 90°(\pi/2)$, describing a rotation into the transverse (x-y) plane and $\beta = 180°(\pi)$ describing an inversion of the spins.

Spin echoes

One of the simplest pulse experiments to be carried out on a system is to produce a spin echo, or, as it is more commonly referred to, a Hahn echo. Under the action of the 90° pulse, applied along x, (ϕ=0°), the spins will be rotated from +z around the x-axis, and end pointing along the -y direction at the end of the pulse. After the pulse, and in the absence of relaxation, the spins will continue to precess around $\mathbf{B}_0$ indefinitely, during a process known as 'free precession.' In the rotating frame, the magnetisation thus remains fixed along -y. In most cases, not all spins will precess at Ω_s due to small offsets in frequency, meaning that the spins will spread out as some precess faster and some slower than Ω_s. This results in 'dephasing' of the spin packet, as the magnetisation spreads out in the transverse plane. If the spins are subject to a second pulse, a period τ later, of flip angle $\beta = 180°$, this will flip the magnetisation in

the transverse plane, reversing the direction of precession around z. The so-called 'dephasing pancake' of spins will then re-combine a period τ after the second pulse, to produce a signal, known as an 'echo.' The sequence is shown in Figure 2.4. The echo is produced as the rotating spins in the transverse plane emit electromagnetic radiation at the precession frequency. As the spin packet recombines, the magnitude of the signal increases dramatically, producing the echo. After the echo, the spins continue free precession about z.

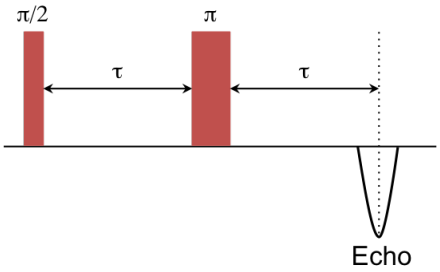

Figure 2.4: Diagram showing the simple Hahn echo pulse sequence, and resulting echo.

In the presence of relaxation however, the amplitude of the echo will decrease as the period τ between the pulses is increased. This decay is caused by a reduction in the total number of spin packets which rephase over time, due to interactions with environment, such as spin-spin interactions. By measuring the echo amplitude as a function of τ, it is possible to obtain the transverse relaxation period, known as the phase memory time, T_m of the spins excited by the pulses. The echo amplitude as a function of τ is typically given by

$$V(2\tau) = V(0)\exp\left(\frac{-2\tau}{T_m}\right) \tag{2.26}$$

Refocused spin echo

After the spin echo sequence, if the spins are subjected to a second inversion π pulse, known as a refocusing pulse, a second spin echo will be produced, a period $2(\tau_1 + \tau_2)$ after the first pulse, as shown in Figure 2.5. This is possible as the spins continue to precess about z in the xy-plane, and can be refocused to produce further echoes, multiple times. The echo amplitude reduce as the interval between the pulses increases, due to relaxation.

2.1.4 Relaxation processes

So far, we have assumed that once energy is put into system, and the spins start to precess in their new state that they do so forever. In reality, this is not the case, as the spins are subject

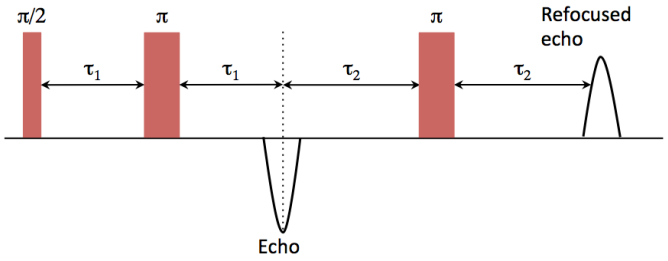

Figure 2.5: Diagram showing the refocused spin echo pulse sequence, and resulting refocused echo.

to relaxation processes, that will cause the system to return to its equilibrium state, $\mathbf{M}_0$ // z. This will occur at different rates in different planes. In the longitudinal direction, the static magnetic field along z induces an anisotropy in space, causing the M_z component to decay back to equilibrium, governed by the equation [54]

$$M_z = M_0\left(1-\exp\left[\frac{-t}{T_1}\right]\right) \tag{2.27}$$

where M_0 is the magnetisation at thermal equilibrium (in the direction of the external magnetic field, B_0) t is the time between excitation and measurement of the echo and T_1 is the time constant required to reduce the z-component of the magnetisation by a factor of e. This process, in the absence of B_1 is caused by lattice-induced transitions between spin levels [55]. This is driven by the absorption or stimulated emission of phonons, mediated by fluctuating local magnetic fields which are driven by lattice vibrations [47]. When placed in the static external magnetic field, each of the magnetic dipoles that make up the bulk magnetisation **M** can align either in the direction of the field, or in opposition to it, corresponding to a lower and higher energy state respectively. The relative occupation of these states is given by the Boltzmann distribution,

$$\frac{N_+}{N_-} = \exp\left(\frac{-\Delta E}{k_B T}\right) \tag{2.28}$$

where N_+ and N_- refer to the population of the antiparallel (higher energy) and parallel (lower energy) states respectively. ΔE refers to the energy difference between these states, as given in Eq. 2.5. This relation states that more of the spins will be in the lower state, parallel to the field as the temperature decreases, and similarly at higher temperatures, the spins will occupy both states equally.

Relaxation in the transverse (xy) plane is governed by a separate time constant, T_2, or as it is more commonly referred to in EPR, T_m. This relaxation tends to be dominated by flip-flop spin-spin interactions, where the spin state changes from α to a β state, and this in turn induces a second spin to change from the β to an α state. This process is called spin-spin relaxation. This most often occurs between electrons and nearby nuclei in the experiments considered here. The transversal relaxation is generally measured in pulsed EPR experiments by recording the magnitude of a spin echo as a function of increasing τ, whose decay is given by

$$M_{xy} = M_0\left(1 - \exp\frac{-t}{T_m}\right) \tag{2.29}$$

where T_m is a time constant for the transversal relaxation. Many processes can contribute to this relaxation, including lifetime broadening (1/2 T_1), spin-spin relaxation (1/T_2') and interactions with nearby protons. Thus, the all encompassing time constant, phase memory time, T_m is generally used.

2.2 PELDOR: Pulsed Electron Double Resonance

The most widely used experiment to measure the dipolar coupling between two spins, is the 4-pulse PELDOR (Pulsed Electron DOuble Resonance) experiment, shown in Figure 2.6. In this experiment, we consider a set of 2 spins, A and B which are separated by a distance $\vec{r}_{AB}$, and both each have different resonance frequencies, ω_A and ω_B. The A spins are selectively excited using pulses of frequency ω_A, and measured using a refocused echo sequence. This monitors the echo amplitude of the A spins in the A-B spin pair, and is commonly referred to as the probe or detection sequence.

At a time t after the first inversion pulse in the probe sequence, an inversion pulse at frequency ω_B inverts the B spins in the pair, and is referred to as the pump pulse. This spin flip caused by the pump pulse, causes a sudden shift in the Larmor frequency of the A spin by $\pm\omega_{dd}$ (Eq. 2.18). This causes the spins to precess with this altered frequency $\omega_A \pm \omega_{dd}$ in the transverse plane, resulting in a non-perfect refocusing of the spins at a time $2(\tau_1+\tau_2)$ after the first pulse. By increasing the time t, that the pump pulse occurs during the dipolar evolution of A spins, the phase lag or phase advance accumulated by the echo will similarly increase, resulting in a periodic modulation of the echo amplitude. The echo amplitude modulation as

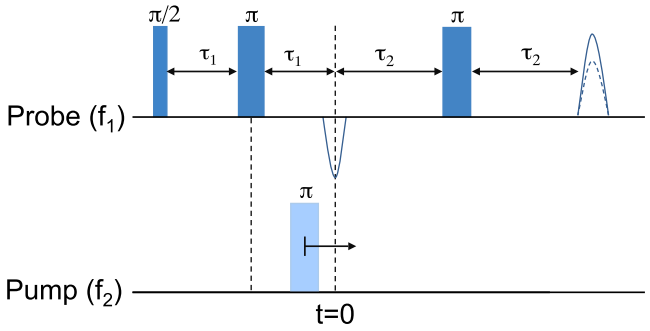

Figure 2.6: Diagram showing the standard 4-pulse PELDOR experiment, consisting of a refocused Hahn echo sequence on the probe or detection sequence (f_1) and a single inversion pulse on pump spin (f_2) sequence.

a function of t is given by

$$V_{intra}(t) = V(0)\cos(\omega_{dd}(\tau - t)) \tag{2.30}$$

where V_0 is the maximum echo amplitude at t=0, and ω_{dd} is given by Eq. 2.18. In the limiting case where the A and B spins are spectrally well separated (and probe pulses do not excite the pump spins and vice versa) and the detection and pump pulses excite the A and B spins fully, the dipolar interaction will lead to a 200% modulation of the signal amplitude during the experiment [56]. In reality, only a fraction of the spins will be excited, resulting in much reduced modulation. The echo amplitude will also be subject to intermolecular interactions, $V_{inter}(t)$ which results in a background decay of the signal. In the glassed samples considered here, this is given by [47]

$$V_{inter}(t) = \exp(-kCF_B|\tau - t|) \tag{2.31}$$

where F_B is the fraction of B spins excited by the pump pulse, C is the concentration of the spins, and the constant k is given by

$$k = \frac{2\pi\mu_0\beta_e^2 g_B g_B}{9\sqrt{3}\hbar} \tag{2.32}$$

assuming a homogeneous distribution of radicals within the sample. Given that it is generally only possible to excite a portion of B spins, and that the signal will be a product of all spin pairs excited in the sample, averaging all distances between pairs, the intramolecular portion of the PELDOR signal, $V_{intra}(t)$ becomes

$$V_{intra}(t) = 1 - \int_0^{\pi/2} \sin\theta_{AB}\lambda(\theta_{AB})[1-\cos(\omega_{dd}(\theta_{AB})(\tau-t))]\,d\theta_{AB} \tag{2.33}$$

which introduces the orientation-dependent modulation depth parameter, $\lambda(\theta_{AB})$ where θ_{AB} is the angle between $\vec{r}_{AB}$ and B_0. It is important to take into consideration the orientation dependence of these parameters in the experiments carried out here, as at higher field (>3.35 T) the Zeeman interaction starts to dominate, and it becomes possible to resolve g-tensor components in the more commonly used nitroxyl radical. This means that it becomes possible to selectively excite the different orthogonal orientations of the nitroxyl during the experiment. The different populations of spins present at each orientation, and at the frequency excited by the pulses will result in different modulation depths.

2.2.1 PELDOR data processing: DeerAnalysis

In order to obtain distance measurements from the PELDOR experiments conducted as part of this thesis, a MATLAB software package maintained by the Jeschke Group at ETH Zürich called DeerAnalysis was utilised [57]. While there are many packages available online which use various methods to allow the user to extract distance determinations from PELDOR time trace data, DeerAnalysis was chosen for use here as it is the most widely used in the current literature and noted for its robust characterisation of supplied data. The package allows the user to import ASCII text files containing the time step and corresponding magnitude values, which is processed to remove background decay as given by Eq. 2.31 using fitting procedures. It then calculates a FFT of the time trace data, which after background removal should be of the form as given in Eq. 2.30, which it fits using robust fitting techniques to find the best fit for the data. It is then able to return a distance distribution, converting the frequency components which relate to the dipolar coupling frequency ω_{dd} into distance values, corresponding to the separation between the spin pairs. The user is also able to verify the fit by using a verification procedure, which iterates through variations in different fitting parameters, such as zero time, background decay start time, background fit dimension, and Tikhonov regularisation parameter.

While DeerAnalysis is useful for obtaining quick and robust fits of most data, it is unable to take into consideration any effects of orientation selection. This is commonly observed as an incomplete Pake pattern, which is obtained using the FFT of the time trace, where parts, typically the shoulders at 0° are missing (c.f. Figure 2.2). Any orientation dependence means

that the distance obtained is a function of the relative orientations of the labels, thus to avoid this, averaging over all orientations must be carried out to obtain the actual distance between labels.

2.3 RIDME: Relaxation Induced Dipolar Modulation Enhancement

Another pulsed dipolar spectroscopy (PDS) technique which is becoming increasingly popular in pulsed EPR experiments to measure distances between spin centres is the Relaxation Induced Dipolar Modulation Enhancement (RIDME) experiment. In this experiment, the dipolar modulation due to a nearby coupled electron is measured by probing and exciting one of the two spins in the pair. The experiment involves producing an echo, and relies on the spontaneous relaxation (and thus inversion) of the coupled spin centre to produce dipolar modulation of the echo. While the spin dynamics are strikingly similar to that of the PELDOR experiment, and can be analysed to produce broadly the same results, the spin dynamics are quite different.

The first RIDME sequence to be reported was the so-called 3-pulse RIDME experiment, shown in Figure 2.7 [42]. In this sequence, a stimulated echo (SE) produced using three $\pi/2$ pulses on the A spins. The latter two pulses in the sequences are separated by T, which is referred to as at the mixing time. This period is optimised to allow for the coupled B spin to spontaneously relax. This performs the same action as the pump pulse in a PELDOR experiment, inducing a shift in precession of the A-spins, which can be measured by recording the echo as the latter two pulses are stepped in the sequence.

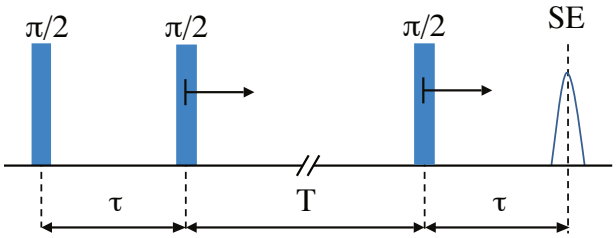

Figure 2.7: Diagram showing the 3-pulse RIDME sequence, consisting of 3 $\pi/2$ pulses, the latter two of which are separated by the 'mixing' time T, and are stepped to record the dipolar modulation of the stimulated echo.

To explain the mechanism behind the dipolar evolution observed here, it is useful to describe it using the vector picture in the rotating frame of the A-spins [43]. The magnetisation starts in the equilibrium position, (0,0,+M_0), before it is acted upon by a $\pi/2$ pulse along the x-axis. This rotates the spin packet into the transverse plane, along y, (0,M_0,0).

The spins are then free precess for a period of τ, resulting in the magnetisation given by $(M_0 \sin\Omega_A\tau, M_0 \cos\Omega_A\tau, 0)$. The second $\pi/2$ pulse transfers the magnetisation into the longitudinal plane, described by $(M_0 \sin\Omega_0\tau, 0, M_0 \sin\Omega_0\tau)$, which is allowed to freely evolve for a period, T, where $T \gg T_m$ the transversal relaxation. This nulls any magnetisation in xy, leaving only the z-component, given by $(0,0,M_0 \cos\Omega_0\tau)$. The final $\pi/2$ pulse then rotates the magnetisation back into the transverse plane, given by $(0,M_0 \sin\Omega_0\tau,0)$ which produces an stimulated echo a period τ after the final pulse. If one of the B-spins which is dipolar coupled to the A-spins spontaneously flips during the mixing time T, the Larmor frequency, Ω_A of the A-spins will be shifted by ω_{dd}. This results in a modulation of the echo, which can be measured by increasing τ. The modulation of the echo is given by $\cos(\omega_{dd}\tau)$. The probability of spontaneous flipping of the partner B-spin is given by [43]

$$\frac{1}{2}\left(1-\exp\left(\frac{-T}{T_1}\right)\right) \tag{2.34}$$

where T_1 is the longitudinal relaxation of the B-spin. One consequence is that the modulation depth maximum is 0.5 of the echo amplitude.

One drawback of this pulse technique is that unlike the 4-pulse PELDOR technique, it is not possible to observe the so-called 'zero-time' defined as the start of the modulation, which occurs immediately after the final pulse. It is not possible to observe $\tau \rightarrow 0$, due to cavity ring down, or dead-time effects that swamp receivers with residual pulse amplitude, making it impossible to observe echoes at τ=0. To overcome this, a dead-time free 5-pulse RIDME pulse sequence was developed by Milikisyants et al. [43], shown in Figure 2.8.

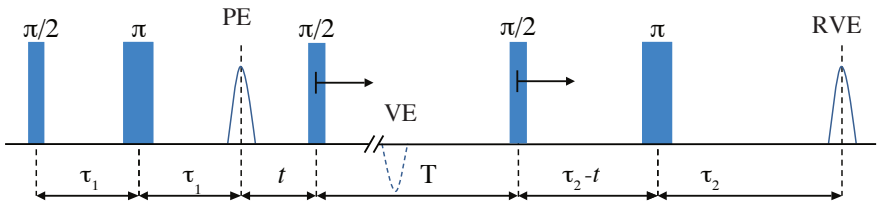

Figure 2.8: Diagram showing the 5-pulse dead-time free RIDME sequence.

In this sequence, a refocused virtual echo (RVE) is used to measure the dipolar modulation of the echo. Pulses 3 and 4 are separated by the mixing time T, and are stepped together as t increases. The period t defines the zero point of the dipolar evolution and is located where the primary echo is formed by the first two pulses in the seqeunce. The zero time is recorded by traversing the pulses through t=0, typically, with t starting at -200 ns. The RVE is formed by

the refocusing of the first virtual echo by the final π pulse in the sequence. Like in the 3-pulse RIDME sequence, if the partner B-spins spontaneously flip during T, the resonance frequency of the A-spins will be shifted by ω_{dd}, with the modulation given by $\cos(\omega_{dd}t)$.

The one drawback of the 5-pulse RIDME sequence is that with the addition of more pulses, more coherent transfer pathways are created, thus there are several instances throughout the sequence where combinations of stimulated, primary and virtual echoes can coincide, resulting in large spikes in amplitude in the measured echo. This can be compensated for by using 8-step phase-cycling, where the phase of the first, third and fourth pulses is cycled, and the detection magnitude is set accordingly. The 8 traces are then combined according to the detection magnitude, removing all unwanted coherences from the detection echo and resulting dipolar modulation trace. The 8-step phase cycling sequence used is shown in Table 2.1.

φ_1	φ_3	φ_4	Detection
+x	+x	+x	+
+x	-x	-x	+
+x	+y	+y	+
+x	-y	-y	+
-x	+x	+x	-
-x	-x	-x	-
-x	+y	+y	-
-x	-y	-y	-

Table 2.1: 8-step phase-cycling sequence used in 5-pulse RIDME experiments. φ_i refers to the ith pulse in the sequence. Detection refers to the magnitude of signal, in the case of - detection, the trace must be inverted before addition to + traces

The resulting trace can then be processed similarly to PELDOR, using background removal and Fourier Transform to obtain the dipolar evolution frequency, ω_{dd}, and thus the separation between the two spin centres.

2.4 Composite pulses

2.4.1 Theory

Composite pulses are defined as a series of contiguous pulses with different phases and lengths [25]. They are designed to perform the same action as a standard inversion (180°, π) or excitation (90°, $\pi/2$) pulses, but use phase changes within the pulse to compensate for errors of applied field (B_1) inhomogeneity and frequency offset. This results in pulses which are able to excite larger populations of spins, enhancing echo amplitudes and thus, improving the signal-to-noise of experiments. Composite pulses are commonly described using the following notation: [49] $\left(\beta_1^0\right)_{\phi 1}\left(\beta_1^0\right)_{\phi 1}\ldots\left(\beta_n^0\right)_{\phi n}$ where $\left(\beta_p^0\right)$ describes the nominal flip angle (usually 90° or 180°) of the sub-pulse p, and ϕp describes its phase, or axis of rotation. Thus, the sequence $90_{45}180_0$ would describe a rotation of 90° around an axis at an angle of 45° from the +x axis towards +y, followed by a 180° rotation around the +x-axis. The first composite pulse was created using simple geometrical arguments considering the comparison of the dephasing of a spin packet during a spin echo immediately after excitation, to the spread in rotation angles of spins experiencing different amplitudes of the applied field, as in the case of inhomogeneity across the sample [25].

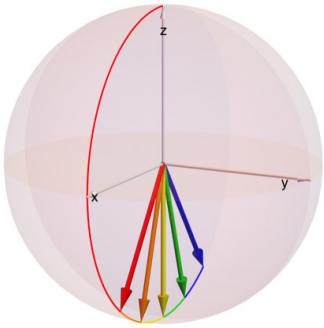

Figure 2.9: Diagram showing the action of a standard 180_{90} pulse on spins experiencing greater than (blue) and less than (red) nominal B_1 field, due to the effect of B_1 inhomogeneity across the sample.

During a pulse, spins experiencing larger than nominal field would overshoot the target angle of rotation, and those experiencing lower than nominal field would undershoot, as shown in Figure 2.9. Overall, this results in a reduced population of spins in the target state, which in the case of a spin echo, results in reduced echo amplitudes. To counteract for this, Levitt et al. proposed creating a sequence that produced an overall 180° rotation of the spins, but

split the overall rotation into three parts, using different phases. The first part involved a 90° rotation around y-axis ($\phi = 90°$) which will rotate spin packets from the equilibrium position along +z towards the x-axis. Errors in amplitude due to inhomogeneity will result in some spins overshooting and some undershooting the target state. This is immediately followed by a 180° pulse applied along the x-axis (ϕ=0°), which will rotate the off-target spins around the x-axis, resulting in spins that were over rotated are rotated back towards the +z-axis by the same angle of deviation from target, and the undershooting spins would be similarly rotated but towards the target of -z. The final part of the sequence is another 90° pulse along y, which will rotate the spins by the same amount as the first pulse, resulting in both the under and overshooting spins in the target -z state. The path taken by a spins experiencing larger than, and less than nominal applied B_1 fields are shown in Figure 2.10.

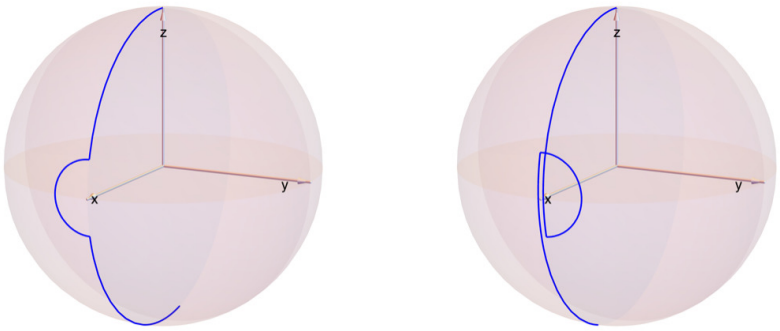

(a) Under-shoot **(b)** Over-shoot

Figure 2.10: Figures showing the spin trajectory of spins under the action of a $90_{90}180_{0}90_{90}$ composite pulse, under the conditions of (a) lower than nominal (under-shoot) and (b) larger than nominal (over-shoot) B_1 field. .

Compensation for frequency offset is slightly less intuitive than compensation for B_1 inhomogeneity, but it is essential for improving excitation across broad line samples. Frequency offset arises due to the fact pulses from the spectrometer are mono-frequency, and the sample consists of electrons with a range of Larmor frequencies, due to interactions with nearby spins in their environment, as well as g-tensor anisotropy. This manifests itself as an increase in the effective flip angle of the spins, which can be considered as the rotation axis being tilted by an angle Δ towards +z [30]. Under the action of an inversion pulse, the rotation would become equivalent of a rotation of Δ about y, followed by 180°about x, and a rotation Δ about -y. The process is described as follows

$$S_x \cos\phi + S_y \sin\phi \xrightarrow{\Delta y} \xrightarrow{180_0} \xrightarrow{\Delta -y} S_x \cos\phi \cos 2\Delta + S_z \cos\phi \sin 2\Delta - S_y \sin\phi \tag{2.35}$$

The phase of the magnetisation vector, i.e. its orientation in the transverse (x-y) plane is thus given by

$$\arctan\left(\frac{-\sin\phi}{\cos\phi\cos 2\Delta}\right) = \arctan\left(\frac{-\tan\phi}{\cos 2\Delta}\right) \tag{2.36}$$

which is only equal to -ϕ in the on-resonance ($\Delta = 0$) case. This means that during a spin echo, the spins will not rephase perfectly, which results in a non-perfect spin echo.

2.4.2 Symmetric and antisymmetric composite pulses

While the performance of a large number of pulses is usually measured by their compensation abilities and bandwidth enhancement, it has been widely remarked over the years, *'I tried using a composite pulse and there was no improvement- in fact, it was slightly worse.'* [30]. This arises from the use of composite pulses in place of inversion pulses in spin echo sequences, where one wishes to utilise the compensation and enhancement provided to improve echo amplitudes. However, most composite pulse sequences cannot produce Hahn echoes, and the mechanics of why this is the case can be explained by considering that when multiple rotations are performed, their product is another rotation in addition to the rotation angles and axes of the individual elements [30]. Most sequences can be categorised into symmetric, antisymmetric and asymmetric sequences, and are described as follows.

In a symmetric composite pulse, the flip angles follow $\beta_1 = \beta_N$ and $\beta_2 = \beta_{N-1}$, with corresponding phases, $\varphi_1 = \varphi_N$, $\varphi_2 = \varphi_{N-1}$. Antisymmetric sequences follow the same pulse length sequence, but have phases following, $\varphi_1 = \varphi_0 + \varphi_1'$, $\varphi_2 = \varphi_0 + \varphi_2' \cdots \varphi_{N-1} = \varphi_0 - \varphi_2'$, $\varphi_N = \varphi_0 - \varphi_1'$, where φ_0 is the central phase of the pulse. The effect of this layout choice is subtle, but has a large effect when considering the performance of the pulse when attempting to rotate off-resonance spin packets. As the derivation from Odedra et al. [30] shows, for symmetric sequences, there is no constraint on the overall rotation axis, meaning that when a pulse is applied off resonance, phase errors will occur, which will reduce the coherence of the pulse, resulting in poorly formed echoes.

In the case of antisymmetric pulses with a central phase $\varphi_0 = 0°$, the rotation will take the form of a rotation in the xy-plane given by phase φ, followed by a rotation in the xz-

plane, and finally another rotation in the xy-plane by -φ. This results in an overall rotation axis in the xz-plane (or the plane containing z and φ_0) regardless of the offset, Δ due to the reverse rotation, -φ which will remove any accumulated phase lag due to offset. The self-phase correcting abilities of the antisymmetric composite pulse sequences make them much more useful in experiments to replace standard $180_0/\pi$ inversion pulses. An example of such a pulse is $60_{180}180_060_{180}$. This sequence is a symmetric/antisymmetric pulse, with phases $\varphi_1 = \varphi_0$+180°, $\varphi_2 = \varphi_0$ and $\varphi_3 = \varphi_0$ -180°, with $\varphi_0 = 0°$. This pulse rotates spins from the equilibrium state along +z, towards the xy-plane around -x, before rotating around +x by 300° (compensating for any under or over-shoot due to B_1 inhomogeneity), before finishing the rotation towards -z about -x. This cancels any phase lag due to frequency offset, by rotating the spins back on themselves, in terms of their phase, while performing the inversion. Using this composite pulse, B_1 inhomogeneity can be compensated for, while the effects of resonance offset phase errors are effectively cancelled out. The action of this pulse on a set of spins, in the absence of B_1 inhomogeneity ($B_1/B_1^0 = 1$) but in the presence of frequency offset, where $\Delta\omega/\Omega_0$=±0.2, is shown in Figure 2.11(a).

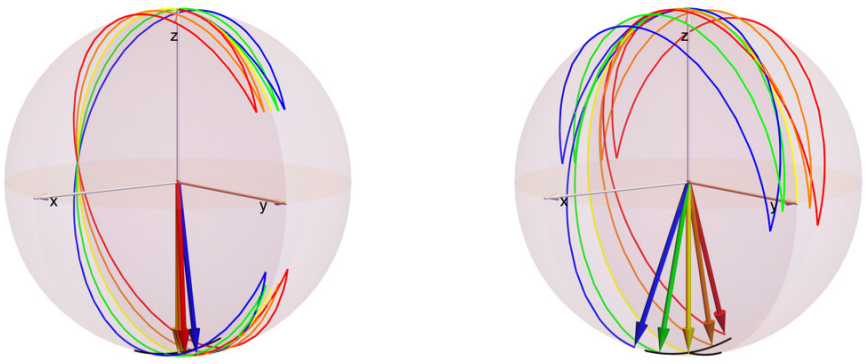

(a) Antisymmetric **(b)** Asymmetric

Figure 2.11: Diagrams showing the effect of applying an antisymmetric composite pulse ($60_{180}300_060_{180}$) (a) and an asymmetric composite pulse ($90_0180_{180}270_0$)(b) on a set of spins with no B_1 inhomogeneity, and up to ±20% frequency offset.

The figure also shows the action of an asymmetric composite sequence, in this case, $90_0180_{180}270_0$, whose overall action is also inversion, but it uses non-symmetric pulse lengths to do so. There is no restriction placed on the overall rotation axis for such pulses, thus they are often referred to as 'variable rotation' pulses. In this example, the pulse does not compensate for phase errors arising due to frequency offset, resulting in spreading of the spin packets at

the end of the pulse, as shown in Figure 2.11(b). This is particularly dramatic in comparison with the action of the antisymmetric pulse, which shows no distortion in phase for moderate frequency offsets. The issue with this induced dispersion of the spin packets at different offsets is that the dispersion will propagate as the spins undergo the action of free precession, and as a result, they will not rephase together to produce an echo. The effect of this in terms of coherence in spin echoes, will be discussed fully in Chapter 3.

It should however be noted that the symmetric and asymmetric sequences may be used where coherence is required, but only if multiple refocusing pulses are applied. By repeating the same composite pulse, phase errors occurring due to the first composite pulse are effectively cancelled by the second composite pulse, due to the opposing direction of the inversion, which reverses the phase distortion. Such sequences are important, as their performance in terms of compensation for B_1 inhomogeneity and limited excitation bandwidths, generally outstrips that of the restrictive antisymmetric sequences.

2.4.3 Inversion sequences for use in EPR and integration into PELDOR experiments

Over the years, a large number of composite pulse sequences have been developed for use in magnetic resonance experiments. Their applications were typically in NMR experiments and targeted B_1 inhomogeneity compensation and increasing excitation bandwidths. The pulses can vary in length and involve many complicated and precise phase changes, as a result of attempts at numerical optimisation to create pulses as opposed to geometrical arguments. For use in experiments in EPR, and in particular in PELDOR experiments, we require short inversion sequences that will not limit pump pulse displacement. Longer sequences tend to provide better compensation and inversion over larger bandwidths, however their length can be restrictive in PELDOR.

In the absence of spin-coupling, the net effect of various composite pulses can be easily calculated by applying rotation matrices, and visualised using contour plots that show the magnitude of inversion as a function of frequency offset and B_1 inhomogeneity, as shown in Figure 2.12. The resonance frequency is given by Ω_0 which is also the frequency of the applied field/pulse. The nominal applied field amplitude to produce the required flip angle of the pulse (usually $\pi/2$ or π) is given by B_1^0. Figure 2.12 gives a number of examples of short, wideband composite π-inversion pulses. Short is defined here as typically no longer than 3 times the

length of a π inversion pulse. In the contour/density plots, the magnitude of the inversion varies from $M_z = +1$ (non-inverted) to $M_z = -1$ (inverted).

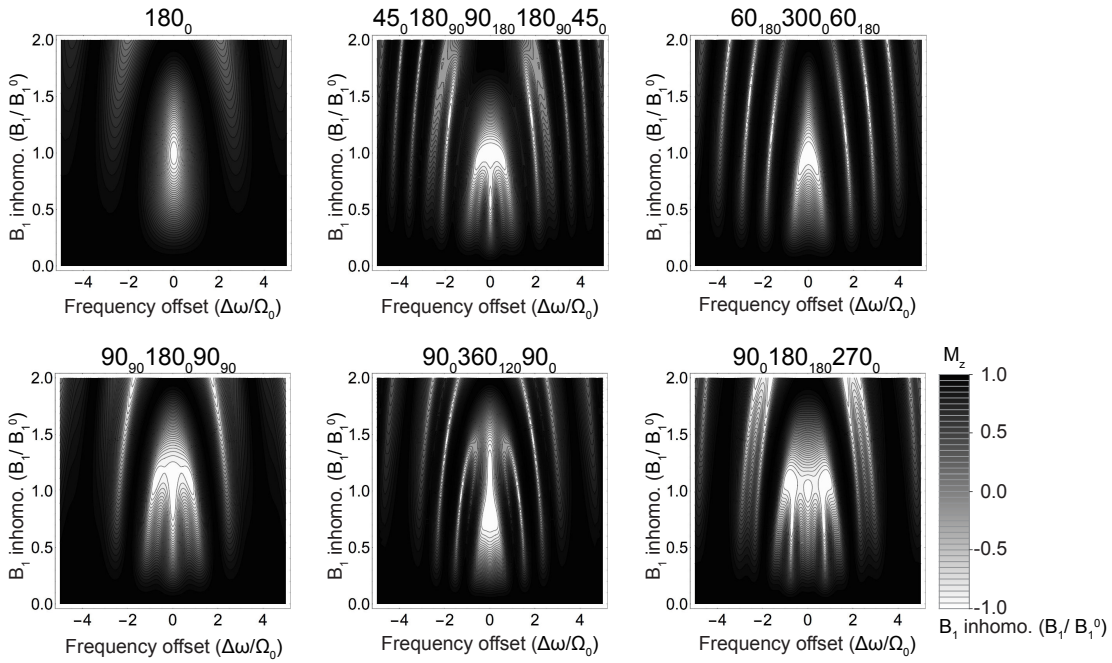

Figure 2.12: Contour plots showing the inversion performance of a range of composite pulses in terms of their ability to invert across frequency offset (x-axis) and in the presence of B_1 inhomogeneity (y-axis), where Ω_0 is the resonant frequency and B_1^0 is the nominal amplitude of the applied pulse. The plot scales between white = 95-100% inversion (M_z = -1) to black = 0% inversion ($M_z = +1$)

The inversion properties a standard 180°/π-inversion pulse are also shown in Figure 2.12 (A) where only a small area around the centre (on-resonance, $B_1^0 = 1$) can invert perfectly. This shows that for any level of applied field inhomogeneity, the spins will not be perfectly inverted over the sample volume. Similarly, it shows that the excitation bandwidth of the pulse is very limited.

Of the composite pulses shown in Figure 2.12, the $90_0180_{180}270_0$ sequence [26] offers the largest compensation for frequency offset, but only compensates for B_1 at large frequency offsets, relative to the standard π inversion pulse. The $90_{90}180_090_{90}$ sequence [25] offers slightly less bandwidth enhancement but offers more B_1 compensation at line centre (zero offset, $\Delta\omega/\Omega_0$=0). This sequence is also shorter and uses smaller 90° phase changes, reducing potential distortion effects during rapid phase changes.

The $90_0360_{120}90_0$ sequence is better at compensating for B_1 inhomogeneity (while offering some compensation for frequency offset) [58]. In a coupled spin system, it is usually assumed that the B_1 field associated with the pulse is larger than the dipolar coupling. In cases

where this is not true, the $45_0180_{90}90_{180}180_{90}45_0$ sequence potentially offers better inversion performance [59]. All the sequences mentioned so far are examples of variable rotation sequences [49], which as mentioned in Section 2.4.2, cannot be used to produce simple Hahn echoes dues to phase distortions arising. However, the $60_{180}300_060_{180}$ is an example of a constant rotation, or antisymmetric pulse, which can be used directly in Hahn echo sequences. However, as its inversion contour plot shows, its performance in terms of inversion over a range of offsets is not as large as other variable rotation sequences.

2.4.4 Frequency offset and bandwidth compensation

The bandwidth enhancement at nominal applied field ($B_1/B_1^0 = 1$) for $90_0180_{180}270_0$, $90_{90}180_090_{90}$ and a 16 ns π rectangular (180°) are shown in Figure 2.13. The figure on the left is the equivalent of taking a horizontal cut through of the contour plot at nominal field. The inversion profiles have been scaled according to a 16 ns π inversion pulse excitation profile. For reference, they are shown overlaid on a typical spectrum of a nitroxyl biradical obtained at W-band. Figure 2.13(a) shows that the composite pulses broaden the bandwidth of excitation around the frequency of the pulse, in comparison with the standard rectangular equivalent. However, the excitation is not uniform around resonance and they both also exhibit large 'wings' of partial excitation outside of the main central lobe. This can attributed to the rapid phase changes occurring during the pulse, which manifest as frequency spikes. The inversion profiles also illustrate that the composite pulses must be separated sufficiently in terms of frequency to avoid excitation overlap.

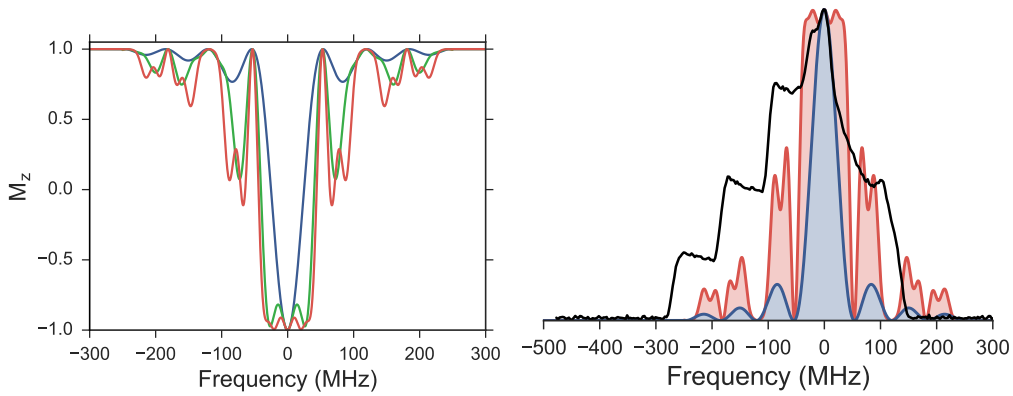

(a) **(b)**

Figure 2.13: (a) Inversion profile (M_z) of rectangular π (blue), $90_0180_{180}270_0$(red) and $90_{90}180_090_{90}$(green) composite pulses. The rectangular pulse is a 16 ns π. (b) shows the inversion profiles of a 16 ns π rectangular (blue) and $90_0180_{180}270_0$ (red) composite pulse overlaid on the absorption spectra of a nitroxyl biradical (black) taken at W-band.

2.5 Amplitude and frequency modulated pulse techniques

Another method that can be used to improve the excitation bandwidth of pulse is to use amplitude and frequency modulated pulses, known as shaped pulses. Such pulses involve sweeping the frequency of the pulse over a finite range of frequencies, and in some cases, the amplitude of the pulse is also modulated. This is in contrast to the more traditionally used rectangular mono-frequency pulse, which can only excite a finite bandwidth of spins around its pulse frequency. Similar to composite pulses, shaped pulses were first introduced into magnetic resonance experiments in NMR, where modulation of the carrier frequency could be easily carried out due to the much lower frequency of operation at kHz level. This gained particular traction in ultra high field NMR experiments, which were often bandwidth limited, as it meant the RF power level could be lowered such to reduce sample heating. The integration into EPR experiments has been much slower, partly due to the requirements for modulation at much higher frequencies, for which the instrumentation has only recently become available. The use of such pulses in standard EPR experiments such as PELDOR has rendered large improvements in modulation depths, and has allowed new experimental protocols, such as 5- and 7-pulse PELDOR experiments. As this thesis does not deal directly with the use of such experiments, only the attempts at implementation (Chapter 8) this part is provided only a background overview to what is a very important development in the field at the time of writing.

2.5.1 Theory of adiabatic, chirp and other wideband pulses in EPR

A useful reference describing the spin dynamics involved in shaped pulses can be found in the work by Tannús and Garwood [60]. The rotation of the magnetisation, **M** using frequency modulated pulses is best visualised in the rotating frame (x',y',z'), which rotates at the instantaneous frequency, ω_{mw}(t) of the pulse. Thus, the direction of the applied field vector, B_1(t) remains fixed, and by convention (ϕ=0°), it points along x'. When the frequency of the pulse differs from the resonance frequency, ω_s, a field is produced along z'-axis, of magnitude, $\Delta\omega/\gamma$ ($\gamma = g_e\mu_B/\hbar$)[1], where $\Delta\omega = \omega_s - \omega_{mw}$, i.e. the frequency offset between the resonance frequency and the frequency of the pulse. Combined with B_1(t), this results in an effective field, $\mathbf{B}_{eff}(t) = \sqrt{\Delta\omega/\gamma B_1(t)}$. As the frequency reduces towards the resonance frequency as a func-

[1] γ refers to the gyromagnetic ratio, which is much more commonly referred to in NMR as each element has a different gyromagnetic ratio. Given that we are only considering the electron here, it is not used in the convention presented so far. It is only used here for neatness in the calculation.

tion of time, the effective field changes its orientation, with an instantaneous angular velocity, $\frac{d\theta}{dt}$, where θ(t) is given by

$$\theta(t) = \arctan\frac{\gamma B_1(t)}{\Delta\omega(t)} \tag{2.37}$$

Thus, as $\Delta\omega \rightarrow 0$, the effective field rotates from +z' towards the transverse plane, resulting in a 90° rotation of the magnetisation, equating to an excitation pulse. If the frequency continues to sweep to -$\Delta\omega$, the magnetisation will continue to follow or precess about $\mathbf{B}_{eff}$(t) resulting in a 180° rotation of **M**, the equivalent of an inversion pulse. The magnetisation is able to follow the effective field as long as the frequency sweep is conducted adiabatically, i.e. slow enough. The restriction requires that the effective field does not change direction faster than the rate at which **M** precesses [61]. This is expressed using the adiabaticity factor, Q, given by [37]

$$Q = \frac{\mathbf{B_{eff}(t)}}{|d\theta/dt|} \gg 1 \tag{2.38}$$

The first type of shaped pulse to be reported in EPR was the sech/tanh pulse [35]. In this sequence, the frequency is modulated by a hyperbolic secant function, and the amplitude by a hyperbolic tangent function. The frequency modulation of the pulse as a function of time is given by

$$\Delta\omega(t) = \Delta\omega_{max}\tanh(\beta t) \tag{2.39}$$

where $\pm\Delta\omega_{max}$ is the width of the frequency sweep, t is its duration and β is a truncation parameter, as the function does not go to zero for small t. The amplitude modulation, B_1(t) is given by

$$B_1(t) = B_1^{max}\,\mathrm{sech}(\beta t) \tag{2.40}$$

where B_1^{max} is the maximum amplitude of the pulse, and β is also a truncation factor. Figure 2.14 shows the in- and out-of-quadrature pulse profiles for a standard 32 ns rectangular π inversion pulse, and for a sech/tanh shaped pulse which is designed to invert over a 200 MHz bandwidth (centred around the carrier frequency, in this case, zero) with an overall pulse length of 120 ns. The shaped pulse was generated using EasySpin's pulse function,

using a truncation factor of β=0.1*t [62]. A comparison of their respective inversion profiles, assuming no adverse effects of resonator profiles/inhomogeneity are shown in Figure 2.15. The inversion profiles were also generated using EasySpin.

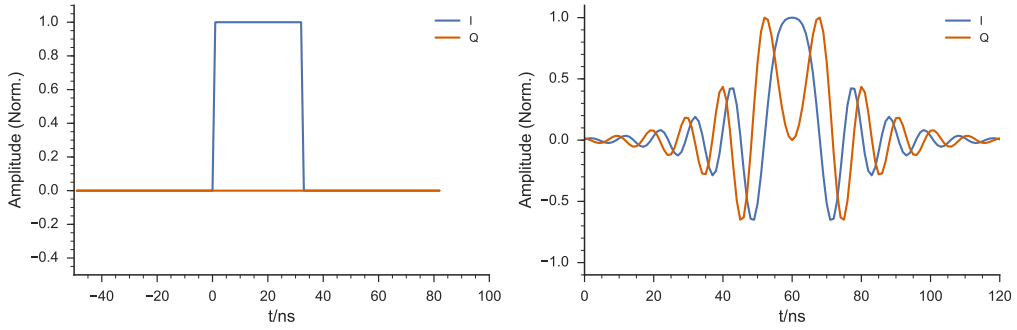

(a) Rectangular 32 ns π pulse **(b)** Sech/Tanh shaped π pulse

Figure 2.14: (a) 32 ns π inversion pulse (b) 120 ns Sech/Tanh π inversion pulse, using β=0.1t truncation factor, and generated using EasySpin [62]

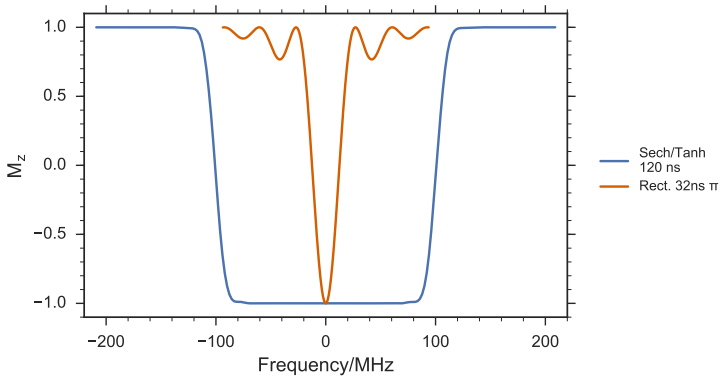

Figure 2.15: Comparison of the inversion profiles of the rectangular pulse (orange) and the sech/tanh shaped pulse shown in Figure 2.14. The shaped pulse shows flat inversion over ±100 MHz, whereas the rectangular pulse shows a sinc-like inversion profile, with inversion over ∼35 MHz. Both were generated using EasySpin [62]

The inversion profile show that the shaped pulse is able to invert spins over a much larger bandwidth than that of the standard rectangular pulse. The shaped pulse also benefits sharp transitions from no-inversion to full-inversion, meaning that pulses of differing frequencies, in experiments such as PELDOR, can be placed closer together, without overlap. This is in contrast to the rectangular pulses, which suffer from partial inversion outside of the main lobe of full excitation, which restricts how close in frequency pulses can be placed. There is a draw back however in using shaped pulses as to ensure high fidelity of inversion, the overall pulse length is usually quite long, usually 120-200 ns [35, 37]. In the case of PELDOR, where one might want to use such a pulse for the pump pulse to increase the modulation depth, the pulse

length will restrict how far one can step the pump pulse before overlap with the final inversion pulse in the sequence occurs (c.f. Figure 2.6). The rectangular pulse however, as it typically much shorter does not suffer this restriction. It has however been demonstrated that shaped pulses can generate up to 3 times larger modulation depth in PELDOR experiments where the pump pulse is replaced by a shaped pulse [35].

2.5.2 Implementation of shaped pulses

In order to implement shaped pulses, one requires a means of modulating both the amplitude and the frequency of pulses produced by the spectrometer. A variety of methods have been reported in the literature, including modifications to the bridge of an existing commercial spectrometer [35, 37, 63], on home-built spectrometers [39] or building new spectrometers that are based around the use of shaped pulses [36, 38]. At the core of these implementations is the arbitrary waveform generator (AWG) which allows the user to produce customised waveform outputs. The output of the AWG is programmed by specifying the voltage/amplitude at each point in the sequence, where the time dependence, or speed is given by the clock rate, typically in the range of GSa/s. The AWG is used to modulate the main carrier frequency used in pulsed operation, typically through the use of up-conversion in a diode mixer,which produces output of the carrier frequency plus the modulated output from the AWG [64]. Standard mixers have 3 ports as shown in Figure 2.16(a). The local oscillator (LO) port takes in the carrier frequency, in this case, typically 8-10 GHz, which is mixed with the intermediate frequency (IF) port signal, which is usually DC (0 Hz) to up to 3.5 GHz. At the RF port, the output is produced which consists of LO, LO + IF, and LO - IF, as shown in Figure 2.16(b). The mixer can also be used to down-convert modulated LO, by applying the modulated signal to the RF port, and the non-modulated LO to the LO port, producing the IF at the IF port (not shown).

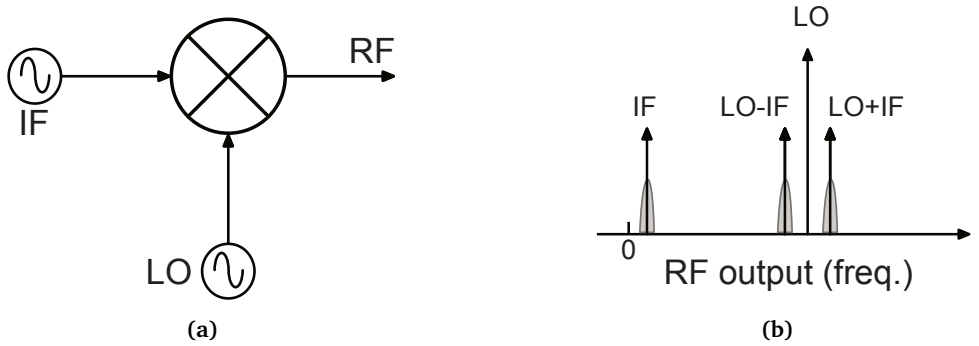

Figure 2.16: (a) Schematic diagram of a basic ideal RF mixer in up-conversion mode (b) diagram of the output from an ideal mixer at the RF port.

A drawback of this sort of up-conversion is that multiple frequencies are produced at the RF output as illustrated in Figure 2.16(a). To overcome this, filtering can be used, so long as there is sufficient difference in the IF and LO frequencies, such that band-pass filtering can cancel the LO and LO - IF, leaving only the LO + IF components can be used. Such a method is used in the AWG spectrometer that was developed at ETH Zürich [38]. This is possible as they are using fast AWG, (12 GSa/s) which allows them to produce IF frequencies around 1.5 GHz, which provides a large enough separation between their LO (typically at 8 GHz) to allow for band-pass filtering to be used.

Where fast AWGs are not available, most groups have resorted to using IQ mixers that, with careful calibration are able to suppress the LO and produce the upper side band (LO + IF) output only. This takes an IF input in the form of its in- and out-of-quadrature components to separate ports, called I and Q, where the Q signal is 90° or $\pi/2$ out of phase with the I signal. The signal is then mixed with LO such that the LO - IF signal is cancelled out. A schematic diagram of the double-balanced mixer and its corresponding RF output produced is shown in Figure 2.17.

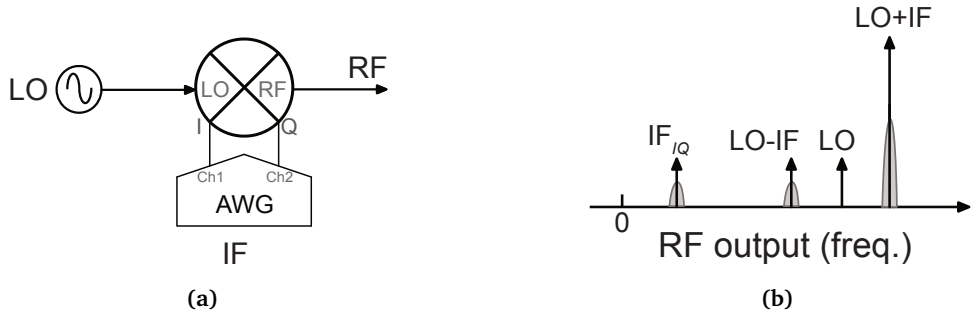

(a) **(b)**

Figure 2.17: (a) Schematic diagram of an ideal double-balanced IQ RF mixer in up-conversion mode (b) diagram of the output from an ideal double-balanced mixer at the RF port.

Most implementations using double-balanced mixers use the pulse oscillator source as the LO, and generate waveforms (IF input) using the AWG, that modulate the signal around LO centre frequency. This allows the full bandwidth offered by the particular AWG to be used to produce broadband shaped pulses. It does however require very careful calibration of the mixer itself, as the performance degrades leading to 'leakage' of LO and the LO-IF frequencies if there are offsets in amplitude, phase or DC offset of the IQ inputs to the mixer. This is discussed more fully in Chapter 8.

2.6 HiPER: High power EPR at 94 GHz

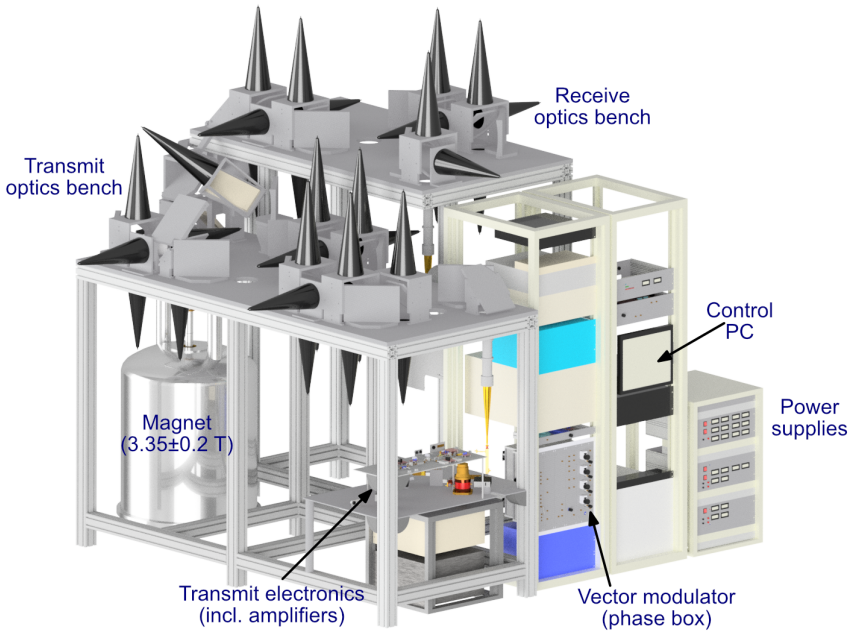

Figure 2.18: CAD view of the HiPER spectrometer, showing the location of various components of the system. Credit to Dr Rob Hunter

The instrument used in the majority of experiments in this thesis, is a home built 94 GHz 1 kW pulsed spectrometer, known as HiPER [24] (shown in Figure 2.18.) The instrument has been developed at St Andrews by the Millimetre Wave and EPR Group, following a £2.6 million Basic Technology grant aimed at 'bringing the NMR paradigm to EPR.' The aim of the project was to develop a spectrometer that offered significant increase in concentration sensitivity versus commercial spectrometers, with a view to be able to measure at much lower concentrations and in a much faster time. The vast majority of commercially available spectrometers utilise resonant cavities in order to increase the applied B_1 field across the sample, however cavities are designed to support single mode within the cavity, which places restrictions on the bandwidth of frequencies that can be supported. To excite broadband samples, and to provide sufficient frequency separation between pulses, larger bandwidth cavities can be used, however, they suffer from overall decreased B_1 field amplitudes, which require longer pulse lengths and thus, lower excitation bandwidths. Another drawback of cavities are the ring-down time that occurs immediately after pulses applied, which can last 100-200 ns, where it is not possible to detect signals from the sample, due to large amplitude pulse reflections in the cavity, which would damage the receiver.

HiPER removes the bandwidth and dead time restrictions of cavity, and instead uses a non-resonant set up, where samples are placed inside a cylindrical transmission line, which is shorted by a small mirror at its base. This set up allows for large sample volumes to be utilised, and it supports a large frequency bandwidth.

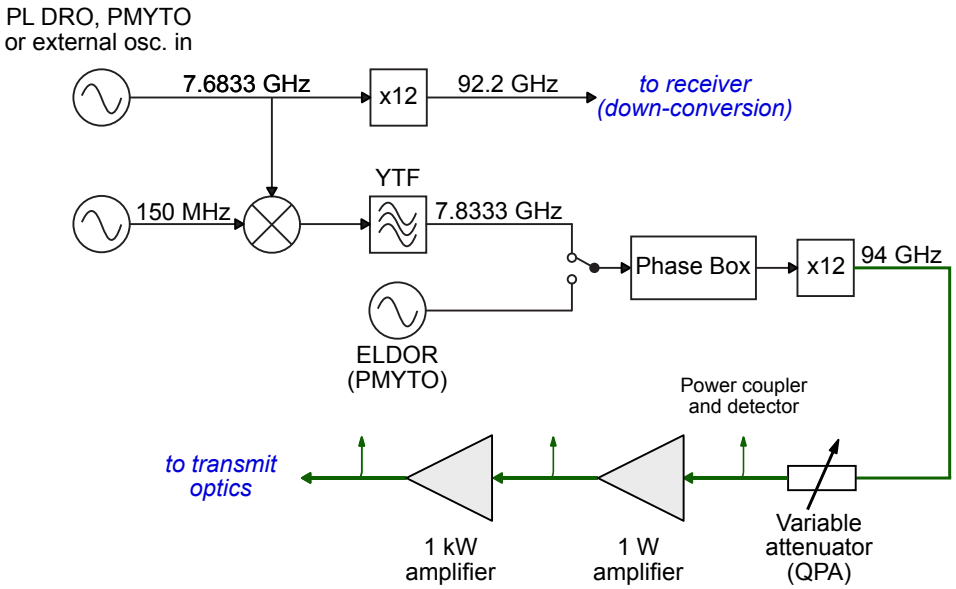

Figure 2.19: System overview of the pulse transmit set up on HiPER, showing the oscillators, phase control box, multipliers, amplifiers and power monitor locations. The thick green line indicates points where the frequency is at 94 GHz. The arrows that are perpendicular to the green 94 GHz line indicate positions of power couplers with power detectors attached.

A simplified system diagram of the transmit chain on HiPER is shown in Figure 2.19. Pulses on HiPER are formed at 7.833 GHz using either a fixed frequency phase-locked dielectric resonant oscillator (DRO) or a tunable, phase-locked permanent magnetic yttrium iron garget (YIG) tuned oscillator (PMYTO) at 7.683 GHz, which is up-converted using a 150 MHz oscillator. The pulses then either bypass or transmit through 1 of 4 phase channels in the vector modulator, which provides arbitrary phase modulation to the signal at 7.833 GHz, before passing through a x12 multiplication chain (VDI) to the transmission frequency of 94 GHz. When the tunable PMYTO oscillator is used as the source, the frequency can be tuned between 93.5 to 94.4 GHz. The pulses are then formed by the main pulse switch, which consists of a double-balanced mixer which provides switch on times as fast as 300 ps. The pulses then pass through the hard/soft pulse network, which consists of fast switch that allows for pulses to pass through an additional variable attenuator to produce lower amplitude pulses. The paths then recombine before passing through a solid-state 1 W amplifier (Quinstar) followed by a 1 kW extended interaction klystron amplifier (EIKA), before entering a feedhorn which directs the pulses to

the transmit optics bench. From there, they then pass through a sequence of mirrors, Faraday rotators and polariser grids, for single mode transmission at 94 GHz. The optics bench then directs the pulses into a 1.8 m long corrugated cylindrical waveguide, which leads into the centre of a 3.35 T superconducting magnet. The waveguide tapers from 46 mm to 3 mm using a feedhorn, where the 94 GHz signal reaches the sample holder. Signals from the sample are then reflected back up through the waveguide, where they are separated from the transmit signals via a polarising grid and directed onto the receive optics bench. This bench similarly consists of an array of mirrors, Faraday rotators and polarising grids, which direct the signal from the sample, typically at the pico-watt level, into a highly sensitive receiver at the end of a feedhorn. The signal passes through the receiver protection switch, which operates to protect the receiver from transmission leakage which may damage the receive mixer. From there, the 94 GHz signal is down-converted coherently through mixing with the 92.2 GHz from the transmit oscillator (after multiplication), producing output at 1.8 GHz. The modulated signal at 1.8 GHz then passes through a 90° splitter, producing the in- and out-of-quadrature parts of the receive signal. Both channels are then down-converted using a 1.8 GHz coherent source, producing the baseband (zero frequency offset) signal. The output is then either directed to 1 GS/s digitiser and averaging card, in the control PC. The main pulse switch is controlled using the 'fast channel' on a 81210 parametric bit error rate testing (ParBERT) system, which operates up to 2.66 GS/s. The switches for pulse sources, and the vector modulator channel select are provided by the other channels which operator 4 times slower. HiPER is set up such that the ParBERT provides 0.5 ns resolution for pulses, and 4 ns resolution for the vector modulator.

2.6.1 Amplifier characterisation

In order to investigate the bandwidth limitations of the system, measurements were carried out monitor the power level as a function of transmit frequency at various points in the transmit chain. There are a number of power couplers in the system, which act as connectors between various stages, but also allow for permanent power monitoring using fast diode power detectors. The detectors have been calibrated as function of power and frequency using a HP 437 power meter. There are three detectors installed on HiPER monitoring the output from the VDI multiplier chain, output from the 1 W amplifier and output from the 1 kW amplifier. In day to day operation on HiPER, all three are monitored on a 20 GS/s LeCroy digital oscilloscope. Power measurements were taken using the oscilloscope as a function of frequency, as shown

in Figure 2.20.

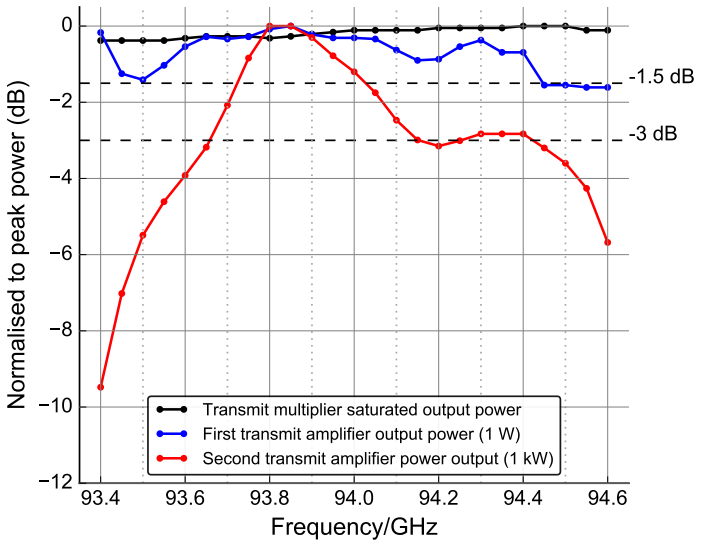

Figure 2.20: Power levels vs frequency at various stages in the transmit chain of the W-band spectrometer, normalised to the peak output. The response of the transmit multipliers (black) and the first transmit amplifier (1 W, blue) is relatively flat over the range 93.4-94.6 GHz, in comparison with the second transmit amplifier (1kW EIKA, red) which causes the largest bandwidth limitation.

The plots shows that the power output from the multipliers (black) is generally flat, with little variation over the range from 93.4 to 94.6 GHz. The 1 W amplifier, shown in blue is generally flat between 93.6 and 94.1 GHz, and shows up to 1.5 dB difference in output between 94.1 and 94.6 GHz. Both devices are driven in saturation, so any changes in amplitude will have minimal effect. The largest variation in power output comes from that of the EIK amplifier (red) which provides peak output at 93.8 GHz, dropping by more than 3 dB at frequencies less than 93.65 GHz and greater than 94.4 GHz. This illustrates that the amplifier can provide output over ∼800 MHz, with some variation in amplitude over the range. It also illustrates that power output varies moderately as a function of frequency, and that the user must bear this in mind when setting up the instrument. Other frequency characterisation carried out on HiPER, showed all other non-electrical components in the system, such as the optics benches and feedhorns were flat over this range, with at maximum 0.5 dB variation in power. This indicates that the bandwidth of the spectrometer is limited by the EIK amplifier.

2.6.2 Non-resonant sample holder

In order to ensure large excitation bandwidths can be utilised in experiments, HiPER uses a non-resonant sample holder. Unlike traditional resonators that use cavity set ups which

offer enhanced B_1 fields over smaller bandwidths, HiPER uses a cylindrical transmission line set up that allows for operation over a large range of frequencies. Sample tubes are loaded into a sample 'puck' as shown in Figure 2.21(b) which consists of a 3 mm diameter smooth walled piece of waveguide, supporting a TE_{11} mode. The puck is set into plastic to allow for easy handling. Its overall length is approximately 30 mm. The sample puck is placed into a spring-loaded mount (Figure 2.21(a)) which is attached to the narrow end of a tapered corrugated feedhorn, with an opening which matches the inner diameter of the puck. The mount is spring-loaded so that the sample puck can be slid rapidly into a circular recess where it is located correctly within the waveguide to facilitate cold sample loading.

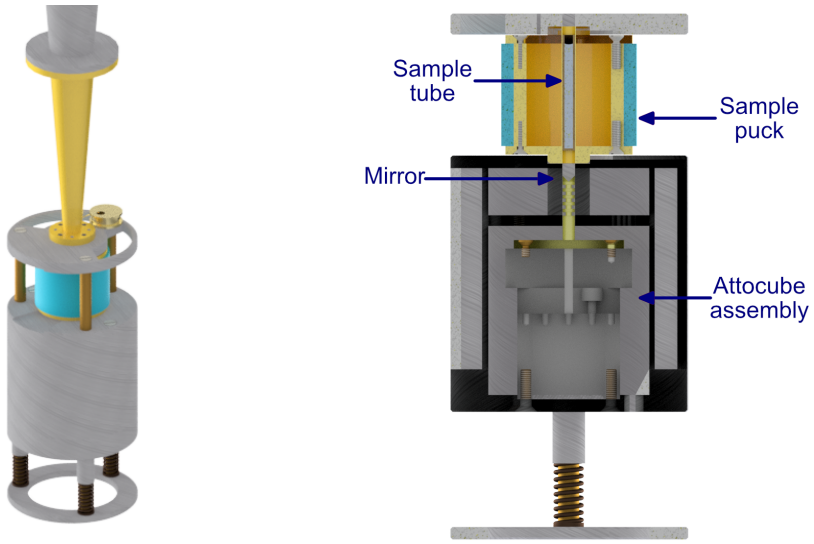

Figure 2.21: CAD images of (a) feedhorn and sample holder attached, (b) cut-through of the sample holder, showing the sample puck with loaded sample, and the Attocube mounted mirror at the bottom. Credit to Dr Rob Hunter for both images.

Below the sample puck, inside the lower 'can' part of the sample mount, a piezo-mounted roof mirror, or back-short is located. The piezos, supplied by Attocube (Munich, Germany) allows the user to precisely adjust the position of the back-short vertically and rotationally to optimise the power-coupling to the sample or minimise cross-polar. The use of a mirror below the sample means that the incident and reflected millimetre wave radiation through the sample, interfere creating a standing wave. By altering the position of the back-short vertically, it is possible to adjust the number of half-wavelengths within the sample, which optimises the signal from the sample itself. Coupled together with the fact that the circular waveguide supports a TE_{11} mode, the B_1 field within the sample will be highly inhomogeneous. The implications of this is discussed fully in Chapter 4.

2.6.3 Composite pulse implementation: Phase modulator

In the original implementation of HiPER, phase control was provided by 4 individual channels consisting of variable phase controls, which could be chosen individually to set the phase of the transmit signal. In the most recent implementation and the one used here, much more flexibility has been built in to the system by allowing the channels to be combined in a binary fashion, permitting for a choice of up to 16 (2^4) phase states. A schematic diagram of the phase box is shown in Figure 2.22. The phase box is situated prior to the x12 multipliers, and thus operates around 7.833 GHz (depending on choice of oscillator). The input signal is applied to a 2-way 0° power splitter, allowing one arm to act as phase reference, while the other arm is split into 4 channels, using a 4-way 0° power splitter. Each of the 4 channels has a separate attenuator and phase shifter, which allows the user to set the phase of the input signal. Each of the 4 phase channels are selected individually or collectively, using 4 fast switches controlled from the ParBERT pulse controller (Agilent, Inc.) which provides 4 ns timing resolution. The signals from the channels are then recombined in phase quadrature with the signal from the reference arm. By varying the attenuation and phase of the channel(s), one can obtain a continuously variable phase shift (up to 74°). Due to the fact that the phase shifting is carried out prior to the x12 multiplier, only one-twelfth of the phase shift is required. Thus, to produce a 360° phase shift at 94 GHz, one would only require a 30° shift in phase at 7.8 GHz.

Using the 4 channels in a binary fashion, one can produce 15 binary weighed steps in phase from 0 to 360° at 94 GHz, by setting the channels to 1.875°, 3.75°, 7.5° and 15° at 7.833 GHz. Since the phase changes required are very small, the accompanying amplitude change is also very small, and is largely eliminated by the levelling amplifier, and the post-multiplication amplifier chain.

Using phase changes on short time scales, such as when implementing composite pulses, can induce large amplitude and frequency distortions, thus it is important to measure what effect phase changes can have. Figure 2.23(a) shows the amplitude response when a $90_0180_{180}270_0$ composite pulse sequence, using a 16 ns π pulse length ($t_{\pi composite}$ = 8+16+24 ns) after multiplication (red) and after the amplification by both the 1 W and 1 kW amplifiers (blue). The 1 W amplifier is a solid state amplifier from Quinstar which features a 6 GHz instantaneous bandwidth, and the 1 kW from CPI has a 1 GHz instantaneous bandwidth, thus offering 1 ns resolution, and is thus considered the bandwidth limiting component in the transmit chain[2].

[2]The 1 W amplifier has also been subjected to amplitude response measurements for composite pulses, and it

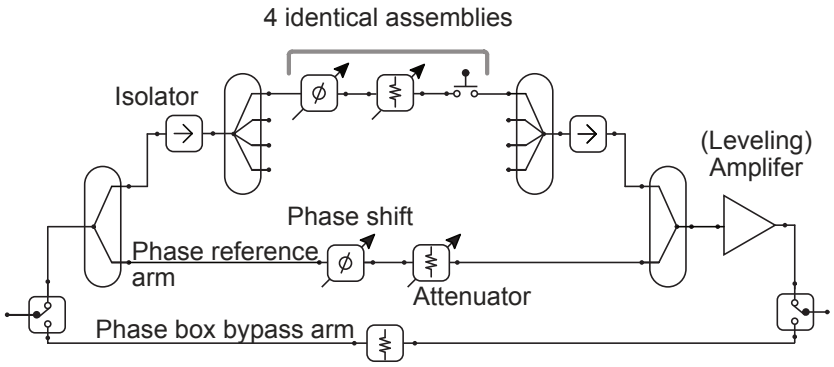

Figure 2.22: Schematic diagram showing the vector modulator phase control box set up used on HiPER, consisting of 4 independent channels that can be combined simultaneously by opening several channel selection switches. The phase of each channel is set using a phase shifter and an attenuator. It also shows the phase box bypass channel.

As can be seen in the figure, the amplitude after multiplication is broadly flat, with small (>5%) distortions occurring during the phase changes, indicating that multiplication is causes minimal amplitude distortion. The post-amplification trace however shows large amplitude drop outs occurring during phase changes, as the phase swaps between 0° and 180° extremely quickly causing a ringing effect. However, as the trace also shows, this resolves within 1-2 ns indicating that it should have miminal impact on the performance of the pulses. It should be pointed out that some of the distortions seen in the Figure are caused by reflections of signals within the cables used for the measurement, known as cable bounce. The peak indicated by the asterisk (*) in Figure 2.23(a) is caused by cable bounce.

Figure 2.23(b) shows the same composite pulse, recorded after down-conversion via the receive chain. It shows the full system response to the composite pulse. This was recorded by sending pulses to the sample holder and recording the back-reflected signal in high power through several sheets of Eccosorb, a type of foam which attenuates millimetre wave signals with minimal distortion, as to not damage the sensitive receiver. The figure shows that the phase is slightly distorted shortly after the phase change, with some signal in the out-of-quadrature channel, but this settles to zero after 2-3 ns. This indicates that the phase response of the system at 94 GHz is extremely good. It would be expected that in conventional cavity based set ups, phase response would be much slower and thus much more distorted due to the bandwidth restrictions of the cavity.

showed ringing on the order of 200 ps, in line with its bandwidth.

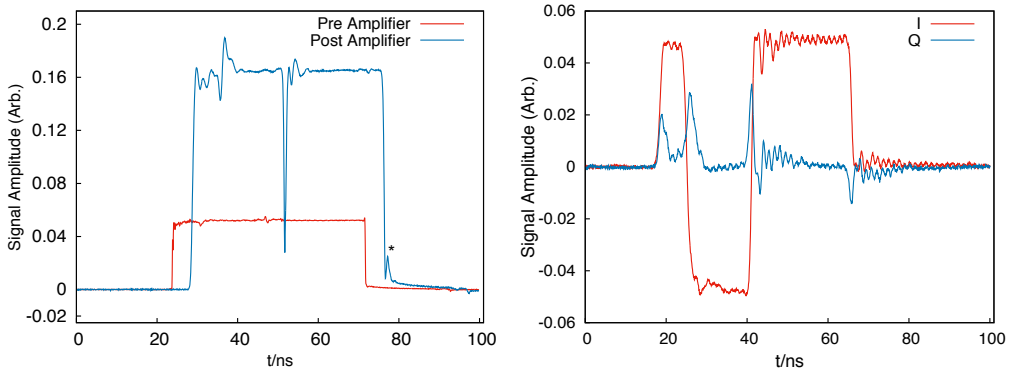

(a) **(b)**

Figure 2.23: (a) Plots showing the pulse power profile of a $90_0180_{180}270_0$ composite pulse, using 8+16+24 ns pulse lengths, prior (red) and after (blue) the 1 kW amplifier (blue), measured using a fast digital oscilloscope and a fast power monitor, showing minimal distortion due to the 1 kW amplifier, and ringing which resolves within 1-2 ns. (b) Output from the IQ detection system via the sample holder showing full system response.

3

Assessing and improving sensitivity

This chapter will focus on procedures to improve sensitivity beyond using pulse techniques, including testing different sample tubes, studying processes to improve sample glassing and how digital filtering might be used in the software to improve signal-to-noise.

3.1 Annealing samples and vitrification

3.1.1 Vitrification

One of the sources of losses when using non-resonant cavities are dielectric losses, caused by interaction of the E-field with the sample, and scattering caused by cracks and imperfections in the glassed sample which reduce the transparency and increase signal loss. While dielectric losses cannot be easily reduced without significantly altering the sample solution, sample cracking can be reduced and removed by altering sample loading and preparation routines prior to testing. Before any cold testing is carried out, the samples are flash-frozen by immersion in liquid nitrogen (77 K), which if performed correctly (plunged) will result in a super-cooled liquid glass state. This process is generally aided by adding 'cryoprotectants' to

the sample solution. This is important, as to successfully vitrify water, it must be cooled at rate of 1 x 10^6 K/s, whereas if the solution consists of 50 % of a cryoprotectant such as glycerol, this reduces to ∼50 K/s [65]. Vitrification occurs as the fast cooling process resists transition into a crystalline solid due to its viscosity. Since water has a very low viscosity, the vitrification process is improved by the addition of viscous substances (cryoprotectants) such as glycerol [66]. This is commonly carried out to preserve biological samples and tissues from damage when freezing, as ice crystals can pierce and damage cell walls and disrupt the structure.

In the EPR case, having a vitrified sample is key to reducing scattering losses caused by the formation of ice crystals. It also helps to avoid aggregation effects in the sample. Theory by Bhat. et al [67] indicates that the minimum concentration for successful vitrification is 40%, as at this point, all of glycerol's hydrogen bonds (6) are occupied by water molecules. Below this concentration, mesoscopic domains of water molecules can form, which will crystallise, disrupting glass formation. Bhat et al. have also produced an empirical formula for calculating the glass transition temperature of water/glycerol mixture, given by

$$T_g = w_1 T_{g1} + w_2 T_{g2} + K w_1 w_2 \tag{3.1}$$

where T_{g1} and T_{g2} refer to the glass transition temperatures of the components of the mixture, w_1 and w_2 are their respective proportions and K is a constant. For water/glycerol, the glass transition temperatures are 132 K and 200.5 K respectively. Bhat et al. calculated the constant K to be -95, thus a 50/50 water/glycerol solution should undergo its glass transition temperature at ∼142.5 K.

3.1.2 Annealing

While conducting experiments on HiPER, it was discovered that the signal amplitudes were much lower than expected, often accompanied by poor isolation between transmit and receive signals, resulting in increased noise. This was attributed to formation of a poor glass upon flash freezing and loading of the sample. When samples are loaded into the spectrometer for a cold experiment, the sample is flash frozen in liquid nitrogen and loaded into a sample puck which is also immersed in liquid nitrogen, before being inserted into the cryostat of the spectrometer at 130 K. To load the sample, the liquid helium cooling is temporarily stopped and the cryostat returns to ambient pressure for a period of approximately 30 seconds, while the waveguide is hoisted out of the cryostat and the sample puck is loaded into the sample holder at the end

of the waveguide, before being lowered back into the cryostat and cooling recommences. At this time, the sample is briefly exposed to ambient air, which should not cause the sample temperature to increase greatly, as air is a poor conductor of heat. The sample and the sample puck will thermalise to the cryostat at 130 K, in the interim before liquid helium cooling is restarted. If the sample warms above 130 K during the process, it is in the region known as 'no man's land' [68] between the temperatures that ice crystals can form, and the temperature at which it is a supercooled liquid, or glass state. The formation of ice crystals changes the dielectric constant of the sample, which can result in loss of signal through the sample, as well as scattering due to cracking.

To reduce this, a protocol has been developed alleviate cracking in the sample, resulting in significantly improved echo signals and much more reproducible results. This involved firstly replacing the previously used quartz sample tubes, with sample tubes made out of the translucent polymer, FEP (Fluorinated Ethylene Propylene). Through flash-freezing experiments on samples inside FEP tubes and quartz tubes, it was discovered that the FEP tubes routinely formed better glassed samples that the quartz equivalent sample tube. As the sample freezes, it does so from the outside nearest the walls of the tube, towards the centre. This was observed as a meniscus formed on the top surface of the tube. This differential cooling will induce stresses as it transitions into a glassy state. The performance of the FEP tube in comparison with the quartz was attributed less mechanical stress being placed on the sample during freezing due to the hydrophobic surface of the FEP tube, and lower differential cooling for the FEP tube versus the quartz. The quartz tubes however are hydrophilic and have a very low coefficient of expansion relative to most samples, which can also exacerbate cracking.

The largest improvement (up to five times enhancement in echo amplitude) has been observed when the samples are subjected to an annealing process after loading into the cryostat. This involves gradually raising the temperature of the cryostat to ∼190-200 K, taking it through the glass transition and through the so-called 'no man's land' region. This is carried out while monitoring a continuous wave microwave signal at 94 GHz through the sample. As the sample goes through its transition, its dielectric constant changes. At this point, the signal through the sample is observed to rapidly decrease. When this occurs, the cryostat is then lowered to the measurement temperature, by reducing the heater and increasing liquid Helium flow rate through the cryostat to maximum. The benefits of this step are attributed to release of stresses within the sample and the formation of better glass in much more controlled conditions, with-

out sudden temperature jumps induced during loading. It has been noted that echo signals have improved by as much as five times in echo amplitude after annealing.

3.2 Concentration sensitivity of HiPER: 1 μM TEMPO

3.2.1 Comparing sample holder set ups

In order to give a fair comparison of a spectrometer's sensitivity, it is important to consider the physical attributes which provide excitation and detection of samples. The main aspects that describe the sensitivity are the cavity used, frequency of operation and power available. When comparing spectrometers, it is often useful use the concentration sensitivity of a given set up, as this takes into account differences such as sample volume, bandwidth of excitation, applied field inhomogeneity, and the associated dielectric losses. In this discussion, this will be factored into a conversion factor c, and a Figure of Merit, F, to quantify the concentration sensitivity of a given set up.

In a critically coupled cavity, the average applied B_1^2 field is given by [48, 69, 70]

$$\left\langle B_1^2 \right\rangle_c = \frac{2Q_L\mu_0}{V_c\omega_0}P_0 \tag{3.2}$$

Where Q_L is the loaded quality factor (Q) of the cavity, P_0 is the available power, μ_0 is the magnetic permeability, V_c is the cavity volume, and ω_0 is the angular frequency of the applied field. The filling factor, η_c of the sample inside the cavity is given by

$$\eta_c \equiv \frac{\int_{V_s} B_1^2 dV}{\int_{V_c} B_1^2 dV} = \frac{V_s \left\langle B_1^2 \right\rangle_s}{V_c \left\langle B_1^2 \right\rangle_c} \tag{3.3}$$

where $\left\langle B_1^2 \right\rangle_s$ refers to the components of the applied field that are perpendicular to the external magnetic field, B_0, and $\left\langle B_1^2 \right\rangle_c$ refer to all B_1 components in the cavity. This implies that the filling factor, η_c is typically < 1. The average B_1 field across the sample in the cavity case is given by

$$\left\langle B_1^2 \right\rangle_s = \left(\frac{2\eta_c Q_L \mu_0}{V_s \omega_0} \right) P_0 = c_c^2 P_0 \tag{3.4}$$

where c_c is the conversion factor of the cavity. This is considered in comparison with the average transverse B_{1t}^2 field in a single mode rectangular waveguide, with a cross sectional

area of A_w and impedance, Z_w

$$\left\langle B_{1t}^2 \right\rangle_w = \frac{2\mu_0}{Z_w A_w} P_0 \tag{3.5}$$

In the case where the waveguide is shorted (i.e. mirror placed at one end, such that B_1 field is reflected back through the sample/waveguide), it will have an effective volume of $V_w = A_w \lambda_g / 2$ where λ_g is the wavelength supported by the waveguide. This causes the average B_1 field to be doubled over the volume due to reflections. Thus, we can define the filling factor of the waveguide, η_w in terms of the effective average B_1 field inside the cavity,

$$\eta_w = \frac{V_s \left\langle B_1^2 \right\rangle_s}{V_w \left\langle B_1^2 \right\rangle_w} \tag{3.6}$$

Assuming the single mode supported by the waveguide is a TE mode, such that $\mu_0 / Z_w = 2\pi/(\omega_0 \lambda_g)$, thus the expression for the B_1 field over the sample can be derived as

$$\left\langle B_1^2 \right\rangle_s = \frac{\eta_w 4\pi\mu_0}{V_s \omega_0} P_0 = c_w^2 P_0 \tag{3.7}$$

While the expressions for $\left\langle B_1^2 \right\rangle$ are useful for comparing different types of cavities, it is generally more convenient to estimate the conversion factor, c by measuring the effective $\pi/2$ pulse length, $t_{\pi/2}$ for a given input power, P_0,

$$c \sim \frac{B_{1s}}{P_0^{1/2}} \sim \frac{\pi}{2\gamma t_{\pi/2}} \cdot \frac{1}{P_0^{1/2}} \sim \frac{90ns}{t_{\pi/2}(ns)} \cdot \frac{1}{P_0^{1/2}} \left[G/W^{1/2} \right] \tag{3.8}$$

where $t_{\pi/2}$ is measured using a Hahn echo experiment. In this case, the B_{1s}^2 field over the sample is calculated as $|\sin(B_1 \gamma t)|$, assuming B_1 is homogeneous. The $\pi/2$ pulse length will determine the excitation bandwidth of the spins within the sample. Once the sample is excited, we need to be able to detect a signal from it, and this will be proportional to the initial magnetisation, m_0 after excitation as

$$m_0 = C \cdot V_s \tanh\left(\frac{\hbar\omega_0}{k_B T}\right) \sim C \cdot V_s \left(\frac{\hbar\omega_0}{k_B T}\right) \tag{3.9}$$

where C is the spin concentration (number of spins per unit volume), V_s is the volume of sample and T is the sample temperature. Signal from the sample is generated and emitted as the magnetisation m_0 precesses about B_0 in the transverse plane. If the sample undergoes

this precession in free space, it will emit a circularly polarised beam of radiation due to the coherent spontaneous emission of the spins. The power emitted by the spins in the sample is given by

$$P_{emission} = \frac{4\pi\mu_0^2\omega_0^2 m^2}{3\lambda^2 Z_0} \tag{3.10}$$

where Z_0 is the impedance of free space, and λ is the free space wavelength. As the radiation is emitted, it is will be modified by its surroundings in terms of impedance Z, and the wavelength of radiation, λ. This will dependent on the set up, whether it is a shorted waveguide or a cavity, as the power emitted from any part of the sample will be dependent on how it will couple to the desired mode in the cavity of the waveguide. Thus, for a critically coupled waveguide/cavity, $P_{emission}$ will be given by

$$P_{emission} = \frac{\eta_c 2Q_L\omega_0^2 m^2}{V_s} = c_c^2\omega_0^2 m_0^2 \tag{3.11}$$

and for the shorted waveguide

$$P_{emission} = \frac{\eta_w 2\pi\omega_0^2 m_0^2}{V_s} = c_w^2\omega_0^2 m_0^2 \tag{3.12}$$

The component of the magnetisation in the transverse plane will be be dependent on the type of experiment carried out, B_1 inhomogeneity across the sample, the bandwidth of excitation, and the relaxation rate of the spins involved. For the case where the entire spectrum is excited, and the B_1 is completely homogeneous, the maximum power to be emitted will be given by

$$P_{max} = c^2\omega_0^2 m_0^2 \tag{3.13}$$

where c is the conversion factor estimated from the effective $\pi/2$ length. The signal will be proportional to the square root of P_{max}, and thus $c \cdot \omega_0 \cdot m_0$, and given that $m_0 \propto \omega_0 V_s$, we can define a Figure of Merit, F, given by

$$F = c \cdot \omega_0^2 V_s \tag{3.14}$$

This term is useful for directly comparing different cavity or waveguide set ups, based on the key features of conversion factor, volume of sample and frequency of operation. From

this equation, we can see that the figure of merit for comparable cavity set ups (with the same conversion factor, c) scales as square of the frequency of operation, inferring that the sensitivity will improve at higher frequencies.

3.2.2 Concentration sensitivity comparison: 1 μM TEMPO test

One of the main aims of this project is to compare and improve the sensitivity of pulse EPR experiments using HiPER, in comparison with commercially available spectrometers. For this comparison, the Bruker Elexsys X-band spectrometer has been utilised, as at the time of measurement, it was regarded as one of the most commonly used 'work horse' spectrometers for PELDOR measurements. This spectrometer operates at 9.5 GHz and uses a cavity resonator, whereas HiPER operates at 94 GHz and uses a non-resonant sample holder set up. The difference in cavity type allows HiPER to probe much broader bandwidths than a cavity resonator, as it is not restricted by the Q-factor and ring-down parameters as in the cavity resonator case.

HiPER has the added advantage that due to the fact it uses a non-resonant cavity, it is also possible to alter the volume of sample measured, increasing the number of spins measured. Using the theory discussed in Section 3.2.1, we an deduce the gain expected using HiPER in comparison with other spectrometers, and for various set ups in each case. This is calculated with reference to an optimised PELDOR cavity set up provided by Bruker, called the MD5 cavity. This operates around 10 GHz and features a $\sim$160 μL effective sample volume. It has a conversion factor, c of 0.3 resulting in a Figure of Merit of 4.8×10^{15} [69]. A number of different HiPER sample tube set ups were tested in this experiment.

Two types of sample tube were tested, both were approximately 45 mm in length, and had a outer diameter of 2.97 mm, and were placed inside an extended sample 'puck' which was 45 mm in length. One of the tubes was made of fluorinated ethylene propylene (FEP) tubing, which was provided by AdTech Polymer Engineering, created by sealing lengths of FEP tubing through melting processes. The tubing had a wall thickness of 1 mm, leaving an inner diameter of $\sim$2 mm. The tubes were filled to sample depths of 20 and 38 mm for comparison of sample volume. The second tube was machined in house out of Rexolite, a hard polystyrene plastic which was chosen for its very low dielectric constant, thus low dissipation/loss properties at 94 GHz. Sample tubes with a wall diameter of 0.5 mm were made by machining blocks of Rexolite, to produce sample tubes with a large sample volume.

The corresponding conversion factors, volumes and calculated Figure of Merit for each of

the set ups relative to the MD5 are summarised below.

Tube	Sample Volume /μL	$t_{\pi/2}$/ns	Conversion Factor	Relative Figure of Merit
FEP, 38 mm fill	119	7.0	0.41	44
FEP, 20 mm fill	61	6.0	0.47	27
Rexolite	186	8.5	0.33	57

Table 3.1: Table showing the relative Figure of Merit in comparison with a Bruker MD5 cavity, for various set ups on HiPER

A direct sensitivity comparison was carried out between the X-band Bruker spectrometer and the 3 tube variants on HiPER, as detailed in Table 3.1, using 1 μM sample of the nitroxyl mono-radical. The radical used was 4-amino TEMPO (4-Amino-2,2,6,6-tetramethylpiperidine-1-oxyl) which is a water-soluble version of TEMPO, a small organic molecule containing a nitroxyl radical. It is structurally similar to the MTSL nitroxyl spin label, but lacks the necessary attachment site to be used in spin labelling.

The sample was prepared by dissolving 4-Amino-TEMPO in deionised water, which was then added to water/glycerol to create a final concentration of 1 μM TEMPO in 60/40 glycerol/water. For the X-band testing, 100 μL was placed inside a sample tube for testing. The W-band sample volumes/tubes used are as given in Table 3.1. The X-band measurement was carried out at 50 K, and the W-band measurement at 58 K. The temperature difference should have minimal effect on the relaxation properties, it is purely due to the fact that the HiPER cryostat operates optimally at 58 K instead of 50 K.

The benchmark for the sensitivity measurement was a simple Hahn echo ($\pi/2 \rightarrow \tau \rightarrow \pi \rightarrow \tau \rightarrow echo$) with $\tau = 2$ μs, thus producing the echo at 4 μs, which is then recorded after 1000 averages.

The signal-to-noise (SNR) for each of the echoes was obtained by taking the ratio of peak amplitude with the root mean square of the noise floor. The results are summarised in Table 3.2.

Tube	RMS noise	Echo peak	SNR	Area under curve
FEP, 38 mm fill	0.29	31	107	553
FEP, 20 mm fill	0.28	18	63	270
Rexolite	0.30	33	112	670

Table 3.2: Table detailing the signal-to-noise comparison for the 3 tube/fill set ups used in the comparison

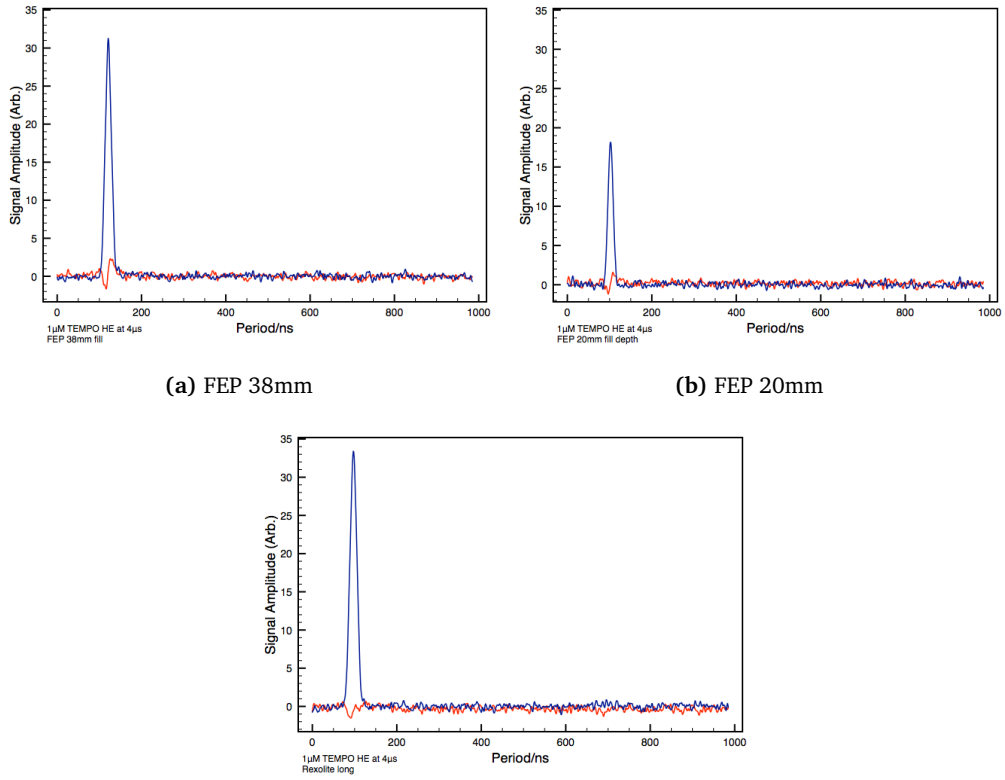

(a) FEP 38mm

(b) FEP 20mm

(c) Rexolite

Figure 3.1: Echo signal obtained for the 1μM TEMPO test using 3 different sample tubes/volumes. Experiment conducted in HiPER at 58 K.

The results obtained can be compared using the Figure of Merit for each of the set ups. For the FEP tube, it indicates that the 38 mm fill should perform 1.63 times better than the 20 mm fill, when taking the effective $\pi/2$ length and volume of fill into account. This factor agrees well (within 5%) with the ratio of echo peaks (1.72) and SNR (1.69). In comparing the 38 mm FEP fill and the Rexolite (which shows the largest SNR), the Figure of Merit predicts a 1.30 enhancement for the Rexolite over the FEP equivalent. This value is not met in terms of SNR (1.04) or peak (1.06) suggesting that the Rexolite is lossy. To take account for the fact that the Rexolite uses much longer pulses, which results in a much broader echo, the area under the curve was measured for both cases, the ratio of which (1.21) is still less than the predicted factor. The lossiness may be indicative of the larger inner radius, which will result in the far edges of the volume being immersed in a B_1 field of a much lower amplitude due to inhomogeneity of the TE_{11} mode supported by the sample holder, which is a Bessel function radially. This means that the additional volume provided by the thinner walled sample tube cannot be fully utilised, and will contribute to a larger distribution in amplitudes across the sample. This partially explains why the Rexolite sample tube required a longer pulse length.

While the Rexolite itself is very low loss at 94 GHz, machining by the workshop resulted in tubes which were very scratched and dirty, which may also contribute to the losses.

While the Rexolite tube does offer the largest signal-to-noise, and does not suffer from hydrophillic glassing issues like quartz sample tubes, it does suffer from some practical issues such that it is not resistant to organic solvents such as Toluene, making it unsuitable for samples in non water/glycerol solvents. It also requires extensive machining to produce the sample tubes themselves, which is costly and time-consuming. The FEP tubes however are resistant to Toluene[1] and require only minimal machining for use in experiments. The machining is due to bulging that occurs when the end of the tube is sealed. Considering that they offer a similar enhancement in signal-to-noise, the FEP tube is better choice for use in EPR experiments.

The results for 1 μM sample of TEMPO measured at X-band are shown in Figure 3.2. This measurement was obtained on our group's own Bruker X-band spectrometer, using the same stock of 1 μM TEMPO as in the W-band measurements. It was not possible to measure the echo at 4 μs due to noise, thus the result shown in Figure 3.2 was obtained for an echo at 2 μs, ($\tau = 1$ μs), which resulted in a signal-to-noise of 10.7. A T_m measurement of the sample indicated that the SNR of the echo at 4 μs should be ~5.5.

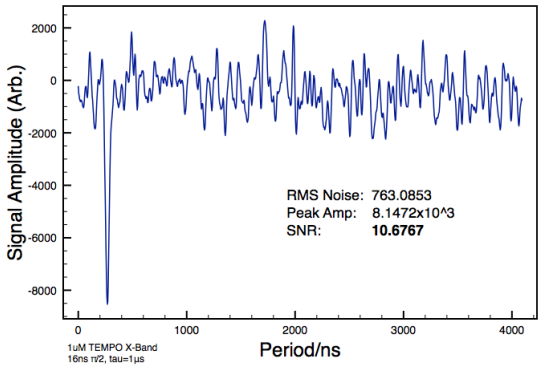

Figure 3.2: Spin echo obtained at X-band at 50 K, recorded with $\tau = 1$ μs, using 160 μL sample of 1 μM TEMPO.

In order to check whether the result was reproducible, Dr Bela Bode, a collaborator in the Chemistry department at St Andrews repeated this experiment using the same sample on their Bruker X-band spectrometer. The results are shown in Figure 3.3. The measurements were carried at the maximum of the nitroxyl spectrum using a 16 ns π pulse length and at the PELDOR observer position using a 32 ns π pulse length, as shown in Figures 3.3(a) and (b)

[1] Tubes were filled with Toluene and left overnight at room temperature in the lab, and no change was observed in the tubes.

respectively.

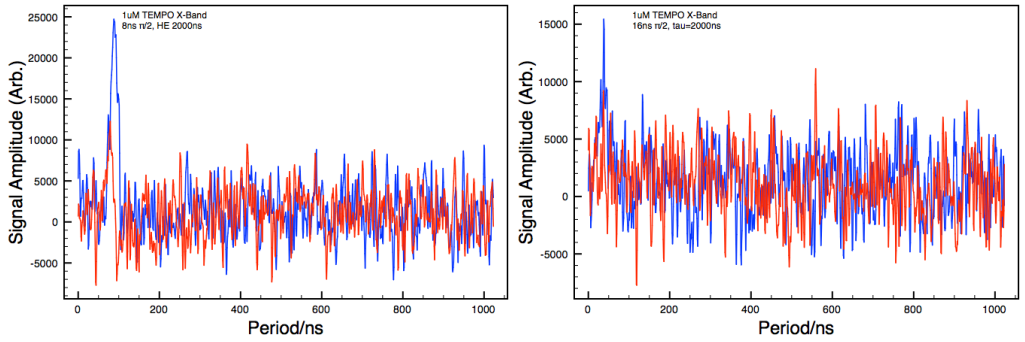

(a) X-band 8ns **(b)** X-band 16ns

Figure 3.3: Data from B.Bode for 1 μM TEMPO spin echo at $\tau = 2$ μs, measured at 50 K using 160 μL sample of 1 μM TEMPO.

The measurements made by the Bode group show a signal-to-noise ratio of 8.3 when placed at the maximum of the spectrum and 3.5 when placed at the observer pump position. This indicates that when observing on the maximum, HiPER's 38 mm fill FEP can provide 12.9 times improved signal-to-noise versus the Bruker X-band when measuring on the maximum. A summary of the SNR for the various set ups is shown in Table 3.3. This does not however compare to the expected enhancement suggested by the Figure of Merit for both set ups. When observing on HiPER, the TEMPO spectrum is approximately 4 times as broad, and given that the pulse lengths used on HiPER and at X-band are approximately similar, the experiments at X-band are able to excite 4 times more spins in comparison with W-band. This results in the reduced enhancement observed.

Tube	SNR	SNR enhancement
FEP, 38 mm fill	107	12.9
FEP, 20 mm fill	63	7.6
Rexolite	112	13.5
X-band (Pump)	8.3	1.0

Table 3.3: Table summarising the SNR results for the 1 μM TEMPO Hahn echo test, as a function of sample tube/experimental set up. Comparison of the SNR achieved on HiPER versus X-band measurement (Figure 3.3(a)) in the pump position is also given.

3.3 Matched filtering of echoes

The aim of this analysis is explore how filtering can be utilised to reduce noise in the measurement of echoes, and to improve signal to noise of progressive experiments, such as PELDOR. This will be carried out using what is known in the literature as 'match filtering' where one uses a template that resembles a known signal, in order to detect resemblance of the template in an unknown, or in most cases, noisy signal [71]. In the case here, we are considering the use of templates that are mathematical functions that can be easily generated in the time domain to match an echo. The goal is to examine how one can efficiently and effectively reduce noise when measuring echoes, and what improvement can be made on the current implementation. All work presented in this section is theoretical, no implementation was made due to time constraints and reprogramming required.

The measurement of signals in pulsed EPR involves measuring echoes in the time domain as a function of magnetic field, or pulse delay. For most set ups, an excellent guide to optimising measurements can be found in Ref. [72]. In this chapter, Jeschke describes how one must optimise cursor placement so to avoid losing any spectral information in the case of measurements as a function of magnetic field, and to optimise signal-to-noise in measurements as a function of pulse delay. He argues that wide cursors should be used for field measurements, such as field swept echoes, as excitation bandwidths of the pulses can lead to line broadening. Thus to obtain signal amplitude at the field measurement position, and to not be complicated by excitation outside of this position, one should measure a window approximately 4 times as broad as the echo itself, centred on the maximum. For pulse delay, or progressive experiments such as T_m or PELDOR, one should measure the echo with a window which is as wide as the longest pulse in the sequence, as this is the optimal setting.

The method described by Jeschke was found to be not directly applicable to HiPER. Due to B_1 inhomogeneity, echoes are broadened in comparison with more conventional EPR spectrometers, such that the 'window as wide as the longest pulse,' which usually equates to ∼50% of echo maximum, is not the optimum set up. Analysis carried out previously by Dr Graham Smith indicated that for progressive experiments optimal cursor placement is ∼30% of echo maximum, and this convention has been utilised ever since. The analysis carried out here is going to compare the 'HiPER protocol' for measurement to the placement of different filters over echoes to reduce noise, and examine their effectiveness to improve signal to noise in a simple PELDOR simulated experiment.

3.3.1 Algorithms for testing

Measurements on HiPER are recorded using a 1 GS/s averaging card, which returns the down-converted baseband in- and out-of-quadrature signals to the HiPER control computer for processing using the control software. These echoes can be recorded at 1 ns resolution and two such recorded echoes will be used in this analysis. Both were obtained during experiments on a room temperature nitroxyl biradical experiment using a refocused echo, comparing the echo enhancement using composite pulses in comparison with standard rectangular pulses. The experiment itself is detailed later in Chapter 5. Similarly in this analysis, standard rectangular and composite echoes will both be analysed. The experimental echoes used are shown in Figure 3.4.

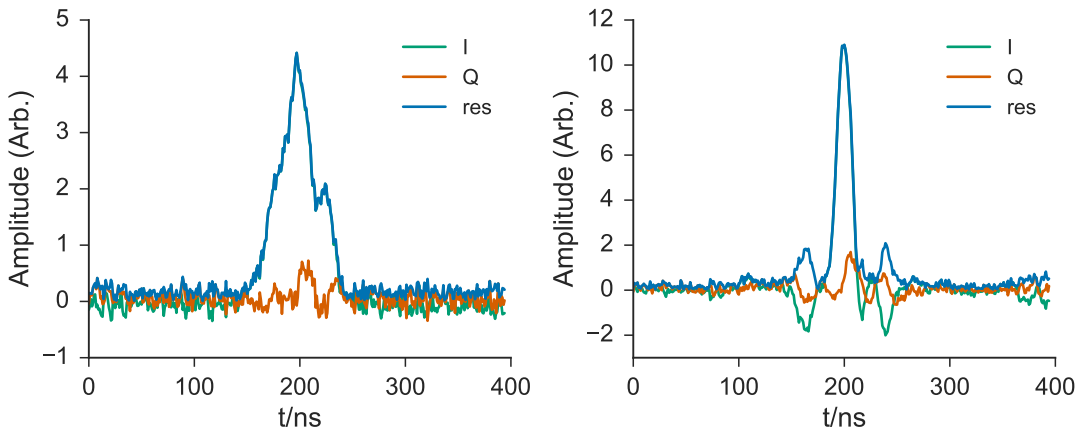

(a) Rectangular

(b) Composite $90_0180_{180}270_0$

Figure 3.4: Echoes used in simulation, (a) using rectangular pulses, (b) using $90_0180_{180}270_0$ composite pulse sequence. Both obtained using 16 ns $\pi/2$ pulses, measured on the Z3 position of the nitroxyl spectrum. I and Q are the in- and out-of-quadrature components of the signal (90° phase difference) and 'res' is the resultant (magnitude) of the signal.

HiPER echo measurement protocol

The current implementation on HiPER to measure echo magnitudes, involves placement of 3 sets of cursors. One set is centred to measure the echo area (area B), and the other two (areas A and C) are offset and of a similar width to area B, used to remove any DC offset. Any effect of DC offset is generally removed in conventional experiments using phase cycling, as it is characterised as a small positive voltage that offsets the signal from zero, and can be removed by subtraction echoes during phase cycling. To avoid using phase cycling, correction for DC offset is made by subtracting a mean of the two areas (A and C) from the main echo area,

area B during the measurement. The cursors are generally set by placing the area B cursors at ∼30% of maximum echo amplitude, with the outer cursors placed at the same width, between the outer cursors and the edge of the window. This is shown in Figure 3.5 for both the (a) rectangular echo and (b) composite echo cases.

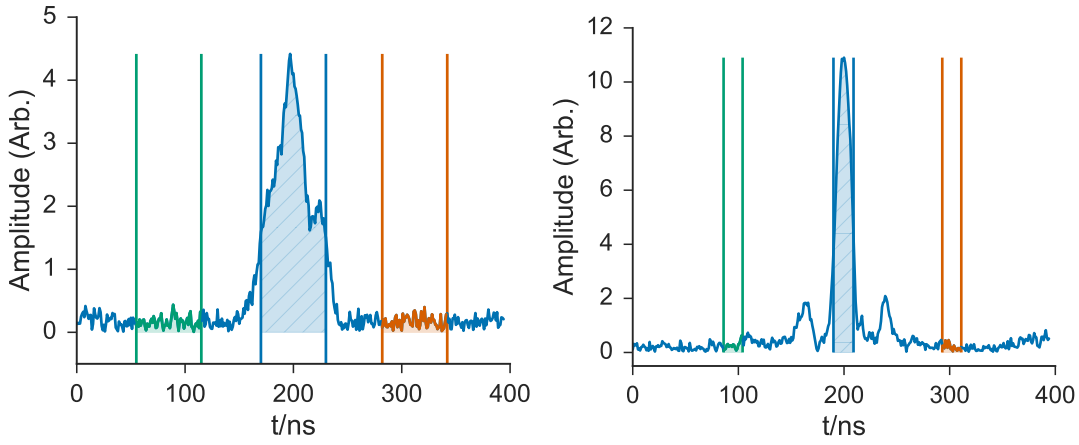

(a) Rectangular **(b)** Composite $90_0180_{180}270_0$

Figure 3.5: Plots illustrating cursor placement using the HiPER protocol, in the case of (a) rectangular pulse echoes and (b) composite pulse echoes, with central cursors (blue) placed at ∼30% of echo maximum. The DC offset correction cursors (green and orange) are placed equidistant to the left and right of the main cursors.

As Figure 3.5 shows, in the case of the rectangular echo (a) the majority of the time trace is analysed, with the parts outside the echo are generally places where there are little or no signal. In the case of the composite echo, where the echo produced is much narrower than the rectangular echo, it results in far narrower cursors, and much smaller DC offset correction areas, which may result in erroneous DC corrections. It should be pointed out at this stage that for the purposes of fair comparison between rectangular and composite pulses, the cursor positions shown in Figure 3.5 have been calculated using an algorithm written in Python, which searches for the nearest neighbour to 30% of echo maximum to calculate the cursor positions and corresponding widths. It then calculates the positions for areas A and C by placing cursors of the same width, centred between the left or right area B cursor and the edge of the echo. When conducting experiments on HiPER, the cursors are placed by eye, thus consistency is not guaranteed. For the purposes of brevity, the option to use interpolation between points, instead of nearest neighbour to find the cursor positions has been ignored, as to reflect the resolution of the averaging card.

The algorithm works by calculating the signal-to-noise ratio of the echo in the presence

of varying degrees of added noise. The algorithm first adds fractional random noise, that is created using a normal or Gaussian distribution of width between 0.01 and 0.3 times of the echo maximum. It then calculates the SNR of the noisy echo to equal the area measured. In this case, area B minus the mean of areas A and C, divided by the noise of each of the segments measured. The noise is calculated using a moving average through all the points on the echo and calculates a residual as the resultant of the trace minus the moving average through the points. The noise is then given by the standard deviation of the residual. The process is shown in Figure 3.6.

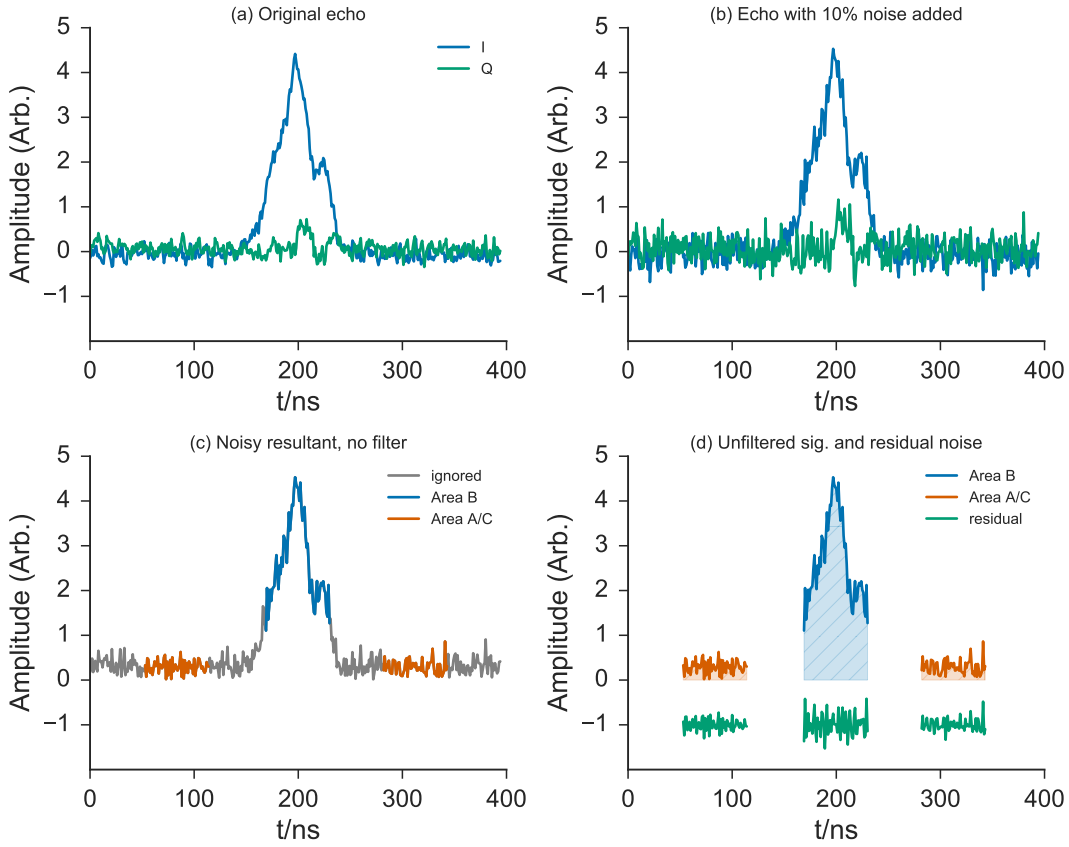

Figure 3.6: Plots illustrating the HiPER echo measurement protocol. (a) raw rectangular echo, (b) with 10% Gaussian noise added, (c) areas to analysed according to placement of cursors at 30% of echo maximum, (d) areas measured (blue and orange) and the residual noise (green) of each of the segments.

Shaped filters

In an attempt to reduce noise across the echo, two shaped filters were used, on the basis of mathematical functions that have a similar shape to an echo. The first is a Gaussian lineshape, created as $y(x) = \exp\left(-x^2\right)$. The second is a sinc-squared function, where $y(x) = (\sin(x)/x)^2$. For all filters used, x varies from -5 to 5. The shape is then scaled to the width of the echo

window. The filters are shown in Figure 3.7.

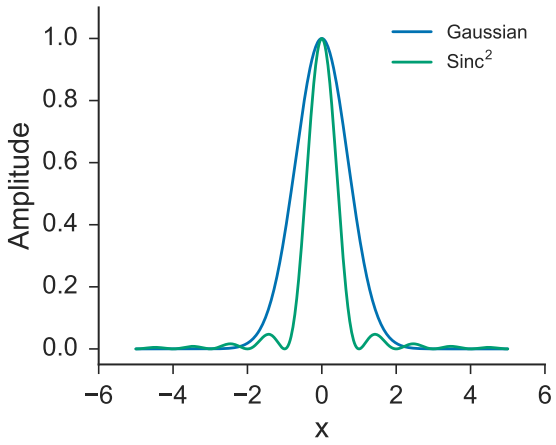

Figure 3.7: Plot showing the shaped filters used in analysis, gaussian (blue) and sinc^2 (green)

The algorithm for each filter works as follows. The raw echo is taken as input and fractional random noise is added, using the same method as for the HiPER filter. The noisy resultant trace (resultant $= \sqrt{I^2 + Q^2}$) then has its DC offset removed by taking a mean of the resultant trace between similar area A and C cursors as in the HiPER filter case, and taking the mean of both parts and subtracting it from the resultant trace. This is then multiplied by the corresponding filter, which varies from 0 to 1. The so-called 'match-filtered' trace's SNR is then calculated as the area under the whole filtered echo, divided by the standard deviation of the residual noise following subtraction of a moving averaging through all the points. For each of the filters, the area is not subject to cursor placement, and the entire area is measured, as the filter itself will zero (or in the case of the sinc filter reduce) any noise outside of the main echo peak. The protocol when applying a sinc^2 filter is shown in Figure 3.8.

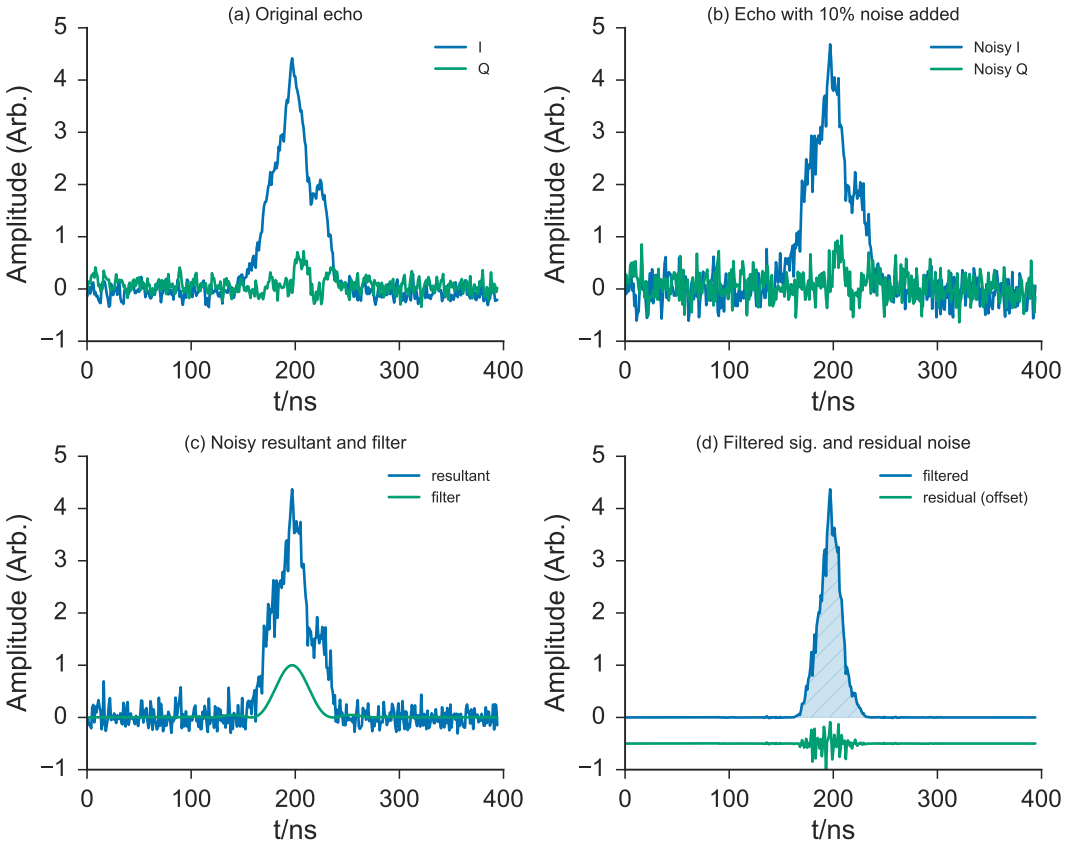

Figure 3.8: Plots illustrating the $\text{sinc}^2(x)$ filter method, (a) raw rectangular echo, (b) with 10% Gaussian noise added, (c) $\text{sinc}^2(x)$ filter to be multiplied by the resultant noisy echo (d) area measured (coloured, blue) and the residual noise (green, offset) of the trace.

Modelled echo filters

To 'best' match the echo shape, a filter was created that uses simulated echoes shapes as the matching filter. The echoes were obtained from the simulation as discussed in Section 4.3.1, which uses the B_1 inhomogeneity profile of HiPER to create Hahn and refocused echoes using rectangular and composite pulses. The echo shapes for a rectangular and a $90_0180_{180}270_0$ composite pulse refocused echo are shown in Figure 3.9. The echo shapes were both padded with zeros at the start and end to match the centre/maximum amplitude of the real and modelled echoes. Interpolation was also used to down-sample the echoes so that they approximately matched the measured echoes, i.e. both were 394 points long. The modelled filters were applied in the same way as the shaped filter, with the relevant (rectangular or composite) modelled echo used for smoothing in place of the Sinc/Gaussian filter. Since the model does not return the in- and out-of-quadrature parts, both filters were made positive by taking the absolute of their values, before being applied to the noisy resultant, as per the algorithm's protocol.

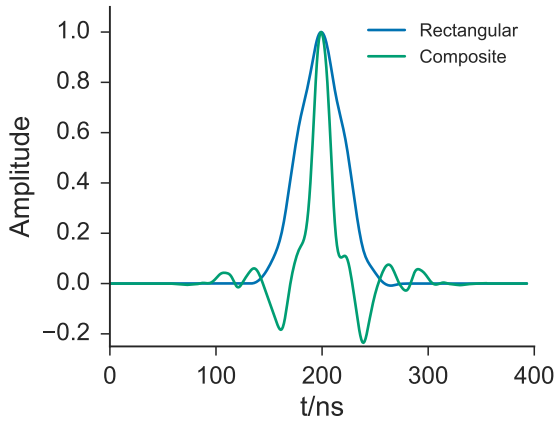

Figure 3.9: Plot showing the modelled echo used in analysis for rectangular echoes (blue) and $90_0180_{180}270_0$ composite echoes (green)

Other filters

Two additional filtering methods were also utilised in this analysis. The first is the so-called 'unmatched' filter, which involves measuring the entire echo trace, albeit with DC offset removed, with no attempt to remove or reduce noise. The area of the echo is taken as the integral of the entire echo. This was included as an example of why filtering, including the use of cursor areas is utilised. The second is a 'top hat' filter which is similar to the HiPER protocol, with cursors placed at 30% of echo amplitude, except that the DC correction is carried out using

the same DC offset correction as in all other methods, and not using mean of areas A and C method as specified Section 3.3.1. This was included to find out whether the SNR improves at all by not subtracting the areas to provide DC offset correction.

A summary of all the filtering methods used is shown in Table 3.4.

Filter name	Description	DC offset removal
HiPER	Area at 30% echo amplitude	Area of echo minus mean of areas between cursors
Top-hat	Area at 30% echo amplitude	
Unmatched	Complete trace, no filter	
Gaussian	Gaussian function filter, complete trace	Trace minus mean of trace between outer cursors
Sinc-squared	$Sinc^2$ function filter, complete trace	
Modelled	Simulated echo filter, complete trace	

Table 3.4: Summary of filtering methods used in the simulation

3.3.2 Echo signal-to-noise testing

In order to compare the effectiveness of different filters on improving signal-to-noise, tests were carried out to measure SNR, magnitude of the echo (i.e. its area) and noise as a function of added fractional noise to both the standard rectangular and composite echoes. The testing involved adding fractional noise to each echo and repeating this 2000 times, with the average of the resulting SNR, echo area and noise for each filter recorded. This was repeated for added fractional noise from 0.01 to 0.3 of the echo maximum. The results for the rectangular echo SNR are shown in Figure 3.10.

The plots indicate that for moderate, up to ∼15% added noise, the shaped and modelled echo filters can provide up to 2 times enhancement in SNR versus the HiPER protocol. The unmatched filter performs similarly to the HiPER protocol, providing slight (10%) enhancement with added noise up to 15%, but its performance degrades as the noise increases. Interestingly, the top hat filter performs worst. The error calculation in the case of the HiPER filter takes into consideration the residuals of areas A and C, as they are involved in the area correction, and thus, the noise is ∼20% lower for the HiPER filter than the top hat. The measured area for the top hat (not shown) is also smaller and decreases with increasing noise, suggesting that subtracting the mean of the resultant trace between the A and C cursors from the echo trace, has

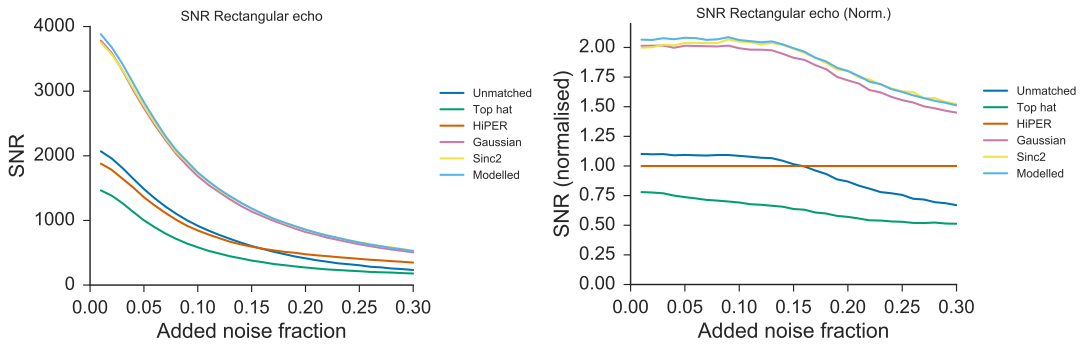

(a) SNR

(b) SNR normalised to HiPER

Figure 3.10: Plots showing analysis that was carried out on the rectangular experimental echo, showing (a) signal-to-noise as a function of fractional added noise when using the 6 filter protocols, (b) signal-to-noise normalised to the corresponding HiPER SNR for comparison purposes.

a greater effect at reducing the magnitude of the signal, than using the mean of the areas for the correction. In the case of the shaped and modelled filters, the noise is taken as the residual of the whole window, the majority of which is at zero following filtering, resulting in noise which greater than a factor of 2 smaller than the HiPER filter noise. The area measured in the case of the shaped filters is obviously slightly reduced, with the sinc-squared filter causing the largest ($\sim$1/3) reduction in echo area. Thus, the enhancement in SNR is caused by the huge reduction in noise of the echo. The modelled echo filter performs similarly to the sinc-squared filter. Theory predicts that the best-matched filter, i.e. the modelled filter should perform the best, as the sinc-squared and gaussian filters only approximate the echo shape, thus are not best-matched. While the modelled filter has an echo area which is on average 20% larger than that of the sinc-squared, the reduction in noise is not as large as for the sinc-squared, which can be attributed to the fact it is broader and does not cancel out as much noise in the measured echo area, resulting in an overall similar SNR performance. Thus, the narrower the filter, more of the noisy echo is multiplied by zero, which reduces more of the noise.

The simulation was repeated using the composite echo (Figure 3.4(b)) the results of the signal-to-noise using the 6 filters are shown in Figure 3.11.

The signal-to-noise analysis as a function of added noise shows that the shaped and modelled echo filters can provide up to 3.5 times enhancement when measuring composite echoes, versus the 2 times when measuring rectangular echoes. The shaped filters provide a similar large reduction in noise, but suffer far less from reduction in echo area (signal) as in the rectangular echo case, with the Gaussian filter providing up to 25% enhancement versus HiPER filter for noise less than 15%. The improvement in echo area can be attributed to the narrowness

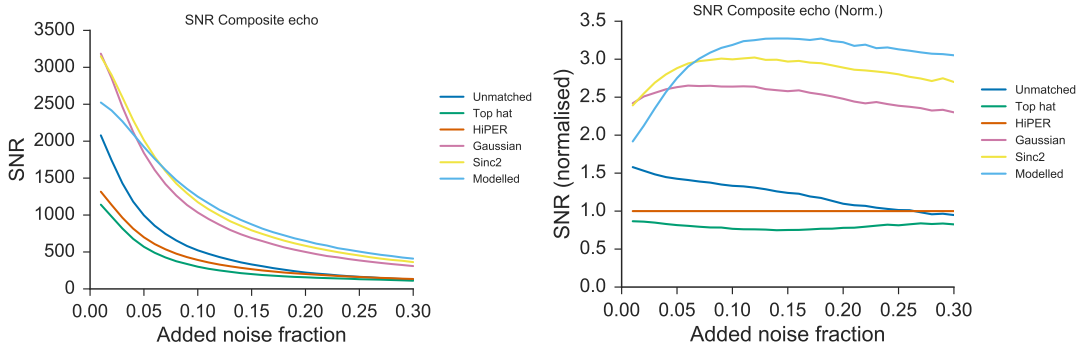

(a) SNR **(b)** SNR normalised to HiPER

Figure 3.11: Plots summarised analysis that was carried out on the composite experimental echo showing (a) signal-to-noise as a function of fractional added noise when using the 6 filter protocols, (b) signal-to-noise normalised to the corresponding HiPER SNR for comparison purposes.

of the echo, and the fact that the area outside of the main peak is not completely suppressed and is able to contribute to the measured magnitude, which in the case of the top hat and HiPER filter, is ignored entirely. However, the broader the filtered echo, the larger the noise, thus resulting in the Gaussian filter having the worst noise reduction ($\sim$1/2) of the 3 shaped and modelled filters, which reduces its overall performance. Theory would suggest that the 'best matched' modelled echo filter should perform best, but it performs worst out the shaped filters when low amounts of fractional noise is added. This is attributed to the fact that the model is not perfect, as discussed later in Section 4.3.2, the echo shape varies as a function of the maximum applied amplitude. As a result, the modelled filter's noise reduction performs worse with low level added noise, and plateaus with the largest reduction of all filters ($<$2/3 reduction) for noise greater than 10%. An interesting observation is that the unmatched filter can provide up to 50% enhancement for low added noise, reducing back to the same level as HiPER SNR as the noise increases to 30%. This can be attributed to the same effect as in the shaped filter case that the area outside of the main peak also contributes to the measured magnitude, albeit, without the benefit of reduced noise.

Overall, the simulation indicates that when measuring composite echoes with small fraction of noise, a sinc-squared filter is best suited to provide the largest enhancement in SNR, and the modelled filter is best suited for cases with large amounts of noise.

3.3.3 PELDOR simulation

While echo SNR provides an indication of the expected improvement, it is much more useful to see how the improvement works in practice, in particular in the case of a PELDOR experi-

ment. For this purpose, a simulation was set up by generating a typical PELDOR oscillation, and generating n echoes which are all scaled by the modulation of the PELDOR oscillation, corresponding to the point at which they would occur in the experiment. Each of the echoes was then subjected to one of the 6 filter algorithms, with the resulting area recorded, as per a standard PELDOR experiment. The simulated PELDOR traces can then be compared to see which algorithm provides the best SNR as a function of added noise. The SNR of the PELDOR traces was calculated by first calculating the magnitude of the signal, which to avoid effects of excessive noise was taken as the maximum minus minimum of a moving average through the trace. This was then divided by the noise, calculated as the standard deviation of the noisy trace minus the moving average.

The simulated 'typical' PELDOR trace used is shown in Figure 3.12(a). The PELDOR traces obtained following the application of the 6 algorithms are shown in Figure Figure 3.12(b). An example of the SNR calculation carried out on the unmatched and sinc-squared, showing the raw trace, moving average and residual noise is shown in Figure 3.13.

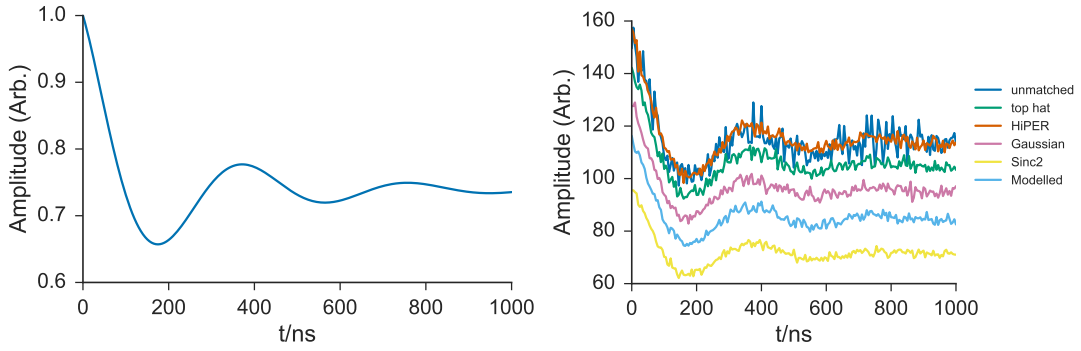

(a) Simulated PELDOR trace

(b) Filters applied

Figure 3.12: Plots showing (a) simulated PELDOR trace (b) resulting PELDOR traces following application of 6 filters to set of PELDOR trace scaled echoes with 10% noise added

It should be pointed out that the traces shown for the application of the algorithm are produced using one iteration of added noise and filtering, and thus, are prone to fluctuations of noise. They are merely shown as examples of the simulation. To get a more appropriate gauge of the performance of the filters, the PELDOR traces were calculated 500 times for each value of added noise, and for each of the filters, with the mean SNR, noise, and area measured recorded. The resulting averaged SNR and the SNR normalised to the HiPER filter for the PELDOR traces using rectangular echoes are shown in Figure 3.14.

The SNR analysis shows that for moderate amounts of noise, up to 6 times enhancement

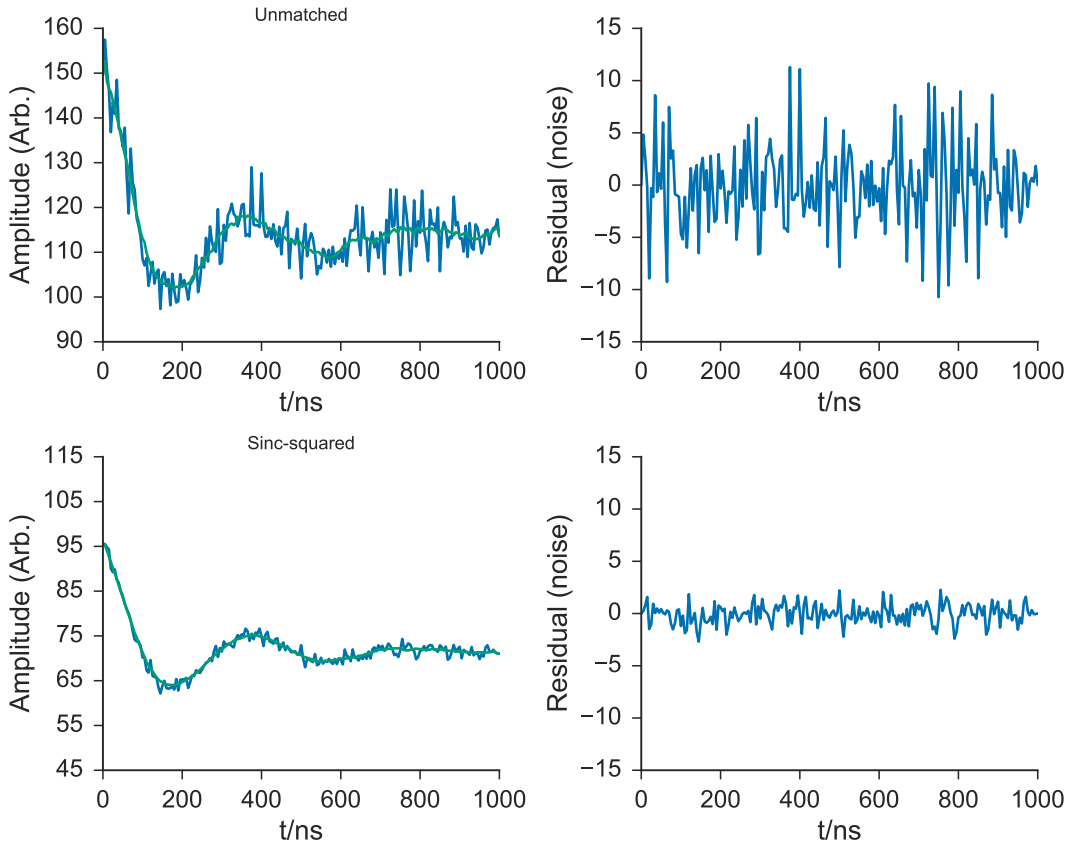

Figure 3.13: Signal-to-noise analysis for unmatched (top) and sinc-squared filter (bottom). The left plots show the raw PELDOR signal following filtering (blue) and the moving average through all the points (green). Right plots show the residual when the moving average is subtracted from the raw signal.

in signal-to-noise can be expected when using the shaped filters, which equates to a factor of 36 in averaging time. The normalised to HiPER filter plot shows a large drop in SNR at fraction of added noise = 0.03. This is due to the fact the noise of the HiPER trace at 0.03 does not follow the same upward trend for this one point, and is smaller than expected for unknown reasons. In general, it would appear that the sinc-squared and modelled filters perform best over all, unmatched filter provides some enhancement, but performance diminishes as the noise increases. Curiously, the tophat filter provides a very good enhancement for small amounts of added noise, but performs similarly to HiPER filter as the noise level increases.

The simulation was repeated using the composite echo. Results are shown in Figure 3.15.

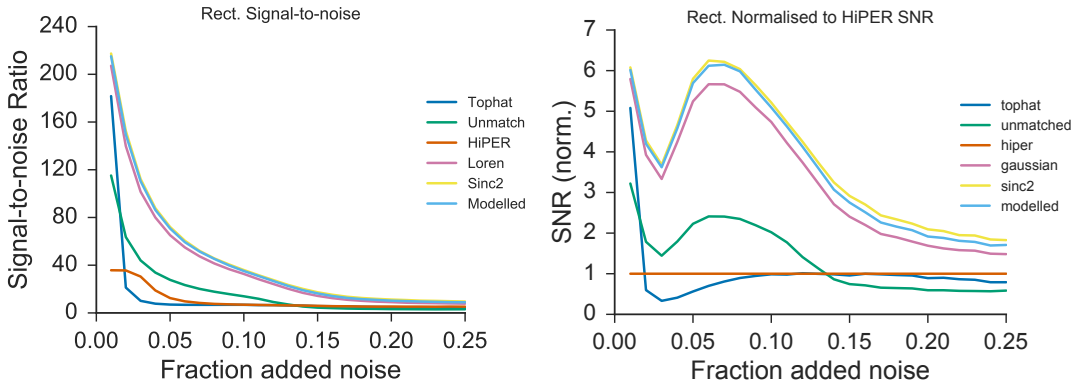

(a) SNR

(b) SNR normalised

Figure 3.14: Plots showing (a) PELDOR trace signal-to-noise as a function of fractional added noise when using the 6 filter protocols, (b) PELDOR trace signal-to-noise normalised to the corresponding HiPER SNR for comparison purposes. Analysis was carried out using rectangular pulse echoes.

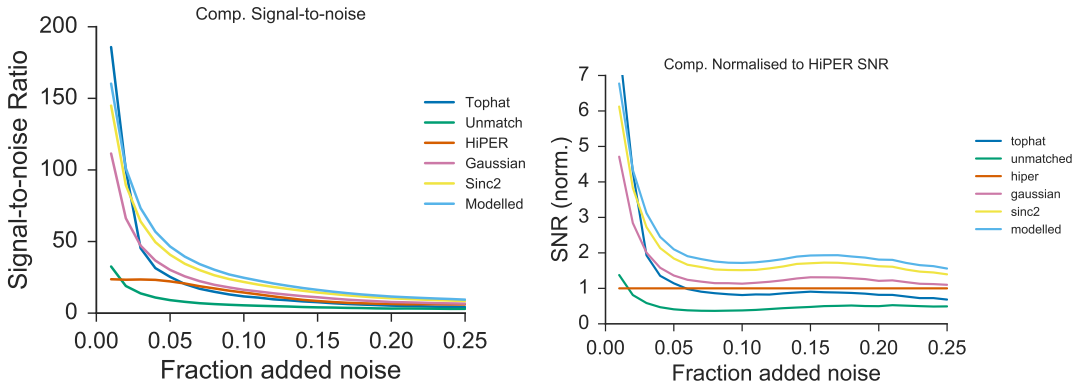

(a) SNR

(b) SNR normalised

Figure 3.15: Plots showing (a) PELDOR trace signal-to-noise as a function of fractional added noise when using the 6 filter protocols, (b) PELDOR trace signal-to-noise normalised to the corresponding HiPER SNR for comparison purposes. Analysis was carried out using the composite pulse echo.

The SNR results for the composite echoes show that for low levels of noise, top hat performs best, followed by the shaped filters, and slight enhancement is given by the unmatched filter. The large SNR for the top hat, which is overall less than that of the HiPER filter, is attributed to the extremely narrow sampling of points, in comparison with other methods, due to the very narrow shape of the main peak of the composite echo. For low levels of added noise, it benefits greatly from a small noise figure, but its overall SNR is diminished by the small echo area measured, and both suffer as the added noise increases. In the case of the shaped filters, as the added noise increases, a factor of $\sim$2 times enhancement is given by the modelled filter, with the Gaussian filter preforming worse out of the three shaped and modelled filters. This is attributed to the fact that despite the Gaussian filter providing the largest magnitude of the shaped filters for moderate added noise (<10%), the noise is comparable to HiPER for most added noise values. The sinc-squared and modelled filters follow similar trends in terms of magnitude and noise, with the modelled filter having both the smallest magnitude and the smallest noise of all the filters. As in the case of the echo analysis, it would appear that the reduction in noise provides a much larger benefit, resulting in the largest overall SNR enhancement.

3.4 Conclusions

In this chapter, we have examined how experimental protocols such as the use of hydrophobic sample tubes, and annealing are important to ensure excellent sensitivity when conducting experiments using the HiPER spectrometer. This has been expanded to compare concentration sensitivity between different types of sample tubes, and different cavity set ups. It was shown that while the thin-walled Rexolite tubes performed best, they did were not the best choice in practice due to machining requirements, lossiness and adverse reactions with organic solvents. The FEP tube was chosen as the new sample tube of choice, as it requires minimal machining and was resistant to the organic solvent, Toulene it was it was tested with. Its echo performance measuring very low concentration sample of a nitroxide mono-radical was compared with the experiments conducted at X-band using a resonator set up, showing HiPER to provide up to 13 times echo enhancement.

The theme of sensitivity enhancement was then applied through the use of simple digital filtering to improve SNR of echoes. Measurement algorithms were used to simulate and compare the current measurement set up on HiPER to other methods that use matched filters to reduce noise. This included the use of echo-like mathematical functions such as Gaussian curves and sinc-squared functions, as well as 'best matched' filters created by modelling echo shapes. It was found that in the case of rectangular echoes, the SNR could be improved by a factor of 2 using modelled and matched filters, in comparison with traditional measurement methods when up to 0.3 times echo amplitude of random noise is added. In the case of composite echoes, up to a factor of 3.5 times enhancement in SNR could be achieved using the matched filter. This analysis was extended to a mock PELDOR simulation, with echoes scaled in amplitude to represent time steps in a PELDOR trace. Each of the echoes then had noise added, before being measured using the filter measurement algorithms. This then produced a PELDOR 'measurement' trace with the signal level and noise dictated by the performance of the filter. In the case of the rectangular echo, it was discovered that up to 6 times improvement in signal-to-noise versus traditional methods can be achieved using the modelled and matched filters. The improvement was not as large in the case of the composite echo PELDOR measurement, where up to a factor of 2 was observed. This effect is surprising, but may be attributed to the fact that in the case of the composite echo, the cursor positions are much narrower, than in the case of the rectangular echo. This means that the composite echo samples $\sim 1/2$ less of the time trace than the rectangular echo, meaning that it also samples less noise, which will scale

as the square-root of the number of samples, thus improving its performance. While all of the matched and modelled filters use the whole time trace window for the measurement, each of them nulls the noise outside of the main peak, which also reduces the overall noise. Thus, one might argue that the filtered composite PELDOR does not show as large an improvement due to the fact that its noise is far lower in the first place. The simulation also does not take into consideration, as will be seen experimentally in Chapters 5 and 6, that the use of composites improves echo amplitudes and modulation depth, which will automatically enhance the SNR with respect to the rectangular echo case. Thus, one will expect the matched filtering to only improve this further.

4

Simulating composite echoes and modelling B_1 inhomogeneity

Some of the work presented in this chapter is based on a journal article published in April 2017 in Journal of Magnetic Resonance, Vol 278, pp 122-133, DOI: 10.1016/j.jmr.2017.03.018.

This chapter will focus on how the B_1 density profile of HiPER can be simulated and what gains can be expected using composite pulses to form echoes. It will discuss comparisons of echoes simulated in different cavity/resonator set ups and compare how factors such as line shape/width and homogeneity of B_1 field can affect the resulting echo shapes.

4.1 Simulating composite pulse echoes

In order to quantify the enhancement provided by composite pulses on HiPER, code was developed to simulate the rotation of spins undergoing the action of various composite pulses. This code was developed by a previous MPhys project student in the group (Scott Cassidy) and adapted for various uses. The code allows for the user to specify functions declaring the

frequency offset, $\Delta\omega_1/\omega_1^0$ and B_1 profile and width, B_1/B_1^0. The code then generates a 2-dimensional array over the specified range of B_1 amplitudes and frequency offsets for use in simulation code.

4.2 B_1 inhomogeneity

4.2.1 B_1 Density profile of HiPER

The non-resonant sample holders used in HiPER consist of a smooth-walled cylindrical metal void of diameter 3 mm and length 30 mm. This is surrounded by a plastic outer, creating a 'puck' of approximate diameter 25 mm. Sample tubes, typically made of a Fluorinated Ethylene Propylene (FEP) tubing of 2.97 mm outer diameter, with 0.5 mm thick walls, are loaded with sample and placed into the sample holder. The sample holder behaves like a length of circular waveguide, which is excited by the millimetre wave radiation incident at the top. The radiation travels through the sample and is reflected off the piezo-mounted roof mirror at the bottom, before being reflected back through the sample. This results in a B_1 field that varies sinusoidally along the length of the sample. The input wave at the top of the sample holder is assumed to be a circularly polarised plane wave. The dominant mode inside a circular waveguide is typically the TE_{11} mode, however due to the fact this waveguide becomes dielectrically loaded when a sample is placed inside, the mode present is a modified TE_{11} mode which is described by the following equation in cylindrical coordinates [73, 74]:

$$B_1(r,\phi,z) = B_1^{max}\left(J_0\left(1.84118\frac{r}{a}\right) - J_2\left(1.84118\frac{r}{a}\right)\cos(2\phi)\right)\cos\left(\frac{\pi z}{2}\right) \tag{4.1}$$

where B_1^{max} is the maximum B_1 amplitude, J_0 and J_2 are zeroth and second order Bessel functions of the first kind respectively and a is the radius of the waveguide from centre to wall. The factor 1.84118 is given by the boundary conditions and frequency cut off for this mode. This results in a B_1 amplitude distribution, which has repeating symmetry over r=0 $\rightarrow$ a, ϕ=0 $\rightarrow \pi/2$ and z=0 $\rightarrow$ 1. The radius of the circular waveguide, a is scaled by the dielectric constant, ϵ_r of the sample tube and sample itself. FEP has a dielectric constant of 2.1 at 1 kHz and 1 MHz, unfortunately no data is available for this material in the region of 100 GHz, so in this model it is assumed to be constant. The dielectric constant for a glassy water/glycerol sample $\epsilon_{sample} = 3.5$ at 100 GHz [75]. The optical path length of the circular waveguide is given by its refractive index, n (n=$\sqrt[2]{\epsilon_r}$) times its thickness. Using this approximation, the

radius of the waveguide a = $\sqrt[2]{\epsilon_{sample}}$ * 1 mm + $\sqrt[2]{\epsilon_{tube}}$ * 0.5 mm = 2.59 mm, and the radius of the B-field within the sample varies from r = 0 → 1.87 mm.

The B_1 density profile was then calculated using code created in Python, using the NumPy and SciPy packages [76, 77]. This was carried out by sampling the B_1 amplitude value at 10,000,000 random points across the repeating cylindrical volume segment. For illustration, Figure 4.1 shows 1,000 randomly sampled points over the cylindrical volume segment.

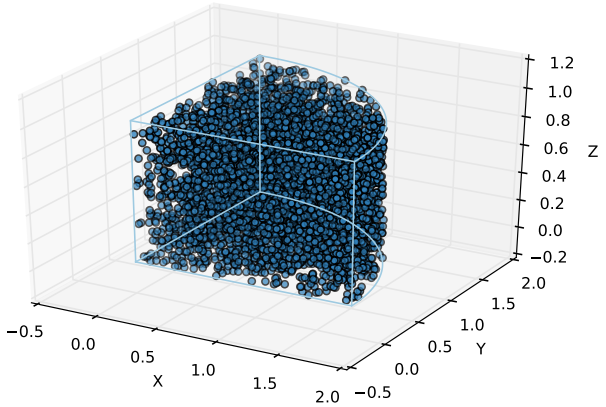

Figure 4.1: Plot showing random sampling over the segment of cylinder between (r=0->1.87 mm,ϕ=0->$\pi/2$, z=0->1) shown in Cartesian coordinates with vertices drawn in light blue. For brevity, the plot shows 1,000 random points, one-ten-thousandth of the number of points sampled in the calculation.

The B_1 amplitude is then evaluated using Eq. 4.1 at each of the points and binned using the NumPy histogram function to count up the number of points with amplitude in the range of bin width, as shown in Figure 4.2. The profile was then exported to Mathematica for use in the main simulation package as a pre-complied calculation of the B_1 profile, to speed up the calculation.

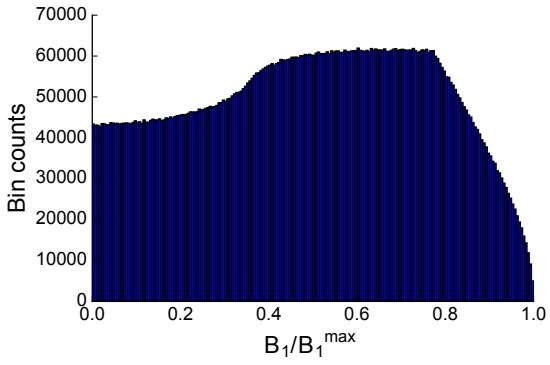

Figure 4.2: Histogram of the B_1 amplitude over the segment of sample, as a function of B_1/B_1^{max}, using 200 bins

The contour plot shown in Figure 4.3 illustrates the B_1 amplitude inside the sample over the symmetric segment at z=0. The radius of the segment has been scaled to the optical path length.

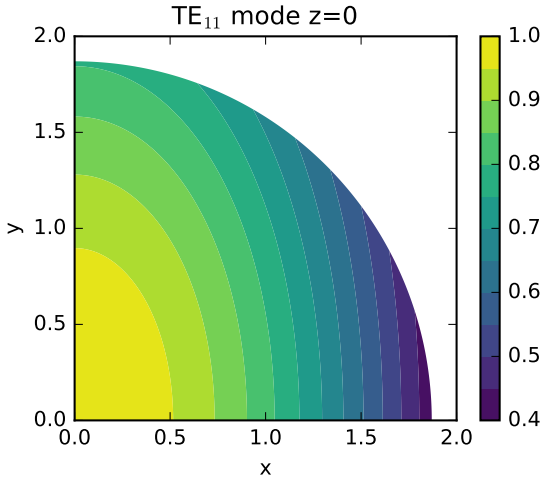

Figure 4.3: Contour plot of the B_1 amplitude inside the sample at z=0, in Cartesian coordinates. The radius has been scaled to the optical path length.

The histogram illustrates the significant inhomogeneity present inside the sample segment, with a significant proportion (20.1%) at $B_1 = 0 \rightarrow 0.20$ of B_1^{max} and only 18.7% at $B_1 = 0.80 \rightarrow 1.0$ of B_1^{max}.

4.2.2 Homogeneous B_1 profile

To aid comparison of the enhancement provided by composite pulses in the inhomogeneous B_1 set up on HiPER, the homogenous B_1 field case was also considered. This is typical of some commercial cavity resonator set ups where the sample is placed such that the B_1 field is broadly flat across the sample volume. Most of these resonator set ups aim to ensure that the E-field within the cavity is at a minimum where the sample is located to reduce dielectric losses, and that the B_1 field is at a maximum here.

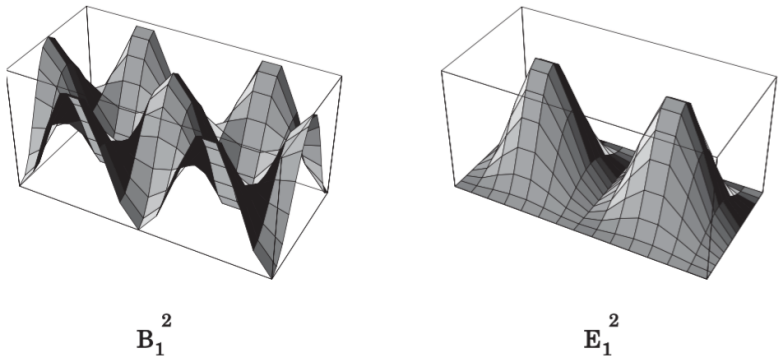

Figure 4.4: Diagrams showing the B and E-field amplitudes within a resonator supporting the TE_{102} mode. (Reproduced from Bruker Technical manual)

Figure 4.4 shows the B and E field amplitudes within the most commonly used cavity set up, the TE_{102} mode. In this set up, the sample is placed in the null between the two peaks of the E-field, and thus in the peak of the B-field. Depending on sample size, this will induce a small distribution on B-field across the sample, but it is considered minimal. It should be noted that the field within the cavity will alter when the sample is placed inside the cavity, as the cavity becomes dielectrically loaded. However, it is generally possible to alter the vertical position of the sample tube to ensure it is located at B-field maximum. This is in contrast to the HiPER set up, where the B and E-fields within the sample are inherently inhomogeneous due to the transmission of the millimetre waves through the sample and consequent standing wave created.

In terms of the simulation, for the homogeneous B_1 case, a δ-function is used such that B_1/B_1^{max}=1 across the sample.

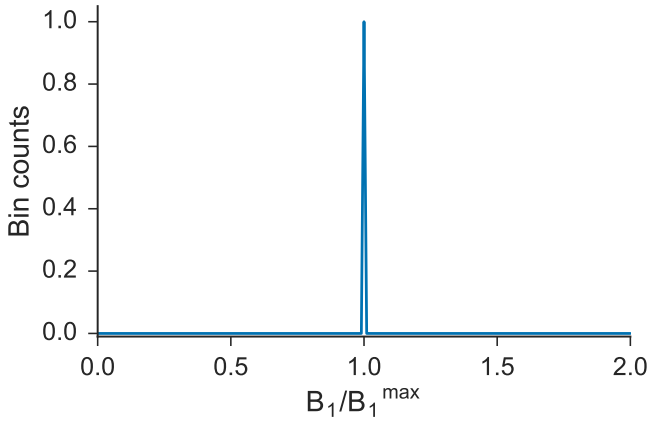

Figure 4.5: Plot of B_1 profile used in the homogeneous B_1 case. It resembles a δ-function at $B_1/B_1^{max} = 1$.

4.2.3 Frequency offset

Frequency offset is defined as a misset between frequency of the pulse, ω_1 and the resonant frequency of the particular spin, Ω_1^0. The bandwidth of frequencies present is defined as a function of its offset from resonant frequency $\Delta\omega_1 = \omega_1 - \Omega_1^0$. This represents the underlying spectrum of spins one is exciting with the composite pulse. The spectrum is specified using functions to express the variation in magnitude with frequency offset. Any spectrum can be specified, and is simply loaded into Mathematica for use in the pre-compiled code to define the range in frequency offsets in the 2-dimensional array of frequency offsets and B_1 inhomogeneity.

In order to assess the performance on broad-line centres in comparison with narrow-line centres, 2 main frequency offset profiles were created for testing. The broad-line centre is defined by the function,

$$f_b\left(\Delta\omega_1/\Omega_1^0\right) = \exp\left(-\left(\frac{\Delta\omega_1/\Omega_1^0}{9}\right)^{16}\right) \tag{4.2}$$

which is broadly flat over the range -10$\leq \left(\Delta\omega_1/\Omega_1^0\right) \leq$10. The narrow function is defined by the function,

$$f_n\left(\Delta\omega_1/\Omega_1^0\right) = \exp\left(-100\left(\Delta\omega_1/\Omega_1^0\right)^2\right) \tag{4.3}$$

which is Gaussian in shape, with the FWHM of $\Delta\omega_1/\Omega_1^0 = \pm\ 0.15$. Both frequency offset

profiles are shown in Figure 4.6

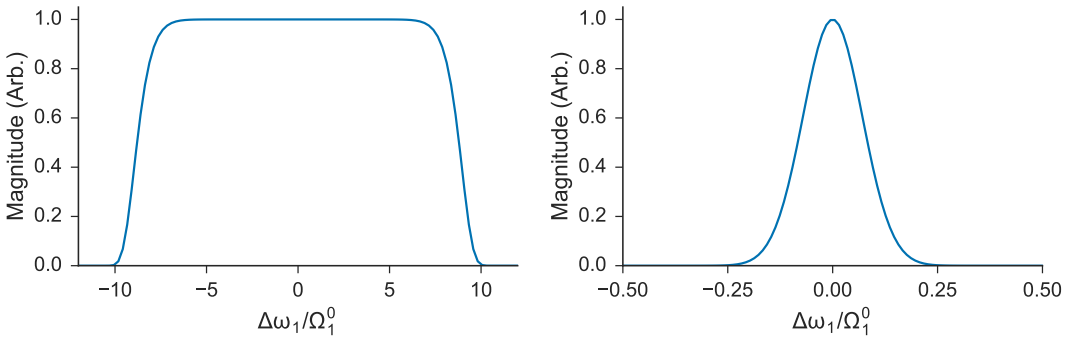

(a) Broad **(b)** Narrow

Figure 4.6: Frequency offset profiles used in simulation.

4.3 Echo Simulations

4.3.1 Hahn echo and Refocused Hahn echo simulations

The effect of frequency offset and B_1 inhomogeneity across the sample on echo amplitude has been simulated using complied code in Mathematica. The frequency offset range and B_1 amplitude range are pre-complied and loaded into a 2-dimensional array to represent the different frequency and amplitude offsets experienced by the spin packets present. The creates a distribution of B_1 amplitudes within the sample, ranging from $0 \leq B_1^0 \leq B_1^{max}$, where B_1^0 is the amplitude that produces the desired flip angle for a given pulse length, at zero frequency offset[1]. The weighting of a spin packet at a particular B_1 field is proportional to the volume of sample experiencing that field. Each spin packet at a given B_1 amplitude and frequency offset is then acted upon by the appropriate rotation matrix for the relevant type of pulse, allowing for any composite pulse sequence to specified. The rotation matrices are defined by their flip angle,

$$\beta = \beta' \sqrt{\left(\frac{B_1}{B_1^0}\right)^2 + \left(\frac{\Delta\omega_1}{\Omega_1^0}\right)^2} \tag{4.4}$$

and its axis of rotation,

[1]Here I am parting with the usual convention defining the amplitude of the pulse as ω_1 with units of frequency, and instead, to keep it unit-less, I am referring to the amplitude as B_1, and using $\Delta\omega_1$ to refer to the offset in frequency of the pulse from the resonance frequency of the spin, Ω_1^0. The terms 'field' and 'amplitude' when referring to B_1 are also used interchangeably.

$$\overrightarrow{r} = \frac{B_1}{B_1^0}\left(\cos\phi\,\hat{i} + \sin\phi\,\hat{j}\right) + \frac{\Delta\omega_1}{\Omega_1^0}\hat{k} \tag{4.5}$$

where β' is the nominal flip angle at zero frequency offset (usually 90° or 180°), Ω_1^0 is the resonant frequency of the spin, $\Delta\omega_1$ is the resonance frequency offset, ϕ is the phase and $\hat{i}, \hat{j}$ and $\hat{k}$ are unit vectors in the x, y and z directions respectively.

Any period of free precession is defined by a delay matrix that rotates each of the vectors around the z'-axis in the rotating frame by angle $\theta = \tau_1\Delta\omega_1$. In the case of the Hahn echo sequence, this consists of a $\pi/2$ rotation matrix, followed a delay matrix of length τ_1, followed by a π or composite-equivalent π inversion pulse rotation matrix, and final delay matrix of τ_1. The model then returns the sum of all the magnetization vectors around the time $2\tau_1$ after the first pulse, showing the echo that is produced.

4.3.2 Optimisation of echo amplitude as a function of B_1^{max}/B_1^0

Due to the distribution of B_1 amplitudes, and thus, flip angles β across the sample, there is an optimum value of B_1^{max}/B_1^0 that provides the best overall echo amplitude for standard rectangular pulses. This can be optimised by using the simulation package in Mathematica to calculate the echo shape as a function of B_1^{max}/B_1^0 for a specified pulse sequence, B_1 inhomogeneity profile and frequency offset profile. This was carried out for the TE_{11} 'HiPER' inhomogeneity profile and the broad-line using a Hahn echo ($\pi/2$ - τ - π - τ - echo) sequence. This was carried out using the interpolation function in Mathematica to scale B_1/B_1^{max} between 0 and 2. Figure 4.7 shows the effect of increasing B_1^{max}/B_1^0 on the echo amplitude and echo shape.

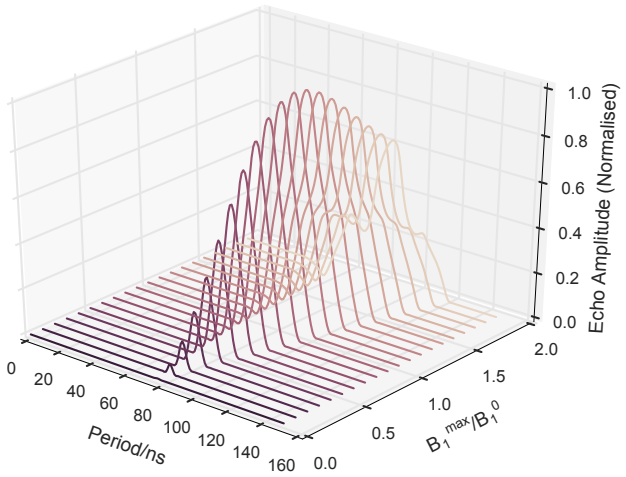

Figure 4.7: Plot showing calculated echo shape as a function of B_1^{max}/B_1^0

Figure 4.7 illustrates how the Hahn echo amplitude increases with increasing B_1 amplitude, until the point that it starts to distort and decrease in amplitude, due to over-rotation of spins. In the absence of B_1 inhomogeneity and when exciting a narrow line, this should occur at $B_1^{max}/B_1^0 = 1$, corresponding to correct rotation of all spins. Figure 4.8 shows how the echo amplitude (a) and integrated echo area (b) varies with increasing B_1 amplitude.

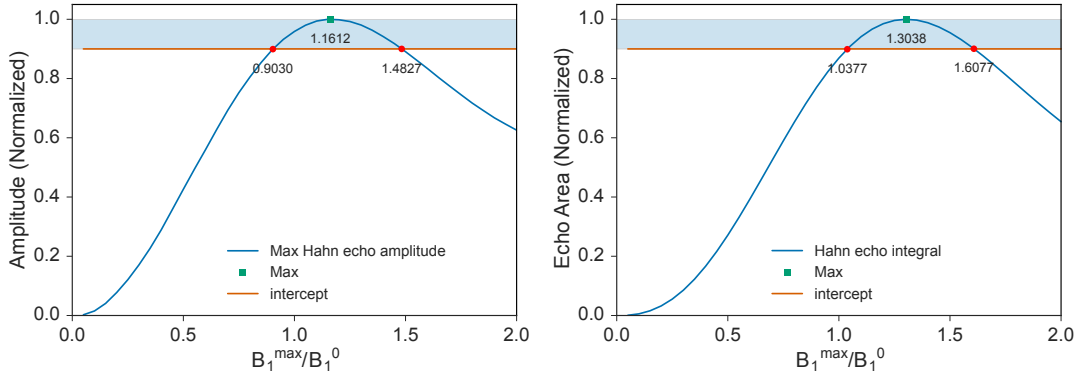

(a) Maximum echo amplitude

(b) Integrated echo area

Figure 4.8: (a) Maximum echo amplitude and (b) echo area/integral as a function of B_1^{max}/B_1^0. The green square shows the maximum. The red circles indicate where the echo amplitude/area is 90% of maximum. The digits underneath indicate B_1^{max}/B_1^0 at that point.

Figure 4.8(a) shows that the maximum echo amplitude is obtained for $B_1^{max}/B_1^0 = 1.16$, and that while the echo amplitude varies within 10% of its maximum, B_1^{max}/B_1^0 amplitude changes between 0.90 and 1.48. In terms of sensitivity, the integrated echo area is proportional to the level of signal, so one seeks to maximise this quantity in order to optimise the signal to noise of the measurement. Figure 4.8(b) shows a maximum for $B_1/B_1^{max} = 1.30$, and variation between 1.04 and 1.61 within 10% of this maximum. This indicates that when there is insufficient granularity/resolution in amplitude or pulse length or if poor signal-to-noise prevents one from obtaining the optimal echo, the B_1 amplitude varies significantly.

4.3.3 Composite echo amplitude as a function of B_1^{max}/B_1^0

Similarly to the process detailed in Section 4.3.2, refocused rectangular and refocused composite echoes were generated for a range of B_1 amplitudes, in order to assess the effect of increasing B_1 amplitude. The refocused Hahn echo was simulated by adding a second inversion pulse that matches the first inversion pulse, introduced a period τ_2 after the echo. This produces an echo at $2(\tau_1 + \tau_2)$ after the first pulse.

Figure 4.9(a) shows absolute echo amplitude and 4.9(b) echo height normalised to the

rectangular pulse, both as a function of B_1 amplitude. In the absolute case, (Figure 4.9(a)) it shows a maximum for rectangular pulses (blue) around $B_1^{max}/B_1^0 = 1.22$ and for $90_0180_{180}270_0$composite at $B_1^{max}/B_1^0 = 1.25$. The optimal amplitude disagrees with that of the of the Hahn echo case. At B_1 amplitudes lower than optimal, the enhancement as shown in Figure 4.9(b) is large but the absolute echo magnitude, as shown in Figure 4.9(a) is small. However, if the optimal amplitude is missed due to granularity in amplitude or misset in pulse length, $B_1^{max}/B_1^0 > 1.22$ provides greater enhancement for composites versus rectangular pulses.

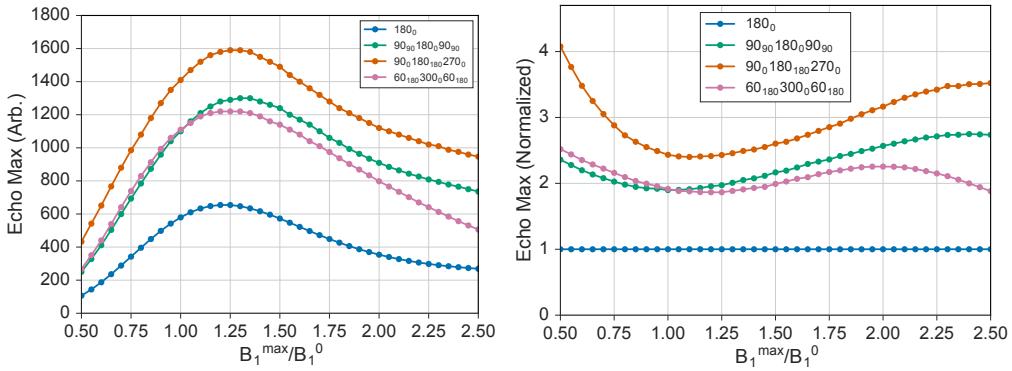

(a) **(b)**

Figure 4.9: (a) Simulation of maximum echo amplitude as a function of B_1^{max}/B_1^0, (b) maximum echo amplitude normalised to the rectangular equivalent to show enhancement as function of B_1^{max}/B_1^0.

4.3.4 Hahn and refocused composite echoes

Following comparison of refocused echo simulation results with experimentally obtained refocused echoes on flat, broadline centres, B_1^{max}/B_1^0 was optimised to the enhancement in echo amplitude achieved. This corresponds to $B_1^{max}/B_1^0 = 1.65$. The enhancement in echo area is also greater for larger B_1^{max}/B_1^0, and as shown in Hahn echo simulation, plausible choice due to misset in B_1 amplitude or pulse length due to insufficient granularity/resolution. Comparison of composite Hahn and refocused echoes using 3 composite sequences and standard rectangular pulses are shown in Figures 4.10(a) and 4.10(b) respectively.

As expected, most of the composite pulses are unable to produce Hahn echoes due to phase distortion resulting from the fact they are variable rotation composites. The constant phase rotation, Wimperis-60, $60_{180}300_060_{180}$ sequence however is able to produce an echo, which has slightly enhanced echo amplitude, but is significantly narrower, reducing the measurable echo area. In the case of the refocused echoes, all sequences are able to produce enhanced echoes, due to the fact the second refocusing pulse reverses the phase distortion. The $90_0180_{180}270_0$

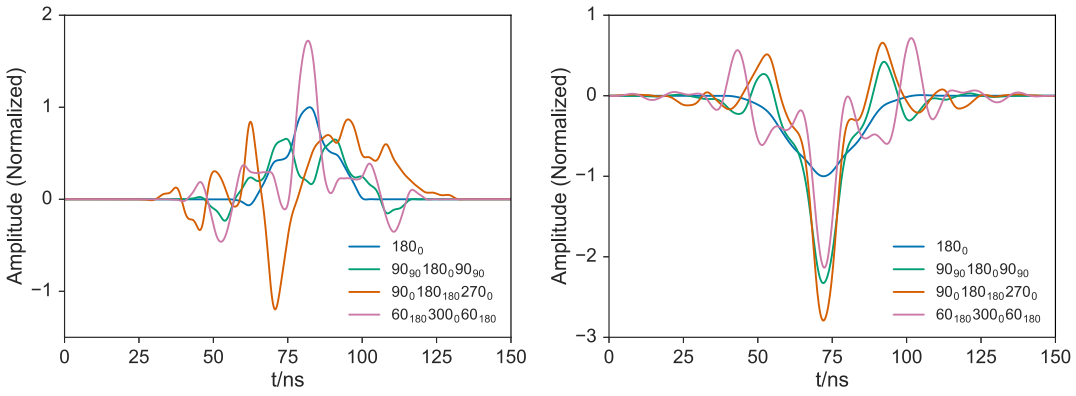

(a) Hahn echoes **(b)** Refocused echoes

Figure 4.10: Simulations of (a) Hahn echoes and (b) refocused echoes using composite and rectangular π pulses. All echoes normalised to the maximum of the rectangular pulse (blue) echo.

sequence provides the largest enhancement at 2.79 times that of the rectangular pulse echo, followed by the $90_{90}180_090_{90}$ sequence and the $60_{180}300_060_{180}$.

4.3.5 Composite echoes: HiPER B_1 versus homogeneous B_1

The echo simulation was also carried out using the homogeneous B_1 profile (Figure 4.5) in order to compare the enhancement expected using composite pulses in more conventional EPR set ups using a resonant cavity. The simulation also uses the broad frequency offset lineshape, as shown in Figure 4.6a. The resulting refocused echoes are shown in Figure 4.11.

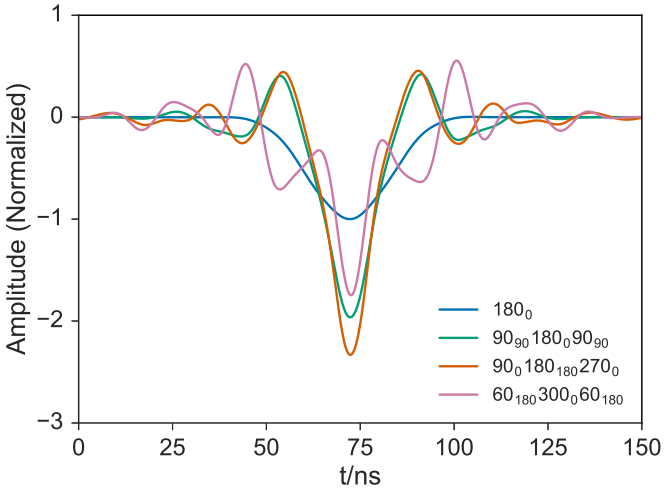

Figure 4.11: Simulation of refocused Hahn echoes using composite and rectangular π pulses on a broad line with homogeneous B_1 profile. All echoes normalised to the maximum of the rectangular pulse (blue) echo.

The simulation shows that composite pulses in the absence of B_1 inhomogeneity, can pro-

vide up to 2.33 times enhancement in echo amplitude using $90_0180_{180}270_0$ sequence when exciting broad line samples. When exciting narrow line samples, the enhancement is negligible due to the fact that standard rectangular pulses can generally excite the majority of the line. It should be noted that the effects of cavity response and bandwidth is not taken into consideration in this simulation, as it assumes no bandwidth restriction is imposed.

4.4 Conclusions

Models of B_1 field present in samples measured using the HiPER spectrometer indicate large variations in amplitude across the sample, resulting in large variations in flip angle of the spins under action of pulses. By sampling the B_1 amplitude at 10,000,000 points across the repeating segment to produce a B_1 density measurement, it was shown that there is a generally even distribution of amplitudes between 0 and 1, with tapering towards the maximum amplitude of 1. The use of simulations to emulate the action of composite pulses under such conditions, shows that significant gains in echo amplitude can be achieved by using these pulses, in particular on broad line systems.

5

Composite PELDOR: Nitroxide bi-radicals

The work presented in this chapter is based on a journal article published in April 2017 in Journal of Magnetic Resonance, Vol 278, pp 122-133, DOI: 10.1016/j.jmr.2017.03.018.

Nitroxyl radicals, or as they are more commonly referred to, nitroxide spin labels are useful tools for EPR studies of biomolecular systems due to their chemical stability and ability to be attached without distorting the underlying structure of the system in question [78]. Due to their small size and, in most cases, non-toxic attributes, they are the most often used spin label for biochemists wishing to measure the structural characteristics of their system in question. In this chapter, the use of composite pulses to improve measurement sensitivity will be examined to see if SNR can be increased in PELDOR experiments.

5.1 Nitroxyl mono-radical: TEMPO

In order to assess the effect of using composite pulses in nitroxyl-based measurements, experiments were carried out on the nitroxyl mono-radical, 4-amino-TEMPO (Structure shown in

Figure 5.1). Measurements on nitroxides at high field are complicated by the fact that the degeneracy of the *g*-tensor is lifted, allowing for different orientations to be selectively excited. Due to the excitation broadening provided by composite pulses, any overlap or additional diffusion effects must be investigated, in particular for different orientations.

In its most basic form, this has been carried out on a mono-radical so that any dipolar or intramolecular instantaneous diffusion effects can be avoided. The sample concentration is also kept low at 50 μM in order to lessen any effect of inter-molecular instantaneous diffusion. It is important when conducting enhancement measurements to ensure that orientational effects are also taken into consideration, by repeating experiments at all orientations on the nitroxide line.

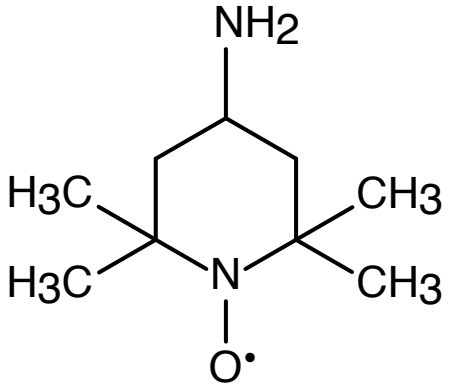

Figure 5.1: Structure of 4-amino-TEMPO.

5.1.1 TEMPO: sample preparation

The sample was made by dissolving 4-amino-TEMPO (Sigma Aldrich) in deionised water and mixed with glycerol to produce final radical concentration of 50 μM TEMPO in 60/40 glycerol/water. This was then loaded into a FEP tube, flash frozen in liquid nitrogen and loaded into a pre-cooled cryostat in HiPER at 130 K. The sample was then annealed to 200 K before the temperature was lowered for measurement at 58 K.

5.1.2 TEMPO: Field swept echo experiment

The field swept echo experiment on the TEMPO sample was carried out at 58 K using a Hahn echo sequence, $\pi/2 \rightarrow \tau \rightarrow \pi \rightarrow \tau \rightarrow echo$, with 16 and 32 ns $\pi/2$ and π pulse lengths and inter-pulse delay $\tau = 250$ ns. The field was swept from 3337 mT to 3367 mT in 0.1 mT steps, with pulse frequency of 93.9996 GHz. Sequence repetition frequency was 500 Hz, averaging 500 shots per point. Resulting spectrum is shown in Figure 5.2.

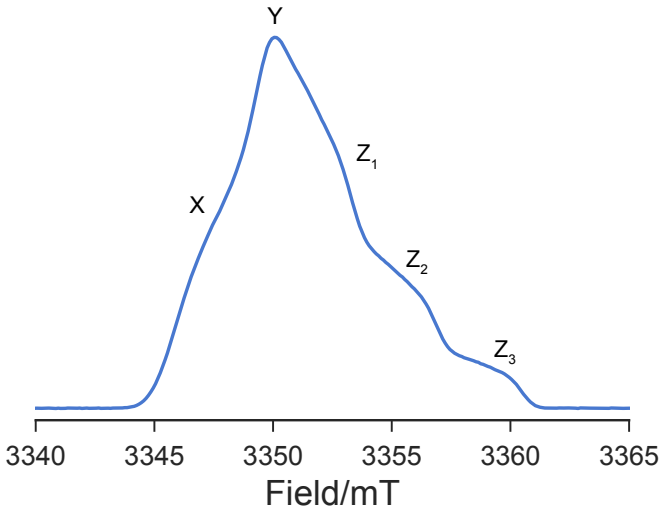

Figure 5.2: Absorption spectra of sample of 4-amino-TEMPO, measured at 58 K using a field swept echo, with 32 ns π pulse lengths, and $\tau = 250$ ns. The labels indicate the approximate orientation positions.

The experiment was also repeated with shorter (broader excitation) pulses, which showed reduced definition of the orientations. By increasing the pulse length, and thus decreasing the excitation bandwidth of the pulses used, more definition was achieved. Figure 5.2 indicates little effect of instantaneous diffusion, which is commonly observed as attenuation of the Y component (main peak) with respect to the left shoulder of X, and the Z components to the right. This is to be expected, due to the low sample concentration which will minimise inter-spin effects.

5.1.3 TEMPO: Composite refocused echo experiments

Composite refocused echoes were measured on the 50 μM sample of TEMPO at different field positions/orientations on the nitroxyl centre. Echoes were obtained using standard, rectangular $\pi/2$ and π pulses and with the equivalent $90_{90}180_{0}90_{90}$ and $90_{0}180_{180}270_{0}$ composite π-inversion pulses. In each case, the initial $\pi/2$ excitation pulse was provided by an 8 ns $\pi/2$ rectangular pulse. The field positions used are X = 3347 mT, Y = 3350 mT, Z_1 = 3352 mT, Z_2 = 3355 mT and Z_3 = 3358 mT. The enhancements provided by the composite pulses are summarised in Table 5.1 and shown in Figure 5.3(a). The experiment was repeated with longer pulses (16 ns $\pi/2$) which halves the excitation bandwidth in comparison with the 8 ns $\pi/2$ experiment. The results are also summarised in Table 5.1 and shown in Figure 5.3(b).

Figure 5.3(a) shows that the enhancement in echo amplitude achieved using composite pulses is not uniform across the nitroxyl spectrum, suggesting some orientational dependence.

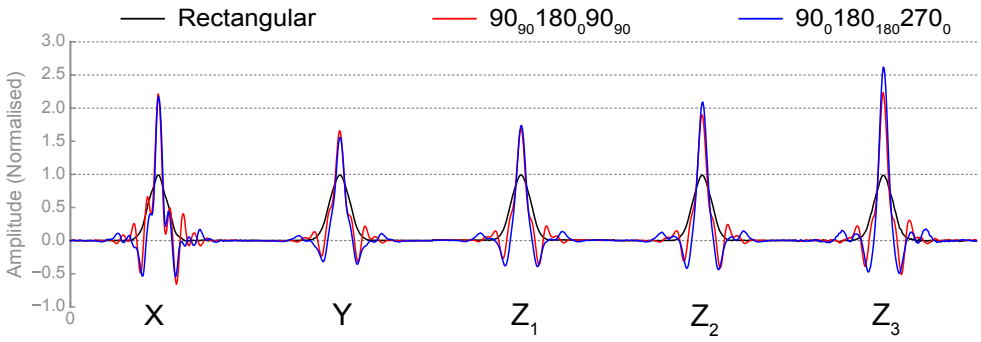

(a) 16 ns π

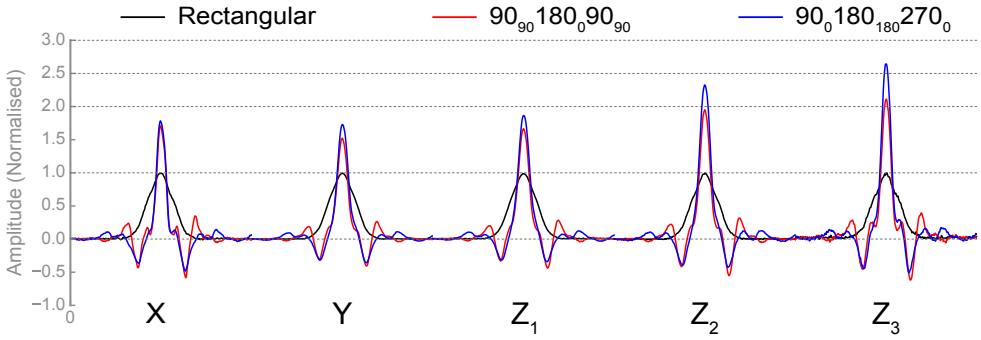

(b) 32 ns π

Figure 5.3: (a) Refocused echoes obtained using sample of TEMPO, using rectangular 16 ns π pulses and composite pulses for corresponding field positions as shown in Figure 5.2. (b) Repeat of (a) using 32 ns π pulse length. All echoes are normalised to the corresponding rectangular echo.

Orientation	**Normal vs. $90_{90}180_{0}90_{90}$ Composite 16 ns π**	**Normal vs. $90_{0}180_{180}270_{0}$ Composite 16 ns π**	**Normal vs. $90_{90}180_{0}90_{90}$ Composite 32 ns π**	**Normal vs. $90_{0}180_{180}270_{0}$ Composite 32 ns π**
X	2.216	2.177	1.790	1.793
Y	1.673	1.570	1.526	1.730
Z_1	1.702	1.749	1.679	1.881
Z_2	1.913	2.104	1.951	2.323
Z_3	2.216	2.593	2.111	2.644

Table 5.1: Echo enhancement with field position for composite versus rectangular refocused echoes, normalised to the rectangular echo amplitude

In particular, it shows that the smallest enhancement is obtained for the Y orientation on the nitroxyl line. The Y and the Z_1 orientations are centrally located in the nitroxide spectrum, thus, both should benefit the most from availability of spins for excitation by the broadband pulse. Given that the addition of broadband excitation reduces it, it suggests other effects are degrading the composite echoes. Simulations on a broad, flat line (Figure 4.10(b)) indicate that up to 2.7 times enhancement in echo amplitude should be possible. In an effort to investigate whether the enhanced bandwidth is degrading performance, the experiment was

repeated with longer pulses to reduce the bandwidth of excitation. The results shown in Figure 5.3(b) show that the echo amplitude enhancement improves marginally with longer pulses and follows similar trend in orientation dependent enhancement, with echoes measured on Z_3 showing the most enhancement. In the case of the mono-radical, effects of intramolecular and intermolecular instantaneous diffusion are not expected, as the label is not directly coupled to another spin and the concentration is low.

5.2 Model nitroxyl bi-radical MSA236

In investigating the applicability of composite pulses for use in more general PELDOR experiments, the rigid model nitroxyl bi-radical MSA236 was used. The sample itself was kindly donated for testing purposes by Jeschke Lab at ETH Zürich, having been synthesized by the Godt group at Universität Bielefeld. The rod-like structure (compound IIIb in [79], shown in Figure 5.4) has a well-defined distance (4.1 nm) between the nitroxyl centres due to its limited flexibility. This particular sample has been set in deuterated *ortho*-terphenyl (D8-*o*TP) at a concentration of 50 μM. *Ortho*-terphenyl is a solid at room temperature, and is easily melted (and thus glassed) around 80 °C, which is trivially achievable in the lab using a heat gun. By placing the sample in a deuterated matrix, the absence of protons reduces the effects of nuclear-electron relaxation between the unpaired electron and its surroundings, extending the transverse relaxation time in comparison with non-deuterated equivalent matrix. This combination allows for testing on this sample to be carried out at room temperature, without the costly requirements of cryogen cooling.

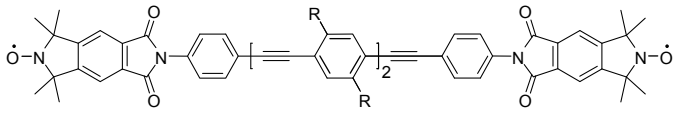

Figure 5.4: Structure of MSA236. The R groups are C_6H_{13}. Distance between radical centres is 4.1 nm.

5.2.1 MSA236: sample preparation

The sample was provided by the Jeschke group in powdered form, which was loaded into a FEP tube, before being melted using a heat gun, (at approximately 80 °C) until a translucent glass was formed. The sample tube was measured to have filled around 2/3 of the tube, corresponding to a sample volume of ~100 μL. The sample was then allowed to re-crystallise and harden to a solid at room temperature, before loading into a sample holder and into the

spectrometer for testing.

5.2.2 MSA236: Field swept echo experiment

The field swept echo experiment on MSA236 was carried out at 291 K using a Hahn echo sequence, $\pi/2 \rightarrow \tau \rightarrow \pi \rightarrow \tau \rightarrow echo$, with 7 and 14 ns $\pi/2$ and π pulse lengths and inter-pulse delay $\tau = 250$ ns. The field was swept from 3337 mT to 3367 mT in 0.1 mT steps, with pulse frequency of 93.9996 GHz. Sequence repetition frequency was 5 kHz, averaging 5,000 shots per point.

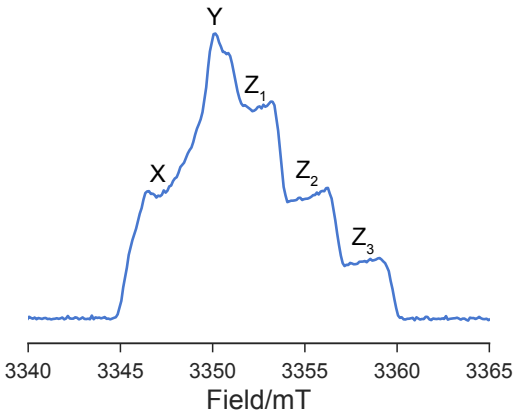

Figure 5.5: Absorption spectrum for the nitroxide bi-radical MSA236 at room temperature, obtained using a field-swept echo experiment, showing positions X, Y, Z_1, Z_2 and Z_3.

In contrast to the field swept echo spectrum of the mono-radical (Figure 5.2), the field swept echo spectrum of the bi-radical (using rectangular pulses) shows the effects of instantaneous diffusion where the X and Y components are attenuated with respect to the Z-components. This is caused by intramolecular instantaneous spin diffusion between the paramagnetic centres in the sample. It is particularly common in rigid bi-radicals such as this one due to strong orientation dependent dipolar coupling between the labels [22].

5.2.3 MSA236: Composite refocused echo experiments

Composite refocused echoes were measured on the MSA236 model nitroxyl bi-radical system at different field positions/orientations on the EPR spectrum nitroxyl centre. Echoes were obtained using standard, rectangular $\pi/2$ and π pulses and with the equivalent $90_{90}180_{0}90_{90}$ and $90_{0}180_{180}270_{0}$ composite π-inversion pulses. In each case, the initial $\pi/2$ excitation pulse was provided by an 8 ns $\pi/2$ rectangular pulse. The field positions used as shown in Figure 5.5 are X = 3347 mT, Y = 3350 mT, $Z_1 = 3352$ mT, $Z_2 = 3355$ mT and $Z_3 = 3358$ mT. The results of

the refocused echo experiments for each of the composite and standard sequences versus field positions are shown in Figure 5.6(a). Similarly to the TEMPO measurements, the refocused echo measurements on MSA236 were repeated using 16 ns $\pi/2$ pulse lengths, results of which are shown in Figure 5.6(b). The enhancements for both sets of experiments are summarised in Table 5.2.

Orientation	**Rectangular vs. $90_{90}180_{0}90_{90}$ Composite 16 ns π**	**Rectangular vs. $90_{0}180_{180}270_{0}$ Composite 16 ns π**	**Rectangular vs. $90_{90}180_{0}90_{90}$ Composite 32 ns π**	**Rectangular vs. $90_{0}180_{180}270_{0}$ Composite 32 ns π**
X	1.266	1.217	1.671	1.752
Y	1.138	1.063	1.425	1.450
Z_1	1.219	1.197	1.672	1.726
Z_2	1.406	1.462	1.974	2.064
Z_3	1.621	1.783	2.175	2.465

Table 5.2: Echo enhancement with field position for composite versus rectangular refocused echoes, normalised to the rectangular echo amplitude

Similarly to the TEMPO refocused echo results shown in Section 5.1.3, the refocused echo enhancement when using composite pulses is also non-uniform with orientation for the model bi-radical system. The enhancement is smallest for Y and Z_1 with 8 ns $\pi/2$ pulse lengths, and shows greatest enhancement for Z_3. The enhancement improves when one uses longer pulses, however, it still follows the same trend for degraded enhancement on Y and best on Z_3. In comparison with the composite echoes obtained on the mono-radical with 8 ns $\pi/2$ pulse lengths, the enhancement obtained on the bi-radical for the same pulse length is significantly degraded for all orientations. The bi-radical shows a much larger enhancement for all orientations at the longer pulse length for all orientations, whereas the mono-radical shows only moderate increase between the shorter and longer pulse measurements. This suggests that the increase in bandwidth is much more detrimental to echo amplitude enhancement in the case of dipolar coupled systems.

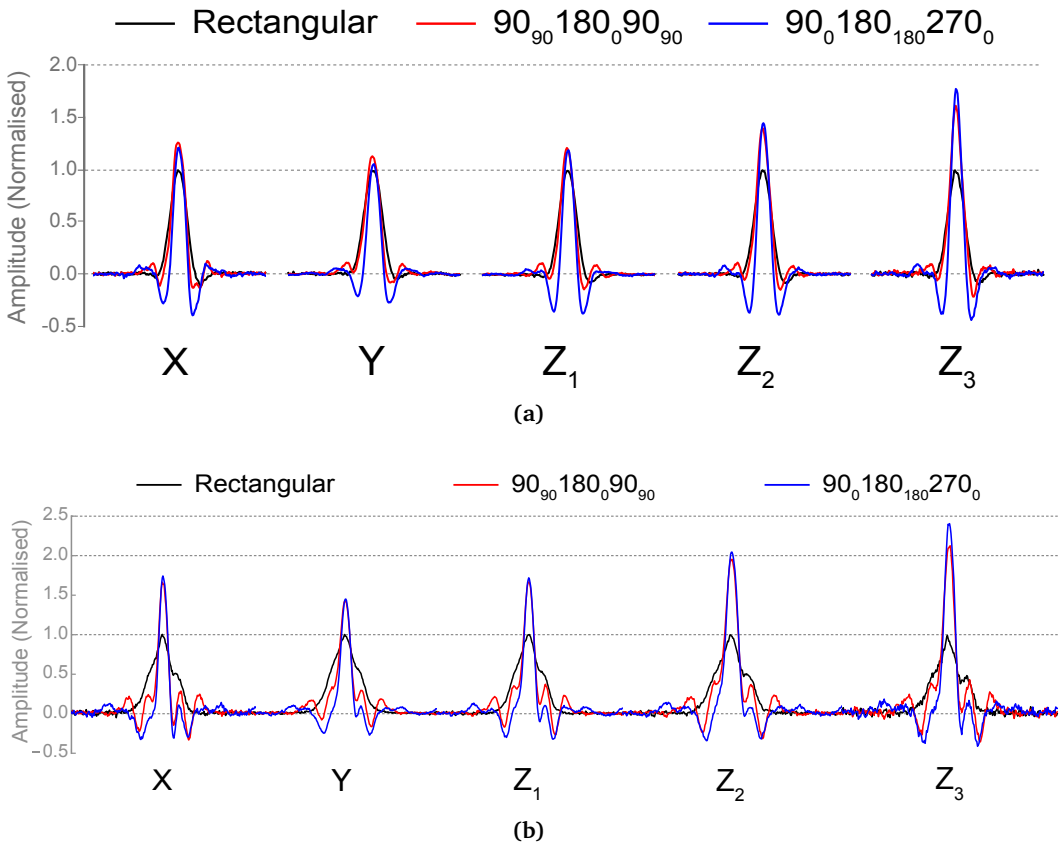

Figure 5.6: (a) Refocused echoes obtained using rectangular 16 ns π pulses and composite pulses for corresponding field positions. (b) Repeat of (a) using 32 ns π pulse length. All echoes are normalised to the corresponding rectangular echo. The shoulder to the right of the main peak in the echo is due to B_1 inhomogeneity.

5.2.4 MSA236: Composite PELDOR

PELDOR experiments were carried out on MSA236 with rectangular π pulses replaced with $90_{90}180_{0}90_{90}$ and $90_{0}180_{180}270_{0}$ inversion pulses. Combinations of the pulse sequences were used to assess the ability of the composite pulses to improve signal-to-noise through different means. This was carried out by replacing the π pulses on the observer (refocused echo) sequence with composites $90_{90}180_{0}90_{90}$ and $90_{0}180_{180}270_{0}$ to increase measured signal, and by replacing the pump inversion π pulse in the pump sequence to invert more partner spins, utilising the increased bandwidth offered by the $90_{90}180_{0}90_{90}$ and $90_{0}180_{180}270_{0}$ sequences to increase modulation depth. The combinations used are shown in Figure 5.7, where (a) represents the standard 4-pulse dead-time free DEER sequence using rectangular pulses, (b) uses a rectangular observer pulse, and a composite pump, (c) uses a composite observer and a rectangular pump and (d) uses both composite observer and composite pump. The resulting DEER traces are shown in Figure 5.8.

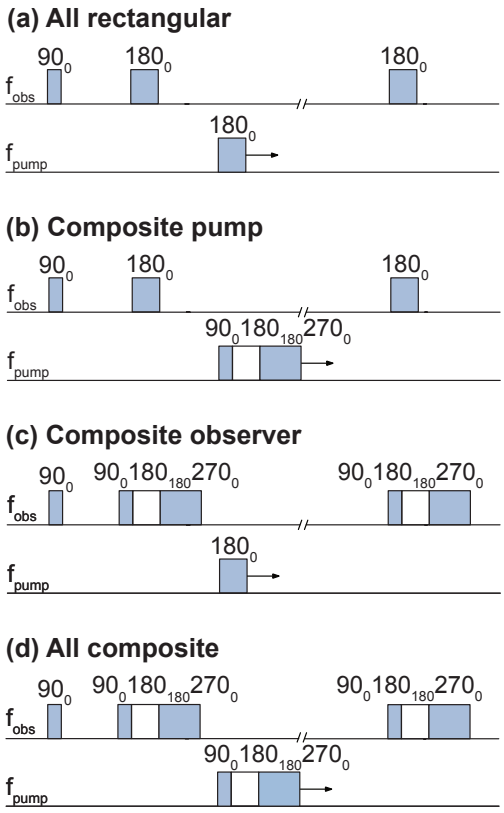

Figure 5.7: Pulse sequence combinations used in MSA236 composite pulse DEER experiments, shown using the $90_{0}180_{180}270_{0}$ composite pulse.

By replacing the pump pulse with a composite (Figure 5.7(b) composite pump), it is expected that this should increase the modulation depth as the broadband pulse increases the

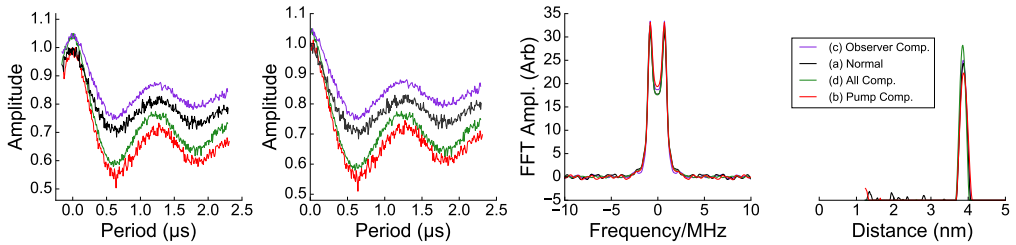

(a) $90_{90}180_{0}90_{90}$

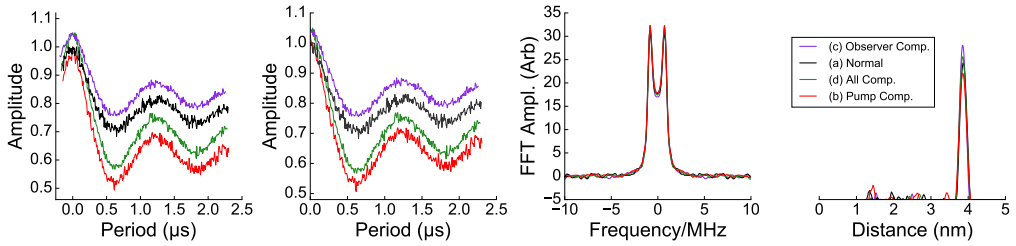

(b) $90_{0}180_{180}270_{0}$

Figure 5.8: DEER comparison using (a) $90_{90}180_{0}90_{90}$ composite π pulse and (b) $90_{0}180_{180}270_{0}$ composite π pulse, using the MSA236 model biradical, observing on Z_3 and pumping Y orientations. The combinations used are all π-rectangular (black), observer π-composite (purple), pump π-composite (red) and all π-composite (green).

number of inverted partner spins in the dipolar coupling term. The expectation from enhancements seen in the refocused echo experiments, is that by replacing the observer pulse with composite pulses (Figure 5.7(c) composite observer), it should increase signal to noise with its enhanced echo amplitude. It should be noted that the positions of pump and observer were the same for normal and composite tests. This was to ensure that the same orientations of spins were selected by the pulses.

The DEER experiment was carried out on the YZ orientation (observer Z_3 and pump Y) using 8 ns $\pi/2$ pulse lengths. This orientation was chosen so that composite pulses on the pump could be utilised fully to excite the large, broad peak of the spectrum at Y. The results for each of the combinations of pulses using the $90_{90}180_{0}90_{90}$ and $90_{0}180_{180}270_{0}$ composite are shown in Figure 5.8. The data were processed using DeerAnalysis 2016 [57].

The left plots in Figure 5.8 show the raw (normalised) traces, left of centre shows the background subtracted data, right of centre shows the FFT of the DEER data or Pake pattern, and the right plots shows the derived distance distributions. The observer composite sequence (Figure 5.7(c)) shown in purple and all π-composite (Figure 5.7(d)), shown in green, have been offset vertically by 0.05 for clarity.

Both experiments show no discernible difference between pump composite and all com-

Pulse Seq.	SNR	SNR vs. Rect.	Mod. Depth vs. Rect.	Sig. vs. Rect.	Noise vs. Rect
Rectangular	31.72	1.00	1.00	1.00	1.00
Pump $90_{90}180_{0}90_{90}$	43.72	1.38	1.57	1.45	1.05
Pump $90_{0}180_{180}270_{0}$	40.23	1.27	1.61	1.50	1.18
Observer $90_{90}180_{0}90_{90}$	41.96	1.32	0.96	1.00	0.76
Observer $90_{0}180_{180}270_{0}$	40.99	1.29	0.94	1.03	0.79
All π-$90_{90}180_{0}90_{90}$	51.52	1.62	1.49	1.43	0.88
All π-$90_{0}180_{180}270_{0}$	55.87	1.76	1.52	1.55	0.88

Table 5.3: SNR comparison of the DEER traces obtained, normalised to the standard rectangular sequence trace

posite cases (shown in red and green respectively), which each exhibit the same level of modulation enhancement (1.50 times that of the normal, rectangular inversion pulse). The same effect is observed with the rectangular and probe composite sequences (shown in black and purple respectively) showing the same modulation depth also. The signal-to-noise ratio (SNR) does vary between the pairs with the same modulation depth. The SNR for each of the averaged traces was calculated simular to the method described in [80] by dividing the magnitude of signal (maximum minus minimum) of the raw DEER data by the standard deviation of the residual noise, which was obtained by subtracting a moving average from the data. The SNR results for MSA236 are summarised in Table 5.3.

Using this metric, the all-π composite $90_{0}180_{180}270_{0}$ sequence increases the SNR by 1.76 compared to the rectangular pulse sequence. This is partly due to a decrease in noise, provided by the narrower composite echo and the increase in modulation depth provided by the broadband composite pump. The $90_{90}180_{0}90_{90}$ all π-composite gives 1.62 times enhancement, which is to be expected as it is slightly less broadband than the $90_{0}180_{180}270_{0}$ sequence and does not provide as large an echo enhancement. The observer composite and pump composite sequences all provide between 1.27 and 1.38 times enhancement in SNR. When comparing the noise figure and the signal magnitude of the traces to that of the rectangular sequence however, we see that while the pump composite sequences provide the largest absolute increase in modulation depth, the increase in signal level is only 1.45-1.50 times, and the noise level in the trace is observed to slightly increase. In the case of the observer composite sequence however, the signal level or integrated echo area, is similar to that of the rectangular sequence, but the overall SNR improves due to the reduction of the noise figure by 21-24%, due to the narrower echo. The noise level scales with the number of time samples measured, so by reducing the width of the window, the noise also reduces. While the echo on the nitroxide does not give

the large echo amplitude enhancement as predicted in the simulation and as achieved in the broad low-spin Fe(III) sample, its integrated echo magnitude is the same as the rectangular echo so it does not suffer from a decrease in signal level, but benefits from the decrease in noise. In DEER traces obtained using all π-composites, the noise decrease is not as large as the observer composite case, but it does benefit from the increase in modulation depth, and these effects combined result in an increase of up to 1.76 times in signal to noise. This equates to a factor of 3 (1.76^2) in averaging time.

5.3 Phase memory time measurements on MSA236 and TEMPO

In order to assess the processes causing the differences in composite echo enhancement with orientation on the mono- and bi-radical nitroxyls, phase memory time (T_m) measurements were carried out. This was carried out using the same operating conditions (i.e. temperature) as for the refocused echo experiments, using a Hahn echo increasing τ progressive experiment. The excitation pulse in both cases was provided by a 16 ns pulse and the refocusing pulse's length was varied to change its flip angle. Decay curves were recovered (using a 20 ns displacement of the refocusing pulse for 401 steps), which had pulse lengths of 32, 16, 8 and 4 ns respectively, corresponding to flip angles of π, $\pi/2$, $\pi/4$ and $\pi/8$ respectively. This was repeated on the X, Y and Z_2 orientations of the nitroxide spectrum, at field positions of 3347 mT, 3350 mT and 3355 mT respectively. The results are shown in Figure 5.9.

The phase memory time measurements are different for both samples due to the fact they were carried out at different temperatures. The MSA236 experiments were carried out at room temperature (291 K), resulting in a bi-exponential decay, in contrast, the decay curve on the TEMPO, which was carried out at 58 K shows a stretched exponential decay. For the purposes of fair comparison, the latter has been used to fit both, producing an 'average' T_m for the bi-exponential fit, and a comparable 'goodness of fit' to the bi-exponential fit. The following equation was used for the fitting:

$$V(\tau) = a * Exp\left(-\left(\frac{\tau}{T_m}\right)^b\right) + c \tag{5.1}$$

where V(τ) describes the magnitude of signal as a function of increasing τ, a, b and c are fitting parameters and T_m is the phase memory time, or time constant of the decay. The fitting was carried out using the Curve Fitting toolbox in MatLAB 2016a, and the results are summarised in Tables 5.4 and 5.5.

Flip Angle θ	**X (3347 mT)/μs**	**Y (3350 mT)/μs**	**Z_2 (3355 mT)μs**
π	2.21	2.27	2.28
$\pi/2$	2.21	2.22	2.26
$\pi/4$	2.20	2.21	2.21
$\pi/8$	2.18	2.21	2.28

Table 5.4: T_m results for TEMPO

Flip Angle θ	**X (3347 mT)/μs**	**Y (3350 mT)/μs**	**Z_2 (3355 mT)μs**
π	0.33	0.15	0.21
$\pi/2$	0.30	0.15	0.20
$\pi/4$	0.24	0.21	0.24
$\pi/8$	0.38	0.30	0.32

Table 5.5: T_m results for MSA236

The curve fitting results for phase memory time (T_m) as a function of flip angle and orientation for TEMPO indicate very little instantaneous diffusion is occurring, as T_m is consistent (within 5%) across all orientations and refocusing flip angle. However, the results for the bi-radical, MSA236 indicate that there is some instantaneous diffusion present due to the large variations in T_m, in particular for Y. Given the low concentration of both samples at 50 μM, in addition to the deuterated matrix (D8-*o*TP) in which the bi-radical is dissolved, the instantaneous diffusion present in MSA236 is most likely intra-molecular in nature, resulting from dipolar coupling between the electron spin-pairs of the molecule itself.

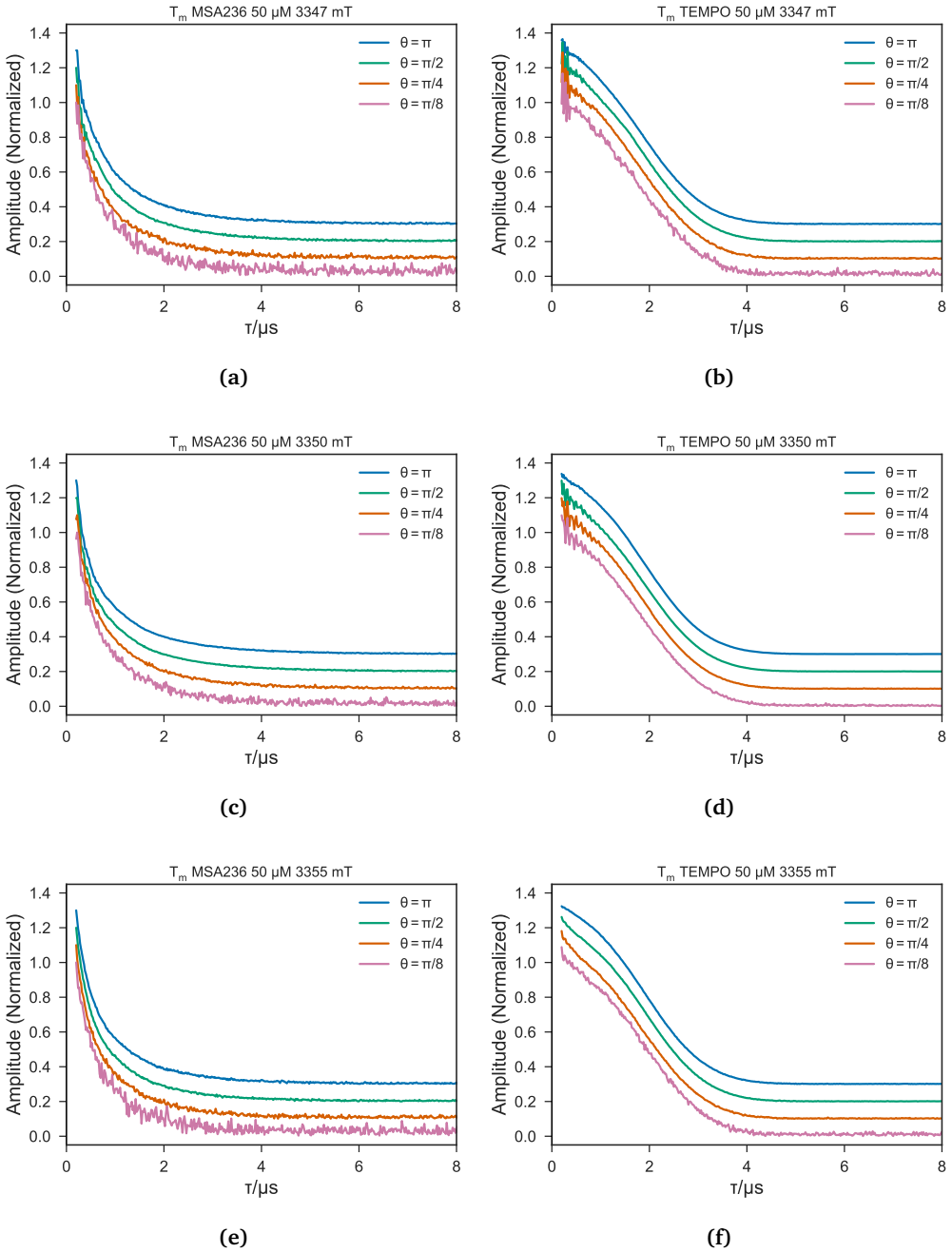

Figure 5.9: Plots of Hahn echo decay versus as a function of flip angle of refocusing pulse with respect to orientation. a),c) and e) show X,Y and Z_2 for MSA236 respectively, and b),d) and f) show X,Y and Z_2 for TEMPO respectively. Plots offset for clarity.

5.4 Conclusions

Experiments were carried out on a nitroxide mono-radical to explore how composite pulse refocused echo enhancement varies as a function of orientation and of excitation bandwidth. The experiments showed some orientation dependence on the enhancement achieved using composite pulses, with the worst performance on X, Y and Z_1 and the best on Z_2 and Z_3. It also showed little difference in enhancement when the pulse lengths were doubled. The experiments were repeated on a model nitroxide bi-radical, which showed little enhancement on X, Y and Z_1 and degraded enhancement (in comparison with the mono-radical) on Z_2 and Z_3. The experiments were repeated with the pulse lengths doubled, resulting the same trend of orientation dependent enhancement and some improvement in echo enhancement. This was still degraded in comparison with the mono-radical. It was confirmed through the use of phase memory time measurements that intramolecular relaxation effects between the spin-pairs in the bi-radical appear to cause the degraded performance. Composite pulses were used in PELDOR experiments on the bi-radical, resulting in up to 1.76 times enhancement in signal-to-noise, equating to a factor of 3 reduction averaging time when using all-π $90_0180_{180}270_0$ composite pulses. This performance was degraded by the effects of intramolecular diffusion, suggesting that broadband pulses are not well suited for use in systems such as the model bi-radical used here.

6

Composite PELDOR: Iron-nitroxides

The work presented in this chapter is based on a journal article published in April 2016 in Journal of Physical Chemistry Letters, Vol 7, pp 1411-1415, DOI: 10.1021/acs.jpclett.6b00456.

This chapter will discuss the use of composite pulses in PELDOR experiments that contain broad metallic paramagnetic centres and nitroxyl spin labels. Such systems are generally challenging due to the broad spectral width of metal centres, which requires broadband pulses to provide sufficient excitation. It is however still advantageous to utilise the embedded metal centre, and other attached spin labels to perform PELDOR measurements between the centres. While spin labels can be attached in various locations within the protein, they also assume many conformations due to the length of the tether (typically 1 nm), which can reduce measurement accuracy. The intrinsic centre is essentially a fixed point within the protein of interest, reducing measurement inaccuracy, in comparison with measuring between two nitroxide spin labels. However, embedded paramagnetic metal centres, exhibit very different spectral and relaxation attributes versus the nitroxyl label; the metallic centre will be extremely broad and relaxes much faster, requiring lower measurement temperatures than that of the label. This

results in challenging measurement conditions. This chapter will discuss how measurements between haem centres and labels in two proteins systems can be carried out successfully at W-band, resulting in a large increase in measurement sensitivity over commercially available X- and Q-band spectrometers.

6.1 Haem-based protein systems

Haem-based proteins are found in all kingdoms of nature and cover a diverse range of functions and variety of biochemical reactions. It is widely remarked that haem proteins and metalloporphyrin-based proteins lie at the basis of life [81]. Understanding their function, such as conformational changes occurring during actions such as ligand binding, is important with the aim of designing synthetic analogues and therapeutics against disease [82]. Most haem-based proteins contain a metalloporphyrin chelating an iron atom. The basic structure of the porphyrin is a tetrapyrrole macrocycle, known as *porphine*, that is ligand-binded (chelated) to a metal atom. The porphine consists of four pyrrole units interconnected by methine bridges. The pyrrole unit itself consists of a 5-member ring made up of 4 carbon atoms and a nitrogen atom. The macrocycle structure of the metal ligating porphyrin, the metalloporphyrin is shown in Figure 6.1.

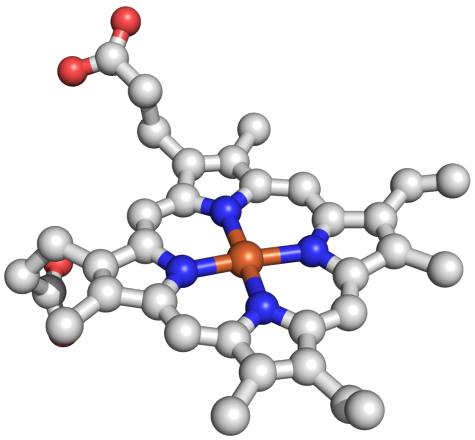

Figure 6.1: Structure of the metalloporphyrin present in the haem protein, myoglobin. The bronze-coloured atom at the centre of the tetrapyrrole structure is an iron atom. Image created in Pymol using the porphyrin centre of the PDB model 1MBI (sperm whale myoglobin).

The presence of the Fe(III) in some of the forms of haem-based proteins makes the protein intrinsically paramagnetic. The porphyrin centre in most systems of this type is regarded as

a fixed point paramagnet within the protein itself, thus it is generally advantageous to use such centres directly in PELDOR measurements [6, 16–20]. Additional paramagnetic centres, usually in the form of spin labels can be attached to the protein itself by engineering cysteine amino acids at specific points along the protein, to react with spin labels through the use of the technique known as site-directed spin-labelling (SDSL). This allows for distance measurements to be carried out between the intrinsic paramagnetic centre and the extrinstic centre of the label, using PELDOR measurements. The label typically has a length of 1 nm, and can adopt many conformations, which can reduce the accuracy of the measurement.

Measurements of this type are however, extremely challenging because haem centres exhibit extremely broad spectra in EPR experiments and rapid electron relaxation, which strongly inhibits the sensitivity required for Fe(III)-nitroxide PELDOR experiments. However, PELDOR experiments have been reported between a low-spin ferric haem and a nitroxide label giving distances of 2.1 [17] and 2.7 nm [18]. These measurements were carried out at X- and Q-band frequencies on a human neuroglobin (NGB) and cytochrome P450cam proteins. The low-spin ferric haem centres in both of these proteins at X-band were spectrally 280 and 80 mT broad respectively. Both measurements were carried out on commercially available spectrometers using standard rectangular pulses and required long averaging time (24 hours in the NGB case), which degrades significantly with increasing spectral width. Other pulsed dipolar distance measurement techniques, such as RIDME [43], can also be utilised for such measurements, as was demonstrated on the spectrally narrower P450cam system, providing a factor of 7 enhancement in sensitivity.

Due to the broadband nature of the intrinsic metal centre in such systems, it is an obvious choice to utilise broadband pulses to improve sensitivity. The use of broadband pulses on more traditional commercial systems is limited in part by the bandwidth of the resonator, which will limit the excitation capabilities of pulses. The proportion of spins excited is proportional to the magnitude of echoes or signals obtained, thus to fully utilise broadband pulses, one requires either complex resonator compensation [37], or use of a non-resonant system, such as HiPER [24].

The two haem-based systems studied here are human neuroglobin (NGB) and sperm whale myoglobin (Mb). The neuroglobin study was conducted in collaboration with Professor Sabine Van Doorslaer from the University of Antwerp. All sample preparation of the neuroglobin mutants was carried out by Professor Sylvia Dewilde at Antwerp. The myoglobin study was

carried out in conjunction with Dr Janet Lovett, and mutants were purified and spin-labelled in St Andrews by Dr Stacey Bell. The plasmid for the myoglobin was provided by Prof Jason Chin at Cambridge University.

6.1.1 Ligand coordination of Fe(III): high-spin versus low-spin state

In its ferric (Fe(III)) state, the electronic configuration of highest occupied orbital, the 3d-orbital has 5 electrons, and 5 orbitals to be filled. According to the Aufbau principle, the lowest energy orbitals are filled first. Each electron has spin 1/2, and according to Pauli's Exclusion Principle, each orbital can be doubly occupied, providing they are in pairs of + and - 1/2 spin state. The coordination of the iron within in the porphyrin ring, results in an octahedral crystal field arrangement of the electronic orbitals due to the presence of 4 electrons (or ligands) from the coordinating nitrogens in the porphyrin and 2 additional coordinating ligands below and above the plane of the porphyrin. This results in 5 possible electron orbitals, namely d_{zx}, d_{yz}, d_{xy}, d_{z^2} and $d_{x^2} - d_{y^2}$, shown in Figure 6.2.

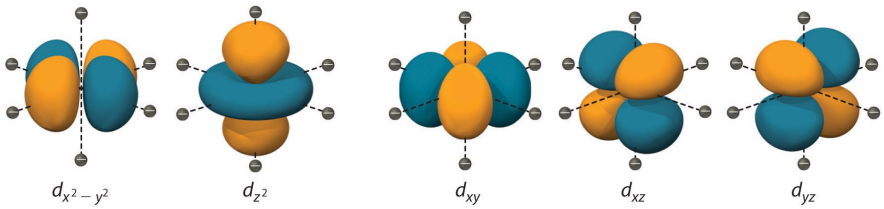

Figure 6.2: Diagram illustrating the shape of the d-orbitals and their positions relative to the 6 ligands in the octahedral arrangement. (Reproduced from [83], under Creative Commons licence)

The former 2 orbitals are concentrated closer to ligands along the axes, resulting in a higher energy state, e_g, due to repulsion, where both orbitals are degenerate. The remaining three orbitals form a lower energy triply degenerate set, t_{2g}, as shown in Figure 6.3(a). The occupancy (shown in Figure 6.3(b)) of the orbitals by the 5 available electrons is thus determined by the separation of the e_g and t_{2g} sets, which in the case of the metalloporphyrin, is determined by what ligands it is coordinated to axially. This separation, Δ_O is called ligand-field splitting parameter. The occupancy of the 5 orbitals is thus determined by the size of the ligand field, such that if the splitting is smaller than the energy cost of placing 2 electrons in one orbital, then the 5 electrons will singly occupy all orbitals, resulting in an overall spin S=5/2, known as a high-spin state. However, if the ligand splitting is large, it becomes more favourable to doubly occupy the lower orbitals, the electrons will arrange such that there are 2 pairs and one unpaired electron, resulting in an overall spin S=1/2, known as a low-spin state.

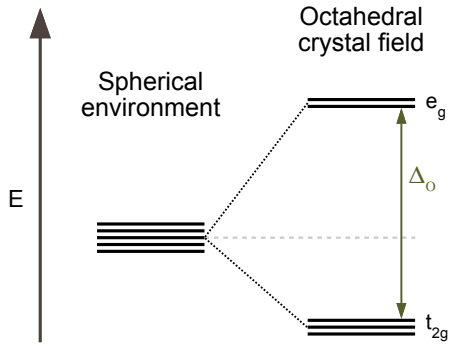

(a) Energy level arrangement

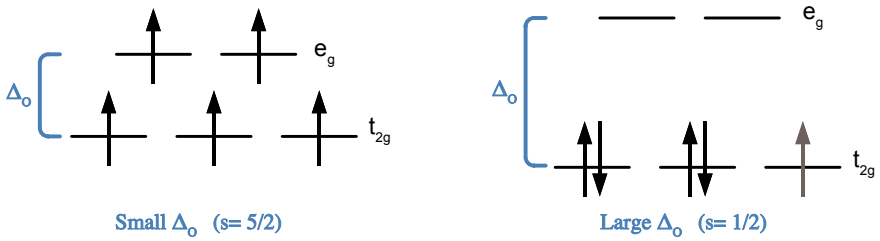

(b) Occupancy as a function of Δ_0

Figure 6.3: (a) Energy level arrangement of the 5 d-orbitals in a spherical (unbound) and octahedral (bound) environment, (b) influence of ligand splitting Δ_O level on occupancy of energy levels.

6.2 Neuroglobin NGB-C120R1

Human neuroglobin (NGB) is a haem protein part of the porphyrin-containing globin proteins which bind oxygen reversibly and are thus crucial in respiratory processes in living species [84]. However, this particular protein's function is still relatively unknown since its discovery in 2000. In this system, the haem iron is coordinated on both sides by histidine residues, which act as a high-field ligand, forcing the iron into a low spin state.

In the case of NGB, the axial ligands are provided by 2 histidines from the nearby helices of the protein itself, shown in Figure 6.4. The helices are colour-coded for clarity, and the histidines are coloured according to the helix they are attached to. Due to the fact the haem iron is coordinated by the two histidines, unlike most globin proteins, NGB cannot functionally bind oxygen. It has been suggested that its function may be involved in detoxifying reactive oxygen or to enhance cell viability under hypoxia [85].

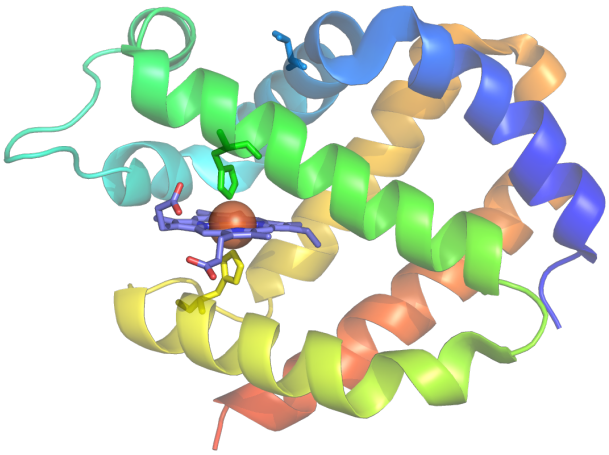

Figure 6.4: Structure of human neuroglobin (NGB) highlighting the location of the two coordinating histidines around the haem iron. These act as high-field ligands to force the haem iron into a low-spin (s=1/2) state. Image created in Pymol using PDB model 1OJ6.

6.2.1 Spin labelling NGB C120R1

Human neuroglobin protein contains 3 cysteines which are available to be spin-labelled by reaction with a (1-oxyl-2,2,5,5-tetramethyl-Δ3-pyrroline-3-methyl) methanethiosulfonate (MTS) nitroxide label, denoted as R1. Reaction with the protein as is, would result in spin labels being attached at 3 sites across the protein, which will make interpreting distance measurements between the iron centre and the labels challenging. In order to simplify this, the protein was mutated to produce a single-cysteine site, so that labels only attach in one location. In the experiments conducted on HiPER and described here, this was carried out with labels attached to Cys 120, which is located on position 19 of the G helix [17]. To simulate the expected distance between the haem iron and the nitroxide label, the Pymol package MtsslWizard [14], was used to attach a MTS label to the site. This package samples the conformational space of the label and calculates which conformations clash with the protein structure. The resulting 'mushroom' of all possible label positions of C120R1 attached to the NGB protein is shown in Figure 6.5. The sample was prepared by our collaborators at University of Antwerp, as detailed in their previous study in Reference [17].

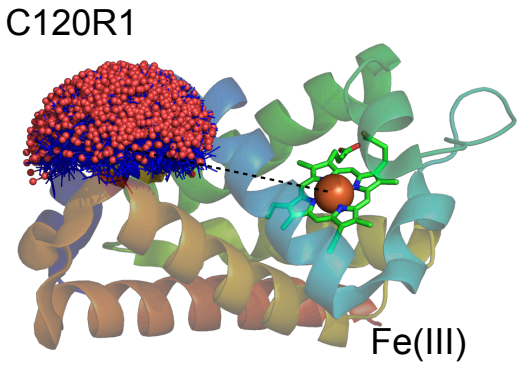

Figure 6.5: Stucture of neuroglobin, labelled at Cys120 using MTS label. Image created in Pymol using PDB model 1OJ6, and spin-labelled using MtsslWizard[14].

6.2.2 Experimental set up

Pulsed experiments were carried out at 94 GHz using HiPER. The prepared NGB-C120R1 sample was mixed 1:1 with glycerol, resulting in a final concentration of 1.1 mM (haem content).

The solution was then loaded into a FEP sample tube before being flash frozen in liquid nitrogen and placed inside a pre-cooled (also in LN_2) sample puck. The sample puck was then loaded into the spectrometer at 140 K before being annealed by gradually raising the temperature to 180 K for a short time. The cryostat was then lowered to 6 K for testing.

6.2.3 Field swept echo experiment

The field swept echo experiment on NGB C120R1 was carried out at 6 K using a Hahn echo sequence, $\pi/2 \rightarrow \tau \rightarrow \pi \rightarrow \tau \rightarrow echo$, with 6 and 12 ns $\pi/2$ and π pulse lengths and inter-pulse delay $\tau = 1$ μs. The field was swept from 3167 mT to 3527 mT in 0.5 mT steps, with pulse frequency of 93.9996 GHz. The resulting spectrum is shown in Figure 6.6. The Hahn echo was optimised on the Fe centre, allowing for a fast sequence repetition frequency (due to its fast relaxation) of 1 kHz, averaging 1,000 shots per point. The nitroxide label is saturated under such conditions as it exhibits extremely long T_1 relaxation, and cannot fully recover between the pulses. The bumps observed to the left and right of the main nitroxide peak are manganese, a common contaminant in samples made using this type of preparation. The manganese is assumed to be in the solution and at low enough concentration to not adversely affect the spin dynamics of the Fe(III) centre and the nitroxide label. It also features an extremely fast (not measurable) T_1, that leads to it only being observed in these circumstances below 10 K.

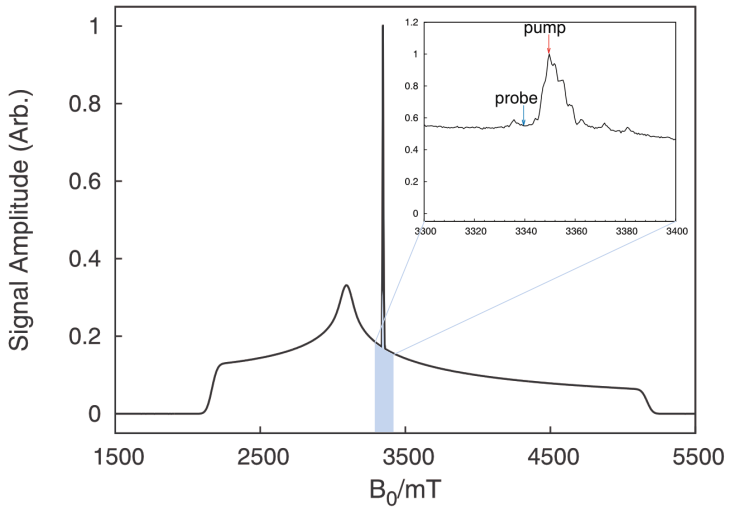

Figure 6.6: NGB C120R1 field-swept echo simulation of the spectra generated using EasySpin[62] at W-band (94 GHz), with experimental data shown inset. Blue shaded part in the simulation indicates the part of spectrum that is viewed in the inset. The full experimental spectrum cannot be viewed due to limitations of the magnet's sweep coil (±200 mT).

6.2.4 Refocused echo experiments

Refocused echo measurements were carried out on NGB C120R1 using a refocused echo sequence to observe echoes on the Fe(III) centre. This was carried out at the probe field location as shown in Figure 6.6, 314 MHz from the g_y position of the nitroxide. Similar to the refocused echo experiments in Chapter 5.1.3, echoes were obtained using standard, rectangular $\pi/2$ and π pulses, and with the equivalent and $90_0180_{180}270_0$ composite π-inversion pulse. The pulse sequence consisted of the observer part of the PELDOR sequence, $\pi/2 \rightarrow \tau_1 \rightarrow \pi \rightarrow (\tau_1 + \tau_2) \rightarrow \pi \rightarrow \tau_2 \rightarrow echo$, with $\pi/2$ and π pulse lengths of 8 and 16 ns respectively and inter-pulse delays $\tau_1 = 198$ ns and $\tau_2 = 750$ ns. The results comparing the rectangular pulse and composite π-pulse echoes are shown in Figure 6.7(a). The echo amplitudes in both cases are normalised to the echo amplitude of the standard pulse.

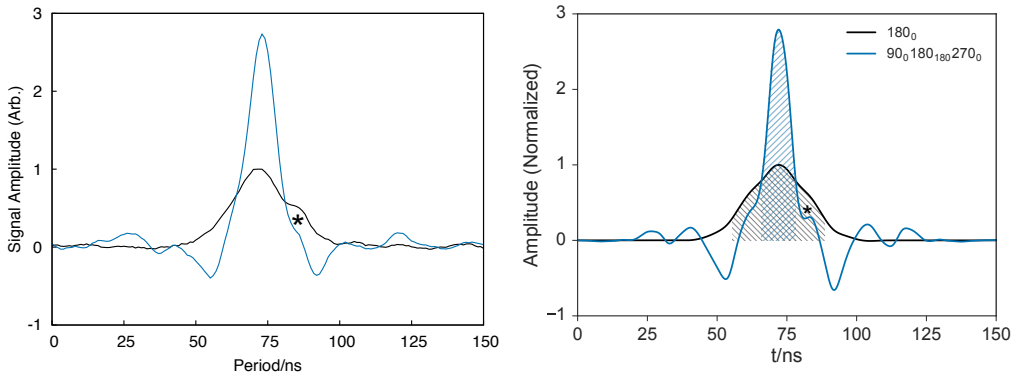

Figure 6.7: (a) Experimentally measured refocused spin echoes of a frozen solution of NGB-C120R1 obtained using the $90_0180_{180}270_0$ composite π-pulse (blue) and standard rectangular π-pulse (black). (b) Simulation of the refocused spin echo, using the same sequences, assuming a flat linewidth over the excitation profile and taking into account the large B_1 inhomogeneity associated with HiPER.

The experimental results show good agreement with the simulated results (see Chapter 4, Section 4.3.4). The small bump to the right of the peak (indicated by asterisk) in both simulation and experiment is a consequence of B_1 inhomogeneity across the sample (in contrast with the case of no inhomogeneity, shown in Chapter 4, Figure 4.11). The simulation indicated that 2.79 times enhancement in echo height can be theoretically expected, whereas the experiment shows a 2.73 times enhancement. In a PELDOR experiment, the more pertinent quantity is the integrated echo signal-to-noise ratio. In both cases, an increase of 1.8 times is observed, assuming rectangular integration windows whose width is defined by the 30% of echo amplitude points, as shown in Figure 6.7(b), with the measured area shown as hatched.

The agreement with the theoretical simulation has been achieved for the special case where the line shape, or underlying spectra in terms of frequency offset is essentially flat over the excitation profile. This is to be expected from the position of the pulses with respect to the Fe(III) line which is flat and broad. It also assumes the effects of instantaneous diffusion are negligible, which is also to be expected. The agreement overall indicates that the excitation is not limited by any other parameters invoked by the system, in particular, system bandwidth.

6.2.5 Composite PELDOR

PELDOR measurements were carried out on NGB-C120R1 using HiPER, by observing on low-spin Fe(III) and pumping the g_y peak of the nitroxide. The separation between pump and probe was 314 MHz, allowing for good separation so to avoid overlap of the extended wings of excitation of the composite pulses. This is also easily accommodated within the excitation bandwidth of the 1 kW amplifier. The choice to pump on the maximum of the nitroxide is to maximise the modulation depth of the measurement, as the largest number of spins of the nitroxide are on g_y, as indicated in the field sweep (Figure 6.6). The position of the probe is also located on the g_y position of the low-spin Fe(III) centre. This orientation is distributed over a large range of dipolar angles, thus reducing effects of orientation selection between the nitroxide and the iron centre. The positions of the pump and probe are also shown in Figure 6.6.

Pulse sequences used were the same as those used in the nitroxide biradical study as discussed in Chapter 5, shown in Figure 5.7. The sequences were carried out using the standard 4-pulse PELDOR sequence, using 8 ns $\pi/2$ and 16 ns π pulses, and the $90_0180_{180}270_0$ composite sequence in place of the composite pulses, with pulse length $t_{\pi Composite} = 8+16+24 =$ 48 ns. The interpulse delays, τ_1 and τ_2 were 198 and 954 ns respectively. The pump pulse was started 100 ns after the first π pulse in the observer sequence and was incremented in 4 ns steps for 201 steps. The cryostat was held at 6 K for the duration of experiments, as this temperature allowed for a fast sequence repetition rate of 1 kHz, allowing for 1,000 averages per point to be carried out. Each sequence was averaged for 9 scans, taking 30 minutes in total to complete. The resulting PELDOR traces for all rectangular, composite probe and rectangular pump, rectangular probe and composite pump and all-π composite are shown in Figure 6.8.

Figure 6.8 shows the PELDOR traces as obtained on HiPER using the standard, combination of standard and composite and all composite PELDOR sequences. All of the data was

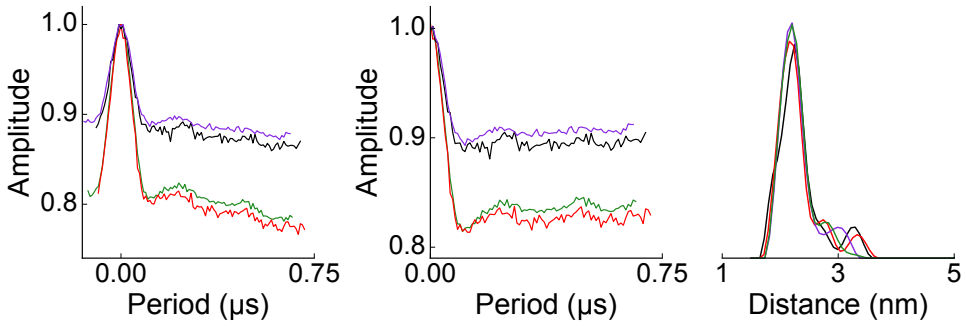

Figure 6.8: NGB-C120R1 PELDOR results showing traces obtained on HiPER using all rectangular π pulses (black), pump composite (red), observer (or probe) composite pulses (purple), and all π-composite pulses (green). The all-π-composite trace (green) has better signal-to-noise and modulation depth over the trace using conventional rectangular pulses (black) for the same number of scans.

processed using DeerAnalysis 2015 [57]. The plot on the left shows the raw, normalised averaged traces obtained, the centre plot shows the data following background subtraction and the right plot shows the resulting distance distributions, obtained by Fourier transform analysis and Tikhonov regularisation fitting of the time traces.

Signal-to-noise analysis was carried out on all 4 sets of data using the same method as described in Chapter 5, by dividing the magnitude of the signal (maximum - minimum) by the standard deviation of the residual noise (obtained by removing a smoothing spline). Results are summarised in Table 6.1.

Sequence	SNR	Normalised ratio
Rectangular	42.40	1.00
All-composite	128.73	3.03
Pump	67.45	1.59
Probe	75.52	1.78

Table 6.1: Comparison of the signal to noise for PELDOR composite sequences used on NGBC120R1.

The composite observer/probe sequence (purple and green, Figure 6.8) shows a 1.8 times improvement in signal-to-noise over the standard, rectangular sequence. This indicates that the composite pulse echo is able to increase signal-to-noise as expected due to the enhancement in echo amplitude and area provided. The composite pump (red) shows an increase in modulation depth of approximately 80%, but due to the fact it is measured using a standard rectangular refocused Hahn echo, its signal-to-noise is only improved by the increase in signal level, resulting in a factor of 1.6 times improvement over the standard rectangular sequence. In the case where composite observer and composite pump pulses are used, the combined benefits of improved echo area and improved modulation depth result in a factor of 3.03 improvement in signal-to-noise over the standard rectangular sequence. The signal to noise of

the averaged traces is proportional to the averaging time squared, meaning that the rectangular sequence would require 9 times longer averaging to produce the same level of SNR as provided in the all-π composite case. This would lengthen the experiment from 30 minutes to 4.5 hours.

6.2.6 Comparison with X-band result

Previous studies of NGB C120R1 using PELDOR were conducted by our collaborators using a commercial Bruker X-band spectrometer. This was carried out at 15 K, using standard rectangular pulses. The spectrometer was set up using the broadband split-ring loop gap MS3 resonator, which permitted excitation of the pump and probe frequencies with a separation of 350 MHz between them. Full details of the experiment can be found in Reference [17]. The experiment was also conducted between the g_y orientation of the Fe(III) centre and the g_y of the nitroxide. A comparison of PELDOR traces obtained at X-band and at W-band using all-composite pulses is shown in Figure 6.9

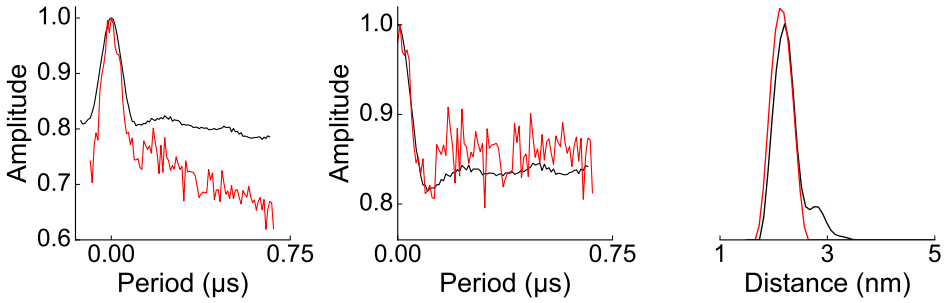

Figure 6.9: NGB-C120R1 PELDOR measurement obtained at X-band using a commercial spectrometer using standard rectangular pulses (red) and at W-band using HiPER with all-π composite pulses (black). The left hand plot shows the raw (normalised) PELDOR data, centre shows the background subtracted data and a right shows the distance distribution, obtained using DEERAnalysis 2015 [57].

Signal-to-noise ratio (SNR) analysis was also carried out on both sets of data using the same method as described in the previous subsection. By this SNR metric, the X-band data has a SNR of 21, and the W-band SNR is 124. Allowing for differences in averaging time (24 hours at X-band versus 30 minutes at W-band), and an increase of ~ 1.3 in sample concentration, this results in an overall enhancement factor of 31, a factor of 3 of which can directly attributed to use of wideband composite pulses. It should be noted also that testing on the neuroglobin was carried out using a sequence repetition frequency of 1 kHz, which was not fully optimised at the time. Later studies on similar low-spin ferric haem systems indicated that repetition rates of 10 kHz to be more appropriate, allowing for a 10 times increase in the number of

waveforms averaged per second, which should provide a further factor of 3 in SNR.

6.3 Myoglobin

The Myoglobin Fe(III)-nitroxide PELDOR study was conducted using spin-labelled sperm whale myoglobin, Mb. Myoglobin is the protein responsible for oxygen storage in muscles. It is able to perform this function as the haem group is ligated on one side, allowing for oxygen binding at the other site.

The particular state of the system used here, the myoglobin is in its reduced state, referred to in the literature as metmyoglobin, with the Fe centre is in the ferric state, allowing for oxygen to ionically bind to the iron in the centre of the haem. In its non-bound configuration, the Fe(III) exists in a high-spin (S=5/2) state due to the fact it is only ligated by a histidine (provided by the nearest helix to the haem) on one side. However, it is possible to convert the haem centre to low-spin by providing an additional axial haem ligand. This can be carried out using a variety of methods, including the addition of potassium cyanide (KCN) which converts oxy-myoglobin to low-spin metmyoglobin or the organic compound imidazole can be used to convert high-spin metmyoglobin to low-spin [86]. In both cases, the KCN or imidazole chelates the Fe atom, creating a high field ligand across the highest occupied electron orbital, creating the more favourable doubly occupied lower t_{2g} orbital, leaving one leftover unpaired electron. The KCN preparation was attempted as part of this study, however it was found to only be partially successful in conversion to the low spin state, and required extensive safety measures to be adhered to during preparation[1]. The imidazole preparation was much easier to carry out in the lab due to not being highly toxic, and provided favourable results in ligating the haem iron. Full information about the preparation of the metmyoglobin mutants can be found in Reference [87].

The spin state of the haem centre after the addition of imidazole was verified by carrying out using UV-vis spectroscopy, as the haem centre absorbs different wavelengths of light, depending on its spin state [88]. This was carried out in the wet lab when the sample was made. The spin state was also additionally verified by carrying out a continuous wave EPR measurement at low temperature. The EPR spectra was obtained at 10 K, and is shown in Figure 6.11. The CW measurement is carried out by irradiating the sample at a fixed frequency,

[1] Preparation involving potassium cyanide required the use of a separate fume cupboard and a first aider had to be present at all times during the handling of KCN. It also placed restrictions on the storing of the protein sample for testing purposes.

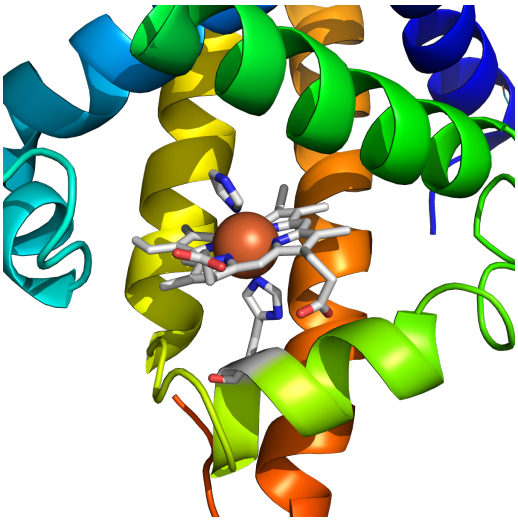

Figure 6.10: Structure of Myoglobin showing the location of the haem within the protein, illustrating the location of its ligating histidine from the F-helix and the addition of imidazole. Image created using Pymol and PDB model 1mbi.

with a continuous wave signal, the external magnetic field, B_0 is then swept until the resonance condition is fulfilled. When this occurs, the absorption of the signal and its reflection is altered, rendering the spectrum of the sample as a function of field. In the spectra shown, this has been converted to g, to allow for field independent identification of spectral features.

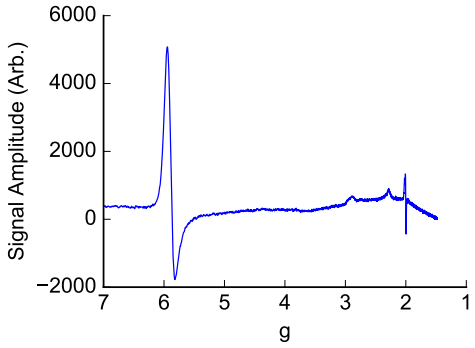

Figure 6.11: cw EPR spectra obtained a sample of metmyoglobin with imidazole at 10 K using a high Q-factor X-band resonator. The spectra is plotted in terms of g along x, and the amplitude of signal along y. It shows presence of the high-spin parallel and perpendicular components at g = 2, and 6, and low spin around g = 1.5 to 3.

The high-spin state of Fe(III) consists of a parallel ($g_{\|}$) and a perpendicular($g_{\perp}$) component at g = 2 and 6 respectively. The low-spin state is characterised by coordination of the single unpaired electron to its surrounding axial ligands, resulting in characteristic broad spread over g_x, g_y and g_z values. The spectra obtained as shown in Figure 6.11 shows some high-spin is present through the sharp peaks at g = 2,6, but good conversion to low-spin state, through the broad peaks shown at low-g between g = 1.5 and g = 3. The peaks agree approximately with

the literature values of **g**=(1.55, 2.28,2.90) [86]. The lowest g-value peak cannot be verified as it is outside the measured range.

Following verification of the low-spin conversion, spin-labelling was carried out. The met-myoglobin was mutated to produce cysteine binding sites at positions S117C and S3C, located on the A and G helices of the protein respectively. Singly mutated and doubly mutated versions were created and reacted with the MTS spin label, R1. This created the singly labelled mutants Mb-S117R1 and Mb-S3R1, and the doubly labelled Mb-S3R1S117R1 mutant for testing. The doubly labelled version is shown in Figure 6.12.

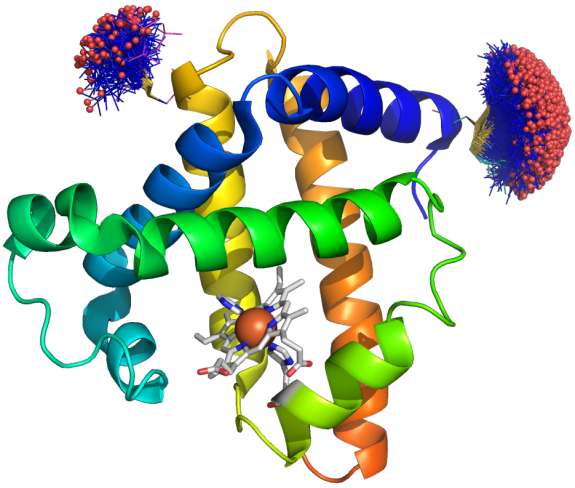

Figure 6.12: Structure of Myoglobin showing the position of the two labels, S117R1 and S3R1. Image created using Pymol using PDB model 1mbi and the MtsslWizard package [14].

6.3.1 Experimental set up

The samples were prepared in 50/50 protein to deutrated glycerol mixture before being loaded into FEP tubes and flash frozen in liquid nitrogen, ready for testing in HiPER. The final protein concentrations were Mb-S3CR1: 0.18 mM, MbS117R1:0.2 mM and Mb-S3R1S117R1: 0.14 mM. The haem content was monitored using UV-vis spectroscopy to determine the occupancy of the protein. The haem content for Mb-S3R1 was determined to be 100%, in contrast with 70% for Mb-S117R1 and 95% for Mb-S3R1S117R1.

The flash frozen sample tubes were then loaded into sample puck that was also submerged in liquid nitrogen, before being loaded into the pre-cooled spectrometer at 130 K. The samples were then annealed by raising the temperature gradually to 180 K, before lowering to the measurement temperature of 6 or 58 K.

6.3.2 Field swept echo experiment

Field sweep echo experiments were carried out using the same settings for the neuroglobin, as discussed in Section 6.2.3, with the echo optimised on the Fe centre. The resulting spectra is shown in Figure 6.13, inset.

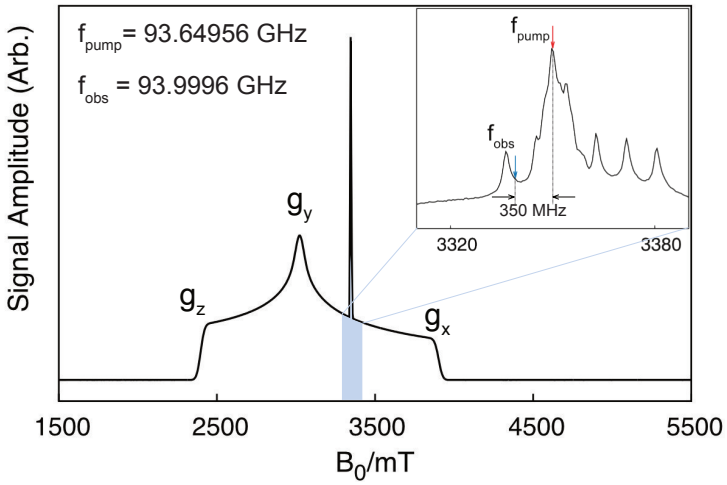

Figure 6.13: Mb-S3R1 field-swept echo simulation of the spectra generated using EasySpin [62] at W-band (94 GHz), with experimental data shown inset. Blue shaded part in the simulation indicates the part of spectrum that is viewed inset. The full experimental spectrum cannot be viewed due to limitations of the magnet's sweep coil (±200 mT).

The full spectrum has been simulated using the EasySpin package [62] in MATLAB, using the g-values, $\mathbf{g} = (1.55, 2.28, 2.90)$ given in Reference [86], and typical g-values for the nitroixde centre, as $\mathbf{g} = (2.0083\ 2.0063\ 2.00240)$. In contrast to the neuroglobin, 6.6 the myoglobin Fe centre is approximately one half as broad.

6.3.3 Fe(III)-nitroxide and bisnitroxide PELDOR

Composite PELDOR experiments were carried out on all 3 samples, measuring between the Fe(III) centre and the g_y of the nitroxide label at 6 K. This was carried out using the all-composite PELDOR sequence, as shown in Figure 6.14, B.

Mb-S3R1 inter-pulse delays were $\tau_1 = 198$ ns and $\tau_2 = 1454$ ns, with 8 ns $\pi/2$ and 16 ns π pulse lengths, resulting in a 8+16+24 ns pulse length for the $90_0180_{180}270_0$ composite

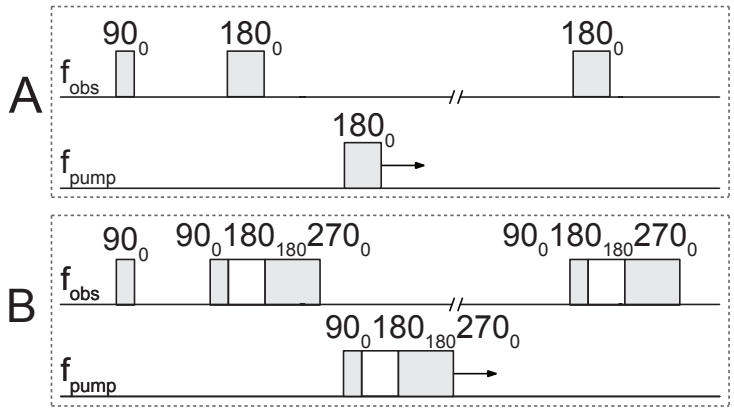

Figure 6.14: Pulse sequences used in PELDOR experiments on Myoglobin mutants. All Fe(III)-nitroxide experiments used the all-π composite sequence (b), and the nitroxide-nitroxide used the standard rectangular pulse sequence, (a).

pulse used here. The pump pulse was started 100 ns after the first π pulse on the observer sequence and was incremented in 8 ns steps for 182 steps. The observer pulse frequency was 93.9996 GHz and the pump frequency was 93.64956 GHz, giving a frequency offset of 350 MHz. This was averaged at 10 kHz for 12 scans taking approximately 37 minutes to run.

Mb-S117R1 inter-pulse delays were $\tau_1 = 244$ ns and $\tau_2 = 964$ ns, with the same pulse lengths as for Mb-S3R1. τ_1 was optimised to minimise the effect of ESEEM (See T_m measurements). This was carried out by monitoring a standard Hahn echo ($\pi/2$-τ-π-*echo*) using rectangular pulses as a function of τ and optimised to give the largest echo. The pump pulse was started 156 ns after the first π pulse on the observer sequence and was incremented in 8 ns steps for 124 steps. The observer pulse frequency was 93.9996 GHz and the pump frequency was 93.64956 GHz, giving a frequency offset of 350 MHz. This was averaged at 10 kHz for 9 scans taking approximately 19 minutes to run.

Mb-S3R1S117R1 inter-pulse delays were $\tau_1 = 226$ ns and $\tau_2 = 1498$ ns, with the same pulse lengths as for Mb-S3R1. The pump pulse was started 124 ns after the first π pulse on the observer sequence and was incremented in 8 ns steps for 187 steps. Observer pulse frequency was 93.9996 GHz and the pump frequency was 93.64956 GHz, giving a frequency offset of 350 MHz. This was averaged at 10 kHz for 12 scans taking approximately 38 minutes to run.

Measurements between the nitroxide labels on the doubly labelled mutant, Mb-S3R1S117R1 were carried out at 58 K with rectangular pulses, using the standard PELDOR sequence as shown in Figure 6.14, A. This was carried out at the higher temperature where the T_1 relaxation of the nitroxide is much more favourable, allowing for sequence repetition rates of 1 kHz. The results of the bisnitroxide measurements are denoted as S3R1-S117R1.

S3R1-S117R1 inter-pulse delays were $\tau_1 = 260$ ns and $\tau_2 = 1990$ ns, with all standard pulses with pulse lengths $t_{\pi/2} = 6$ ns and $t_\pi = 12$ ns. The pump pulse was started 100 ns after the first π pulse on the observer sequence and was incremented in 8 ns steps for 262 steps. Frequency of observer pulse was 93.78516 GHz (g_z) and the pump pulse was 93.92004 GHz (g_y), giving a frequency offset of 134 MHz. This was averaged at 1 kHz for a single scan, which took approximately 5 minutes to run. The PELDOR results for all 4 measurements are shown in Figure 6.15.

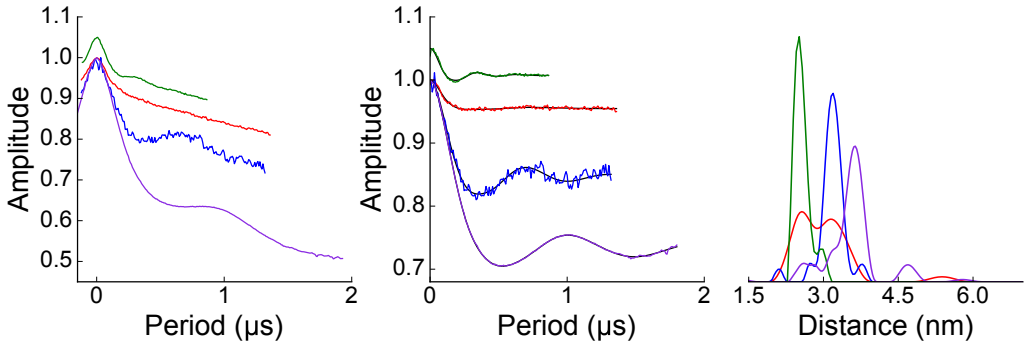

Figure 6.15: PELDOR results obtained at W-band for Mb-S3R1 (blue), MbS117R1(green), Mb-S3R1-S117R1 taken at 6 K with observer Mb, pump nitroxide (red), and Mb-S3R1-S117R1 taken at 58 K with observer nitroxide g_z and pump nitroxide g_y (purple). Left panel shows normalised raw data, centre shows data post-background subtraction with black line showing the fit obtained using DeerAnalysis2015 [57] and right showing the resulting distance distribution for each of the traces

All traces were analysed using DeerAnalysis 2015 [57] to subtract the background decay and fit the time traces to obtain an approximate distance distribution. In the case of the singly labelled mutants, Mb-S3R1 and Mb-S117R1, shown in Figure 6.15 in blue and green respectively, show distances between the Fe(III) centre and the spin labels to be 3.17 nm and 2.57 nm respectively. The doubly labelled mutant, Mb-S3R1S117R1 Fe-Nitroxide measurement results in a flat, featureless PELDOR trace, whose distance distribution shows slight peaks which overlay the distances obtained for the singly labelled versions. While this result agrees with the singly labelled versions, it cannot be recommended as a primary method of determining the Fe-N distances due to the lack of confidence in the fitting.

Large differences in the modulation depth have been observed between the Mb-S117R1 and Mb-S3R1, which achieved 5 and 20% modulation respectively. The exact cause for this difference is not known, as there is no evidence of incomplete spin labelling in either sample which would contribute to a reduction in modulation depth. The haem content of Mb-S117R1 is slightly lower at 70% than that of the Mb-S3R1 sample, however this would not be expected to reduce modulation depth as this would result in less observer spins to excite which would

reduce the overall magnitude of the signal, assuming any 'free' haem is removed through washing. Another possible reason could be orientation selection of the label. The excitation of the Fe centre will utilise only a small fraction of the spins present, representing a very narrow band of angles in Y orientation. While g_y on both the label and the Fe centre is well distributed around the sphere, the label can only assume a number of conformations, depending on its nearby environment. These conformations have been predicted using MtsslWizard [14], and as shown in Figure 6.12, the S117R1 label conformations cover a much smaller distribution of angles. Because the PELDOR measurement is carried out between g_y on both centres, if the label has less spin pairs in this orientation, the modulation depth is also expected to drop. Given that an orientation study was not carried out on this system, by pumping the other nitroxide orientations as well, one can only speculate whether this is a cause of the reduction in modulation depth as observed here.

The measurement between the two nitroxide centres on the doubly labelled mutant shows excellent signal to noise for a single scan experiment. This was carried out using rectangular pulses to avoid overlap effects between the pump and observer pulses. Given the label concentration, (280 μM) the sample signal was extremely good and did not require any additional improvement from broadband observer pulses. The distance distribution indicates a label separation of 3.67 nm.

6.3.4 Rotamer library modelling of distances

In order to verify the distances obtained and check the sample has not mutated or undergone extreme misfolding during mutagenesis, the distances between the labels and the Fe centre have been modelled using two packages, MMM (Multiscale Modelling of Molecular systems) [15] and MtsslWizard [14]. Both packages use x-ray crystallography derived structures of proteins, and pre-calculated rotamer libraries containing all possible conformations of the label to calculate inter-spin distance distributions. The rotamer libraries simulate flexibility of the structure/bonds in spin labels to calculate all possible conformations of the nitroxide spin tag when attached to specific sites within the protein. Both packages use different techniques to simulate the rotamers, with MMM using a large database of pre-calculated rotamers to reflect a range of physical parameters (such as temperature and solvent) whereas MtsslWizard allows the user to calculate based on Van der Waals restrictions and swiftness of calculation. Both methods of modelling are used broadly in the field of EPR, so both are used here for comparison.

In the case of MMM, 3 custom rotamer libraries were used, following advice from one of the developers, Dr Yevhen Polyhach at ETH Zürich as to which would be must accurate for our system. These were R1A UFF 216 298K, R1A UFF 216 CASD 298K and R1A Xray 298K, which are all specialist libraries for the R1 spin label.

The MtsslWizard simulation was carried out using the 'loose' Van der Waals approximation, which allows for conformations of labels closer than 0.45 nm to the protein structure, i.e. below the VdW 'cut off.' This assumption is generally found to provide the most accurate distance distributions in practice. The simulation also utilised the 'painstaking' thoroughness search rotamer search setting to calculate 1,500 chi angle conformations of the label. The chi angle is defined as the angle between the carbon-carbon bonds on the tether of the MTS label between its attachment point and the radical.

In modelling the Fe(III)-R1 distance, both packages simulate the Fe centre to be a fixed point coordinate within the structure and measure the distance between this coordinate and the coordinates of the nitroxyl radical in all possible calculated conformations of the labels. It then totals all possible distances and returns the corresponding distance distribution. Figure 6.16 shows a comparison of distance distributions obtained using fitting of the PELDOR data, (black) and the distributions predicted by MMM and MtsslWizard (coloured) for all mutants and and the different 4 PELDOR measurements carried out. It also shows the corresponding raw experimental data, background corrected data and the resulting Pake patterns as obtained using DeerAnalysis 2015.

For each of the mutants, the simulated distances were up to 0.3 nm different than experimentally measured at W-band. However, this is within the bounds of accuracy of the rotamer-library-based approach, although we also do not rule out contributions from freezing induced changes to the spin label. Orientational effects can reduce the accuracy of PELDOR measurements at W-band. Although the haem is expected to be relatively rigid, and the pump pulse will be highly selective, a broad range of Euler angles will still be excited by a probe pulse situated towards the centre of the Fe spectrum. Similarly an even broader range of Euler angles is excited by the wideband pump pulse centred on the g_y part of nitroxide, which is also expected to have a rather broad range of orientations with respect to the haem. Thus a reasonable approximation to a full Pake pattern is expected, although not fully observed. It should be noted that the maximum frequency offset between pump and probe is limited by the 800 MHz bandwidth of the 1 kW amplifier used on HiPER, making it impossible to probe other

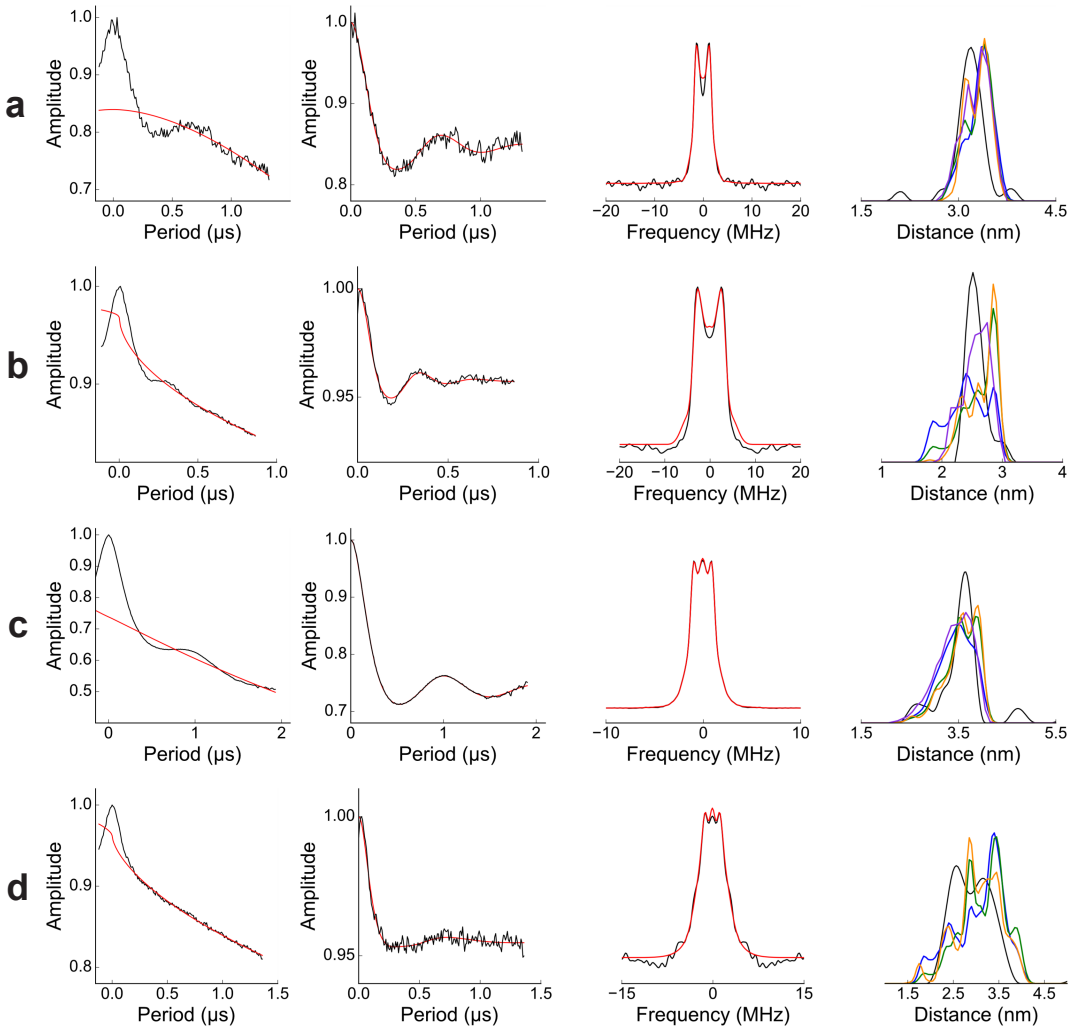

Figure 6.16: PELDOR data for all Metmyoglobin mutants and their comparisons with various rotamer library derived distance distribution simulations. (a) Mb-S3R1 at 6 K, (b) Mb-S117R1 at 6 K, (c) Mb-S3R1-S117R1 at 58 K and (d) Mb-S3R1-S117R1 at 6 K. Column 1 shows normalised experimental data with background fit in red, column 2 shows background corrected data (black) with red line showing the fit obtained using DeerAnalysis2015. Column 3 shows the resulting Fourier transform of data in column 2 (Pake pattern) and column 4 showing the resulting distance distribution (black) using MMM libraries: R1A UFF 216 298K (blue), R1A UFF 216 CASD 298K (green) and R1A Xray 298K (orange), and MtsslWizard in purple.

orientations of the Fe centre. The spin density is also expected to be largely centred on the Fe, as nitrogen and proton hyperfine couplings are relatively small, as indicated in Reference [89].

6.3.5 Comparison with Q-band

A direct PELDOR sensitivity comparison was carried out between Q-band and W-band using Mb-S117R1 system, shown in Figure 6.17. The Q-band measurements were carried out on our research group's commericial spectrometer. The Bruker Elexsys E580 system utilises a high

power (150 W) travelling wave tube (TWT) amplifier with a probe supporting a cylindrical resonator (ER 5106QT-2w). This particular resonator operates around 34 GHz in the TE012 mode. The Q-band measurements were conducted at 15 K (which was limited by T_1 relaxation time). The frequency of separation between the pump and probe was 80 MHz, which was limited by the cavity. This involved observing on the Fe and pumping the peak of the nitroxide.

The inter-pulse delays were $\tau_1 = 216$ ns and $\tau_2 = 1000$ ns, using standard rectangular pulses of 32 ns. The pump pulse had a length of 26 ns and was started 80 ns after the first π pulse on the observer sequence. This was incremented in 8 ns steps for 132 steps. Additionally, the sequence utilised nuclear modulation averaging by altering τ_1 in order to remove ESEEM effects from the traces. This averaging is included in the overall number of scans. The sequence repetition rate used was 3.3 kHz, which was limited by the spectrometer, for 36 scans taking approximately 18 minutes to run. The W-band measurements were made at 6 K as described previously, using all composite pulses and averaged for the same time as the Q-band measurements.

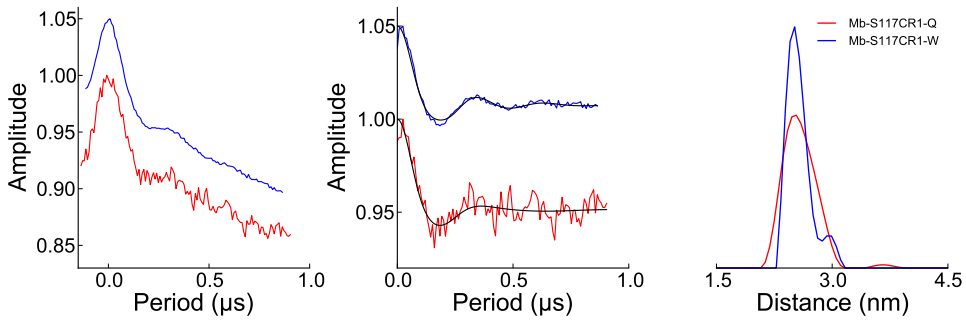

Figure 6.17: Comparison of W-band with composite pulses (blue) and Q-band (red) PELDOR traces obtained using sample Mb-S117CR1. Left shows raw normalised data, centre shows data after background correction with fit added, and right shows the corresponding distance distributions.

Signal-to-noise ratios for Q-band and W-band were calculated to be 28 and 156 respectively. This equates to an improvement of 5.5 times in signal-to-noise using HiPER versus the commercial Q-band spectrometer. It should be noted however that HiPER can accommodate a much larger sample volume (80-150 μL, 90μL in this case), in comparison with 60 μL used in the Q-band experiments. The spectrum is however almost 3 times broader at W-band versus Q-band.

6.3.6 Q-band versus W-band relaxation study

T_1 relaxation as a function of temperature

While conducting the comparison experiments on the Fe(III)-nitroxide experiments between W-band and X/Q-band, it was observed that it was possible to measure at much lower temperatures and with much higher repetition rates at W-band. In order to investigate why this might be the case, experiments were carried out comparing the longitudinal relaxation (T_1) as a function of temperature at Q and W-band on Mb-S3R1S117R1, observing on the Fe centre, in probe position as per the PELDOR experiments.

The inversion recovery experiment was performed using the pulse sequence as shown in Figure 6.18. The pulsed experiment works by using an initial π pulse to invert spins from equilibrium into the excited (-Z) state, then a Hahn echo ($\pi/2 \rightarrow \pi \rightarrow echo$) sequence is displaced away from the initial inversion pulse and its echo recorded. The greater the time between the initial inversion and the Hahn echo sequence, the longer the spins have to recover, resulting in a trace that illustrates the longitudinal relaxation of the spins. It is essential to phase cycle or use different oscillators to remove any spurious echoes from the trace. In the case of HiPER, the DRO oscillator was used for the Hahn echo, and the PMYTO oscillator was set to 93.9996 GHz for the inverting pulse (to match the frequency of the DRO). The Bruker spectrometer used a standard PulseSPEL program to run the experiment, and phase cycling to remove spurii from the traces.

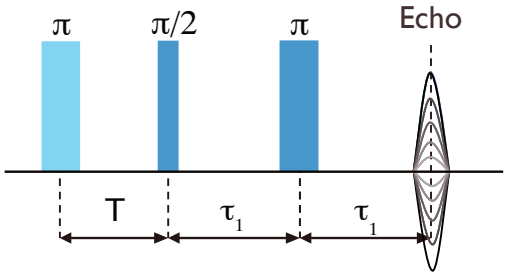

Figure 6.18: Diagram showing the T_1 relaxation pulse sequence used. The light blue inversion pulse is same frequency, but incoherent to the darker blue pulses.

In the experiments carried out at W-band, $\tau = 276$ ns, which was chosen to minimise ESEEM, and T was incremented from 50 ns in 100 ns steps for 601 steps, $\pi/2$ and π pulse lengths were 5 and 10 ns and the sequence repetition frequency was set to 100 Hz. The low repetition frequency was also chosen to reduce any saturation between shots. The trace was normalised by repeating the experiment without the initial inversion pulse, and averaging the

echo amplitude obtained to obtain the fully relaxed value.

In the Q-band experiments, $\tau = 312$ ns, also chosen to minimize ESEEM, T was incremented from 380 ns in 3000 ns steps for 1200 steps at 5, 6, 8 K, at 10 K it was incremented from 380 ns in 1000 ns steps for 600 steps, and at 15 K it was incremented in 100 ns steps for 600 steps. The $\pi/2$ and π pulse lengths were 16 and 32 ns and the sequence repetition frequency was set to 250 Hz.

The W-band and Q-band curves are shown in Figure 6.19(a) and 6.19(b), where it should be noted that sensitivity decreases rapidly with increasing temperature. The data was fitted using MATLAB curve fitting toolbox, to the equation f(x) = c - a*exp(-b*x) where b = t/T_1. The T_1 fits versus temperature are summarised in Tables 6.2 and 6.3.

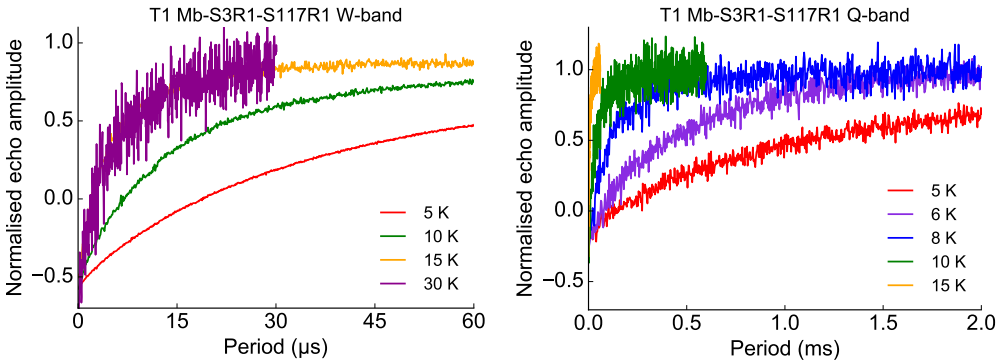

(a) W-band T_1 **(b)** Q-band T_1

Figure 6.19: Inversion recovery experimental results obtained at (a) W-band and (b) Q-band as a function of temperature.

Temperature/K	$T_1/\mu s$
5	30.60 ± 0.20
10	14.07 ± 0.14
15	6.01 ± 0.14
30	5.86 ± 0.47

Table 6.2: Summary of curve fitting results for T_1 measurements carried out at W-band, as shown in Figure 6.19.

The results show that the T_1 relaxation at W-band is significantly faster than that at Q-band. At 5 K the T_1 of the Mb is 30.8 μs at W-band and 1.1 ms at Q-band. The shorter T_1 allows much faster averaging of data in PELDOR measurements at W-band versus Q-band, allowing for more waveforms to be acquired per second, thus increasing the SNR. At higher fields, direct spin-lattice relaxation process becomes dominant over the Raman relaxation process [90, 91], which significantly increases the relaxation rate. The direct process is expected

Temperature/K	$T_1/\mu s$
5	1103 ± 32
6	520.8 ± 14.8
8	149.4 ± 8.7
10	47.03 ± 3.88
15	6.544 ± 0.29

Table 6.3: Summary of curve fitting results for T_1 measurements carried out at Q-band, as shown in Figure 6.19.

to scale as $T^{-1}B_0^4$, and thus has a very strong field (B_0) dependence which becomes significant at W-band. Lower temperatures also increases the signal magnitude due to the Boltzmann distribution, as the lower (ground) state is more highly populated at lower temperatures. This indicates that even if the experiments were carried out at temperatures where their relaxation rate was similar, the higher field experiment would have a larger echo amplitude due to the fact it is at a lower temperature. It should, however be noted that the T_1 of the Fe at Q-band at its measurement temperature of 15 K is faster than that of the the T_1 measured at the measurement temperature at W-band, at $\sim$ 5 μs versus $\sim$14 μs. This indicates the Q-band would benefit from a slight reduction in temperature, in order to accommodate the more favourable longitudinal as in the W-band case. This slight reduction would be expected to increase the signal slightly, but not as significantly as in the W-band case, where the significantly lower temperature benefits from Boltzmann distribution effects.

T_m relaxation as a function of temperature

Phase memory time (T_m) measurements were carried out at W-band and Q-band on the doubly labelled Mb-S3R1-S117R1 at the probe (Fe(III)) position using the following sequence: $\pi/2 \rightarrow T \rightarrow \pi \rightarrow T \rightarrow echo$. This was conducted to gauge the severity of the ESEEM effect as a function of field and frequency, and to also determine the distance measurement limitation using such systems.

At W-band this was carried out with $\pi/2$ and π pulses of 5 and 10 ns. T was incremented from 200 ns in 10 ns steps for 301 steps. This was carried out at 5, 15 and 25 K. At Q-band the pulse lengths were 16 and 32 ns, and T was incremented from 180 ns in 4 ns steps for 1024 steps. This was carried out at 5, 10 and 15 K. Results are shown in Figure 6.20.

As seen in Figure 6.20, both W-band and Q-band show strong ESEEM effects in the echo decay. This is shown through the modulation of the echo decay at small T, due to coupling of the Fe(III) to nitrogen and protons in the surrounding porphyrin ring. The effect is much

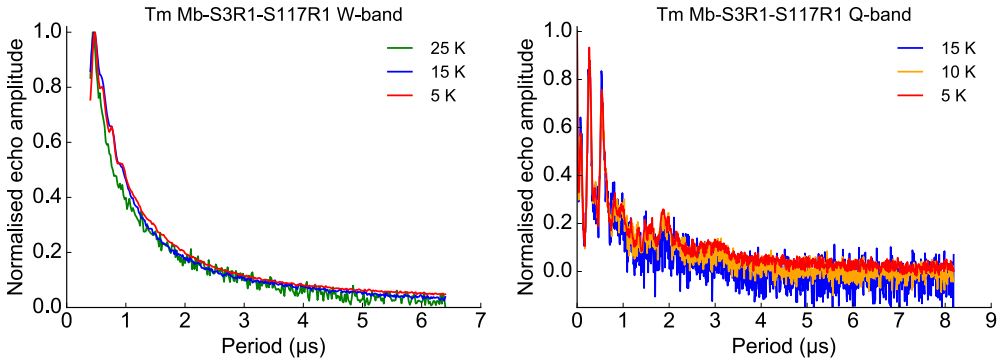

(a) W-band T_1 **(b)** Q-band T_1

Figure 6.20: Phase memory time (T_m) experimental results obtained at (a) W-band and (b) Q-band as a function of temperature.

more pronounced at Q-band than at W-band, which is why nuclear modulation averaging was utilised when conducting the Q-band PELDOR, whereas at W-band τ_1 was optimised. The T_m at W-band at 5 K is approximately 1.1 μs. This limits the distance that can be measured using PELDOR, as at least 1.75 periods of dipolar modulation is generally required to sufficiently resolve the distance distribution [2]. At $t = T_m$ point, the echo has a magnitude that is $\sim 1/e$ the size of the echo at t=0, thus, to measure at $t > T_m$ requires extensive averaging as it is expected that the echo will be very noisy due to its small amplitude. For a T_m of 1.1 μs, and imposing 1.75 dipolar evolutions requirement, it means that one can expect to be able to resolve a maximum distance of 3.2 nm. This is calculated using the relation, $r_{AB}[\text{nm}] = \sqrt[3]{t_{\perp}[\mu s] * 52.16}$ [5]. While the Mb-S117R1 measurement distance of 2.57 nm was comfortably within this bound, the Mb-S3R1 at 3.17 nm is at the near limit, which explains its poor SNR in comparison. This observation however is assuming that the T_m for the singly labelled mutants matches that of the doubly labelled mutants, on which the phase memory time measurement was made.

6.4 Conclusions

In this chapter, composite pulses were used in PELDOR experiments on iron-nitroxide systems resulting in large gains in measurement sensitivity and measurement run time. This was initially tested on a human neuroglobin (NGB) by observing using the broad metallic low-spin iron haem centre, and inverting the nitroxide spin label using the pump pulse. Initial measurements as X-band on this system required 24 hour averaging time, and still resulted in poor signal-to-noise [17]. By replacing the observer sequence π pulses in the PELDOR experiment with composite pulses, the resulting composite echo was 2.7 times larger than the rectangular equivalent, resulting in a 1.78 times improvement in echo area, and thus 1.78 times enhancement in signal-to-noise. By replacing the pump pulse with a composite pulse, and observing using rectangular pulses, a much larger bandwidth of spins were excited and inverted by the pump pulse, resulting in 80% enhancement in modulation depth. This increase in signal level resulted in an overall increase in signal to noise of 1.59 times in comparison with the rectangular PELDOR sequence. The benefits of the enhanced composite echo and improved modulation depth were combined by using a all-π composite PELDOR sequence, which gave an overall enhancement of a factor of 3 versus the rectangular pulse sequence. Thus, by replacing inversion pulses with composite equivalents, one is able to reduce the averaging time required by a factor of 9. In comparison with the results achieved at X-band, this equated to a factor of 31 times improvement in sensitivity, using composite PELDOR at W-band versus the rectangular equivalent on a X-band Bruker spectrometer.

This work was explored further through measurements on a similar haem iron protein system with the Myoglobin project. This involved further iron-nitroxide PELDOR experiments on 3 mutants of a myoglobin protein, two singly-labelled and a doubly-labelled version. Using all-π composite PELDOR, measurements could be obtained in 20-40 minutes. Measurements on the singly-labelled mutants were compared with those obtained using the doubly-labelled mutant, which showed the distance distribution to agree well. They were also compared to distance distributions generated using modelling packages and found to not agree exactly. It was discovered by conducting inversion recovery relaxation measurements that one of the contributing factors to the large sensitivity enhancements at W-band versus lower frequency/field measurements was due to the different relaxation processes involved at higher field. At higher field (W-band, 3.35 T), the T_1 relaxation of the Fe centre was significantly faster at lower temperatures than at Q-band (1.1 T) allowing for many more waveforms to be acquired per

second, increasing the SNR. This is due to direct spin-lattice relaxation processes that become dominant over Raman relaxation processes. This meant that experiments at W-band could be conducted at much lower temperatures (6 K) where it also benefits from Boltzmann distribution effects, increasing the echo amplitude. PELDOR results on one of the singly labelled mutants were carried out at Q-band for SNR comparison purposes, where it was shown that HiPER still offers a 5.5 times improvement in SNR, equating to a factor of $\sim$25 in averaging time.

7

Cobalt-Nitroxide orientational PELDOR and RIDME study

This chapter will discuss orientational PDS measurements carried out on a model system with a Cobalt metal centre, and two nitroxide labels. Systems like this have previously been studied at X and Q-band, where combinations of single and double nitoxyl-metal measurements have been carried out [44, 45, 92] to explore the relative orientations of the labels and metal centre. This study is focused on a doubly labelled version measured at W-band, where it is possible to resolve the relative orientations of the nitroxide label. The aim is to explore how high field PDS techniques can be utilised to measure the relative orientation between the labels, and also between the metal centre and the labels, in particular using RIDME. At the time of writing, this is the first demonstration of orientation selective measurements carried out using the single-frequency RIDME technique.

Unlike the haem-based systems discussed in the previous chapter, the Co(II) centre is not chelated to a porphyrin, but it is also coordinated by nitrogens, provided by 6 surrounding

pyridine groups. Pyridine groups are structurally similar to the benzene ring, but in the case of the pyridine, one of the six methine (carbon-hydrogen) groups is substituted for a nitrogen. Four pyridine groups bond via reduction (removal of hydrogen) to produce terpyridine. In this complex, the terpyridine is attached to a linker containing a nitroxyl spin label, creating the monomer unit. Two units then join, ligating Co(II) in the centre, between the six central nitrogens from the bis-terpyridine units. This creates a rod-like dimer structure with the Co(II) at the centre, and two nitroxide labels at either end, as shown in Figure 7.1.

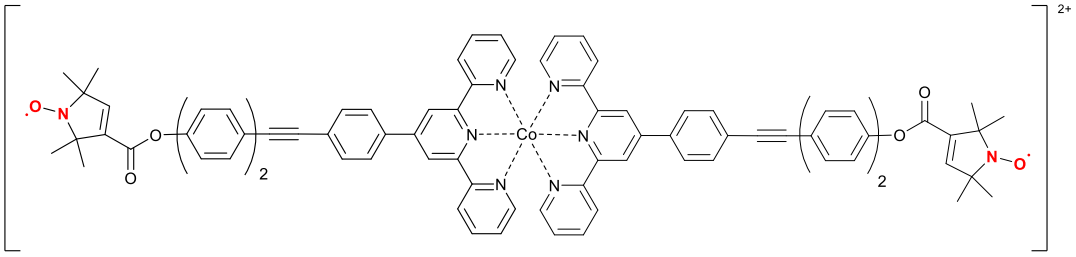

Figure 7.1: Diagram showing the structure of Co(II)-Terpyrdine model system used in this study.

Similar to the Fe(III) haem systems considered in Chapter 6, the Co(II) centre is in a low-spin state due to the high-field ligand action of its coordinating nitrogens. The reduced Co(II) itself has an electronic configuration where its highest occupied orbital is 3d, which has 7 electrons. In the case where it is not ligated, the Co(II) centre has an overall spin $S = 5/2$, however, under the action of a high-field ligand, such as that provided its 6 coordinating nitrogens here, the d-orbital's lower t_{2g} level is doubly occupied with 6 of the 7 electrons, and the additional 7th is unpaired in an e_g level orbital (see Figure 6.3(b)). This results in an overall spin state of $S = 1/2$. The low-spin state results in axial g-tensors, which have been previously determined by Kremer et al. [93].

This model system allows for orientation selective studies to be carried out between the two labels, and between the Co(II) centre and the labels. The aim of the experiments are to investigate how Relaxation Induced Dipolar Modulation Enhancement (RIDME) can be utilised along with more traditional PELDOR techniques to explore structural information about such a system. The first part of this chapter will focus on the orientation selective RIDME (osRIDME) measurements and orientation selective PELDOR (osPELDOR) measurements, all conducted using standard rectangular pulses, and will discuss the combination of all measurements to provide understanding of the structure of the system.

This study has been conducted in collaboration with Dr Bela Bode's research group in the

School of Chemistry at St Andrews. All samples were synthesised by his PhD student (at the time) Dr Angeliki Giannoulis, and all EPR measurements presented here were carried out by the author.

7.1 Co(II)-Terpyridine: Orientation predictions

Based on extensive orientation studies that have been carried out previously at W-band on bisnitroxide model systems [22], and the expected g-tensor alignment of the Co(II) terpyridine centre as determined by Kremer et al. [93], it is possible to make predictions for where parallel and perpendicular components of the dipolar oscillations will occur. The nitroxyl g-tensors can be assigned relative to the molecular framework, such that g_x is collinear along the bond joining the N-O group, g_y is perpendicular to g_x in the plane of N-O bond, and g_z is perpendicular to both g_x and g_y, out of the plane. This is shown in Figure 7.2.

From this assignment and with reference to the molecular structure of Co(II)-terpyridine (Figure 7.1), we can assign $\vec{r}_{AB}$, the vector joining the two spin centres to run parallel with the molecular backbone of the molecule, such that g_x is approximately $\sim$ 20-30° off axis from $\vec{r}_{AB}$. Thus, g_y and g_z should be both perpendicular to $\vec{r}_{AB}$.

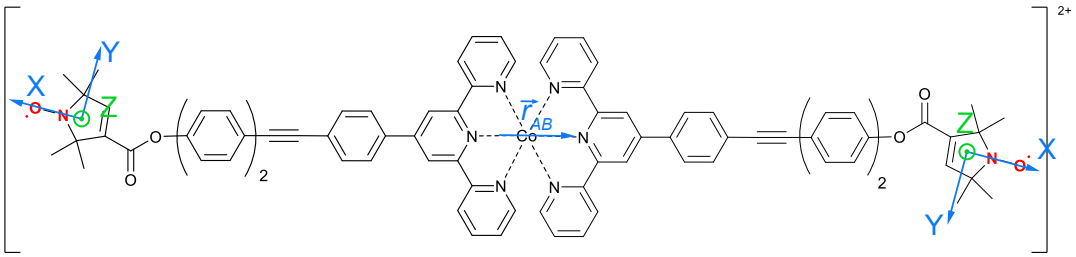

Figure 7.2: Annotated version of Figure 7.1 showing the orientation of r_{AB} and the g-tensor orientations of the $NO^{\bullet}$ radicals.

While the molecule itself is regarded to be moderately rigid, there will be some flexibility between the terpyridine unit and the linker connecting the nitroxyl group. This will result in the nitroxyl tracing out a cone of opening $\sim$25°, which will lead to a mixing of the XX and XY components. In the simplest case, where g_x is parallel to $\vec{r}_{AB}$, and both g_y and g_z are thus perpendicular to $\vec{r}_{AB}$, the dipolar oscillation frequencies given in Table 7.1 would be expected.

The table shows that one should expect $\nu_{\|}$, the double frequency on XX and $\nu_{\perp}$, the single frequency ($\nu_{\perp} = 2\nu_{\|}$) on YY, ZZ, ZY, and YZ, with no modulation occurring between XZ, ZX, YX and XY, as there should be no collinear components in these orientations. Due to the

	X	Y	Z
X	$\nu_{\parallel}$	-	-
Y	-	$\nu_{\perp}$	$\nu_{\perp}$
Z	-	$\nu_{\perp}$	$\nu_{\perp}$

Table 7.1: Orientation frequencies expected between relative orientations of the NO$^{\bullet}$-NO$^{\bullet}$ centres

symmetry of the pairs, one can carry out a full orientation measurement by measuring just 6 pairs of pump and probe.

In order to predict assignment of $\nu_{\parallel}$ and $\nu_{\perp}$ between the Co(II) centre and the nitroxyl centres, relative to $\vec{r}_{AB}$, one requires insight of the assigned orientation of the Co(II) g-tensors relative to the terpyridine group. From the literature, Kremer et al [93] have determined g-values as $\vec{g}$ = (2.26, 2.09,2.03), with the lowest g-value, g_z to be orientated in the direction of central bond of the terpyridine group, and thus aligned along $\vec{r}_{AB}$. Due to the bandwidth restrictions of the W-band instrument, we can expect to observe the orientation of Co(II) closest to the nitroxyl centre (g=2.003 to 2.008), which will correspond to Co(II) g_z. Based on this, we should thus expect NO g_x-Co(II) to have the largest $\nu_{\parallel}$ oscillation, and little oscillation in both NO g_y and NO g_z orientations, as neither are collinear with Co(II) g_z and $\vec{r}_{AB}$.

The RIDME experiment is used to measure the relative orientation of NO$^{\bullet}$ to $\vec{r}_{AB}$, as its dipolar oscillation is dependent on spontaneous relaxation of the Co(II) centre, and is independent of the orientation of the Co(II) centre. Unlike PELDOR, where the dipolar oscillation is only possible between the particular orientation of Co(II) chosen by the probe pulses, RIDME only measures the relative orientation of the observed nitroxide relative to $\vec{r}_{AB}$. Thus, it can be used to confirm the assignment of NO$^{\bullet}$ relative to $\vec{r}_{AB}$, as determined in the NO$^{\bullet}$-NO$^{\bullet}$ osPELDOR.

7.2 Sample prep and field swept echo

The sample was prepared in a similar way to the synthesis described in Reference [92], except using Co(II) instead of Zn(II). The model was dissolved in an optimised glass-forming solvent consisting of 80% deutrated DMSO-d_6:10% D_2O:10% Ethylene glycol, to provide bis-terpyridine concentration of 200 μM. The sample was loaded into a FEP tube ($\sim$100 μL) flash frozen and loaded into a pre-cooled sample puck. This was then loaded into the precooled cryostat at 130 K, before attempting to anneal it. The initial load and subsequent temperature increase showed a dramatic reduction in cross-polar signal at $\sim$175 K, suggesting that the sample was annealed. However, due to the presence of large proportion of DMSO, the sample did not follow the same annealing process as observed in samples in a water/glycerol

glassy matrix/solvent. The sample suffered greatly from cracking at different temperatures, characterised by large, sudden jumps in amplitude of the cross polar cw signal, in particular at 60 K, resulting in a reduction of the observed echo signal when measured. The solve this, the temperature was raised to take it above its glass transition temperature, to remove the cracks, before being quickly lowered, using a high flow rate of liquid helium, to 11 K for testing. This method ensured minimal cracking occurred.

A field swept echo experiment was set up by optimising a Hahn echo on the Co(II) centre. This was carried out by optimising the length $\pi/2$ and π pulses used in the Hahn echo sequence at maximum pulse power, and altering the position of the roof mirror to provide the optimal echo amplitude. The $\pi/2$ and π pulse lengths were set to 5 and 10 ns respectively. The Hahn echo sequence was set up with $\tau = 250$ ns. The field was then reset, and measurement of the spectra was obtained between 3167 mT and 3397 mT, in 0.4 mT steps. The resulting spectrum is shown in Figure 7.3.

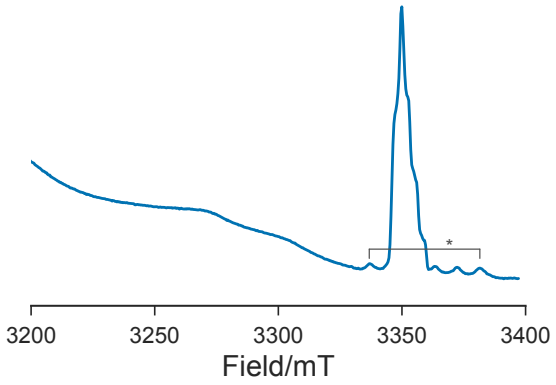

Figure 7.3: Absorption spectrum obtained using a field swept echo experiment on Co(II)-terpyridine model system at 11 K. The spectra shows the underlining broad Co^{2+} line and the nitroxide label. The 5 bumps shown around the nitroxide line (asterisk) are Manganese contaminants.

The spectra illustrates the extent of the Co(II) line at 94 GHz, showing a broad line which decreases in magnitude to the low field side of the nitroxide line. It also shows that there are manganese contaminants present in this sample.

In order to accurately determine the field positions on the nitroxide for later orientation selective measurements, the field swept echo experiment was repeated at 30 K, with the echo optimised on the nitroxide line. This was carried out using 6.5 ns $\pi/2$, 13 ns π pulse lengths and $\tau = 400$ ns. The field was stepped in 0.1 mT steps, from 3340 to 3365 mT. The resulting spectrum is shown in Figure 7.5.

7.3 Co(II)-Terpyridine: Relaxation studies

In order to optimise the temperature in the PELDOR and RIDME studies, longitudinal relaxation measurements were carried out on the Co(II) centre. This was conducted using an inversion recovery experiment, using the same sequence as given in Figure 6.18, with pulse lengths of $\pi/2 = 9$ ns and $\pi = 18$ ns, $\tau = 250$ ns where T was incremented from 50 ns in 100 ns steps for 801 steps. The sequence repetition rate was set to 100 Hz, with 100 waveforms averaged per point. This was carried out at 20 and 30 K. The data was normalised by repeating the sequence, without the initial inversion pulse, and normalising the decay curve to the average of the normalisation sequence magnitude. The results are shown in Figure 7.4

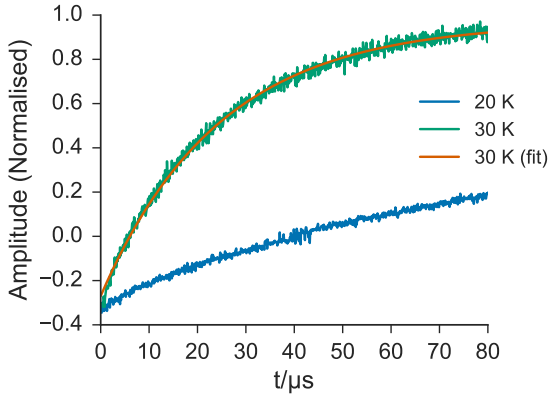

Figure 7.4: T_1 relaxation measurement conducted via inversion recovery as a function of temperature at 3,317.15 mT. Fit (orange) for 30 K data was obtained used Curve Fitting Toolbox in MATLAB.

The curves show a dramatic difference in T_1 relaxation between 20 and 30 K, with the 20 K echo recovering $\sim$ 30% of maximal echo amplitude after 80 μs. The Curve Fitting toolbox in MatLAB 2016b was used to determine T_1 as a function of temperature, using the relation:

$$V(t) = M_0\left(1 - 2\exp\left(\frac{-t}{T_1}\right)\right) \tag{7.1}$$

The 30 K data curve showed the magnetisation had recovered to $\sim$97% of full recovery amplitude, V(t) = 1 by the end of the trace, returning T_1(20 K) = 24.49 $\pm$ 0.34 μs. However it was not possible to obtain a fit to the data at 20 K, due to the limited recovery of the magnetisation. The value obtained at 30 K was in broad agreement with that obtained during experiments on the sample at X and Q-band, and was sufficient to optimise the RIDME experiment.

7.4 Orientation selective PELDOR NO•-NO•

To explore the flexibility of the molecule, and determine the molecular backbone, or $\vec{r}_{AB}$ vector of the system, osPELDOR experiments were carried out between the two nitroxide labels. At W-band, it is possible to resolve the 3 orthogonal orientations of the label with respect to the main field, B_0. Thus, by placing pump and probe pulses appropriately, it is possible to determine the relative orientations of the labels to the field. If the orientations are collinear, large modulation depths are observed, whereas non-collinear orientations are not. The experiments were carried out using 6 measuremsents, with pump and probe locations as shown in Figure 7.5. It should be noted that all measurements were carried out with probe pulses placed on the lower magnitude field position, with the larger magnitude used as pump, to maximise modulation depth.

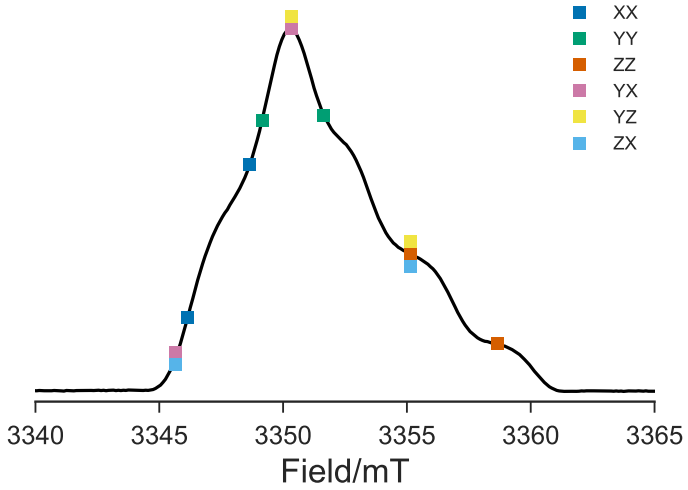

Figure 7.5: Pump and probe positions used in the NO-NO osPELDOR experiments

PELDOR experiments were carried out at 10 K, and not at 50-58 K as typically used for bisnitroxide measurements, due to instabilities in the sample at 58 K which led to frequent cracking and increased loss of signal within the sample. While going to lower temperature increases the amplitude of signal, the T_1 relaxation increases considerably, resulting in much slower sequence repetition frequencies (SRF) and thus, less waveforms can be averaged per second. In the previous study of this sample at Q-band, 20 K was used, but it was found that the best SNR could be achieved at 10 K, using a SRF of 20 Hz. It should be noted, this was also limited by the stability of the EIK amplifier in the system, which produces random fluctuations in output at SRF $<$ 20 Hz.

The osPELDOR experiments were carried out using the standard 4-pulse PELDOR sequence (shown in Figure 6.14(a)) with $\tau_1 = 200$ ns, $\tau_2 = 4800$ ns. The pump pulse was started 100 ns after the first inversion probe pulse and displaced 20 ns per step for 221 steps. The pulse lengths for each experiment were optimised based on excitation bandwidth requirements and power available at the particular frequency. All probe pulses were carried out using the main fixed oscillator (DRO) on HiPER with $f_1 = 93.9996$ GHz, with the main field set to the offset indicated in the field swept echo experiment (Figure 7.5), and the pump pulse frequency, f_2, set using either an external input oscillator or the internal phase locked tunable oscillator (PYMTO) to produce the required offset. The power level/amplitude of the pulses was optimised by setting the main W-band attenuator to produce the required pulse amplitude for the chosen pulse length on the probe pulses, then the amplitude required for the pump pulses was set by directing pump pulses along the variable attenuator pulse path, and level set by optimising its attenuation. The parameters used in the experiment are summarised in Table 7.2.

Pump Probe	Field/mT	f_2/GHz	Offset/MHz	Probe (π/2,π)/ns	Pump π/ns
XX	3346.15	93.939	70	6,12	13
YX	3345.65	93.868	131	6,12	10
YY	3349.15	93.929	70	16,32	28
XZ	3355.15	94.265	-265	6,12	18
YZ	3355.15	94.134	-135	16.32	38
ZZ	3358.15	94.069	-70	12,24	26

Table 7.2: osPELDOR parameters

The data was then processed using DeerAnalysis 2015 [57], to remove background decay and to calculate the frequency components of the time trace data. The data and resulting Pake patterns are shown in Figure 7.6.

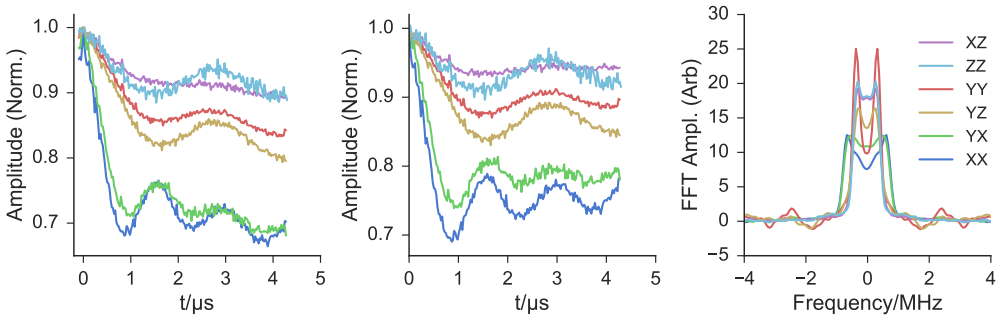

Figure 7.6: Plot showing the osPELDOR data obtained between the NO-NO groups of the Co(II)-Terpyridine model system, with left showing normalised raw data, centre data post background subtraction, and right showing the Fourier transform of the centre trace, or Pake pattern.

	X	Y	Z
X	$\nu_{\parallel}$	*DNO*	*DNO*
Y	$\nu_{\parallel}$	$\nu_{\perp}$	*DNO*
Z	$\sim \nu_{\perp}$	$\nu_{\perp}$	$\nu_{\perp}$

Table 7.3: Orientation frequencies measured frequencies between relative orientations of the NO•-NO• centres. DNO cells were not observed, and the greyed cells do not agree with predicted orientations (Table 7.1), in the case of rigid model approximation.

The data shows that the PELDOR oscillation is strongly orientationally selective, as 2 out of 6 traces obtained have double the dipolar frequency of the other 4. There are some discrepancies between the predicted frequencies as a function of relative orientation and those measured. This is summarised in Table 7.3. The XX orientation shows the expected double frequency ($\nu_{\parallel}$) inferring XX to be parallel to $\vec{r}_{AB}$, and ZZ, YY and ZY all show the expected single frequency ($\nu_{\perp}$) inferring that they are perpendicular to $\vec{r}_{AB}$. There is some modulation seen in the remaining measurements that does not agree with the predicted case, in that YX shows strong $\nu_{\parallel}$ oscillations and ZX shows much weaker $\nu_{\perp}$ oscillation. In the case of the YX measurement, this can be attributed to the tilting of x with respect to $\vec{r}_{AB}$, from the flexibility of the linker, leading to the nitroxyl group assuming a cone of conformations, centred around $\vec{r}_{AB}$. This will permit in certain conformations for Y to be parallel to $\vec{r}_{AB}$. It should also be noted that the g_y exhibits an extremely broad range of Euler angles, which makes it a poor choice for precise orientation selectivity. The small modulation on ZX can be attributed directly to the flexibility of the molecule, and given its small modulation depth, it suggests that there are very few labels with collinear g_x and g_z. This modulation behaviour was also observed in the previous W-band bisnitroxide study [22], as mentioned earlier in this section, with oscillation in YX and ZX, and was modelled by the tilting of x with respect to $\vec{r}_{AB}$, modelled with the cone of conformations from the linker.

7.5 Co(II)-Terpyridine: PELDOR Co(II)-NO•

PELDOR measurements were also carried out between Co(II) centre and the 3 orthogonal orientations of the nitroxide, in order to gauge the relative orientation between the portion of Co(II) spins excited by the probe pulses and the nitroxide orientations. The probe pulse was placed at 3332 mT, and pump pulses were placed at NO $g_x = 3347$ mT, NO $g_y = 3350$ mT and NO $g_z = 3355$ mT, as shown in Figure 7.7. The offset was chosen to maximise the Co(II) signal magnitude, as it becomes larger further from the nitroxyl part of the spectrum. The field position 3337 mT was also considered, as it would reduce frequency offset between pump and probe pulses, but would involve measuring on top of a manganese peak, which may cause erroneous effects in the measurement. In order to place the probe at 3332 mT, and pump pulses around 3355 mT, it required large frequency offsets to be accommodated within the spectrometer, ranging from 420 MHz to 644 MHz. While this is possible within the usable bandwidth of the amplifier ($\sim$ 800 MHz), it is not possible to use the fixed-frequency (DRO) oscillator for one of pulses (with the magnetic field positioned for this location on the spectrum), and simultaneously use the tunable (PMYTO) oscillator for the other pulse, as this would place the other pulse outside the usable bandwidth, which is centred around the DRO frequency of 94 GHz. Instead, the sweep coil position is located such that both pulses can be given moderate offset from 94 GHz, with both pulse frequencies provided by tunable oscillators. The power output from the spectrometer varies as a function of frequency, so to avoid any complications and to ensure consistency of excitation, the probe pulses on Co(II) were kept fixed at 94.4 GHz for all experiments. This meant that the pump pulses were offset from this position by +150, +182 and +230 G. The sweep coil field was set to -7 G, resulting in pump frequencies of $f_x = 93.9804$ GHz, $f_y = 93.8908$ GHz and $f_z = 93.7564$ GHz.

Probe and pump pulse lengths were optimised for power levels available at their respective frequencies. The probe used 6 and 12 ns $\pi/2$ and π pulse lengths, with pump pulses on NO g_x, NO g_y and NO g_z using 12, 13 and 12 ns π pulses respectively. The experiment was carried out using the standard 4 pulse PELDOR sequence (Figure 2.6), with $\tau_1 = 250$ ns and $\tau_2 = 850$ ns. The pump pulse was started 100 ns after the first probe inversion pulse, and was displaced 8 ns per step for 101 steps. This was carried out at 15 K to optimise the SRF of the sequence when observing using the metal centre. In this case it was carried out using SRF of 1 kHz, with 1,000 averages taken per point.

The PELDOR results are shown in Figure 7.8.

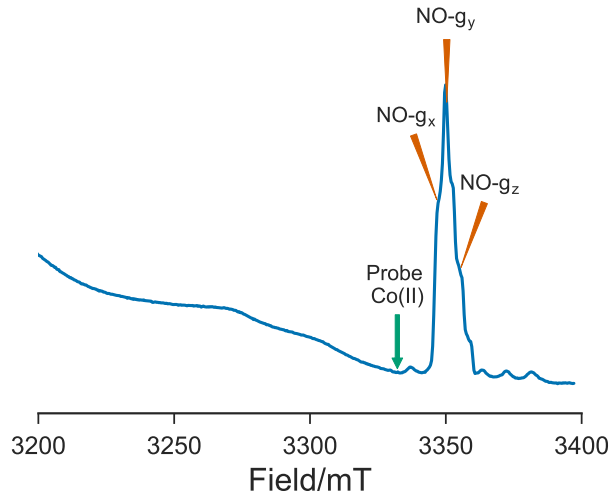

Figure 7.7: Pump and probe positions used in the Co(II)-N PELDOR experiments

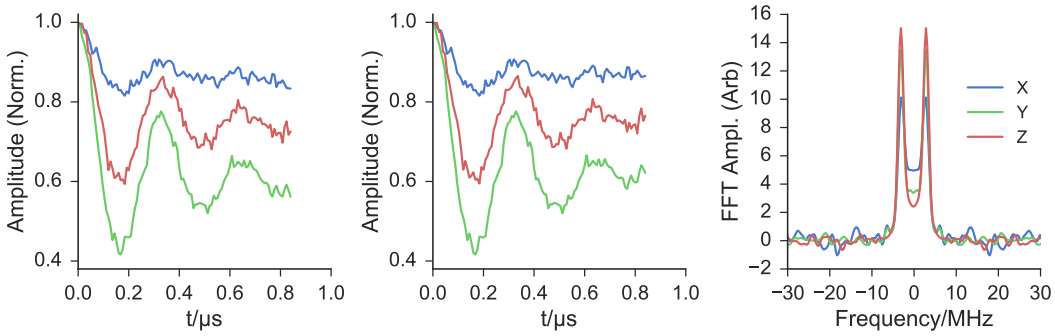

Figure 7.8: PELDOR results obtained between low-g Co(II) and the 3 orientations of the nitroxide centre. Left shows raw, normalised data, centre background subtracted, and right shows the FFT of the centre plot.

The Co(II) probe position excites the 'low-g' orientation of the Cobalt centre, which according to Kremer et al's analysis, should be g_z which is orientated parallel to $\vec{r}_{AB}$. The NO•-NO• results infer g_y and g_z of the nitroxide centre to be perpendicular to $\vec{r}_{AB}$, thus it should be expected that the PELDOR measurement should have returned large double frequency ($\nu_{\|}$) modulation between Co(II)-NO g_x and little to no modulation on Co(II)-NO g_y and Co(II)-NO g_z. The opposite is observed here. The results in Figure 7.8 show large, single frequency ($\nu_{\perp}$) modulation on Co(II)-NO g_y and Co(II)-NO g_z and a much smaller modulation on Co(II)-NO g_x. The strong presence of the double frequency between the Cobalt centre and orientations of the nitroxide centre which have been previously proven to be perpendicular to $\vec{r}_{AB}$, infers that the assignment of the low-g component of the Co(II)-terpyridine to be aligned parallel to $\vec{r}_{AB}$ is incorrect, and it is must perpendicular to $\vec{r}_{AB}$. The NO•-NO• measurement points strongly to NO g_x being parallel to $\vec{r}_{AB}$, thus the small modulation depth showing the single frequency

component ($\nu_\perp$) must be as a direct result of the flexibility of the dimer structure, which allows for a limited fraction of conformations with g_x of the nitroxide to be perpendicular to $\vec{r}_{AB}$.

Due to the broadband nature of Co(II)-terpyridine centre, the pump pulse can only invert a small fraction of the spins, thus it probes a very selective portion of all orientations possible. Thus the W-band measurement gives high confidence that Kremer et al's assignment from 1982 is incorrect. A similar issue was also found during the EPR study of a Cu(II)-terpyridine system [94], where the authors used modern Density Functional Theory (DFT) calculations to verify the assignment, and found DFT to agree with their EPR observations. The issue was attributed to an 'unusual convention' used in g-tensor assignment in a number of articles at the time.

Following on from this result, DFT calculations were carried by St Andrews' computational NMR group, led by Prof Michael Bühl on the Co(II)-terpyridine centre. The group was able to verify using DFT calculations that the g-tensor corresponding to the central pyridine (i.e. along $\vec{r}_{AB}$) to be the largest g-value, not the smallest, as suggested by Kremer et al, inferring a swap of $g_x$and g_z in the notation. This result then agrees with the Co(II)-NO$^\bullet$ osPELDOR data presented here, where the lowest g-value Co(II) is observed, and it corresponds to an orientation that is perpendicular to the molecular backbone, $\vec{r}_{AB}$.

7.6 Co(II)-Terpyridine: RIDME

The main purpose of this study was to explore the effectiveness of using the single-frequency PDS technique, RIDME (Relaxation Inducted Dipolar Modulation Enhancement) to extract orientation information from metal-nitroxide systems. The RIDME technique is best utilised in systems where there is a large difference in longitudinal relaxation between the spin centres present. This means it is not best suited for $NO^{\bullet}$-$NO^{\bullet}$ systems, where T_1 is approximately equal, but is ideal for measuring between $NO^{\bullet}$ and metal centres. RIDME is advantageous over PELDOR as an observation is generally carried out using the centre with the longest T_1, enhancing sensitivity, and removing the requirement for excessively low temperatures and high sequence repetition rates. In a direct comparison, it has been reported that RIDME in favourable circumstances can offer an enhancement in SNR of 7 over PELDOR measurements [18].

RIDME relies on the relaxation of the faster relaxing centre to produce the dipolar modulation effect. A pulse sequence is carried out on one set of spins A, and should any coupled B spins spontaneously flip, the observed A-spins precesion frequency will be shifted by ω_{dd}, resulting in a modulation of its echo amplitude. The shift in ω_{dd} similar to the PELDOR experiment, is dependent on the orientation of $\vec{r}_{AB}$, the vector joining the two spin centres, with the static magnetic field, B_0.

7.6.1 3-pulse RIDME

RIDME measurements were carried out on the Co(II)-terpyridine system by observing on the 3 orientations of the $NO^{\bullet}$ centre. This experiment was conducted initially using the non deadtime free 3 pulse sequence and later using the full 5-pulse deadtime free method. The 3 and 5-pulse sequences are shown in Figure 7.9.

The mixing time, T for the measurement was obtained from the T_1 measurement which returned 24.5 μs at 30 K (Figure 7.4) and was thus set to 25 μs. The 3-pulse sequence was used initially to check that dipolar oscillation could be observed. This was carried out on the NO g_y and NO g_z orientations, with $\tau = 120$ ns and 5.5 ns $\pi/2$ pulse lengths. The latter 2 pulses in the sequence were displaced in 8 ns steps for 126 steps. The resulting time traces are shown in Figure 7.10.

It is difficult to extract distances from this 3 pulse experiment as the zero time of the

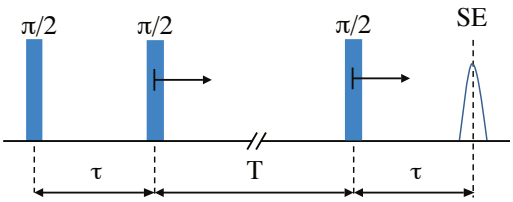

(a) 3-pulse

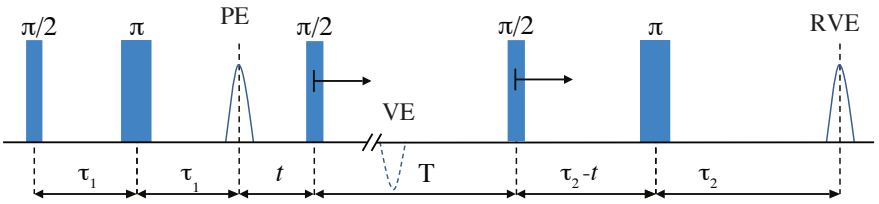

(b) 5-pulse

Figure 7.9: (a) 3-pulse RIDME sequence, (b) 5-pulse RIDME sequence.

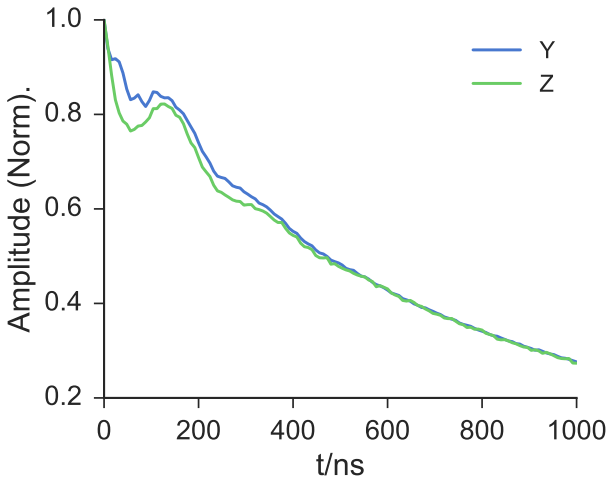

Figure 7.10: Normalised time traces obtained using 3-pulse RIDME sequence to observe on g_y and g_z orientations of the nitroxide centre. Traces show some modulation, and strong background decay.

oscillation is not observed. It does however show evidence of oscillation, which indicates that the mixing time is appropriate to observe the RIDME effect at this temperature.

7.6.2 5-pulse RIDME and phase cycling

5-pulse RIDME experiment requires 8-step phase cycling in order to remove echo crossings from the traces, that occur due to the number of pulses, and thus, large number of coherence transfer pathways involved in the measurement. This was carried out on HiPER using the 4-channel vector modulator, with each channel set manually to produce the required +x, +y, -x and -y phases. It should be noted that the +x was set by merely bypassing the vector modulator. At the time of the experiment, HiPER did not have 8-step phase-cycling programming,

requiring each of the 8 traces to be acquired individually, and to be manually processed to produce the desired time trace. The phase cycling used is summarised in Table 7.4.

φ_1	φ_3	φ_4	Detection
+x	+x	+x	+
+x	-x	-x	+
+x	+y	+y	+
+x	-y	-y	+
-x	+x	+x	-
-x	-x	-x	-
-x	+y	+y	-
-x	-y	-y	-

Table 7.4: 8-step phase-cycling sequence used during the 5-pulse RIDME experiments. φ_i refers to the i^{th} pulse in the sequence. Detection refers to the magnitude of signal, in the case of - detection, the trace must be inverted before addition to + traces

In contrast to other experiments on HiPER, where the magnitude or resultant of the in- and out-of-quadrature signal (Resultant $= \sqrt{I^2 + Q^2}$) is used, in order to maintain the sign of the signal, the in-quadrature signal is used, with the global phase adjusted at the start of the experiment such that all signal is in the in-quadrature channel. As an example of how severely the echo crossings affect the acquired traces, Figure 7.11(a) shows the 8 phase cycled traces obtained during the measurement on NO g_z, and Figure 7.11(b) shows the addition of all positive and all negative resolves all echo-crossing effects.

The final part of processing involves multiplying the negative detection trace by -1 to make it positive, then adding it to the positive detection trace. The resulting trace can then be processed similarly to PELDOR traces using DeerAnalysis [57].

7.6.3 RIDME experimental set up

The 5-pulse RIDME experiments on HiPER were carried out using the 5-pulse sequence as detailed in Figure 7.9(b). τ_1 was set to 400 ns, $\tau_2 = 2.4$ μs and $T_{mix} = 25$ μs. The traces were obtained by observing on field positions, $g_x = 3347$ mT, $g_y = 3350$ mT and $g_z = 3355$ mT, and using $\pi/2$ and π pulse lengths of 24 and 48 ns respectively. The sequence repetition rate was kept low due to the slow relaxation of the nitroxide at 30 K and was optimised to 100 Hz, with 70 averages taken per point. The 3rd and 4th pulses in the sequence were displaced by 8 ns per point for 126 points. This meant that each of the 8 phase cycle traces took approximately 2 minutes to obtain, thus, each trace in total took approximately 20 minutes to obtain in total. The slight delay was induced by the lack of internal programming to carry

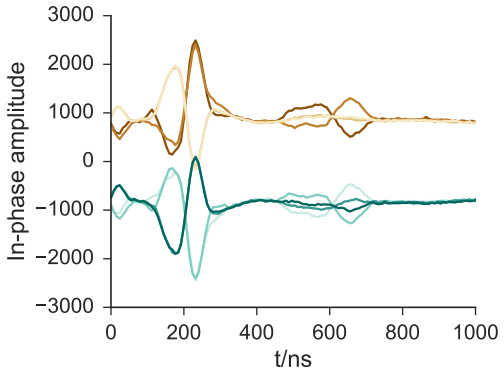

(a) 3-pulse

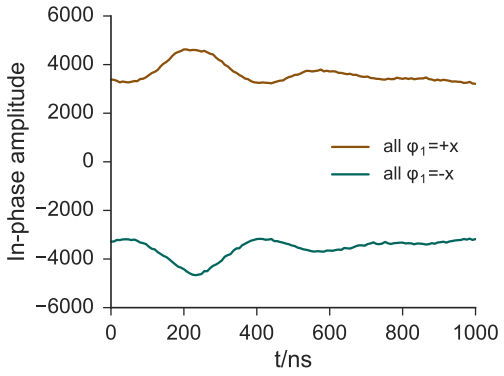

(b) 5-pulse

Figure 7.11: (a) resulting 8 traces obtained using phase cycling, with all postive detection shown in brown and negative detection shown in green, (b) sum of the respective positive and negative detection sequences, showing how phase cycling removes all spurious echo crossings.

out the phase cycling automatically, and thus the requirement for the phase to be manually selected and set for each trace.

Initially, in an attempt to optimise the signal-to-noise of the traces at such low repetition frequencies, short, hard pulse lengths of 8 ns $\pi/2$ were utilised. Unfortunately, this led to ESEEM artefacts appearing in the final traces that could not be removed by phase cycling, as shown in Figure 7.12. From the FFT of the data, it was determined that the frequency of the artefact, (∼18 MHz) corresponded to deuterium hyperfine, a rarely observed effect at W-band. Fortunately, it was possible to remove the ESEEM from the traces by using softer, longer pulses whose excitation bandwidth does not invoke ESEEM modulation effects. Figure 7.12 shows the resulting 5-pulse RIDME traces obtained on the g_y orientation of the nitroxide using 24, 32, and 48 ns π pulse lengths, and shows how the severity of the ESEEM artefact reduces with increasing pulse length until it is removed completely (48 ns π).

It should be noted that the Jeschke Group at ETH Zürich have also found this effect in their RIDME experiments at Q-band, and propose instead that the ESEEM be removed through

averaging traces [46]. This involves using a 64-step phase cycling sequence, consisting of the standard 8-step phase cycle, and a further 8 iterations where τ_1 and τ_2 are altered to average through the full oscillation period of the deuterium oscillation. This technique was not utilised in this instance largely due to the programming required to implement it.

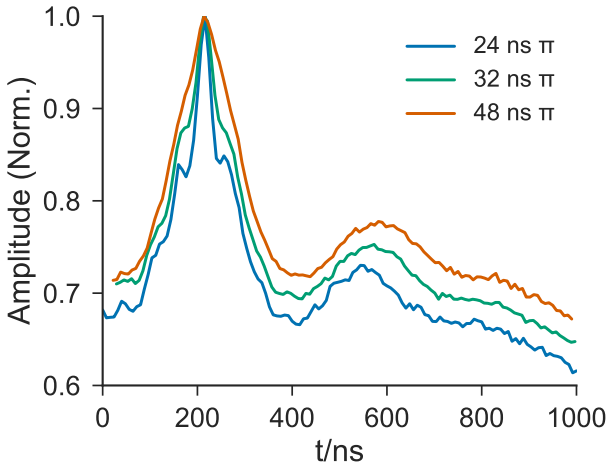

Figure 7.12: RIDME traces obtained using different pulse lengths/excitation bandwidths on g_y orientation of the nitroxide. The shorter pulse lengths result in ESEEM modulation in the traces, due to excitation of deuterium which is coupled to the nitroxide. At 48 ns π pulse length, no ESEEM is observed.

Following the ESEEM investigation, RIDME traces were obtained using the optimised pulse lengths, and the parameters as detailed previously. The data was then manually post-processed to remove echo-crossing artefacts before being processed using DeerAnalysis [57] to remove background decay and to produce the FFT of the time traces. It should be noted that DeerAnalysis cannot account for any orientation selection, thus it has not been used at this stage for any distance determination. The resulting traces are shown in Figure 7.13.

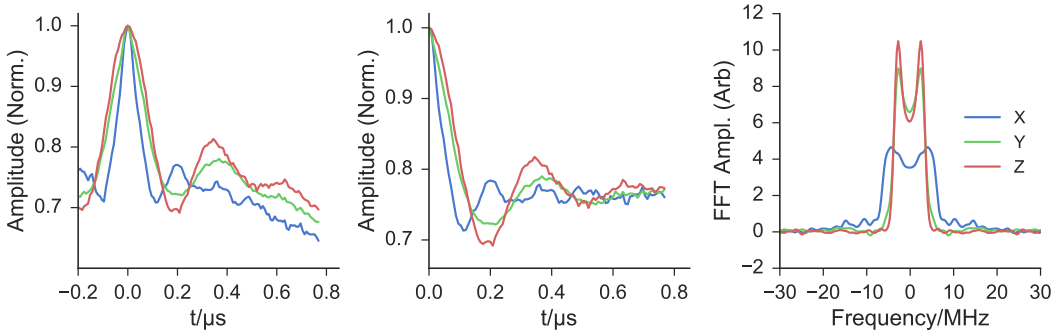

Figure 7.13: RIDME results obtained on Co(II)-Terpyridine model system, observing on the 3 orientations of the nitroxide centre. Left shows raw, normalised data, centre shows background subtracted, and right shows the FFT of the centre plot.

The osRIDME results shown in Figure 7.13, show evidence of orientation selectivity, as two different frequencies are observed across the three orientations. The g_x orientation of the nitroxide (blue) shows the double frequency $\nu_{\|}$, and both g_y and g_z (red and green) orientations show the single frequency, $\nu_{\perp}$. Following the osPELDOR analysis, this is to be expected, as it infers g_x of the nitroxide to be parallel to $\vec{r}_{AB}$ and g_y and g_z to be perpendicular to $\vec{r}_{AB}$.

The dipolar modulation effect observed during the RIDME experiment is a result of spontaneous relaxation of the Co(II) centre during T_{mix}, and the resulting dipolar effect depends on the orientation of $\vec{r}_{AB}$ and the external magnetic field, B_0. The Co(II) centre relaxation is orientation independent, and acts merely to flip of the coupled spin within the pair, resulting in dephasing of the observed echo. The NO$^{\bullet}$ allows one to choose one of the three orthogonal orientations on the nitroxyl relative to $\vec{r}_{AB}$ to observe. When observing any given orientation of the nitroxide, it is only resonant when parallel to the main field, and the dipolar modulation frequency is dependent only on the orientation of $\vec{r}_{AB}$ with respect to the main field. Thus, if the double frequency $\nu_{\|}$, is returned when observing on g_x, it infers that g_x is aligned parallel to $\vec{r}_{AB}$, It does not infer anything about the relative orientation of the Co(II) centre, as in this experiment, it acts only as a point magnetic moment, which is coupled to the nitroxide centre. The modulation depth is near identical across all 3 orientations, which, although not verified[1] indicates the T_1 relaxation of the Co(II) centre is not expected to be orientation dependent.

Previous studies on this system using osRIDME at Q-band were able to observe some difference in the dipolar modulation frequency when observing on g_x of the nitroxide, but were unable to differentiate fully between the single and double frequencies, unlike at W-band. At the time of writing, this is the first demonstration of orientation selectivity observed using RIDME. In comparison with the equivalent PELDOR measurement, RIDME was previously regarded as not strongly orientation selective, due to the observation of a more complete Pake doublet [18]. PELDOR on metal centres is inherently orientationally selective due to its broadband nature and the limited excitation of pulses, which will inevitably selective a narrow range of orientations. While RIDME removes this restriction, as no pulses directly excite the metal centre, in the case of a rigid system, orientation effects can be very severe, as observed here, leading to poor distance determination.

[1] To measure on all orientations of the Cobalt centre, it would require shifting of the magnet's main coil, which has been in a persistent (stable) closed loop state since Septemeber 2013.

7.7 Co(II)-Terpyridine: Orientation summary

In conclusion, it is evident that all three experiments are essential to determine the relative orientation of the spin centres and the molecule, through pulsed dipolar spectroscopy. While the $NO^{\bullet}$-$NO^{\bullet}$ osPELDOR was able to determine the relative orientations, and attribute flexibility in some cases of the labels to the molecular backbone ($\vec{r}_{AB}$), does not provide information on the the orientation of the metal centre to the label. The Co(II)-$NO^{\bullet}$ osPELDOR was able to attribute the relative orientation of the portion of the Co(II) (low-g) centre observed in the experiment to the orientations of the $NO^{\bullet}$ labels. However, modulation was only observed where the spin centres were collinear, with the modulation depth indicating the portions of spins present fitting this state. The RIDME experiment was able to confirm the orientation of the $NO^{\bullet}$ labels with respect to the molecular backbone, $\vec{r}_{AB}$, as the dipolar modulation was determined by the orientation of $\vec{r}_{AB}$to the external magnetic field, and had no dependency on the orientation of the metal centre.

From the experiments we are able to summarise that the Co(II)-(bis)terpyridine model system is a moderately rigid structure, and it has been verified to assume the expected structure when observed using pulsed dipolar spectroscopy techniques. The nitroxide label has a degree of flexibility due to the double linker used to attach the nitroxyl label to the terpyridine group. Previous studies [22] have shown that this flexibility leads to a mixing of XX and XY states, as the label traces out a cone of possible conformations around the linker point, which was also observed here. This is also shown through the weak modulation seen in states that should have no oscillation, such as ZX and YX.

The orientation selective PELDOR carried out between the Co(II) centre and the nitroxide label was able to attribute the relative orientation of the 'low-g' part of the Co(II) centre and the orientations of the $NO^{\bullet}$ centres. This experiment gave an unexpected result, which was not in agreement with previous studies carried out on the Co(II)-terpyridine centre with regard to the orientation of g-values of the metal centre when ligated within the terpyridine structures. The experiment showed 'low-g' Co(II) to be perpendicular to $\vec{r}_{AB}$, as given by the observed dipolar frequency, and the large modulation depth when orientations proven in other experiments to also be perpendicular to $\vec{r}_{AB}$ (Y and Z) were pumped. The experiment only showed weak single ($\nu_{\perp}$) frequency when pumping NO g_x, which was attributed to flexibility of the label, leading to some conformations where O g_x is perpendicular to $\vec{r}_{AB}$.

The RIDME experiment showed strong confirmation of the orientations of the NO$^\bullet$ with respect to $\vec{r}_{AB}$, with the Co(II) centre acting as a point magnetic moment, independent of its orientation. The dipolar coupling of the metal centre and the NO$^\bullet$ labels result in modulation of the observed echo, whose frequency of modulation is dependent on the relative orientation of $\vec{r}_{AB}$to the external field. The experiment strongly returned the double frequency ($\nu_{\|}$) when observing on NO-g_x and showed the same modulation depth, albeit with the single frequency ($\nu_{\perp}$) when observing on NO-g_y and NO-g_z. This result is expected from both sets of PELDOR measurements, which assign g_x of the nitroxide to be generally collinear with the molecular backbone (and $\vec{r}_{AB}$) and thus g_y and g_z to be perpendicular to this.

This result is particularly gratifying as it shows that orientation selective measurements can be carried out, without the requirement for observation of both sets of spins with selective pulses. Metal centres are extremely broad, and it becomes impossible to carry out orientation selective PELDOR measurements at high fields between spin labels. At the time of writing, there is no spectrometer (at fields greater than 3 T) in existence that allows for observation with offsets greater than 1 GHz (∼35 mT). As demonstrated here, this results in osPELDOR measurements that are restricted by the orientation of the metal centre which is closest to the nitroxide centre. RIDME measurements however, while independent of the orientation of the metal centre, can offer the ability to pin down the relative orientation of observed spin centre to the vector which joins the two spins. For this rigid model system, it is thus trivial to assign orientations. However, in the case of myoglobin or neuroglobin systems measured in Chapter 6, where the MTS label is much less rigid, it is expected it will be more challenging to resolve the relative orientation of the label to $\vec{r}_{AB}$. However, more rigid labels such as the bipedal Rx label [23], should provide much more favourable outcomes in terms of osRIDME.

8

Frequency and Amplitude Modulated Pulses for use in EPR experiments

This chapter will discuss preliminary work to date to implement an arbitrary waveform generator on our group's X/Q-band Bruker spectrometer. The main aim of this project is to harness the ability to use frequency and amplitude modulated pulses which offer far larger excitation bandwidths than composite pulses, to improve sensitivity, and improve flexibility of experiments on the spectrometer.

Modulated pulses have been utilised in EPR experiments since they were first reported by Spindler et al. in 2012 [35]. Since then, various EPR groups have implemented modifications to their current spectrometers set ups, or in a few cases, built entirely new spectrometers based around AWGs to use such pulses. This chapter will discuss the design plans for a dual-channel modification to bring modulated pulses to both the coherent and ELDOR channels of a X/Q-band Bruker spectrometer and an implementation on HiPER.

8.1 Designing AWG implementation for Bruker X/Q-band spectrometer

Following on from recent successes of the the Stoll Lab at University of Washington, demonstrating the feasibility of coherent shaped pulses on their similar Bruker spectrometer [63], a similar design was created for use in St Andrews. In the Stoll Lab set up, they utilised a 4.6 GSa/s Keysight arbitrary waveform generator, which was spliced in using a double-balanced IQ mixer in parallel to the current coherent channels in their Bruker spectrometer. In their paper they detail how this set up allows the user to modulate coherent pulses only, which leads to the creation of many coherence transfer pathways when using multiple pulse experiments such as PELDOR. This is avoided in standard experiments to an extent, through the use of a separate incoherent frequency source for the pump pulse. Through averaging, any coherences occurring between the pump and probe pulses are random, and thus average to zero. To overcome this coherence problem, the Stoll Lab have resorted to using 16 to 128 step phase cycling to remove imperfections from their measurements.

8.1.1 Dual channel modulation set up

In the St Andrews implementation, the plan was to utilise a dual-channel set up, with modulation provided to both the coherent (detection/observer) channel and the ELDOR oscillator for pump pulses. This will allow the user, in the case of PELDOR experiments, to modulate both the observer and pump pulses, thus utilising bandwidth enhancement and bandwidth sculpting to improve modulation depth and improve signal to noise without the requirement for lengthy phase cycling.

The implementation was to be carried out within the Bruker X-band bridge, where all pulse forming is carried out, allowing for use at both X and Q-band. The Q-band set up on our particular spectrometer, a Bruker Elexsys E580 is implemented as a separate Q-band 'bridge' which takes in the X-band pulse input and uses mixers to up-convert the pulses to the required frequencies around 33-34 GHz. For simplicity, and following common usage, we will refer to this band of frequencies used here as 'Q-band' but the reader should be aware that this is not an officially recognised frequency designation, and the correct term for this band of frequencies is 'K_a-band.'[1]

[1] Q-band is not referenced explicitly in standards held by institutions such as IEEE, thus it is inconsistently referenced in the literature, but it is commonly used to refer to frequencies between 33 and 50 GHz. In particular,

Figure 8.1 shows a schematic overview of the transmit chain of the Bruker bridge in our spectrometer. The bridge, much like HiPER uses two oscillators, one for coherent observation (source) and the other (ELDOR) for incoherent pump pulses in PELDOR experiments. On the coherent channel, phase cycling and individual pulse power levels are set using the SPFU (Standard Pulse Forming Unit) and MPFU (Microwave Pulse Forming Unit) channels. The set up allows for pulses to be directed through any of the 3 channels, controlled by the PatternJet software control. The pulses are then combined with pulses from the ELDOR source, before passing through the main pulse gate switch. For Q-band operation, the pulses are then directed to the IF out from the X-band bridge and into the Q-band bridge for subsequent up-conversion and amplification before entering the resonator. In the case of the X-band select, the pulses are directed through the amplifier and then to the resonator.

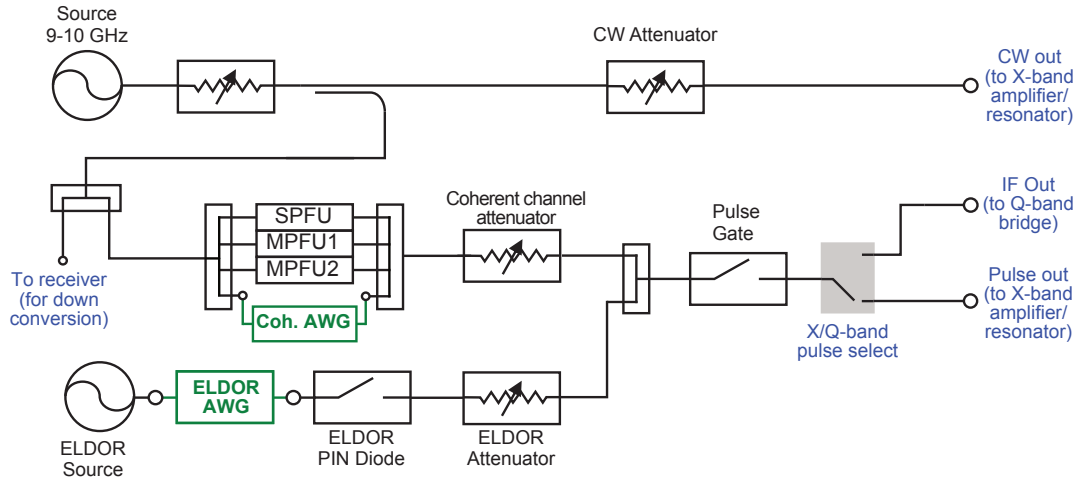

Figure 8.1: Schematic diagram of the main components of the Bruker bridge for transmit. The parts in green show where the AWG is to be inserted. The diagram has been adapted from one kindly supplied by the Stoll Lab.

To implement the AWG the plan was to develop two sets of modulation plates to accommodate the various components required to modulate the 9 GHz pulses for both channels, and to do it in such a way that the spectrometer could be operated normally, without having to open the bridge and 'unplug' components each time. The idea was to run cables from inside the box to outside, perform modulation and run cables back in, ensuring that the power levels were balanced throughout, as though the AWG did not exist. To perform this on the coherent channel, it can be placed in parallel to the current SPFU and MPFU channels in the spare slot on the 4-way splitter, ensuring that any delays for additional cable lengths is accounted for. This

Bruker uses it to refer to its spectrometer that operates around 33 GHz, whereas IEEE recognises K_a-band as frequencies between 26.5 and 40 GHz, thus both are equally applicable.

is similar to the implementation in the Stoll Lab. In the case of the ELDOR channel, there are no power splitters between the ELDOR source and where it is recombined with the coherent channel. Thus, the plan was to run cables to a pair of switches outside the box, which in their non-powered state, would just act as an extra cable length between the source and the pin switch, and in their powered-state would modulate the ELDOR source using the AWG. Both implementations require careful power level measurements between various points inside the bridge to make sure that one could compensate for any power losses due to components and lengths of cable, and ensure the power level that is returned to the system post-modulation matches that of the non-modulated power level to guard against any component damage. "Helpfully," all components in the bridge were powder-coated so to remove any identifying features or model numbers that might assist in working this out. We are grateful to the Stoll Lab who were able to provide us with a helpful schematic diagram showing all the levels on their system, which we were able to verify on our bridge using power meters[2].

The modulation plate design schematics for the coherent and ELDOR channels are shown in Figure 8.2. Both use a Marki MLIQ0416 double-balanced mixer to produce the modulated output, using the relevant Bruker source as the local oscillator (LO), with 2 channels from the AWG providing the in- and out-of-quadrature (I and Q) intermediate frequency (IF) inputs. Unlike a standard mixer which produces the LO ±IF frequencies at the RF output port, the double balanced mixer, if calibrated correctly, produces only the upper side band (USB) components (LO+IF) at the RF port, removing the requirement for filtering. This is key in this application, as the AWG operates at 1 GSa/s limiting its bandwidth to ∼400 MHz [95], thus the user often wishes to modulate around the LO frequency to maximise useful bandwidth, thus, it is difficult to use filtering without significantly diminishing the bandwidth available. The power level supplied from the splitter, and coupled with various cable losses (∼1.25 dB per m [96]) mean that significant amplification is required to produce the required drive level for the IQ mixer, which in this case is approximately 11-18 dBm. The mixer has a conversion loss of approximately 8-10 dB, such that in the case of both channels, additional attenuation is required in order to match the level back into the system.

[2]While all Bruker spectrometers that are produced are generally the same, it is wildly remarked that following upgrades by Bruker later on, each spectrometer becomes in many ways bespoke, and one can confirm, the power levels of the Bruker bridge in St Andrews did not, in any way, match that of the Bruker bridge in the Stoll Lab.

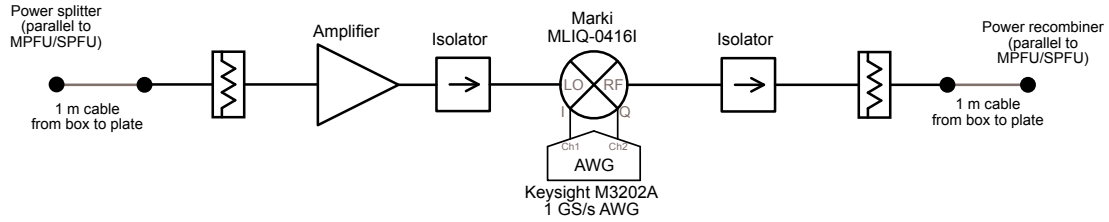

(a) Coherent channel modulation plate

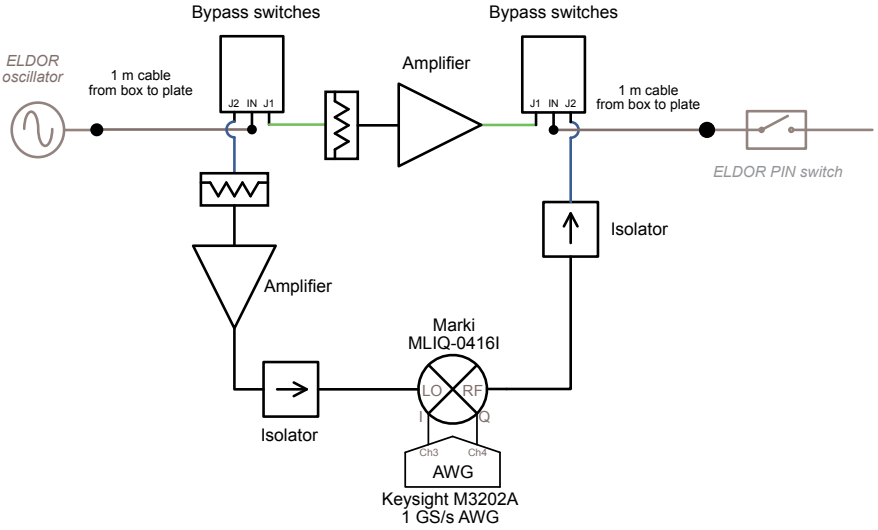

(b) ELDOR channel modulation plate

Figure 8.2: Schematic diagrams of the (a) coherent and (b) ELDOR channel modulation plates to be implemented on the Bruker. Their locations in the Bruker bridge are detailed in green in Figure 8.1.

8.2 Keysight M3202A arbitrary waveform generator: programming and control

The arbitrary waveform generator from Keysight Technologies, (model M3202A) is a 14-bit 1 GSa/s 400 MHz bandwidth, 4-channel AWG. 14-bit defines the granularity of the waveform amplitude, stating that there are 2^{14} (16,384) amplitude levels available to each channel, and 1 GSa/s specifies the rate at which amplitude can be changed, and the bandwidth capability merely specifies that it can sensibly reproduce a 400 MHz waveform before clipping due to lack of resolution occurs. The AWG was supplied in a PXIe (PCI eXtensions for Instrumentation Express) format, which requires it to be mounted inside an external PXIe rack to provide power, timing and control. Keysight also supplied said PXIe rack, interface card and PCIe host controller for connection to a desktop PC. This allowed for the AWG to be connected and controlled using extremely fast PCIe connectivity (commonly used for graphics cards), allowing for up to 8 GB/s of data transfer rates. The software and drivers also allowed for control via various programming interfaces, including LabVIEW, Python, C and MATLAB. The

latter was chosen for applications described here as it allowed for simple script-based control and data processing all within the same software environment.

Waveforms on the AWG can be specified using in the in-built function generator to produce sinusoidal, triangular or square wave output, or using the arbitrary waveform function. The former produces output based on the amplitude, DC offset, phase, and frequency requested, whereas the latter produces output based on a user uploaded wavetable specifying the amplitude as a function of time, which is normalised to the amplitude or peak voltage output requested. The arbitrary waveform function can also utilise the DC offset function, which places a offset in voltage across the entire waveform. The maximum output each channel can produce has been set as ±1.5 V (∼13 dBm), however, stable output is only guaranteed up to ±1 V (10 dBm). The arbitrary waveform function also requires the user to specify the required clock rate, which will set how fast the wave table output is applied.

This particular type of arbitrary waveform generator is also able to produce phase coherent output, meaning that any accumulated phase between channels can be removed to ensure phase coherence between them. This is essential when using double-balanced mixers, as the phase offset between the I and Q inputs must be precisely set in order to minimise leakage at other frequencies.

When running arbitrary waveforms, the AWG was programmed to produce output following a trigger signal, which was supplied from an external source. The AWG would then repeat or 'play' the specified output on each subsequent trigger until the function was terminated. This would then stop the running of the AWG, and follow a close procedure to successfully close the AWG, wipe its onboard RAM, and return it to a state awaiting the next run. This meant that it was possible to compartmentalise the running of the AWG into a simple function call, allowing integration into measurement scripts in MATLAB.

8.2.1 AWG waveform generation

Waveforms were loaded into the AWG by importing comma separated value files containing an array of normalised values that specified the voltage output for each clock point. The AWG then produces an output of the values, normalised to the amplitude specified by the user when initialising the program to run the AWG. The pulse sequences were generated using EasySpin 5.1.10 using the pulse function [62]. This allows for the user to easily generate frequency and amplitude modulated pulses by specifying the type of modulation, pulse length,

frequency sweep and clock rate parameters. The code then returns the wave table as a complex array, whose real and imaginary parts were then exported to csv files. The pulse function in EasySpin also allows the user to estimate the excitation profile of the generated pulse sequence. An example of this is shown in Figure 8.3, showing a 250 ns shaped pulse, which utilises Gaussian amplitude modulation, and frequency modulation following the so-called 'uniform Q' algorithm [97]. The pulse, in the absence of resonator profile and external component distortion is able to perfectly invert all spins over a range of 300 MHz, as requested. This was generated based on an AWG clock rate of 1 GSa/s, which sets the fundamental bandwidth resolution of the pulse. It should be noted that other shaped pulse types/pulse lengths and bandwidths may not be able to reproduce such sharp frequency cut off as seen in this case, this pulse is shown for example purposes only.

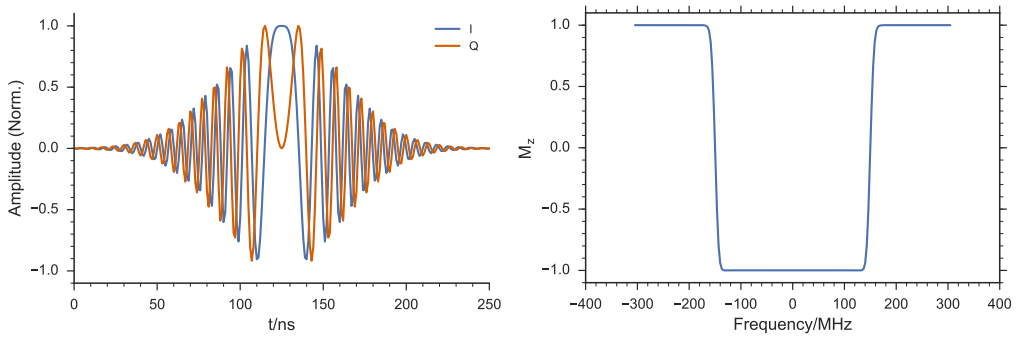

(a) Wave table **(b)** Inversion profile

Figure 8.3: (a) Plot showing the I and Q components of an amplitude and frequency modulated Gaussian/uniform Q pulse, sweeping over 300 MHz, with an overall pulse length of 250 ns. (b) Calculated inversion profile of the pulse shown in (a), showing sharp inversion edges at ±150 MHz.

8.3 Keysight M3202A arbitrary waveform generator: characterisation

In order to ensure accurate up-conversion through the mixer, it was essential to characterise the output produced by the AWG at various frequencies. To carry out these measurements (and others related to mixer calibration), equipment made available on loan from Keysight including a 13 GHz, 40 GSa/s oscilloscope (Keysight DSA91304A) and a 20 GHz signal generator (Keysight E8267A). It was possible to connect to both pieces of kit via GPIB (General Purpose Interface Bus) to control, and in the case of the oscilloscope, to retrieve measurements. This was controlled in MATLAB, which allowed for operation of all pieces of kit and subsequent analysis to be carried out using scripts.

AWG: Amplitude as a function of frequency

An initial measurement was made to characterise the amplitude variation of the output from the 4 channels as a function of frequency when producing a standard sinusoidal signal. This was carried out by changing the frequency of the output between 1 and 400 MHz, in 1 MHz steps at constant amplitude, then pausing briefly to measure the peak-to-peak amplitude of the signal on the oscilloscope. The oscilloscope then returned the peak-to-peak amplitude which was then recorded into an array, as a function of the frequency of the signal. Figure 8.4 shows the amplitude of channels 1 and 2 of the oscilloscope as a function of frequency, for a requested amplitude (V_{peak}) of 0.35 V. It shows that the amplitude is not flat over the range, and varies by up to 0.5 dB across the range. While this variation is small, it does show that the AWG is unable to produce equal output across all channels.

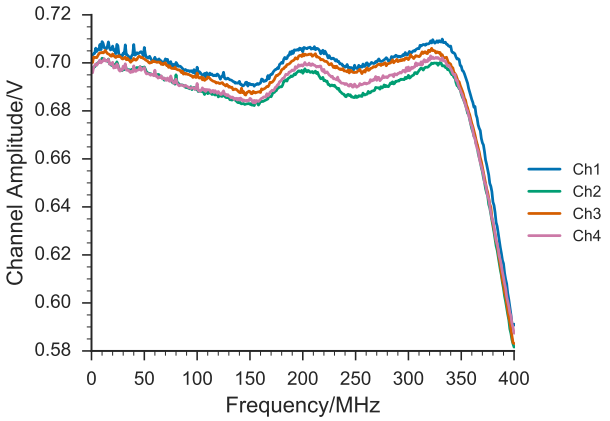

Figure 8.4: Plot showing the peak-to-peak amplitude of the output from all 4 channels of the AWG as a function of frequency. It shows that the channels differ in amplitude and it is not flat across the range, tapering off significantly at frequencies greater than 340 MHz.

To correct for this variation and to equalise the output, the amplitude of the signal has to be specified for each frequency, where its amplitude is set to a level which corrects the variation. This is calculated by normalising the trace to the largest amplitude of the pair of channels (in this case, channels 1 and 3) and taking a moving average through the points to remove any noise. The correction at each point is then double the amplitude difference between the amplitude at that point to the maximum output, thus creating a mirror image of the measured output. This is illustrated in Figure 8.5(a) for channels 1 and 2, with the corrected versions shown as dashed lines. The correction is then applied by using linear interpolation function which returns the amplitude correction factor for any specified frequency within the range. The code uses the interpolation function to find the required correction factor this and

applies this to the amplitude. The result of using the correction factor to channels 1 and 2, in comparison with the non-corrected output is shown in Figure 8.5(b). The result shows that the application of simple correction factor can effectively correct the output of the AWG as a function of frequency.

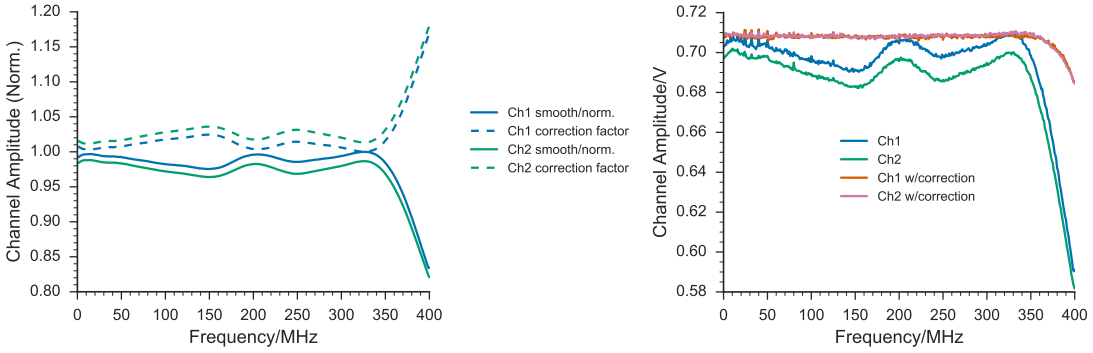

(a) Requested waveform **(b)** Measured waveform

Figure 8.5: (a) Plot showing the smoothed and normalised peak-to-peak amplitude as measured on channels 1 and 2 (solid lines) and the corresponding mirror image correction factor (dashed lines) for each channel. (b) amplitude output measured showing the before and after correction is applied to channels 1 and 2.

8.3.1 AWG frequency swept pulse correction

It was observed that the amplitude output of the AWG during a swept pulse sequence was not flat across the range, and additionally, there appeared to be phase roll off occurring, indicating that the AWG was unable to accurately reproduce the requested waveform. To correct for this, measurements of the output waveform were recorded on a fast oscilloscope (Lecroy) and compared to the ideal, or requested waveform using the transfer function estimate, (`tfestimate()`) function in MATLAB 2016a. This function estimates the relationship H_1 between the input x(t) and the output y(t), as the following,

$$H_1(f) = \frac{P_{yx}(f)}{P_{xx}(f)} \tag{8.1}$$

where $P_{xx}(f)$ is the power spectral density of the input, x and $P_{yx}(f)$ is the cross power spectral density of the input, x and the output y. The power spectral density is a discrete time Fourier transform (DTFT) of the time-domain signal, and the cross power spectral density is a DTFT of the convolution of the two signals [98]. The transfer function estimate function in MATLAB carries out the relevant DTFT calculations using Welch's periodogram method [99] to compare the input and output signals from the AWG in the frequency domain, returning

the difference between the two. In this method, windowing is used to average across the waveform, and identify its amplitude variation as a function of frequency. By inputting both channels input, representing the real and imaginary (or 90° phase shifted) parts of the waveform as a complex array of values, it is also possible to recover the phase variation as a function of frequency. The algorithm used to process the data here was adapted from one created by Dr Johannes Mckay at NHMFL Tallahassee, Florida, to account for similar roll off observed on their AWG.

The algorithm works as follows:

- Load in waveform recorded on fast oscilloscope, user selects the location of the start of waveform and exports it to the workspace as a variable.

- User indicates type, length and frequency sweep parameters of the waveform uploaded to the AWG. Algorithm generates over-sampled version of the waveform sampled at the clock rate of the oscilloscope (20 GSa/s) and a version sampled at the clock rate of the AWG (1 GSa/s).

- The code uses minimisation based on the start of the waveform variable to find the start of the waveform, then it uses interpolation at the sample rate of the oscilloscope to export the correct length of waveform, discarding parts of the trace that are not the waveform itself. It repeats this for the imaginary waveform.

- The transfer function then takes the complex (I +iQ) total of the over-sampled ideal waveform as input, and uses the complex (I +iQ) total as the output. The windowing level is set to ensure good overlap of the samples, to ensure good resolution of the frequency components. The transfer function returns the complex transfer function Txy over the frequency range, W.

- Transfer function correction is then applied by down-sampling both the transfer function and the measured waveform, so it matches the sample rate of the AWG (which is significantly slower than the oscilloscope). This is carried out by interpolating the frequency-shifted Txy over the range of frequencies corresponding to the sample rate of the AWG (i.e. ± 1 GSa $s^{-1}/2$). The Fourier transform of the down-sampled interpolated measured signal is then divided by the interpolated transfer function, creating the corrected signal.

- The corrected signal is then returned to the time-domain by means of inverse Fourier transform, producing the real and imaginary parts of the waveform.
- The waveform is then normalised and exported to the relevant file format for re-loading onto the AWG

To show this in practice, a rectangular/linear, fixed amplitude linear frequency swept pulse, sweeping from -100 MHz to +100 MHz in a linear fashion, over 7 μs was uploaded to the AWG, producing the real components on channel 1, and the imaginary on channel 2. The resulting output was recorded (in this case) on the LeCroy Wavemaster 8620A 20 GSa/s, 6 GHz analogue bandwidth, real time oscilloscope. The original waveform and the resulting output as measured by the oscilloscope are shown in Figure 8.6.

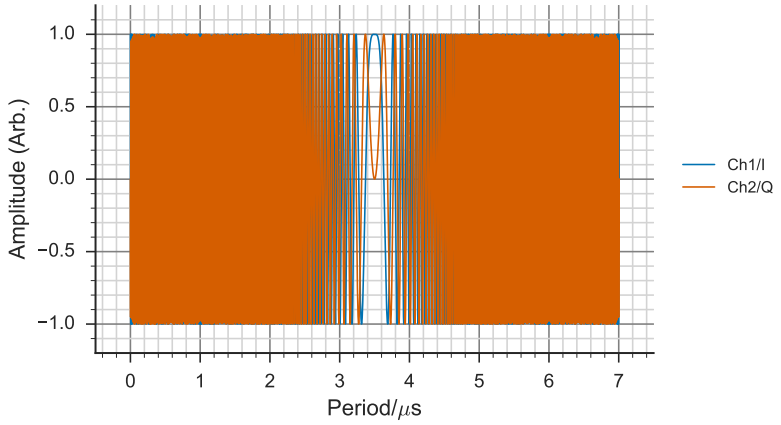

(a) Requested waveform

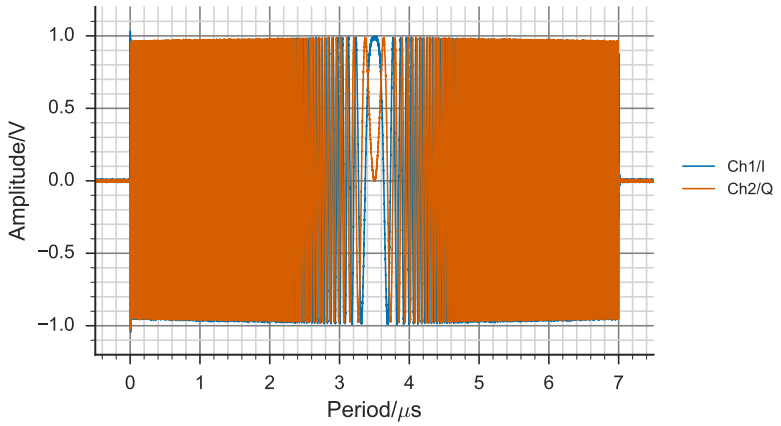

(b) Measured waveform

Figure 8.6: Plots showing (a) requested waveform and (b) the resulting output from the Keysight M3202A arbitrary waveform generator for a frequency sweep from -100 to 100 MHz. The resulting waveform shows the effects of amplitude roll-off as it goes through the highest frequency parts.

The resulting output shows slight amplitude compression at the edges of the waveform,

where it is producing the largest frequency components. This indicates that its pulse behaviour appears to be repeating that of the continuous-wave output as a function of frequency, which showed a similar decline in amplitude over this range.

The transfer function algorithm was applied to the output from the AWG, and Figure 8.7(a) shows the channel 1/I measured output on top of the expected output. Figure 8.7(b) shows a zoomed portion of the waveform, illustrating the phase roll off that also occurs.

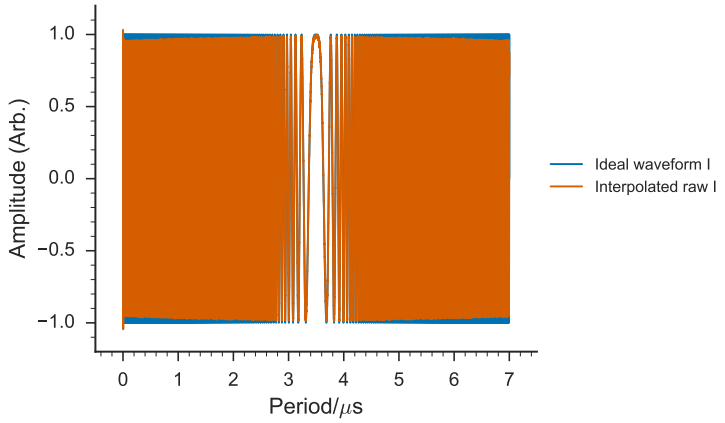

(a) Measured versus ideal I

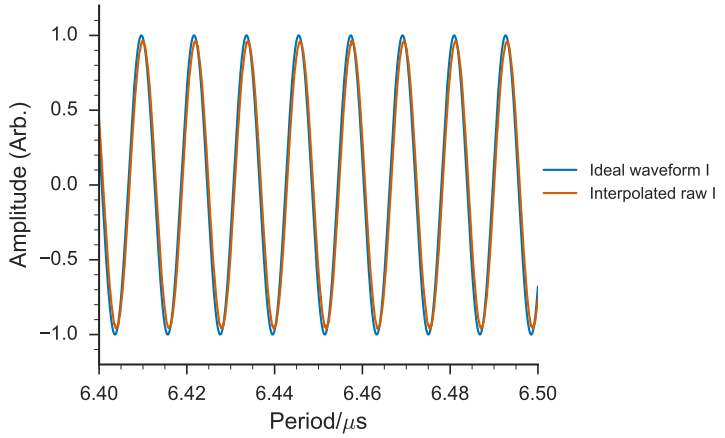

(b) Zoomed

Figure 8.7: (a) showing the comparison of the real components of the waveform, as measured from Ch1 of the AWG, in comparison with the ideal case, showing the effect of amplitude roll off, (b) zoomed part, showing the difference in phase between ideal and measured waveforms between 6.42 and 6.43 μs due to phase roll off of the pulse.

The magnitude and phase of the waveform as measured by the transfer function estimate algorithm are shown in Figure 8.8. The magnitude plot shows that the amplitude shows a linear increase as the frequency goes from -100 MHz to zero, and a similarly symmetric decrease as the frequency increases from zero to +100 MHz, up to 0.5 dB of difference. The phase

follows an inverted parabolic trend, centred on zero frequency, with deviations in phase up to ∼12-14°.

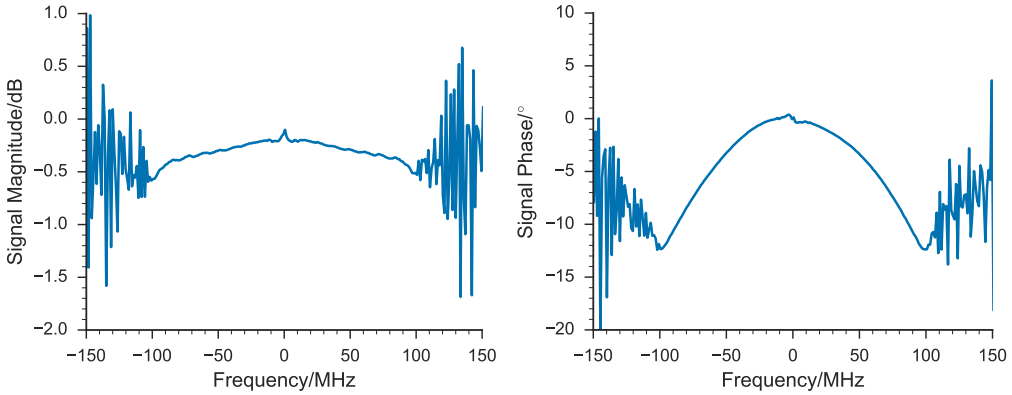

(a) Transfer function magnitude **(b)** Transfer function phase

Figure 8.8: (a) and (b) the magnitude and phase of the raw output of the the waveform from the AWG, as measured by the transfer function estimate algorithm.

Using the transfer function, a corrected version of the waveform was produced as shown in Figure 8.9. The waveform shows the opposite trend in amplitude roll off to that of the measured waveform, the idea being that by reducing the parts providing maximal amplitude and increasing those that provide reduced amplitude, the result should be a flat waveform. The corrected waveform was then uploaded to the AWG and its output recorded. The resulting output is shown in Figure 8.10. The corrected measured waveform in comparison with the initial non-corrected waveform (Figure 8.6(b)) shows a much more uniform amplitude across the pulse.

To check the performance of the corrected waveform, its transfer function was also determined in comparison with the ideal pulse. The results in comparison with the non-corrected versions are shown in Figure 8.11, with the corrected transfer functions shown in green. The corrected versions show flat magnitude and phase across the bandwidth of the pulse, indicating that the application of the transfer function estimate is able to rectify phase and amplitude roll off on the output of the AWG.

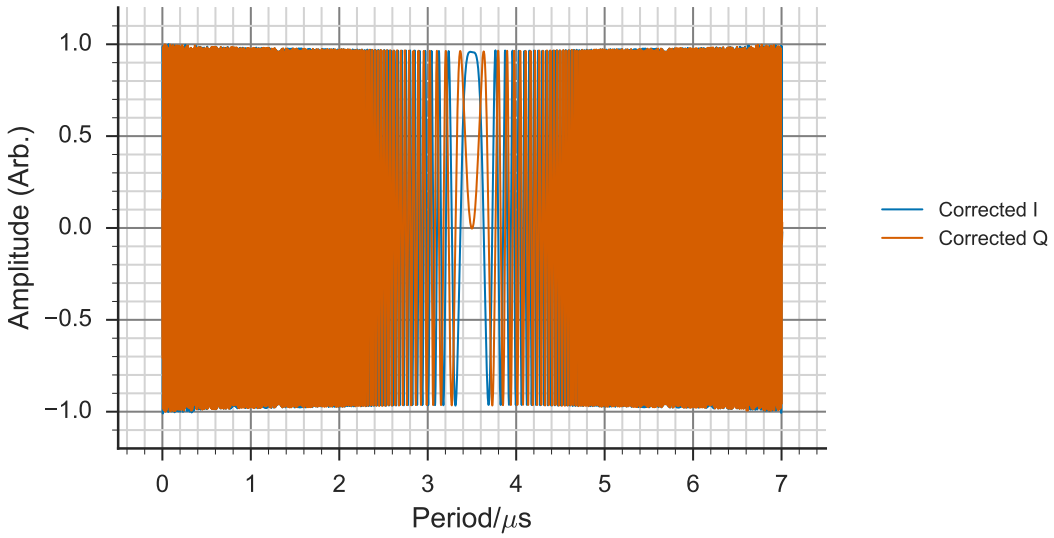

Figure 8.9: Plot showing the resulting waveform uploaded to the AWG after transfer function estimate was applied.

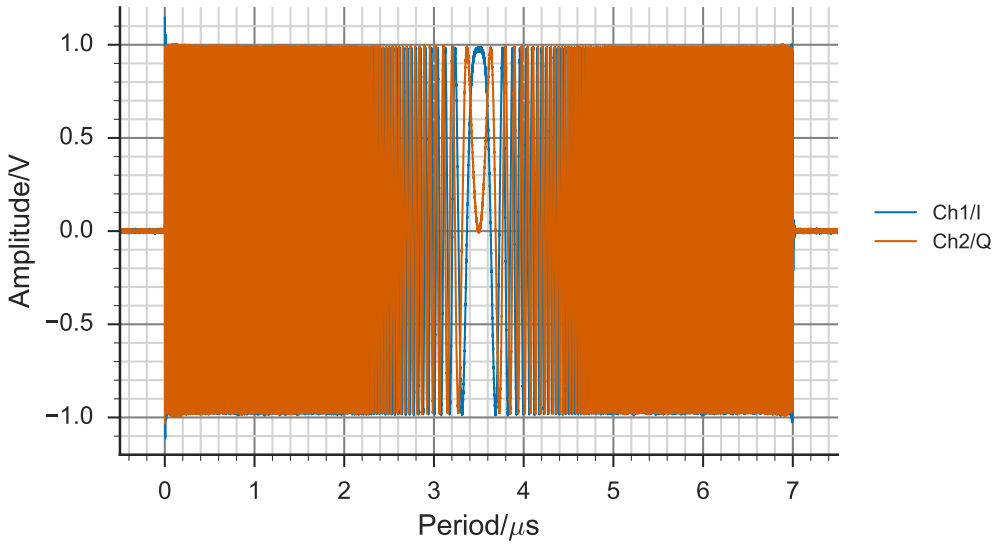

Figure 8.10: Plot showing the resulting waveform uploaded to the AWG after transfer function estimate was applied.

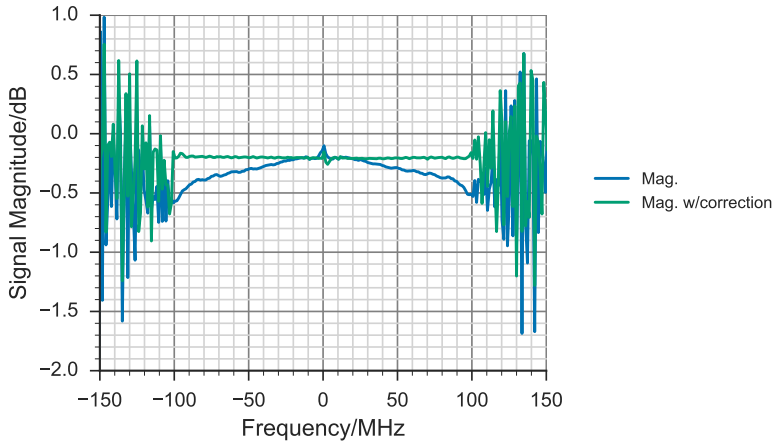

(a) Transfer function magnitude

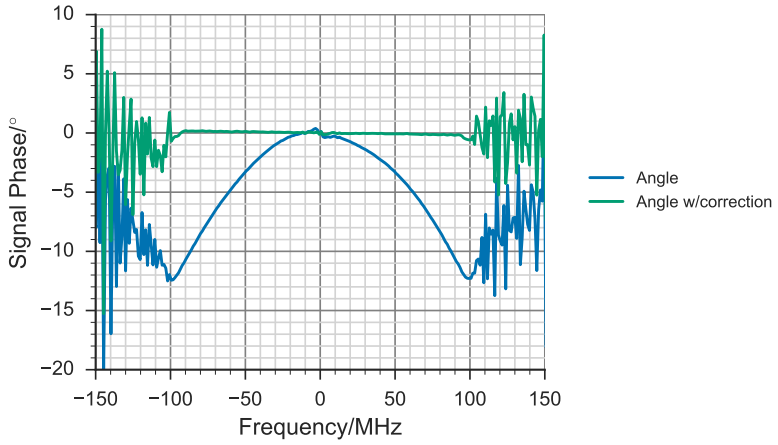

(b) Transfer function phase

Figure 8.11: Plots showing the (a) magnitude and (b) phase as a function of frequency before (blue) and after (green) application of the correction. It shows that transfer function estimate works well to remove amplitude and phase roll-off in the output from the AWG.

8.4 Mixer characterisation

While double-balanced mixers are useful for up-conversion without the requirement for filtering, they require careful calibration to ensure leakage of unwanted signals is kept to a minimum. There are three main problems when working with IQ mixers: amplitude imbalance between the two IF inputs, phase between channels is not 90° and LO leakage through the RF port occurring when no voltage is applied, or incorrect level of voltage is applied. Kaufmann et al. [36] detail procedures to calculate amplitude, phase and DC offset corrections required to sufficient suppression of the LO and lower side-band signals.

In their set up, they were able to acquire the output from their mixer, using a sampling oscilloscope which allows one to observe repetitive signals at very high sampling rates, i.e. ∼10 GHz modulated signal from the mixer. The IQ inputs to their mixer were supplied using two 1 GHz DAC board, which operate similarly to arbitrary waveform generators. Their boards were also able to supply triggering at the resolution of the clock rate (i.e 1 GSa/s) of the board, which could be supplied to the sampling oscilloscope to measure the output. This allowed them to stroboscopically reconstruct the amplitude and phase of the mixer output, and compare to the input. They could then use fitting procedures to work out the required amplitude, phase and DC offset required to produce the required output.

An attempt was made to carry this out in St Andrews. However it was not possible to make the AWG, the signal generator, trigger source for the AWG and the trigger source for the oscilloscope phase coherent, despite using a common 10 MHz reference on all devices. This resulted in ∼120 ps measurement jitter on the edge of the pulse when measured on the oscilloscope. This meant that the phase could not be reconstructed accurately between runs. Instead, an attempt was made to carry out the correction using the transfer function calibration procedure to correct for phase and amplitude errors. The DC offset was corrected for by iterating through small DC offsets while monitoring the LO leakage on a spectrum analyser. Both methods will be described in this section.

8.4.1 DC offset correction

To compensate for LO leakage, the correct DC offset must be applied to each of the IQ inputs to the mixer, as a function of LO frequency. This can be carried out by applying LO drive to the mixer, while monitoring the RF output on a spectrum analyser, which displays a Fourier

transform of the signal applied to its input, and thus provides the relative magnitude of the signal as a function of frequency. The LO level is then monitored as small DC voltages are applied to both the I and Q ports of the mixer by setting the levels on the AWG. This was carried out by connecting the spectrum analyser (HP 8593A) via GPIB, and using commands to retrieve the LO peak magnitude as a function of LO frequency and of DC offset levels.

A script was created in MATLAB which first sets the required LO frequency from the signal generator, then initialises the AWG to produce the required I and Q DC offset voltage, before reading the LO leakage level on the spectrum analyser, and storing this in an array. The script then iterates through creating a 2D array of LO leakage levels as a function of I and Q DC voltage levels. This was initially carried out using DC offsets between ±0.015 V on each channel, in steps of 0.002 V for LO frequencies between 9.6 and 10 GHz, which indicated that the majority of minimum LO leakage levels could be found in the top left quadrant, with I offsets between 0 and 0.015 V, and Q offsets between -0.015 and 0 V. The script was then re-run using the smallest DC voltage resolution available (0.001 V) over this reduced range. The LO frequency was stepped in 10 MHz steps, with said LO leakage array produced at each LO frequency. Figure 8.12 shows a contour plot of the LO leakage at 9.61 GHz as a function of DC offset. It shows a minimum at DC I= 0.005 V and DC Q = -0.007 V, which produced the lowest smallest LO leakage over the range of -58.6 dBm[3] which is approximately 22 dB smaller than the 0 V leakage level. Thus, a small variation in the offset level can render a large reduction in the LO leakage. Figure 8.13 shows the minimum DC offset voltages found as a function of LO drive frequency. The top left plot suggests there is some periodicity to the offset required as a function of frequency, however the measurement is limited by granularity of the possible DC offset levels allowed and the step size of the measurement.

[3] Levels quoted here can only be trusted relative to other LO leakage levels given and not absolutely, as the spectrum analyser used here was last calibrated when the author started primary school (1995).

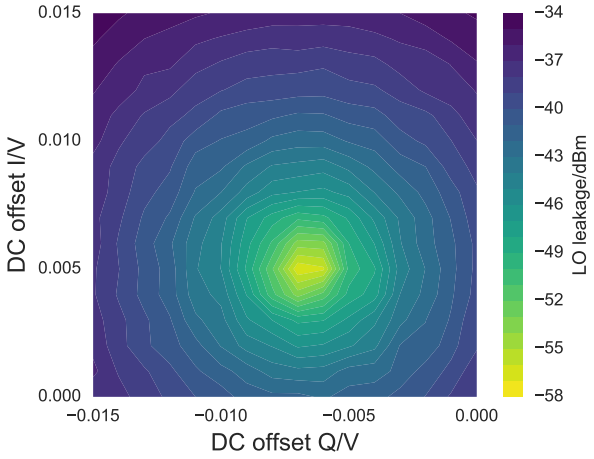

Figure 8.12: Contour plot showing the level of LO leakage through the mixer at 9.61 GHz as a function of I and Q DC offset voltage.

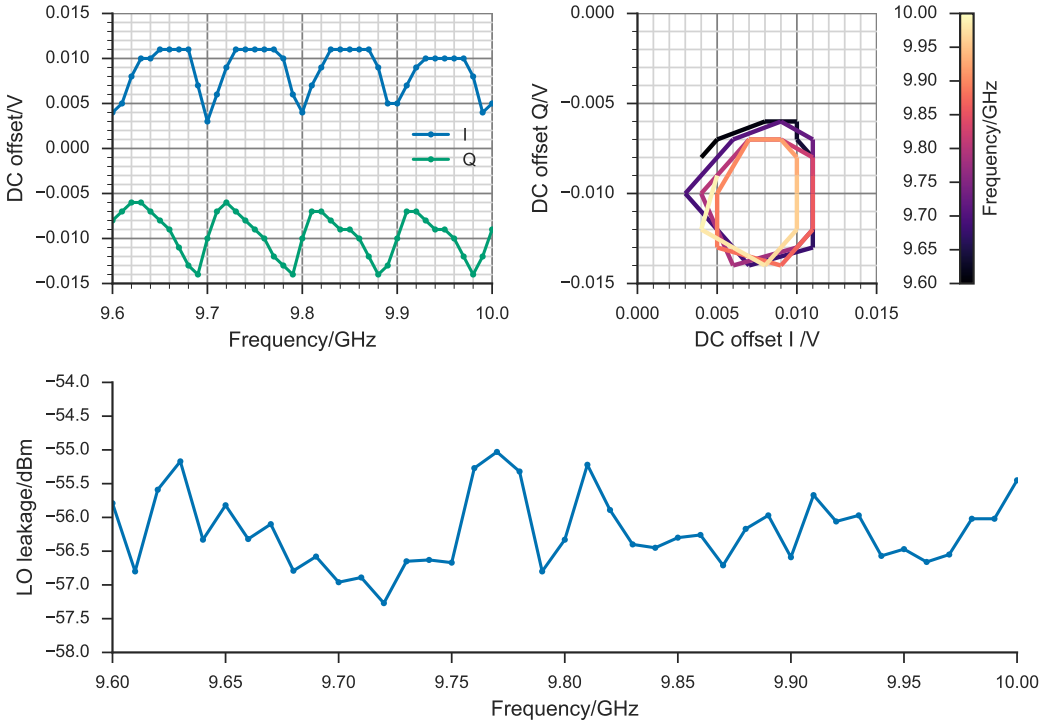

Figure 8.13: (top left) DC offset voltages for I and Q producing minimum LO leakage as a function of LO frequency (top right) DC offset I vs DC offset Q, (bottom) Resulting LO leakage level using the optimum DC offset parameters found as a function of LO frequency.

Following the measurement, the resulting optimised DC offset levels for the I and Q channels were used in an interpolation function to calculate the approximate offset as a function of LO frequency, to thus, work out the optimal DC offset for any specified frequency between 9.6 and 10 GHz. This was utilised similarly to the amplitude correction interpolation function

discussed in Section 8.3, so that the script can find out the correct DC offset to use. This was tested using a range of LO frequencies not previously tested, and showed excellent suppression of the LO. It was also tested in conjunction with the amplitude correction function for sinusoidal waveforms, where, with some minor tweaks to the phase between the channels, it was able to produce up to 50 dB of isolation between the upper side band and the LO.

8.4.2 Up-converted waveform transfer function compensation

While the 40 GSa/s fast oscilloscope can measure the 9 GHz modulated output from the mixer, it is not possible to utilise averaging to reduce noise due to jitter on the pulse, which caused instability in the oscilloscope triggering function. This caused spurious modulation to be observed in the middle of the chirp envelope, thus making it unsuitable for measurement purposes. However, it was possible to record single shot waveforms, which can be de-noised using filtering. The idea was to record the up-converted output, which consists of the LO + IF signal, then down-convert it to remove the LO signal, thus recovering the IF, which can be processed using the transfer function estimate method described earlier to perform the required correction. The down-conversion of the waveform can be performed easily using the `rfmixer()` function included in EasySpin 5.1.8.

To demonstrate this, a rectangular/linear fixed amplitude frequency swept pulse was generated and uploaded to the AWG. This pulse sequence was 4 μs long, and swept from -200 MHz to +200 MHz in a linear fashion, with a fixed amplitude. The real and imaginary parts of the waveform were used as the IQ inputs to the mixer. The LO was set to 9.96 GHz, and output from the mixer was recorded on the oscilloscope. Single shot events were uploaded to MATLAB for processing. The resulting waveform and its FFT are shown in Figure 8.14.

The raw output plot (Figure 8.14(a)) shows some distortion and variation of the amplitude across the pulse, which is broadly periodic in nature. It was observed that changing the LO drive frequency, the distortion would similarly change, suggesting that it is a beating effect occurring inside the mixer due to non-linearities. The FFT shows a large peak at zero frequency from the DC level signal, and main peaks around ± 10 GHz, which are approximately the width of the pulse, ±200 MHz, and it also shows some noise outside of these regions. The raw signal was then down-converted using `rfmixer()` function in EasySpin to remove the 9.96 GHz components, and return the modulated signal at base band. The result of this, and its corresponding FFT are shown in Figure 8.15.

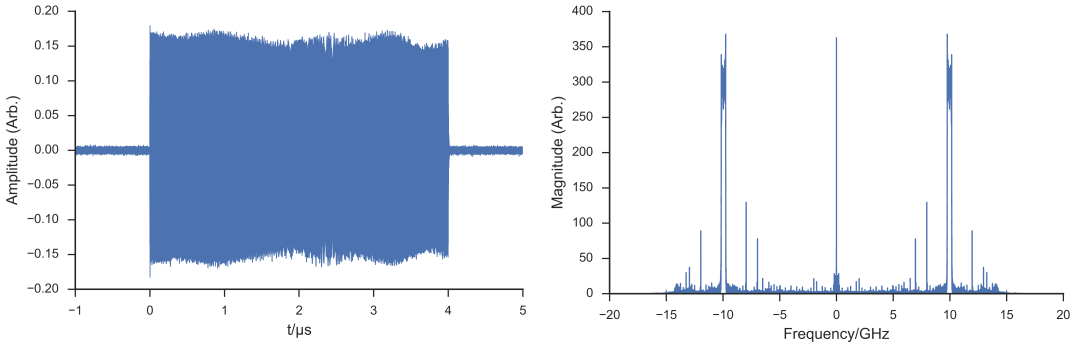

(a) Raw output **(b)** FFT

Figure 8.14: (a) Raw output from Marki MLIQ0416 mixer as measured on the oscilloscope, for a 4 μs ±200 MHz linear fixed amplitude frequency swept pulse, upconverted using a 9.96 GHz LO drive, (b) a frequency shifted FFT of (a)

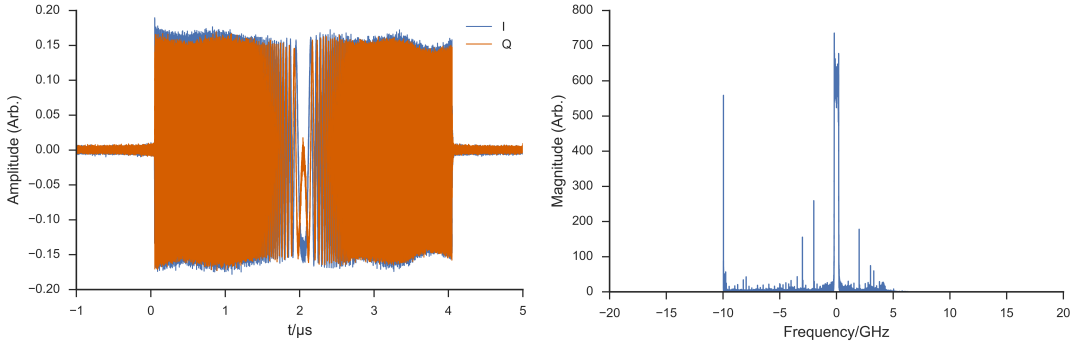

(a) Down-converted raw output **(b)** FFT

Figure 8.15: (a) Down-converted mixer output (b) FFT of the down-converted signal

The time-domain version of the down-converted signal (Figure 8.15(a)) shows what looks like a noisy version of the ideal signal. The FFT of the down-converted signal (Figure 8.15(b)) shows a large spike at -10 GHz, and the same clustering of noise outside of the ±200 MHz sweep width, which is now centred around the zero frequency. It is not possible to use this noisy version to recover the transfer function through the mixer, so filtering methods were deployed to remove all signal outside of the main envelope in an attempt to de-noise the down-converted signal. This was carried out in MATLAB using the `filtfilt` function, which is available in the Signal Processing Toolbox. It was utilised as it is a so-called zero-phase filtering method, which analyses the data in the both the forward and reverse directions, to not cause any phase distortion when filtering. This is essential, as the transfer function will estimate both the phase and magnitude of the pulse to provide corrections. For the ±200 MHz frequency sweep, the width of the filter was set to 500 MHz, so to not adversely clip or

distort the signal. The results of applying this filter to the down-converted waveform and the corresponding FFT are shown in Figure 8.16.

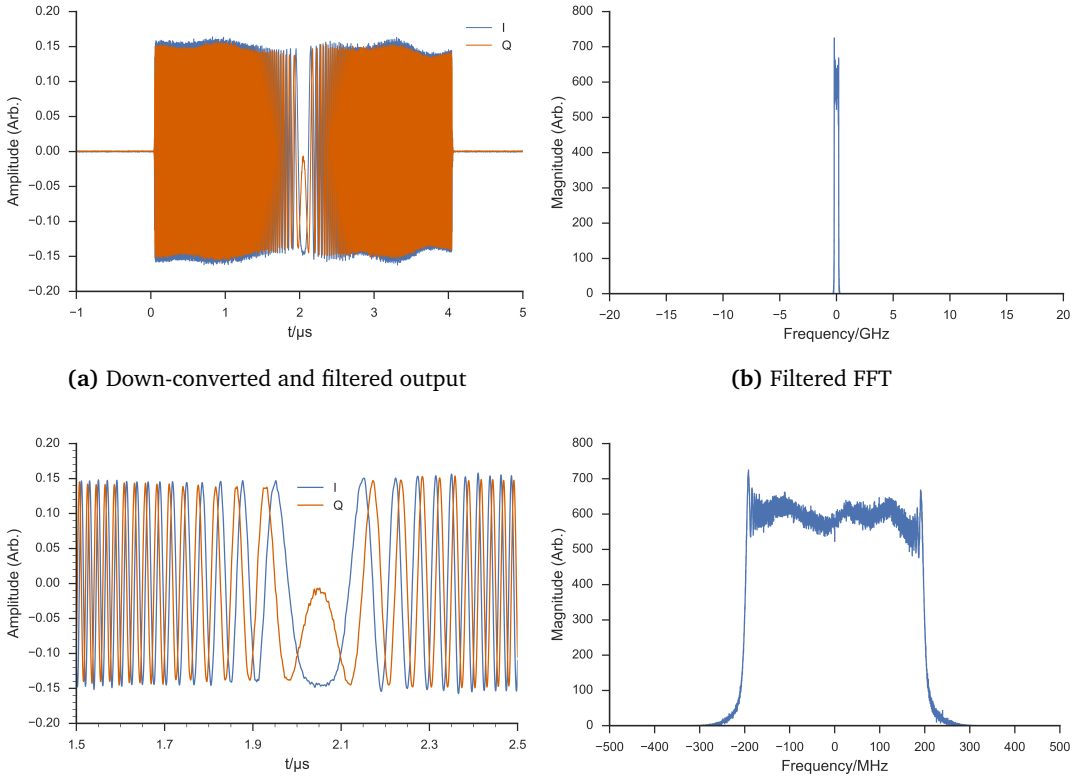

(a) Down-converted and filtered output

(b) Filtered FFT

(c) Down-converted and filtered output

(d) Filtered FFT

Figure 8.16: (a) Down-converted mixer and filtered output (b) FFT of the down-converted filtered signal, (c) and (d) show the centre of plots (a) and (b)

The figure shows a cleaned up version of the down-converted version that is shown in Figure 8.16(a), showing most of the noise is a result of frequencies outside of the main carrier. The de-noising is shown best in the zoomed in version of the time domain plot (Fig 8.16(c)) showing the centre of the waveform, with little noise present. The time-domain plot of the filtered signal shows the same amplitude variations as the pre-filtered version, and the same phase relationship between the I and Q parts, i.e. both show I to be negative in the middle of the pulse, indicating that the filtering process has not adversely distorted the signal. The baseband signal resembles the initial waveform uploaded to the AWG, albeit with beating-style magnitude distortion and significant phase distortion. The amplitude variation as a function of frequency over the waveform is shown in the zoomed FFT plot. However, the resulting post-filtered time-domain signal is now in a state that it can be analysed using the same transfer function algorithm that was utilised to correct for distortions in the output from the AWG. The

transfer function estimate magnitude and phase for the mixer output waveform are shown in Figure 8.17.

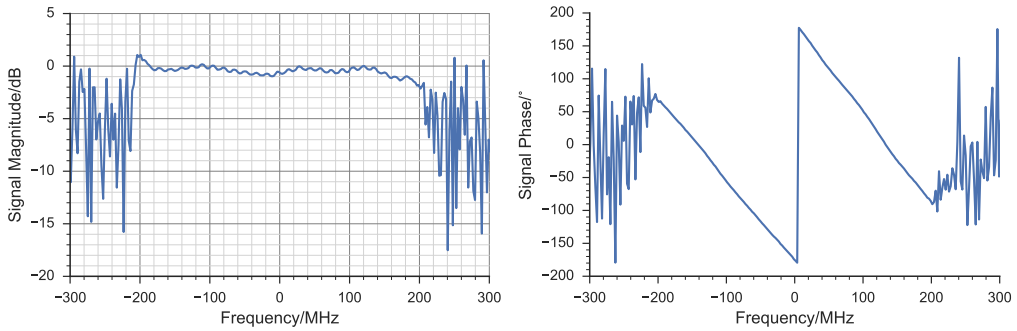

(a) Transfer function magnitude **(b)** Transfer function phase

Figure 8.17: (a) and (b) the magnitude and phase of the filtered and down-converted output from the mixer, as measured by the transfer function estimate algorithm.

The transfer function shows a 3 dB variation in amplitude across the pulse at the extreme band edges, which is approximately a 30% variation in overall amplitude. This would mean that if this pulse was used on a sample in a non-resonant cavity, in the absence of B_1 inhomogeneity, parts excited at -200 MHz would see a B_1 field which is enhanced in strength, leading most likely, depending on nominal B_1 field, to over-rotation of the spins, whereas those at +200 MHz would see a weaker B_1 field, leading to under-rotation. Thus, without correction, this frequency swept pulse has created B_1 inhomogeneity as a function of sweep width. More worryingly, are the huge phase distortions occurring during the pulse, with up to ±180° changes. Initially, this could be put down to distortions arising from the down-conversion and filtering processes, however, the method was initially tested on an ideal waveform, which was up-converted and down-converted in EasySpin, before being subjected to the filtering process and no adverse phase distortions were observed. There were significant phase distortions observed when using a non zero-phase filter, such as butter() in MATLAB, which imposed a parabolic phase shape to the signal during filtering.

The transfer function estimate was also used to generate the corrected waveform to see if it can correct for distortions through the mixer. The waveform generated and subsequently used is shown in Figure 8.18.

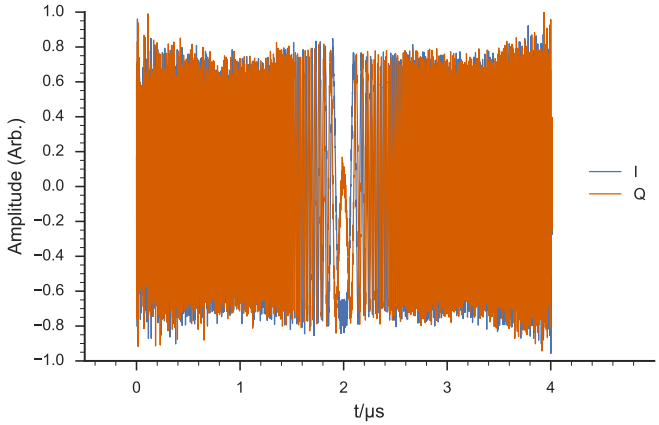

Figure 8.18: Corrected waveform produced using the transfer function estimate algorithm to correct for distortion of the signal through the mixer.

The waveform generated is noisy, which is a result of the noise on the transfer function estimate, which is down-sampled using interpolation to 1 GSa/s to match the clock rate of the AWG, in order to apply the correction to the waveform out of the AWG. The noise could perhaps be improved by employing a Gaussian filter to the waveform, as Kaufmann et al. [36] indicated, but this was not carried out here. The resulting output from the mixer using this corrected waveform as the I and Q input at the same LO frequency is shown in Figure 8.19.

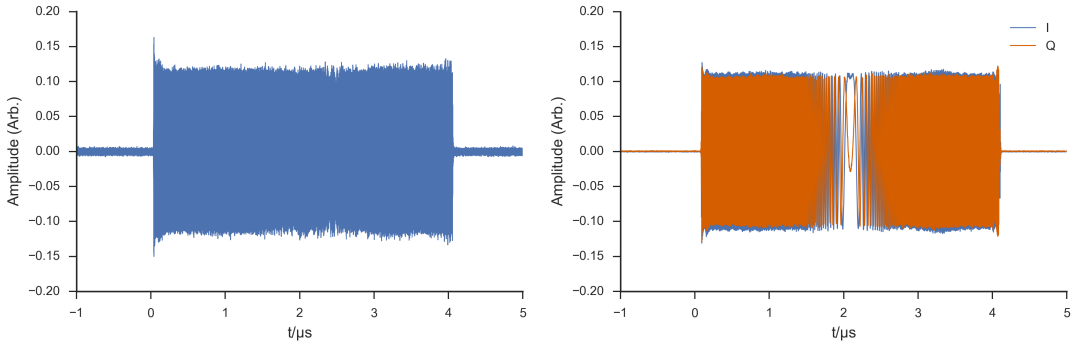

(a) Raw output **(b)** down-converted and filtered

Figure 8.19: (a) Raw output from Marki MLIQ0416 mixer as measured on the oscilloscope, using the corrected waveform, (b)a down-converted and filtered version of (a)

The raw output from the mixer created using the corrected version of the waveform is relatively flat and consistent across the waveform, in contrast to the initial recorded waveform, with no correction applied shown in Figure 8.14(a). The waveform was similarly down-converted and filtered, the result of which is shown in Figure 8.19(b). It also shows that the phase has also benefited from the correction, as the centre of the pulse, as it goes through

zero frequency shows a maximum on I and a minimum on Q, reproducing the ideal waveform. It still shows a slight difference in magnitude between the two channels, but this is probably due to the fact that channel 2's output is generally smaller than channel 1, as was discovered during the amplitude correction testing in section balh.

The down-converted and filtered waveform was also analysed using the transfer function magnitude to examine how the amplitude and phase varies across the pulse. This is shown in Figure 8.20.

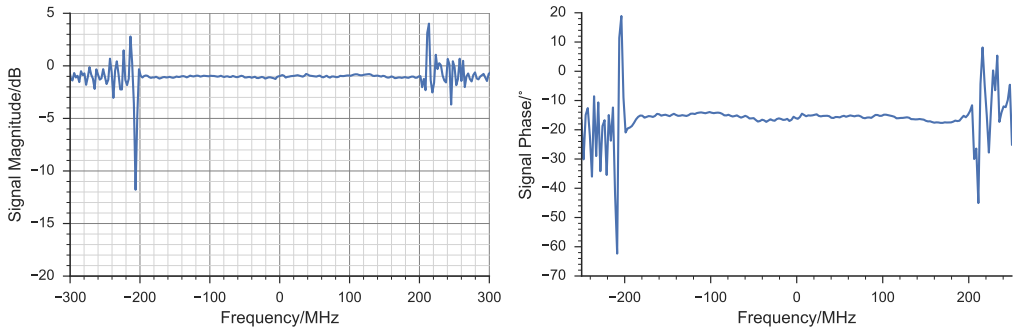

(a) Transfer function magnitude **(b)** Transfer function phase

Figure 8.20: (a) and (b) the magnitude and phase of the filtered and down-converted output from the mixer using the corrected waveform input, as measured by the transfer function estimate algorithm.

The transfer function estimate shows that the magnitude is broadly flat across the pulse, less than 0.5 dB variation, a huge improvement on the 3 dB variation observed in the pre-correction measurement. It is however 1 dB smaller in magnitude when compared to the ideal pulse, which can be attributed to normalisation of the pulse envelope which is distorted slightly by the large spike at the start of the pulse, as shown on the raw RF out measured from the mixer (Fig. 8.19(a)). The spike is most likely due to noise and ringing as the waveform starts, and mixer switches on. One might hope that more filtering of the waveform after the correction is applied might be able to reduce this slightly. The phase variation over the pulse is also greatly improved with the large phase spike observed in the transfer function estimate of the first waveform has been completely removed in the corrected version. The plot of phase as a function of frequency shown in Figure 8.20(b) shows a broadly flat phase over the pulse, with up to 4° variation. The phase however is not centred around zero, but around -16° suggesting that there is still an amount of distortion occurring, whether through correction or measurement. Flatness of the phase over the pulse is encouraging, showing that the correction, in spite of its noisy appearance does work.

Overall, the transfer function estimate method applied to the output from the mixer has shown that it is possible to correct for distortions caused by up-conversion through the mixer. However, experiments have shown that the distortions are both IF and LO frequency dependent, meaning that in order to provide compensation for all pulses through the mixer, one requires all pulses to be calibrated, and for all LO frequencies required. Alternatively, one needs to be able to predict the distortion that will occur for a particular frequency sweep width and predict the LO distortion that will occur, so that any user generated waveform can be calibrated appropriately to correct the distortion. This will also require to be completed for both mixers as planned for use in the system, as no two mixers are perfectly identical. The distortion may also vary with drive levels supplied to both the LO and the IF port, meaning exact calibration for a range of inputs will also be required, and calibration for the specific pairing of channels used also, as not all channels produce identical output levels when identical levels are requested.

Before the oscilloscope was returned to Keysight, 7 GB of waveforms, spanning various LO frequencies, frequency sweep widths and pulse lengths were obtained in an attempt to map the distortion and produce correction algorithms. Unfortunately, due to time constraints this work was not completed as part of this thesis. However, it does reflect many months of careful work that should hopefully pave a way forward for completion of this project.

9

Conclusion

This thesis has focused on methodologies to improve the sensitivity of pulsed dipolar spectroscopy experiments in EPR, using experimental protocols and pulse techniques. This has been conducted using the home-built 94 GHz spectrometer, HiPER, exploring the caveats, constraints and merits of using high field EPR for sensitive measurements. One of the main advantages of the HiPER system is its novel use of a non-resonant sample holder, removing the restrictions imposed by a frequency-limiting resonator, which allows for broadband excitation of samples, whose only limitation is the bandwidth of the amplifier (∼800 MHz). This has the advantage also of increasing the sample volume, and thus the number of spins measured during any given experiment. The main caveat to this set up however, was not amplifier bandwidth, but the applied field (B_1) inhomogeneity that was induced by the non-resonant shorted cylindrical waveguide sample holder set up. Inhomogeneity was a problem also faced by EPR's nuclear counterpart, NMR, and where pulse sequences called composite pulses were proposed to correct for this. By using discrete phase modulation, it is possible to compensate for the effects of amplitude variances across the sample. Until this point, composite pulses have had little reported use in EPR, but their benefits in improving signal-to-noise in experiments

conducted on HiPER have been considerable.

The theoretical maximum enhancement that can be provided by composite pulses on HiPER was explored extensively by modelling the B_1 profile inside the sample. This was then used in a simulation of the echo profiles of simple Hahn echoes using standard rectangular pulses as well as composite pulses, and the resulting echo profiles for refocused Hahn echoes, where the ubiquity for use in 4-pulse PELDOR experiments is much more relevant. It was interesting to investigate signal-to-noise optimisation as a function of maximum amplitude, to discover that the echo area 'sweet spot' differs from that of the maximum echo amplitude. It was also interesting to extend this to refocused echoes to discover where the maximum enhancement can be found when using composite pulses. It points to the idea that this could be implemented as an optimisation routine when running experiments in the future, to ensure the optimal echo area is measured to improve signal-to-noise as a function of pulse amplitude. The study also provided the means to investigate the effects of composite pulses in the case of homogeneous B_1 profiles, to answer the question often posed by anyone in EPR when you talk to them about composite pulses: *'yes, but what enhancement can I expect on my Bruker spectrometer?'* The simulations in this case indicated that up to 2.4 times enhancement in echo amplitude is possible when observing broad line systems. The simulation however does not take into consideration the effects of ring-down in the cavity, which may adversely affect performance due to rapid and large phase changes required.

As well as utilising composite pulses in experiments, work was carried out to investigate protocols to improve sensitivity. This was prompted by difficulties in reproducibility when conducting experiments on HiPER. Signal amplitudes from samples were highly variable at times when using sample tubes made out of quartz. Samples had a tendency to crack, caused by hydrophilic surfaces and the low coefficient of expansion of quartz when cooled. Cracking of the sample increases scattering, and thus the lossiness of the sample. Two new types of sample tubes, one made of Rexolite and the other from Fluorinated Ethylene Propylene (FEP) were tested for use. Both offered better glassing properties due to the hydrophobic surface and more favourable coefficient of expansion when flash frozen. While the Rexolite provided a much larger signal amplitude due to its thinner walls and increased sample volume, it was not resistant to some organic solvents and suffered from losses due to machining processes involved in making the tubes. The FEP tube thus replaced the quartz tube when conducting standard EPR experiments on HiPER, offering a similar sample volume, but with

more reliable results. Additionally, temperature cycling to anneal samples after loading into a pre-cooled cryostat were also examined, showing that warming the sample above its glass transition temperature can also help to alleviate cracking, further improving signal amplitudes and enhancing sensitivity.

Simulations into the use of simple digital filters, known as matched filters to reduce noise in echo measurements showed promising results. In the case of rectangular echoes, with moderate levels of added random noise, SNR could be improved by a factor of 2 by using a best-matched modelled echo filter, and by up to a factor of 3.5 in the case of composite echoes. This was also applied to a mock PELDOR measurement, where a factor of 6 was achieved in the case of rectangular echoes, and a factor of 2 for composite echoes. While this methodology shows great potential to improve signal-to-noise, there are many caveats to the measurement algorithms. All enhancements are compared to the 'typical' traditional HiPER measurement method of 3 sets of cursors, where their width is set at 30% of the echo maximum. However, this disadvantages the composite echo, as its main peak of the echo is extremely narrow, which, puts it at it disadvantage for DC offset removal. It would benefit from some further study to see what effect broadening the DC offset cursors has on SNR of the HiPER measurement algorithm when used on narrow composite pulses. While conducting the mock PELDOR simulation, random noise had a large effect on the overall result, suggesting that the study would also benefit from a larger number of averages, which may require more efficient code to be developed to carry this out, as current attempts required significant time to run on a desktop computer.

The first attempt at composite pulses in PELDOR experiments described in this thesis explored how they might be utilised in the often-used nitroxide-nitroxide experiment. It was discovered through comparison with a mono-radical that the enhancement provided by composite pulses was orientation dependent, with the best performance observed on the edge of the spectrum, in what is known as the Z_3 orientation. Signal amplitude is often limited here as it has the lowest concentration of spins, thus it was fortunate that the composite echo performed best here, as it is the best potential to enhance SNR in this position. Its use in PELDOR experiments on a model nitroxide bi-radical showed that by replacing all inversion π pulses in the PELDOR sequence with composites, up to 1.78 times enhancement in SNR could be achieved, equating to a factor of 3 in averaging time. This was not as large as expected, as the echo simulations indicated that 1.8 times enhancement in echo amplitude should be

achieved in the observer sequence alone, which combined with enhanced modulation depth, the signal level will be increased, thus increasing the overall SNR. This was however not the case. Studies of refocused echo enhancement as a function of orientation revealed a similar, but more severe trend in orientation dependent enhancement in the case of the biradical. By lengthening pulses and thus decreasing the excitation bandwidth, the composite enhancement improved. This suggested some form of spin diffusion was occurring, which was confirmed through T_m studies on both the mono- and bi-radical samples, showing diffusion was strongly present in the case of the bi-radical. Overall, this suggested that the enhancement in excitation bandwidth afforded by the composite pulses has a detrimental effect. However, it suggests that in the case where there is limited applied field amplitude, and pulses are long as a result, composite pulses will be able to provide enhancement in echo amplitude.

The use of composite pulses in measurements between low-spin ferric haem centres and nitroxide spin labels provided an excellent test bed to investigate the advantages of HiPER to conduct such experiments. The first system, human neuroglobin (NGB) was extremely challenging to measure at X-band due to its broad spectra and fast relaxation times. Thus, it seems counter-intuitive that large gains in sensitivity would be achieved when measuring at higher fields, where the spectrum broadens significantly further. However, at higher field the longitudinal relaxation of Fe(III) centre becomes much more favourable at low temperatures, allowing for more waveform averaging per second. Composite pulses were used on the observer sequence to provide enhanced echoes, where they gave enhancements in line with the theoretical simulated maximum, resulting in an improvement in SNR versus standard pulses. This was further improved by replacing the pump pulse with a composite, where it enhanced the modulation depth by 80%. Both were combined in the all-π composite PELDOR sequence achieving a factor of 3.03 times improvement in signal-to-noise versus standard rectangular pulses. This is significant, as it equates to factor of 9 in averaging time, achieved by pulse replacement. In comparison with the measurements at X-band on the NGB-C120R1 system, measurements on HiPER equated to a factor of 31 times improvement in SNR, and a reduction in measurement time from 24 hours to 30 minutes. This result introduces the feasibility of exploring orientation dependent measurements on such systems, as it reduces the measurement time in line with the ubiquitous nitroxide-nitroxide PELDOR experiment. Further study was conducted on another haem-protein, myoglobin, where distances up to 3.2 nm were measured, which at the time of writing is the largest iron-nitroxide distance measured to date. It was also extended to a doubly-labelled nitroxide mutant, where the triangular distance between the

iron centre and the two labels was measured. SNR comparison on the shorter singly-labelled mutant was carried out with PELDOR conducted at Q-band, showing HiPER to provide a 5.5 times enhancement in signal-to-noise. Comparisons of the longitudinal relaxation of the iron centre at Q- and W-band illustrated the field dependent relaxation of such systems as a function of temperature, which according to the literature should scale as $T^{-1}B_0^4$, due to direct relaxation processes becoming dominant at higher fields and the lower temperatures. Thus, large differences in T_1 were observed below 10 K. This meant that measurements conducted at W-band could take advantage of the fast sequence repetition frequency provided by HiPER, to average many more waveforms per second, further improving the signal-to-noise.

In the penultimate chapter of this thesis, the single-frequency RIDME technique was utilised to provide distance and orientation measurements between a metal centre and two nitroxide centres in a rigid model system. This measurement is the first successful demonstration of the dead-time free 5-pulse RIDME experiment to be carried out on HiPER. The Co(II)-(bis)terpyridine model system allowed for comparative orientational measurements between the metal centre and the nitroxide labels using both PELDOR and RIDME, rendering interesting results. It showed that in PELDOR, observer pulses on the metal centre selectively excite a single orientation of spins, which can only be observed when the partner spins are collinear. From this result, combined with the orientation assignment from the $NO^{\bullet}$-$NO^{\bullet}$ osPELDOR, it was discovered that orientation of g-values assigned to the metal centre when ligated by the terpyridine structures given previously in the literature to be incorrect. The osRIDME measurements, conducted by observing on the orthogonal orientations of the nitroxide centre rendered the relative orientation of the $NO^{\bullet}$ labels with respect to the molecular backbone $\vec{r}_{AB}$. This was shown as the dipolar modulation frequency was found to vary as a function of orientation. This result was particularly gratifying as is showed for the first time that RIDME could be utilised to provide orientation measurements between spin labels and extremely broad metal centres. This was made possible here partly due to the rigidity of the system itself, which made assigning relative orientations trivial as a function of modulation depth and dipolar coupling frequency. The extension of this to the haem-proteins as discussed in the previous chapter will be less trivial to resolve due to the flexibility of the MTS nitroxide label that was used. However, the use of more rigid spin labels such as the bipedal Rx label may render orientational measurements using osRIDME much more feasible.

The final chapter of this thesis described the initial work carried out to implement fre-

quency and amplitude modulated pulses on a Bruker X/Q-band spectrometer. Following design of modulation plates, this chapter concerned programming and calibration of the AWG, and calibrating the IQ mixers. It was shown that the effects of amplitude and phase roll-off from the AWG, as well as frequency-dependent amplitude variation in CW mode, could be measured and calibrated out using transfer function estimates and interpolation functions. Protocols to correct for imperfections in the modulated output from the mixers proved the most challenging. A methodology was developed to measure the direct output, down-convert it and filter it, before using the transfer function estimate to produce a corrected waveform through AWG. This was shown to successfully reduce amplitude variations across the pulse width from 3 dB to less than 0.5 dB. The phase variation across the pulse was reduced to less than 5° post correction. This demonstrated that the mixers can be successfully calibrated, however the dependency on both the IF and LO frequency meant that further work is required to implement this fully. Unfortunately due to time constraints and measurement jitter issues, this work was not completed. However, if the AWG is replaced with a much faster version, one will be able to skip this lengthy correction process by generating the modulated IF directly, for example around 1.5 GHz, allowing the use of a standard 3-port mixer and filters to remove LO and LO-IF signals on up-conversion. Nevertheless, this methodology proves that slower, 1 GSa/s AWGs are capable of producing single side-band output on up-conversion from IQ mixers following careful calibration procedures.

Bibliography

[1] Denise R. Ferrier PhD. Biochemistry (Lippincott Illustrated Reviews Series). LWW, 2013. ISBN 1451175620.

[2] Peter P Borbat, Elka R Georgieva, and Jack H Freed. Improved Sensitivity for Long-Distance Measurements in Biomolecules: Five-Pulse Double Electron-Electron Resonance. The journal of physical chemistry letters, 4(1):170–175, jan 2013. ISSN 1948-7185. doi: 10.1021/jz301788n.

[3] Andrew Bowman, Colin M Hammond, Andrew Stirling, Richard Ward, Weifeng Shang, Hassane El-Mkami, David A Robinson, Dmitri I Svergun, David G Norman, and Tom Owen-Hughes. The histone chaperones Vps75 and Nap1 form ring-like, tetrameric structures in solution. Nucleic acids research, 42(9):6038–51, may 2014. ISSN 1362-4962. doi: 10.1093/nar/gku232.

[4] Hassane El Mkami and David G Norman. EPR Distance Measurements in Deuterated Proteins. Methods in enzymology, 564:125–52, jan 2015. ISSN 1557-7988. doi: 10.1016/bs.mie.2015.05.027.

[5] Gunnar W Reginsson and Olav Schiemann. Pulsed electron-electron double resonance: beyond nanometre distance measurements on biomacromolecules. The Biochemical journal, 434(3):353–63, mar 2011. ISSN 1470-8728. doi: 10.1042/BJ20101871.

[6] Christopher W M Kay, Hassane El Mkami, Richard Cammack, and Robert W Evans. Pulsed ELDOR determination of the intramolecular distance between the metal binding sites in Dicupric human serum transferrin and lactoferrin. Journal of the American Chemical Society, 129(16):4868–9, apr 2007. ISSN 0002-7863. doi: 10.1021/ja068966j.

[7] Elka R Georgieva, Trudy F Ramlall, Peter P Borbat, Jack H Freed, and David Eliezer. Membrane-bound alpha-synuclein forms an extended helix: long-distance pulsed ESR measurements using vesicles, bicelles, and rodlike micelles. Journal of the American Chemical Society, 130(39):12856–7, oct 2008. ISSN 1520-5126. doi: 10.1021/ja804517m.

[8] Bela E Bode, Dominik Margraf, Jörn Plackmeyer, Gerd Dürner, Thomas F Prisner, and Olav Schiemann. Counting the monomers in nanometer-sized oligomers by pulsed electron-electron double resonance. Journal of the American Chemical Society, 129(21):6736–45, may 2007. ISSN 0002-7863. doi: 10.1021/ja065787t.

[9] Marina Bennati, John H Robblee, Veronica Mugnaini, Joanne Stubbe, Jack H Freed, and Peter Borbat. EPR distance measurements support a model for long-range radical initia-

tion in E. coli ribonucleotide reductase. Journal of the American Chemical Society, 127 (43):15014–5, nov 2005. ISSN 0002-7863. doi: 10.1021/ja054991y.

[10] Janet E. Banham, Christiane R. Timmel, Rachel J. M. Abbott, Susan M. Lea, and Gunnar Jeschke. The Characterization of Weak ProteinâĂŞProtein Interactions: Evidence from DEER for the Trimerization of a von Willebrand Factor A Domain in Solution. Angewandte Chemie International Edition, 45(7):1058–1061, feb 2006. ISSN 1433-7851. doi: 10.1002/anie.200503720.

[11] R. Ward, M. Zoltner, L. Beer, H. El Mkami, I. R. Henderson, T. Palmer, and D. G. Norman. The Orientation of a Tandem POTRA Domain Pair, of the Beta-Barrel Assembly Protein BamA, Determined by PELDOR Spectroscopy. Structure, 17(9):1187–1194, sep 2009. ISSN 09692126. doi: 10.1016/j.str.2009.07.011.

[12] A D Milov, A B Ponomarev, and Yu.D. Tsvetkov. Electron-electron double resonance in electron spin echo: Model biradical systems and the sensitized photolysis of decalin. Chemical Physics Letters, 110(1):67–72, 1984. ISSN 0009-2614. doi: 10.1016/0009-2614(84)80148-7.

[13] M Pannier, S Veit, A Godt, G Jeschke, and H W Spiess. Dead-time free measurement of dipole-dipole interactions between electron spins. Journal of magnetic resonance (San Diego, Calif. : 1997), 142(2):331–340, dec 2000. ISSN 1090-7807. doi: 10.1006/jmre.1999.1944.

[14] Gregor Hagelueken, Richard Ward, James H Naismith, and Olav Schiemann. MtsslWizard: In Silico Spin-Labeling and Generation of Distance Distributions in PyMOL. Applied magnetic resonance, 42(3):377–391, apr 2012. ISSN 0937-9347. doi: 10.1007/s00723-012-0314-0.

[15] Yevhen Polyhach, Enrica Bordignon, and Gunnar Jeschke. Rotamer libraries of spin labelled cysteines for protein studies. Physical chemistry chemical physics : PCCP, 13(6):2356–66, feb 2011. ISSN 1463-9084. doi: 10.1039/c0cp01865a.

[16] Daniella Goldfarb. Gd(3+) spin labeling for distance measurements by pulse EPR spectroscopy. Physical chemistry chemical physics : PCCP, 16(21):9685–99, may 2014. ISSN 1463-9084. doi: 10.1039/c3cp53822b.

[17] M. Ezhevskaya, E. Bordignon, Y. Polyhach, L. Moens, S. Dewilde, G. Jeschke, and S. Van Doorslaer. Distance determination between low-spin ferric haem and nitroxide spin label using DEER: the neuroglobin case. Molecular Physics, 111(18-19):2855–2864, jul 2013. ISSN 0026-8976. doi: 10.1080/00268976.2013.813592.

[18] Dinar Abdullin, Fraser Duthie, Andreas Meyer, Elisa S. Müller, Gregor Hagelueken, and Olav Schiemann. Comparison of PELDOR and RIDME for Distance Measurements between Nitroxides and Low-Spin Fe(III) Ions. Journal of Physical Chemistry B, 119(43):13539–13542, jun 2015. ISSN 15205207. doi: 10.1021/acs.jpcb.5b02118.

[19] Marilena Di Valentin, Marco Albertini, Enrico Zurlo, Marina Gobbo, and Donatella Carbonera. Porphyrin triplet state as a potential spin label for nanometer distance measure-

ments by PELDOR spectroscopy. Journal of the American Chemical Society, 136(18): 6582–5, may 2014. ISSN 1520-5126. doi: 10.1021/ja502615n.

[20] Ilia Kaminker, Morgan Bye, Natanel Mendelman, Kristmann Gislason, Snorri Th Sigurdsson, and Daniella Goldfarb. Distance measurements between manganese(II) and nitroxide spin-labels by DEER determine a binding site of Mn(2+) in the HP92 loop of ribosomal RNA. Physical chemistry chemical physics : PCCP, 17(23):15098–102, jun 2015. ISSN 1463-9084. doi: 10.1039/c5cp01624j.

[21] A. Dubinskii, Yu Grishin, A. Savitsky, and K. Möbius. Submicrosecond field-jump device for pulsed high-field ELDOR. Applied Magnetic Resonance, 22(3):369–386, sep 2002. ISSN 0937-9347. doi: 10.1007/BF03166118.

[22] Gunnar W. Reginsson, Robert I. Hunter, Paul A S Cruickshank, David R. Bolton, Snorri Th. Sigurdsson, Graham M. Smith, and Olav Schiemann. W-band PELDOR with 1 kW microwave power: Molecular geometry, flexibility and exchange coupling. Journal of Magnetic Resonance, 216:175–182, 2012. ISSN 10907807. doi: 10.1016/j.jmr.2012.01.019.

[23] M A Stevens, J E McKay, J L S Robinson, H El Mkami, G M Smith, and D G Norman. The use of the Rx spin label in orientation measurement on proteins, by EPR. Physical chemistry chemical physics : PCCP, oct 2015. ISSN 1463-9084. doi: 10.1039/c5cp04753f.

[24] Paul A S Cruickshank, David R. Bolton, Duncan A. Robertson, Robert I. Hunter, Richard J. Wylde, and Graham M. Smith. A kilowatt pulsed 94 GHz electron paramagnetic resonance spectrometer with high concentration sensitivity, high instantaneous bandwidth, and low dead time. Review of Scientific Instruments, 80(10):103102, 2009. ISSN 00346748. doi: 10.1063/1.3239402.

[25] Malcolm H. Levitt and Ray Freeman. NMR population inversion using a composite pulse. Journal of Magnetic Resonance, 33(2):473–476, feb 1979. ISSN 00222364. doi: 10.1016/0022-2364(79)90265-8.

[26] A.J Shaka and Ray Freeman. A composite 180° pulse for spatial localization. Journal of Magnetic Resonance (1969), 63(3):596–600, jul 1985. ISSN 00222364. doi: 10.1016/0022-2364(85)90252-5.

[27] T.M Barbara, R Tycko, and D.P Weitekamp. Composite sequences for efficient double-quantum Excitation over a range of spin coupling strengths. Journal of Magnetic Resonance (1969), 62(1):54–64, mar 1985. ISSN 00222364. doi: 10.1016/0022-2364(85)90295-1.

[28] Van D M Koroleva, Soumyajit Mandal, Yi-Qiao Song, and Martin D Hürlimann. Broadband CPMG sequence with short composite refocusing pulses. Journal of magnetic resonance (San Diego, Calif. : 1997), 230:64–75, may 2013. ISSN 1096-0856. doi: 10.1016/j.jmr.2013.01.006.

[29] A J Shaka and A Pines. Symmetric phase-alternating composite pulses. Journal of Magnetic Resonance (1969), 71(3):495–503, 1987. ISSN 0022-2364. doi: 10.1016/0022-2364(87)90249-6.

[30] Smita Odedra and Stephen Wimperis. Use of composite refocusing pulses to form spin echoes. Journal of Magnetic Resonance, 214(1):68–75, 2011. ISSN 10907807. doi: 10.1016/j.jmr.2011.10.006.

[31] R. Tycko. Broadband Population Inversion. Physical Review Letters, 51(9):775–777, aug 1983. ISSN 0031-9007. doi: 10.1103/PhysRevLett.51.775.

[32] R. Tycko and A. Pines. Iterative schemes for broad-band and narrow-band population inversion in NMR. Chemical Physics Letters, 111(4-5):462–467, nov 1984. ISSN 00092614. doi: 10.1016/0009-2614(84)85541-4.

[33] Richard H Crepeau, Antonue DulÇŘć, Jeff Gorcester, Timothy R Saarinen, and Jack H Freed. Composite pulses in time-domain ESR. Journal of Magnetic Resonance (1969), 84(1):184–190, aug 1989. ISSN 00222364. doi: 10.1016/0022-2364(89)90017-6.

[34] Igor V. Koptyug, Stefan H. Bossmann, and Nicholas J. Turro. Inversion-Recovery of Nitroxide Spin Labels in Solution and Microheterogeneous Environments. Journal of the American Chemical Society, 118(6):1435–1445, jan 1996. ISSN 0002-7863. doi: 10.1021/ja952152d.

[35] Philipp E Spindler, Steffen J Glaser, Thomas E Skinner, and Thomas F Prisner. Broadband inversion PELDOR spectroscopy with partially adiabatic shaped pulses. Angewandte Chemie (International ed. in English), 52(12):3425–9, mar 2013. ISSN 1521-3773. doi: 10.1002/anie.201207777.

[36] Thomas Kaufmann, Timothy J. Keller, John M. Franck, Ryan P. Barnes, Steffen J. Glaser, John M. Martinis, and Songi Han. DAC-board based X-band EPR spectrometer with arbitrary waveform control. Journal of Magnetic Resonance, 235:95–108, 2013.

[37] Andrin Doll, Stephan Pribitzer, René Tschaggelar, and Gunnar Jeschke. Adiabatic and fast passage ultra-wideband inversion in pulsed EPR. Journal of Magnetic Resonance, 230:27–39, 2013.

[38] Andrin Doll and Gunnar Jeschke. Fourier-transform electron spin resonance with bandwidth-compensated chirp pulses. Journal of magnetic resonance (San Diego, Calif. : 1997), 246:18–26, sep 2014. ISSN 1096-0856. doi: 10.1016/j.jmr.2014.06.016.

[39] Thorsten Bahrenberg, Yael Rosenski, Raanan Carmieli, Koby Zibzener, Mian Qi, Veronica Frydman, Adelheid Godt, Daniella Goldfarb, and Akiva Feintuch. Improved sensitivity for W-band Gd(III)-Gd(III) and nitroxide-nitroxide DEER measurements with shaped pulses. Journal of Magnetic Resonance, 283:1–13, oct 2017. ISSN 10907807. doi: 10.1016/j.jmr.2017.08.003.

[40] Ilia Kaminker, Ryan Barnes, and Songi Han. Arbitrary waveform modulated pulse EPR at 200 GHz. Journal of Magnetic Resonance, 279:81–90, 2017. ISSN 10960856. doi: 10.1016/j.jmr.2017.04.016.

[41] Claire L. Motion, Janet E. Lovett, Stacey Bell, Scott L. Cassidy, Paul A. S. Cruickshank, David R. Bolton, Robert I. Hunter, Hassane El Mkami, Sabine Van Doorslaer, and Graham M. Smith. DEER Sensitivity between Iron Centers and Nitroxides in Heme-Containing Proteins Improves Dramatically Using Broadband, High-Field EPR. The Journal of Physical Chemistry Letters, 7(8):1411–1415, apr 2016. ISSN 1948-7185. doi: 10.1021/acs.jpclett.6b00456.

[42] L. V. Kulik, S. A. Dzuba, I. A. Grigoryev, and Yu D. Tsvetkov. Electron dipole-dipole interaction in ESEEM of nitroxide biradicals. Chemical Physics Letters, 343(3-4):315–324, aug 2001. ISSN 00092614. doi: 10.1016/S0009-2614(01)00721-7.

[43] Sergey Milikisyants, Francesco Scarpelli, Michelina G Finiguerra, Marcellus Ubbink, and Martina Huber. A pulsed EPR method to determine distances between paramagnetic centers with strong spectral anisotropy and radicals: the dead-time free RIDME sequence. Journal of magnetic resonance (San Diego, Calif. : 1997), 201(1):48–56, nov 2009. ISSN 1096-0856. doi: 10.1016/j.jmr.2009.08.008.

[44] Andreas Meyer, Dinar Abdullin, Gregor Schnakenburg, Olav Schiemann, G. R. Eaton, S. S. Eaton, A. Kutateladze, F. Neese, H. Jung, and N. Scrutton. Single and double nitroxide labeled bis(terpyridine)-copper(ii): influence of orientation selectivity and multispin effects on PELDOR and RIDME. Phys. Chem. Chem. Phys., 18(13):9262–9271, mar 2016. ISSN 1463-9076. doi: 10.1039/C5CP07621H.

[45] Angeliki Giannoulis, Maria Oranges, and Bela E. Bode. Monitoring Complex Formation by Relaxation-Induced Pulse Electron Paramagnetic Resonance Distance Measurements. ChemPhysChem, jul 2017. ISSN 14394235. doi: 10.1002/cphc.201700666.

[46] Katharina Keller, Andrin Doll, Mian Qi, Adelheid Godt, Gunnar Jeschke, and Maxim Yulikov. Averaging of nuclear modulation artefacts in RIDME experiments. Journal of Magnetic Resonance, 272:108–113, nov 2016. ISSN 10907807. doi: 10.1016/j.jmr.2016.09.016.

[47] Arthur Schweiger and Gunnar Jeschke. Principles of Pulse Electron Paramagnetic Resonance. Oxford University Press, 2001.

[48] Charles Poole. Electron spin resonance : a comprehensive treatise on experimental techniques. Wiley, New York u.a, 1967. ISBN 978-0470693865.

[49] Malcolm H Levitt. Composite Pulses. In eMagRes, pages 1396–1411. Wiley, Chichester, UK, 2007. ISBN 9780470034590. doi: 10.1002/9780470034590.emrstm0086.

[50] A Abragam and B Bleaney. Electron paramagnetic resonance of transition ions. Clarendon Press, Oxford, 1970. ISBN 978-0-19-965152-8.

[51] Peter P Borbat and Jack H Freed. Pulse Dipolar Electron Spin Resonance: Distance Measurements, pages 1–82. Springer Berlin Heidelberg, Berlin, Heidelberg, 2013. ISBN 978-3-642-39125-5. doi: 10.1007/430_2012_82.

[52] Gunnar Jeschke, Yevhen Polyhach, M. J. E. Sternberg, E. Perozo, P. Fajer, M. Huber, S. S. Eaton, H. K. Kroh, L. Song, C. E. Cobb, E. J. Hustedt, and A. H. Beth. Distance measurements on spin-labelled biomacromolecules by pulsed electron paramagnetic resonance. Physical Chemistry Chemical Physics, 9(16):1895, apr 2007. ISSN 1463-9076. doi: 10.1039/b614920k.

[53] G. E. Pake. Nuclear Resonance Absorption in Hydrated Crystals: Fine Structure of the Proton Line. The Journal of Chemical Physics, 16(4):327–336, apr 1948. ISSN 0021-9606. doi: 10.1063/1.1746878.

[54] F. Bloch, W. W. Hansen, and Martin Packard. Nuclear Induction. Physical Review, 69 (3-4):127–127, 1946. ISSN 0031-899X. doi: 10.1103/PhysRev.69.127.

[55] J.E. Wertz and J.R. Bolton. Electron spin resonance: elementary theory and practical applications. Chapman and Hall, 1986. ISBN 9780412011610.

[56] Olav Schiemann and Thomas F Prisner. Long-range distance determinations in biomacromolecules by EPR spectroscopy. Quarterly reviews of biophysics, 40(1):1–53, feb 2007. ISSN 0033-5835. doi: 10.1017/S003358350700460X.

[57] G. Jeschke, V. Chechik, P. Ionita, A. Godt, H. Zimmermann, J. Banham, C. R. Timmel, D. Hilger, and H. Jung. DeerAnalysis2006âĂŤa comprehensive software package for analyzing pulsed ELDOR data. Applied Magnetic Resonance, 30(3-4):473–498, jun 2006. ISSN 0937-9347. doi: 10.1007/BF03166213.

[58] Malcolm H Levitt. Symmetrical composite pulse sequences for NMR population inversion. I. Compensation of radiofrequency field inhomogeneity. Journal of Magnetic Resonance, 48(2):234–264, 1982. ISSN 0022-2364. doi: 10.1016/0022-2364(82)90275-X.

[59] R. Tycko, a. Pines, and J. Guckenheimer. Fixed point theory of iterative excitation schemes in NMR. The Journal of Chemical Physics, 83(6):2775, 1985. ISSN 00219606. doi: 10.1063/1.449228.

[60] A Tannús and M Garwood. Adiabatic pulses. NMR in biomedicine, 10(8):423–34, dec 1997. ISSN 0952-3480.

[61] J Baum, R Tycko, and A Pines. Broadband and adiabatic inversion of a two-level system by phase-modulated pulses. Phys. Rev. A, 32(6):3435–3447, dec 1985.

[62] Stefan Stoll and Arthur Schweiger. EasySpin, a comprehensive software package for spectral simulation and analysis in EPR. Journal of magnetic resonance (San Diego, Calif. : 1997), 178(1):42–55, jan 2006. ISSN 1090-7807. doi: 10.1016/j.jmr.2005.08.013.

[63] Claudia E. Tait and Stefan Stoll. Coherent pump pulses in Double Electron Electron Resonance spectroscopy. Phys. Chem. Chem. Phys., 18(27):18470–18485, 2016. ISSN 1463-9076. doi: 10.1039/C6CP03555H.

[64] Stephen Maas. The RF and microwave circuit design cookbook. Artech House, Boston, 1998. ISBN 0-89006-973-5.

[65] Jesse B. Hopkins, Ryan Badeau, Matthew Warkentin, and Robert E. Thorne. Effect of common cryoprotectants on critical warming rates and ice formation in aqueous solutions. Cryobiology, 65(3):169–178, dec 2012. ISSN 00112240. doi: 10.1016/j.cryobiol.2012.05.010.

[66] Joseph Kestin, Mordechai Sokolov, and William A. Wakeham. Viscosity of liquid water in the range âĹŠ8 ÂřC to 150 ÂřC. Journal of Physical and Chemical Reference Data, 7 (3):941–948, jul 1978. ISSN 0047-2689. doi: 10.1063/1.555581. URL http://aip.scitation.org/doi/10.1063/1.555581.

[67] Debamalya Banerjee and S. V. Bhat. Vitrification, relaxation and free volume in glycerol-water binary liquid mixture: Spin probe ESR studies. Journal of Non-Crystalline Solids, 355(50-51):2433–2438, dec 2009. ISSN 00223093. doi: 10.1016/j.jnoncrysol.2009.08.045.

[68] Debamalya Banerjee, Shrivalli N Bhat, Subray V Bhat, and Dino Leporini. Molecular probe dynamics reveals suppression of ice-like regions in strongly confined supercooled water. PloS one, 7(9):e44382, jan 2012. ISSN 1932-6203. doi: 10.1371/journal.pone.0044382.

[69] Graham M. Smith, Paul A. S. Cruickshank, David R. Bolton, and Duncan A. Robertson. Electron Paramagnetic Resonance, volume 21 of Electron Paramagnetic Resonance. Royal Society of Chemistry, Cambridge, dec 2008. ISBN 978-0-85404-373-6. doi: 10.1039/9781847558886.

[70] David E. Budil and Keith A. Earle. Sample Resonators for Quasioptical EPR. In Biological Magnetic Resonance, volume 22, pages 353–399. 2004. doi: 10.1007/978-1-4757-4379-1_11.

[71] G. Turin. An introduction to matched filters. IEEE Transactions on Information Theory, 6(3):311–329, jun 1960. ISSN 0018-9448. doi: 10.1109/TIT.1960.1057571.

[72] Gunnar Jeschke. Instrumentation and Experimental Setup. In ESR Spectroscopy in Membrane Biophysics, pages 17–47. Springer US, Boston, MA, 2007. doi: 10.1007/978-0-387-49367-1_2.

[73] A D Olver, P J B Clarricoats, A A Kishk, and L Shafai. Microwave Horns and Feeds. IET, The Institution of Engineering and Technology, Michael Faraday House, Six Hills Way, Stevenage SG1 2AY, UK, jan 1994. ISBN 0780311159. doi: 10.1049/PBEW039E.

[74] P.B. J. Clarricoats and A.D. Olver. Corrugated horns for microwave antennas. Electromagnetic Waves. Institution of Engineering and Technology, 1984. ISBN 0863410030, 9780863410031. doi: 10.1049/PBEW018E.

[75] Emilio A. Nanni, Alexander B. Barnes, Yoh Matsuki, Paul P. Woskov, Bjorn Corzilius, Robert G. Griffin, and Richard J. Temkin. Optimization of THz wave coupling into samples in DNP/NMR spectroscopy. In 35th International Conference on Infrared, Millimeter, and Terahertz Waves, pages 1–3. IEEE, sep 2010. ISBN 978-1-4244-6655-9. doi: 10.1109/ICIMW.2010.5612956.

[76] SteÌĄfan van der Walt, S Chris Colbert, and GaeÌĺl Varoquaux. The NumPy Array: A Structure for Efficient Numerical Computation. Computing in Science & Engineering, 13 (2):22–30, mar 2011. ISSN 1521-9615. doi: 10.1109/MCSE.2011.37.

[77] Eric Jones, Travis Oliphant, Pearu Peterson, et al. SciPy: Open source scientific tools for Python, 2001–. URL http://www.scipy.org/. [Online; accessed 15/09/2017].

[78] Marius M. Haugland, Edward A. Anderson, and Janet E. Lovett. Tuning the properties of nitroxide spin labels for use in electron paramagnetic resonance spectroscopy through chemical modification of the nitroxide framework. volume 25, pages 1–34. Royal Society of Chemistry, 2017. doi: 10.1039/9781782629436-00001.

[79] Gunnar Jeschke, Muhammad Sajid, Miriam Schulte, Navid Ramezanian, Aleksei Volkov, Herbert Zimmermann, and Adelheid Godt. Flexibility of shape-persistent molecular building blocks composed of p-phenylene and ethynylene units. Journal of the American Chemical Society, 132(29):10107–10117, jul 2010. ISSN 00027863. doi: 10.1021/ja102983b.

[80] F. Mentink-Vigier, A. Collauto, A. Feintuch, I. Kaminker, V. Tarle, and D. Goldfarb. Increasing sensitivity of pulse EPR experiments using echo train detection schemes. Journal of Magnetic Resonance, 236:117–125, 2013.

[81] Sabine Van Doorslaer. Probing the StructureâĂŞFunction Relationship of Heme Proteins Using Multifrequency Pulse EPR Techniques. pages 397–417. Springer New York, 2009. doi: 10.1007/978-0-387-84856-3_8.

[82] L. Charles Dickinson and M. C. R. Symons. Electron spin resonance of haemoglobin and myoglobin. Chemical Society Reviews, 12(4):387–414, jan 1983. ISSN 0306-0012. doi: 10.1039/cs9831200387.

[83] Libretexts. Crystal field theory, Jun 2017. URL https://chem.libretexts.org/Core/Inorganic_Chemistry/Crystal_Field_Theory/Crystal_Field_Theory. [Online; accessed 20/09/2017].

[84] Thorsten Burmester, Bettina Weich, Sigrid Reinhardt, and Thomas Hankeln. A vertebrate globin expressed in the brain. Nature, 407(6803):520–523, sep 2000. ISSN 00280836. doi: 10.1038/35035093.

[85] Thorsten Burmester and Thomas Hankeln. What is the function of neuroglobin? Journal of Experimental Biology, 212(10), 2009.

[86] Y Zhou, B E Bowler, K Lynch, S S Eaton, and G R Eaton. Interspin distances in spin-labeled metmyoglobin variants determined by saturation recovery EPR. Biophysical journal, 79 (2):1039–52, aug 2000. ISSN 0006-3495. doi: 10.1016/S0006-3495(00)76358-2.

[87] Stacey Bell and Stacey. Site-directed spin-labelling of proteins for EPR spectroscopy : application to protein complexes and development of new methods for cysteine rich proteins. jun 2016.

[88] G I Hanania, A Yeghiayan, and B F Cameron. Absorption spectra of sperm-whale ferrimyoglobin. The Biochemical journal, 98(1):189–92, jan 1966. ISSN 0264-6021.

[89] Evi Vinck, Sabine Van Doorslaer, Sylvia Dewilde, and Luc Moens. Structural change of the heme pocket due to disulfide bridge formation is significantly larger for neuroglobin than for cytoglobin. Journal of the American Chemical Society, 126(14):4516–7, apr 2004. ISSN 0002-7863. doi: 10.1021/ja0383322.

[90] A. M. Witowski, C. Kutter, and P. Wyder. Spin-Lattice Relaxation at High Magnetic Fields: A Tool for Electron-Phonon Coupling Studies. Physical Review Letters, 78(20):3951–3954, may 1997. ISSN 0031-9007. doi: 10.1103/PhysRevLett.78.3951.

[91] S. S. Eaton, J. Harbridge, G. A. Rinard, G. R. Eaton, and R. T. Weber. Frequency dependence of electron spin relaxation for threeS = 1/2 species doped into diamagnetic solid hosts. Applied Magnetic Resonance, 20(1-2):151–157, feb 2001. ISSN 0937-9347. doi: 10.1007/BF03162316.

[92] K. Ackermann, A. Giannoulis, D. B. Cordes, A. M. Z. Slawin, B. E. Bode, J. Banham, C. R. Timmel, D. Hilger, and H. Jung. Assessing dimerisation degree and cooperativity in a biomimetic small-molecule model by pulsed EPR. Chem. Commun., 51(25):5257–5260, mar 2015. ISSN 1359-7345. doi: 10.1039/C4CC08656B.

[93] S. Kremer, W. Henke, and D. Reinen. High-spin-low-spin equilibriums of cobalt(2+) in the terpyridine complexes Co(terpy)2X2.nH2O. Inorganic Chemistry, 21(8):3013–3022, aug 1982. ISSN 0020-1669. doi: 10.1021/ic00138a019.

[94] Evelyn Narr, Herbert Zimmermann, Adelheid Godt, Daniella Goldfarb, and Gunnar Jeschke. Structure and dynamics of copper complexes with 2,2âĂš:6âĂš,2âĂş-terpyridines in glassy matrices. Phys. Chem. Chem. Phys., 5(18):3959–3967, sep 2003. ISSN 1463-9076. doi: 10.1039/B305764J.

[95] M3202a pxie arbitrary waveform generator, 1 gsa/s, 14 bit, 400 mhz. URL http://www.keysight.com/en/pd-2747446-pn-M3202A/pxie-arbitrary-waveform-generator-1-gs-s-14-bit-400-mhz?pm=PL&nid=-33321.1193058&cc=GB&lc=eng.

[96] Atlantic Microwave. Coaxial cable assemblies standard lengths - asf series 0.141 reformable copper/tin composite sma male connectors. URL http://www.atlantecrf.com/products/cable_assemblies_cables_adapters_&_connectors/cable_assemblies/coaxial_cable_assemblies_asf_141.htm.

[97] Michael Garwood and Lance DelaBarre. The Return of the Frequency Sweep: Designing Adiabatic Pulses for Contemporary NMR. Journal of Magnetic Resonance, 153(2):155–177, dec 2001. ISSN 10907807. doi: 10.1006/jmre.2001.2340.

[98] Petre Stoica. Spectral analysis of signals. Pearson/Prentice Hall, Upper Saddle River, N.J, 2005. ISBN 0-13-113956-8.

[99] P. Welch. The use of fast Fourier transform for the estimation of power spectra: A method based on time averaging over short, modified periodograms. IEEE Transactions on Audio and Electroacoustics, 15(2):70–73, jun 1967. ISSN 0018-9278. doi: 10.1109/TAU.1967.1161901.